

APL TDR 64-82

RESEARCH AND DEVELOPMENT OF FLUID AMPLIFIERS FOR TURBOPROPULSION SYSTEM CONTROL

June 30, 1964

DSR 9159-2

Department of Mechanical
Engineering
Massachusetts Institute of
Technology

Contract AF 33(657)-8384

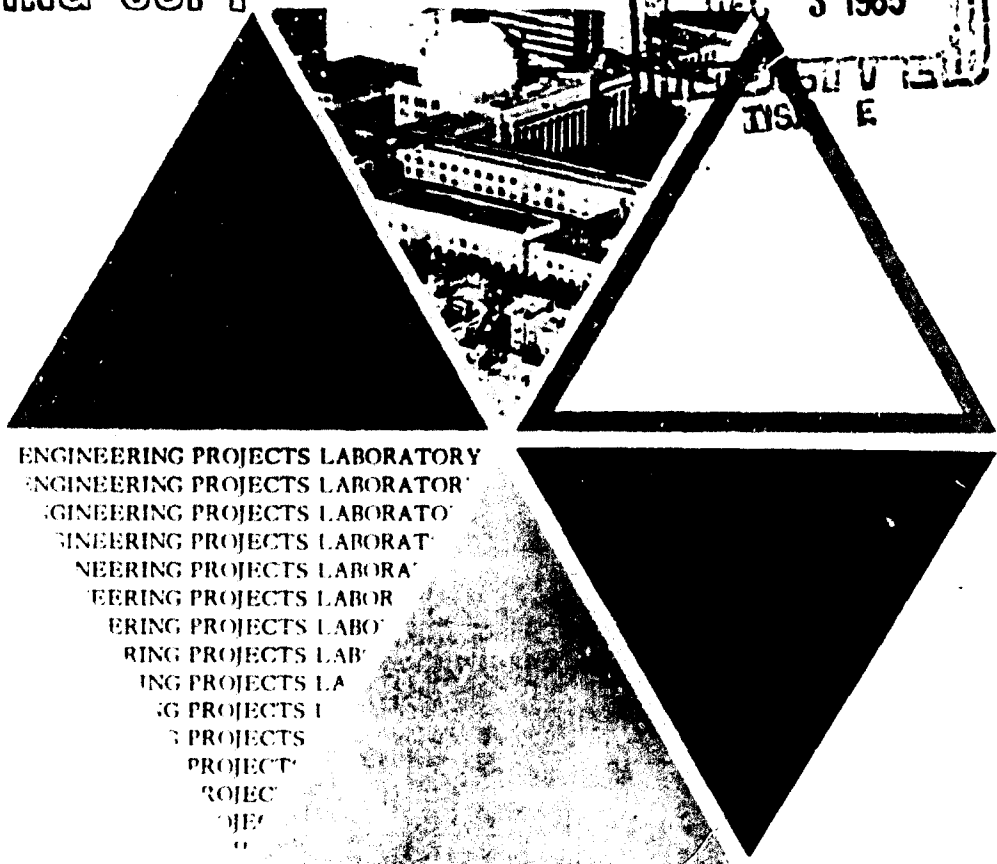
AD624091

CLEARINGHOUSE FOR FEDERAL SCIENTIFIC AND TECHNICAL INFORMATION	
Hardcopy	Microfiche
\$6.00	\$1.50 2/1/65
ARCHIVE COPY	

PROCESSING COPY

Code 1

DDC
DEC 3 1965
U.S. GOVERNMENT
PRINTING OFFICE



ENGINEERING PROJECTS LABORATORY
ENGINEERING PROJECTS LABORATOR
ENGINEERING PROJECTS LABORATO
ENGINEERING PROJECTS LABORAT
ENGINEERING PROJECTS LABORA
ENGINEERING PROJECTS LABOR
ENGINEERING PROJECTS LABO
ENGINEERING PROJECTS LAB
ENGINEERING PROJECTS LA
ENGINEERING PROJECTS I
ENGINEERING PROJECTS
ENGINEERING PROJECT
ENGINEERING PROJEC
ENGINEERING PROJEC

**Best
Available
Copy**

NOTICES

When Government drawings, specifications, or other data are used for any purpose other than in connection with a definitely related Government procurement operation, the United States Government thereby incurs no responsibility nor any obligation whatsoever; and the fact that the Government may have formulated, furnished, or in any way supplied the said drawings, specifications, or other data, is not to be regarded by implication or otherwise as in any manner licensing the holder or any other person or corporation, or conveying any rights or permission to manufacture, use or sell any patented invention that in any way be related thereto.

Qualified requesters may obtain copies of this report from the Defense Documentation Center (DDC), (formerly ASTIA), Cameron Station, Bldg. 5, 5010 Duke Street, Alexandria, Virginia, 22314.

This report has been released to the Office of Technical Services, U. S. Department of Commerce, Washington 25, D.C. for sale to the general public.

Copies of this report should not be returned to the Research and Technology Division, Wright-Patterson Air Force Base, Ohio, unless return is required by security considerations, contractual obligations, or notice on a specific document.

APL TDR 64-82

RESEARCH AND DEVELOPMENT OF FLUID AMPLIFIERS FOR
TURBOPROPULSION SYSTEM CONTROL

TECHNICAL DOCUMENTARY REPORT NO. APL TDR 64-82

JUNE 30, 1964

AF Aero Propulsion Laboratory
Research and Technology Division
Air Force Systems Command
Wright-Patterson Air Force Base, Ohio

Project No. 3066, Task No. 306603

(Prepared under Contract No. AF 33(657)-8384 by the Engineering
Projects Laboratory, Massachusetts Institute of Technology, Cambridge
Massachusetts - 02139).

FOREWORD

This is the final report of the Engineering Projects Laboratory's two-year contract AF 33(657)-8384 with the Aero Propulsion Laboratory, Research and Technology Division, U. S. Air Force, Wright-Patterson Air Force Base, Ohio. Together with the first annual report (DSR 9159-1), a professional paper, and some theses, written and not yet written, it contains the salient results of the study.

Principal direction has been by F. T. Brown, Assistant Professor of Mechanical Engineering, although until his departure from M. I. T. in July 1963, J. L. Shearer, Associate Professor of Mechanical Engineering provided general direction. The following are largely responsible for their respective chapters:

Chapter 1	F. T. Brown
Chapter 2	K. N. Reid, Instructor
Chapter 3	R. J. Gurski, Instructor
Chapter 4	F. T. Brown
Chapter 5	S. D. Graber, Research Assistant
Chapter 6	A. H. Greenleaf, Research Assistant
Chapter 7	W. B. Bails, Research Assistant (written by F. T. Brown)

ABSTRACT

Techniques for sensing the relative threat of flow instabilities in jet engines have been a long sought-after goal. This is the final report of a study aimed at determining the feasibility of certain types of fluid jet amplifiers used as fast pressure and temperature sensors. The background of the project, the environment in which the fluid sensors must operate, and initial results have been presented in the first annual report.

The more theoretical aspects of the present report include a study of the statics and dynamics of the interaction of a fluid jet and a receiver port, the dynamics of the controlled deflections of jets in fluid amplifiers, and the dynamic analysis of fluid systems. The more applied aspects include the design of a fluid-relay stall-cell sensor, a fluid diode possibly useful for sensing blade wakes or stall cells, and a unique reference-frequency pneumatic oscillator.

TABLE OF CONTENTS

1.	INTRODUCTION	1
2.	JET-RECEIVER STUDIES	4
	2.1. Background	4
	2.2. Receiver-Diffuser Steady-State Performance	5
	2.3. Jet-Receiver Dynamic Interaction Studies	33
3.	DYNAMIC ANALYSIS OF CONTROLLED JET DEFLECTION	101
	3.1. LaPlace Transform Solution of the Jet Equations	101
	3.2. Solution of the Jet Equations Using Various Finite Difference Approximations to the Space Derivatives	111
	3.3. Characteristic Curves of Partial Differential Equations	118
	3.4. Generalized Transmission Processes	123
	3.5. Monotone Processes	128
	3.6. A Possible Model for the Fluid Jet Modulator	135
4.	THE DYNAMICS OF SYSTEMS	140
	4.1. The Transmission of Waves in Lines	140
	4.2. The Stability of Fluid Systems	141
5.	STALL CELL SENSOR	142
	5.1. Introduction	142
	5.2. Bistable Jet Amplification	142
	5.3. Theoretical Study	144
	5.4. Experimental Study	155
	5.5. Conclusions	164
6.	DESIGN OF A TEMPERATURE-INSENSITIVE PNEUMATIC OSCILLATOR	167
	6.1. Introduction	167
	6.2. Circular-Motion Oscillator	169
	6.3. Problems Affecting the Configuration	170
	6.4. Stability Analysis for Continuous $F(r)$	170
	6.5. Temperature Compensation	180
	6.6. Lateral Stiffness of the Springs as a Function of the Compression	182
	6.7. Configurations to Provide Driving Force and Output	186
	6.8. Design of the Springs	197
	6.9. Construction of the Third Oscillator	198

	6.10. Testing of the Third Oscillator	205
	6.11. Conclusions	210
	6.12. Other Oscillators	212
7.	FLUID DIODE SENSOR	220
	7.1. Introduction and Summary	220
	7.2. Dynamic Analysis	220
	7.3. Static Testing - Small Scale Models	227
	7.4. Dynamic Testing - Small Scale Models	227
	7.5. Static Testing - Tesla Diode	227
8.	REFERENCES	255

LIST OF FIGURES

1.	Concept of Velocity Profile Uniformity	7
2.	Velocity Profile Smoothing in a Constant-Area Passage	8
3.	Constant-Area Diffusion of Nonuniform Streams	12
4.	Velocity Profile Development in a Circular Constant-Area Duct Displaced 15 Diameters from an Axially-Aligned Nozzle	13
5.	Typical Pressure Efficiency for Area Change Diffusers	25
6.	Flow Conditions in a 7.5° Diffuser with Five Diameters of Entry Length; Reynolds No. = 2×10^6 (Ref. 25)	27
7a.	Definition of Diffuser Variables	29
7b.	Influence of Diffuser Geometry on Point of Maximum Static Pressure Recovery	29
8.	Effect of Entrance and Exit Section Length on Diffuser Pressure Efficiency (Ref. 16)	30
9.	Schematic of Apparatus for Studying Steady-State Characteristics of a Three-Way Jet Modulator	34
10.	Pressure-Flow Characteristics of a Three-Way Modulator	35
11.	Demonstrated "Active" Sources	38
12.	Block Diagram of Single-Receiver Jet-Modulator System	40
13.	Typical Passive and Active Source Characteristics	40
14.	Concept of Static Stability "In-the-Small"	42
15.	Experimental Technique for Determining the Characteristic Curve of a Passive Source	44
16.	Concept of Point-By-Point Measurement of an Active Source Characteristic	45
17.	Experimental Technique for Determining the Static Characteristics of an Active Source	46
18.	Measured Static Characteristic of an Active Source	48
19.	Active Source Coupled to a Transmission Line Blocked at its Downstream End	55
20.	Attenuation per Cycle of Small Amplitude Sine Waves in Rigid, Isothermal Wall, Laminar-Flow, Circular Air Line	61

21.	Magnitude of Line Characteristic Impedance	62
22.	Graphical Interpretation of Eq. (38)	66
23.	Graphical Stability Analysis of an Active Source Coupled to a Lossless Transmission Line	67
24.	Graphical Stability Analysis of an Active Source Transmission Line System Including Effects of Line Friction	68
25.	Active Source Coupled to a Load Chamber	70
26.	Graphical Interpretation of Eqs. (40), (42) and (43)	73
27.	Graphical Solutions for an Active Source Coupled to a Capacitive Plus Resistive Load	74
28.	Active Source Coupled to a Transmission Line Terminated by a Load Chamber and Resistance	76
29.	Graphical Interpretation of Eqs. (45), (46), (47), (48) and (49)	78
30.	Graphical Stability Analysis of an Active Source Coupled to a Lossless Transmission Line Terminated by Capacitive Plus Resistive Load	79
31.	Transmission Line Divided into 4-Sections	81
32.	Graphical Interpretation of Example 3 for a Line Divided into Four Sections	82
33.	Surge Frequency of a Lossless Transmission Line Terminated by a Simple Tank	90a
34.	Pressure Oscillations at the Blocked End (Downstream) of a Constant Diameter Transmission Line Coupled to an Active Source. (Conf. 3)	92
35.	Comparison of Predicted and Experimental Measurements of Pressure Oscillation Amplitude for an Active Source Coupled to a Transmission Line	94
36.	Pressure Oscillations in a Blocked Chamber Coupled to an Active Source (Conf. 3)	95
37.	Pressure Oscillations in a Blocked Chamber Coupled to an Active Source (Conf. 3)	96
38.	Comparison of Theoretical and Experimental Surge Frequencies of a Transmission Line Terminated by a Simple Chamber	98
39.	Experimental Measurements of Pressure Oscillation Amplitude in a Chamber Coupled to an Active Source by Means of a Six-inch Line	99
40.	Comparison of Predictions and Experimental Measurements of Pressure Oscillation Amplitude for an Active Source Coupled to a Transmission Line Terminated by a Chamber	100

41.	Control Volume Around a Segment of Jet	102
42.	Step Change in Pressure Over a Finite Distance	105
43.	Response of Jet Equations to Step and Exponential Inputs	108
44.	Computed Jet Equation Response - Case I - Step Input	113
45.	Computed Jet Equation Response - Case V - Step Input	116
46.	Computed Jet Equation Response - Case V - Exponential Input	117
47.	Characteristic Curves for Wave Equation	119
48.	Finite Difference Solution of Wave Equation	120
49.	Characteristic Curve for Jet Equation	122
50.	Step Response of a Monotone	129
51.	Frequency Response of a Monotone	129
52.	Step Response of a Simple Lag	129
53.	Monotone Approximations for Jet Equations	133
54.	Non-Functional Block Diagram of a Pressure Controlled Fluid Jet Modulator	136
55.	Functional Block Diagram of a Pressure Controlled Fluid Jet Modulator	138
56.	Discharge Region Giving Static Instability	143
57.	Discharge Region With Control Lines Added	143
58.	Proposed Stall Sensing Arrangement	145
59.	Stall Sensor Unit	146
60.	Jet In Vicinity of Knife Edge	148
61.	Dimensional Limits for Bistable Operation	151
62.	Atmospheric Flow Coefficient from Van Koeving Data	153
63.	Solution of Eq. (168) for $X_0' = 4.36$, $AR = 3.02$	156
64.	Test Model With Receiver Tubes Installed	157
65.	Separation Pocket formed With Attached Jet Small β and Large l Favor Reattachment	158
66.	Schematic of Dynamic Test Set Up	160
67.	Dynamic Test Apparatus	161
68.	Random Flipping of Jet Due to Control Port Noise	163
69.	Pulse-Width-Modulator Input Signal	165
70.	Dynamic Test Results with 25 per cent Modulation	166

71.	Jet Amplifier-Oscillator	168
72.	Vibrating Shaft and Disk	168
73.	A Suggested Driving-Force Versus Radius Curve	168
74.	Stability of an Oscillator with a Discontinuous Driving Force	171
75.	General Oscillator Configuration for the Stability Analysis	171
76.	Inverse Nyquist Plot for System Without Load or Lag	175
77.	Interpretation of Stability Analysis	175
78.	Inverse Nyquist Plot for System With Lag.	175
79.	Inverse Nyquist Plot for System with Load	178
80.	Hypothetical Disk Motion	178
81.	Notation for Analysis of Oscillator with Movable End Support	178
82.	Variation of Modulus of Elasticity with Temperature	181
83.	Temperature-Compensating Oscillator	181
84.	Cantilever Beam with Lateral and Axial End Loads	183
85.	Modification of Fig. 84.	183
86.	First Test Oscillator	187
87.	Radial Flow Force on the Edge of a Disk	187
87a.	Photograph of First Test Oscillator	187a
88.	Second Test Oscillator	189
89.	Disk-Hole and Flow Configurations	189
89b.	Photograph of Second Test Oscillator	189a
90.	Oscillator with a Pneumatic Lag in the Amplitude-Sensing Mechanism	191
91.	Third Test Oscillator Driving Mechanism	191
93.	Third Oscillator Driving Forces for a Given Displacement	193
94.	Effective Area Versus Radius	193
95.	Other Damping Curves	195
96.	$r/d/A/d^2$ and $A/d^2/r/d$ Versus r/d	195
97.	Temperature-Insensitive Pneumatic Oscillator	200
98.	Detail of Vibrating Disk	201
99.	Third Test Model Assembly	202
99a.	Photograph of Third Test Model Assembly	202a

100.	Third Oscillator Test Setup	206a
101a.	Third Oscillator Output (Tracings from Photographs)	207
101b.	Third Oscillator Output (Tracings from Photographs)	208
102.	Results of Frequency-Tension Test	209
103.	Jet Amplifier-Controlled Oscillator	211
105.	Another Oscillator	213
106.	Housing Detail	214
107.	Detail of Vibrating Disk	215
108.	Outlet Port Plate Detail	216
109.	Inlet Port Plate Detail	217
110.	Bottom Support Detail	218
111.	Top Support Detail	219
112.	Nonlinear Analysis of Response to Step-Function "Unsaturated" Case	223
113.	Nonlinear Analysis of Single Diode Sensor, Forward, $\Delta\tau/\tau\omega = 0.7$	224
114.	Nonlinear Analysis of Single Diode Sensor, Reversed $\Delta\tau/\tau_{av} = 0.7$	225
115.	Nonlinear Analysis of Pressure Difference in Diode Sensors With Opposite Polarity $\Delta\tau/\tau\omega = 0.7$	226
116.	Frequency Response, 3-D Nozzle Diode (0.040) Forward, With Linear and Nonlinear Theory	228
117.	Frequency Response - 3-D Nozzle Diode (0.040) Reverse, With Linear and Nonlinear Theory	229
118.	Nonlinear Analysis of Pressure Difference in Diode Sensors With Opposite Polarity $\Delta\tau/\tau = 0.156$	230
119a.	3-D Nozzle Diode, Small Scale	231
119b.	2-D Nozzle Diode, Small Scale	231
120a.	Vortex Diode, Small Scale	232
120b.	Diffuser Diode, Small Scale	232
121.	Pressure-Flow Characteristics, 3-D Nozzle Diode (0.040), Small Scale	233
122.	Pressure-Flow Characteristics, 3-D Nozzle Diode, Small Scale (0.020)	234
123.	Pressure-Flow Characteristics, 2-D Nozzle Diode, Small Scale	235
124.	Pressure-Flow Characteristics, Vortex Diode, Small Scale	236
125.	Pressure-Flow Characteristics, Diffuser Diode, Small Scale	237
126.	Test Set Up Schematic	238

127.	Pressure Pulse Generator	239
128.	Signal From Pulse Generator	240
129.	Frequency Response, 2-D Nozzle Diode	241
130.	Frequency Response, 3-D Nozzle Diode (0.020)	242
131.	Pressure Difference, 3-D Nozzle Diode (0.040)	243
132.	Frequency Response, Vortex Diode, Reverse	244
133.	Frequency Response, Vortex Diode, Forward	245
134.	Pressure Difference, Vortex Diode	246
135.	Frequency Response, Diffuser Diode, Reverse	247
136.	Frequency Response, Diffuser, Diode, Forward	250
137.	Pressure Difference, Diffuser Diode	251
138.	Photograph of Tesla Diode	252
139.	Results of Static Measurements of Tesla Diode	254

1. INTRODUCTION

Techniques for sensing the relative threat of flow instabilities in jet engines have been a long sought-after goal. The present study has been directed toward the possible use of fluid jet amplifiers with no moving parts to sense stall cells and blade-wake widths, and to extend the basic knowledge of these complex 6-port amplifiers which also have many other military and non-military uses. In addition, a pneumatic oscillator was developed, using some moving but non-sliding parts, which has a frequency largely insensitive to pressure and temperature changes.

The background of the present project, the environment in which fluid sensors must operate, and initial results under the contract are presented in the first annual report.

The Engineering Projects Laboratory depends on Master's and Doctor's degree candidates for the bulk of its effort. It is impossible to accurately predict, let alone control, the durations of several adequate thesis investigations, particularly at the doctorate level. Consequently, only two Master's theses have been completed under the contract (a third was abortive), while two most pertinent doctoral theses and one Master's thesis are unfinished, a fact reflected in this report. Estimated completion dates for all three are in August of this year. All theses are or will be available at cost from the Engineering Projects Laboratory, Document Room 3-154, M.I.T., Cambridge 39, Massachusetts.

The first few chapters emphasize the more theoretical aspects of the work, and the last few the more practical. Chapter 2 describes an extensive study by K. N. Reid into the statics and dynamics of the interaction of a fluid jet and a receiver port. A partially-theoretical partially-experimental approach toward static diffuser optimization with a non-uniform inlet-velocity profile is presented, although the experimental work itself is as yet mostly undone. The dynamics of fluid lines with a jet incident at one

Manuscript released by the authors June 1964 for publication as an RTD Technical Documentary Report.

end was investigated in detail both analytically and experimentally, with good agreement. It is shown that most oscillations can be quantitatively predicted from static measurements of the active upstream pressure-flow characteristics at the jet-end of the line, plus theoretical considerations for the passive part of the line and associated volumes, restrictions, etc. Viscous wall shear is shown to substantially dampen most oscillations. (L. E. Johnston, a doctoral fellowship student unsupported by this contract, is studying the problem of two parallel lines coupled by a jet incident at one end.)

The dynamics of the controlled deflection of jets in fluid amplifiers and relays is the subject of Chapter 3, prepared by R. J. Gurski. Continuing from the presentation in the first annual report, a mathematical model for the dynamics of the jet under control is presented. The dynamic control impedances as well as the dynamic response of a system is the goal of this as-yet-incomplete effort. Considerable use of digital and analog computers is involved.

The dynamic analysis of systems is discussed briefly in Chapter 4 including references to Engineering Projects Laboratory publications on fluid lines and a general approach toward predicting the stability of fluid systems. This latter development, sponsored by the present contract, is presented in detail at the Harry Diamond Laboratories' Second Fluid Amplification Symposium. Also in Chapter 4 the effect of bends on the dynamic response of lines is discussed.

In Chapter 5, S. D. Graber presents his work on bistable fluid-jet relays motivated by the desirability of sensing stall cells in axial-flow compressors. Background work was presented by R. J. Gurski in the first annual report. Graber concentrates on the static stability of the jet. Sensitivity of the device depends on a small stability margin for the deflected states of the jet; rapid dynamic response depends on a large instability for the center position of the jet. These conditions run counter to one another but an optimum configuration exists. Dynamic experimental results reveal a frequency limitation.

Chapter 6 by A. H. Greenleaf, presents the development of a fluid oscillator which is intended to be efficient and have a frequency insensitive

to large operating temperature and pressure changes. Mass-spring oscillators of several types were considered, and a circularly-oscillating wire-supported disk adopted. Pressure insensitivity results from a tangential driving force, perpendicular to the radial spring force. Consequent dynamic stability problems are analyzed and then configurationally avoided. Temperature sensitivity, resulting from changes in Young's modulus for the wire springs, is compensated by an axial sub-buckling force induced by a temperature-sensitive sealed bellows. Although the final breadboard model worked with respect to its significant features, further minor development is indicated for a truly useful oscillator.

In the first annual report a fluid-diode-blade-wake sensor was proposed, and linear analyses and initial experimental results discussed. In Chapter 7 of the present report the conclusion of this work is presented. A nonlinear dynamic analysis is given. Of the three types of diodes studied by W. B. Bails only the vortex diode has marginally adequate experimental static characteristics, but unfortunately this diode has dynamic characteristics which fall short of the high-frequency goal. The Tesla diode, patented some 40 years ago, was given brief static testing and found to be superior to all the others. All the devices, however, are shown to be ineffective at low Reynolds numbers, greatly limiting small-scale applications such as the desired sensor.

2. JET-RECEIVER STUDIES

2.1. Background

Various aspects of the over-all problem of jet-receiver-diffuser steady-state and dynamic performance has been discussed by the writer in previous reports on this and another contract, Ref. 1 and 2, as well as in the writer's M.I.T. ScD. Thesis Proposal (Ref. 3). The discussions of static performance dealt primarily with problem definition and the adequacy and limitations of the available literature in providing a basis for static performance prediction. It was shown that the over-all problem of static performance prediction can be separated conceptually into several related fundamental hydrodynamic problems. For convenience, these problems were classified as follows: flow through "short tube" orifices and nozzles, flow of "controlled" submerged jets, diffusion of nonuniform turbulent streams in constant-area passages, and conversion of kinetic to potential energy in "slow expansion" and "sudden expansion" diffusers.

In the previous annual report on the present contract, (Ref. 1), the problem of jet-receiver dynamic interactions was discussed. The potential "causes and effects" of receiver pressure oscillations were briefly discussed. A simple experiment was outlined which was designed to study the dynamic behavior of the interaction region. The experiment was designed so that the reflection coefficient of the source terminal (i. e., the interaction region) could be measured. No significant experimental results were available at the time of writing.

The goal of the over-all program of study of jet-receiver performance is to provide a critical portion of the information necessary for rational design of jet modulator systems. Included in this report (Secs. 2.2 and 2.3) are analytical and experimental results obtained to date on certain of the jet-receiver static and dynamic problems thought to be particularly critical in terms of accomplishment of the desired goal.

2.2. Receiver-Diffuser Steady-State Performance

2.2.1. General Characteristics of Diffusion Processes

The underlying problem of receiver-diffuser design is the establishment of an optimum internal geometry based on a desired criterion of merit. For example, one interesting and important "optimal" problem involves maximizing the ratio of the power recovered in the receiver-diffuser to the power available at the nozzle supply conditions. Regardless of the type of optimal problem, the function of the receiver-diffuser is basically the same: that of efficiently transforming the kinetic energy of a high velocity submerged jet into controllable potential energy.

It is apparent on consideration of the fundamental character of a free submerged jet that the receiver-diffuser inlet velocity profile will be nonuniform in character. Perhaps the most important single problem affecting steady-state performance prediction is a complete characterization of the receiver inlet velocity profile. Certainly a complete description of this velocity profile must take into account the critical geometrical and operational parameters. One interesting question is: how far back (toward the nozzle) into the otherwise free submerged jet is the disturbance introduced by the receiver actually propagated? Answers to these questions are goals of future experimental studies.

Having described the characteristics of the flow in the "free" region between the nozzle exit and the receiver inlet, the next problem to be encountered is a description of the flow within the receiver-diffuser. Diffusion of a stream in internal flow, in the sense of increasing static pressure, is accomplished by means of velocity profile "smoothing" and/or simple area change. It is well known that diffusion takes place in a diverging passage, the most common type of diffuser, due to the area change itself. It is often forgotten that changes in the velocity profile also affect the diffusion process, i. e., the ability of a passage to transform energy from kinetic to potential. Equally important, but less well known, is the fact that diffusion may take place in a constant-area passage due to the effect of velocity profile smoothing.

In order to understand the process of constant-area diffusion, it is necessary to introduce the concept of uniformity of a fluid stream. Uniformity refers to the closeness to which the transverse profile of the longitudinal velocity approaches a "rectangular" profile (see Fig. 1). A convenient quantitative measure of the uniformity of a velocity profile is the momentum coefficient defined as follows:

$$\alpha = \frac{\text{true momentum of the stream}}{\text{momentum based on the continuity average velocity}}$$

Thus

$$\alpha = \frac{\int V^2 dA}{\bar{V}_A^2} \quad (1)$$

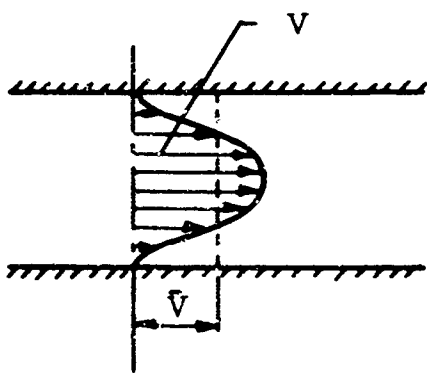
Considering now the constant-area passage shown in Fig. 2, the law of conservation of momentum requires that

$$P_2 - P_1 = \rho \bar{V}_1^2 (\alpha_1 - \alpha_2) - \frac{4\tau_w L}{D} \quad (2)$$

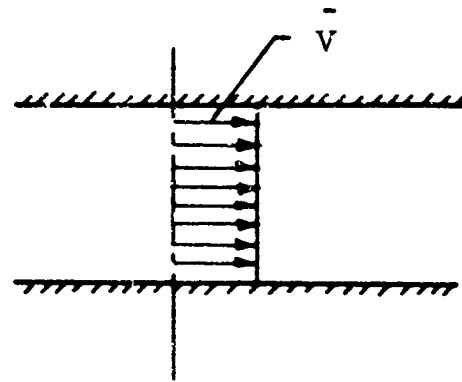
where

- P_1 = static pressure at station 1
- P_2 = static pressure at station 2
- $\bar{V}_1 = \bar{V}_2$ = continuity average velocity
- α_1 and α_2 = momentum coefficients
- τ_w = wall shear stress
- ρ = fluid mass density

Thus the difference in static pressure at two stations is a function of the difference in the velocity profile shapes (given by α_1 and α_2) at the two sections and the wall friction forces which act between the two stations. It is well known that the velocity profile of the flow in a constant-area passage tends to stabilize along the passage, i. e., asymptotically approach



a. Nonuniform



b. Uniform

Fig. 1. Concept of Velocity Profile Uniformity

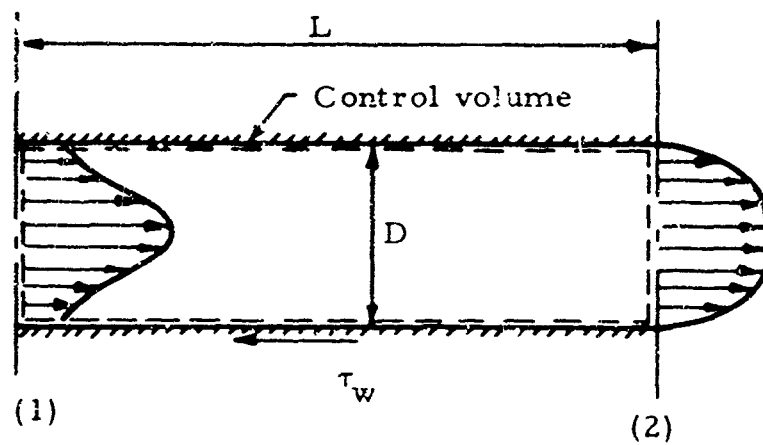


Fig. 2. Velocity Profile Smoothing in a Constant-Area Passage.

a "fully-developed" profile. With laminar flow, the profile always approaches the well-known parabolic profile at a distance sufficiently far down the passage. Likewise, in turbulent flow, the profile tends asymptotically to the familiar n -th power law profile. It is interesting that the value of n for a $1/7$ -th power profile is approximately 1.02.

If the profile at a station in the passage is highly nonuniform (n is much greater than the corresponding fully developed value), then Eq. (2) shows that an increase in profile uniformity may cause an increase in static pressure which outweighs the decrease due to wall shear. Certainly if the passage is long enough, wall friction will eventually dominate. It should be noted that constant-area diffusion is accompanied by inherent energy loss, as in any diffusion process. An empirical approach to the study of constant-area turbulent diffusion is discussed in Sec. 2.2.3.

In a passage whose area increases in the direction of flow, the "profile smoothing" form of diffusion is superimposed on the area change form. Area-change diffusion, in the sense of increasing static pressure, ceases when the area change effect is balanced by the wall shear effect. Energy losses in area-change diffusers primarily result from velocity profile smoothing, wall shear, and separation. Experience indicates that a nonuniform velocity profile at the entrance to a "slow expansion" area-change diffuser leads to a significantly larger over-all energy loss than would occur with a more uniform inlet profile (see Sec. 2.2.4).

On the basis of this qualitative understanding of diffusion processes, past experience with jet pumps and ejectors, and considerations of practical geometry from the standpoint of construction, the following hypotheses are made (Ref. 2):

1. There exists a "best" length of constant-area passage together with a "best" geometry of the increasing-area passage such that the efficiency of the diffusion process is maximized for a given set of conditions.

2. There exists a "best" length of constant-area passage together with a "best" geometry of the increasing-area passage such that the desired "shape" of the static pressure-flow characteristic is obtained at the maximum possible efficiency.

These hypotheses must, of course, be verified by suitable analysis and experiment.

A combined analytical and experimental program is underway which is aimed at defining the term "best" in a quantitative way. Preliminary results of this study are given in Secs. 2.2.3 and 2.2.4.

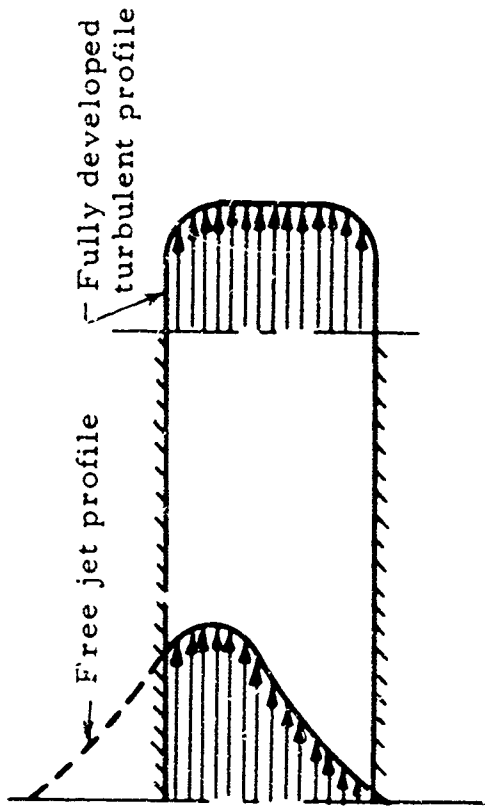
2.2.2. Constant-Area Turbulent Diffusion in Jet Modulators

In a sense, the problem of constant-area turbulent diffusion belongs to a class of problems known as "entry length" problems. A brief discussion of the character of these problems is given in Ref. 2. The velocity profile development of a turbulent stream in the constant-area diffuser of a jet modulator differs in the following respects from that encountered in the usual entry length problems:

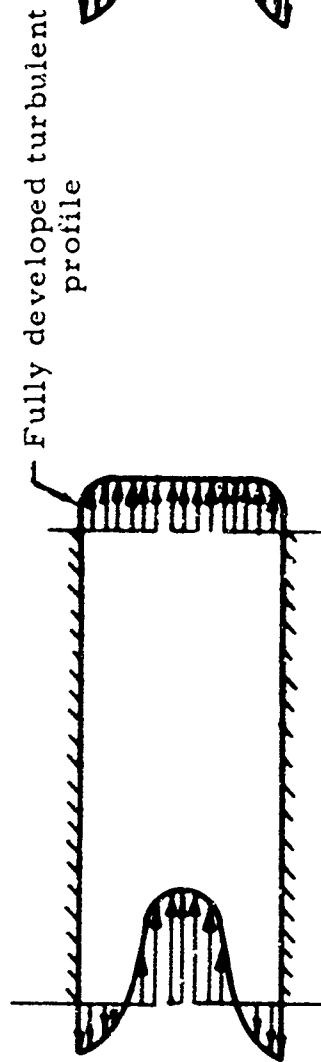
1. The velocity profile at the inlet section of the passage is very nonuniform and, in fact, may be nonsymmetrical as well,
2. The flow is already "fully developed" turbulent shear flow or at least has a relatively high turbulence intensity when it enters the passage,
3. Development of the velocity profile in the direction of flow is primarily due to the transfer of momentum between fluid layers under the action of turbulent shear stresses. The wall shear stress is small in comparison with the turbulent stresses, at least for several diameters along the passage,
4. The development of the profile is accompanied by an initial rise in static pressure; ultimately the point is reached where wall shear becomes important and the static pressure begins to decrease.

5. Transition from an unusually nonuniform profile to one having the same degree of uniformity as the corresponding fully developed turbulent pipe flow, takes place in only a few diameters rather than the customary 20 - 50 diameters required in the usual entry length problem.

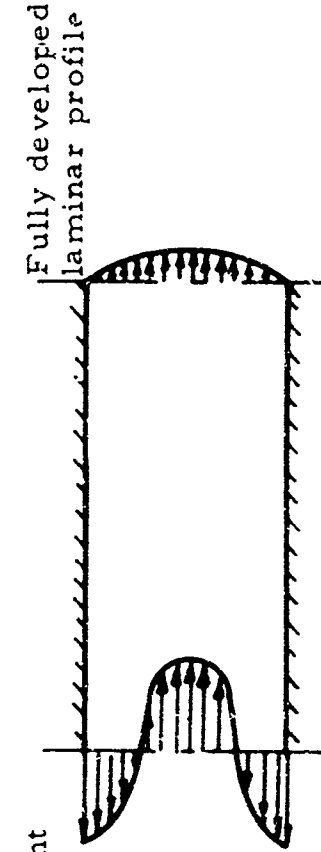
Figure 3 serves to illustrate schematically what might be expected to occur in constant-area diffusion. In Cases a and b, it is assumed that the flow in the passage is turbulent and that the velocity profile is identical to the profile in the corresponding section of an unobstructed free submerged jet. These two cases represent one end of the spectrum of interest, i. e., the situation which should exist when no throttling takes place downstream of the diffuser (receiver input impedance is essentially zero). When considerable throttling takes place (receiver input impedance becomes very large), the flow in the passage may be laminar rather than turbulent. Certainly as the receiver input impedance approaches infinity, the flow in the passage must proceed from turbulent to laminar. Cases c and d of Fig. 3 illustrate cases of high, but not infinite, receiver input impedance (i. e., finite through flow). In all cases, the corresponding fully developed profile is approached. Very little beyond qualitative reasoning exists to substantiate the schematic representations of Fig. 3. However, the results of a single experiment reported in a 1950 PhD. thesis by H. L. Grimmer (Ref. 4), provides some measure of verification for Case a. Grimmer measured the velocity profile in a circular constant-area duct displaced 15 diameters from an axially-aligned nozzle. It should be noted that there was no throttling of the flow leaving the downstream end of the duct, and consequently, the static pressure at the exit plane was atmospheric. These data are reproduced in Fig. 4. Since the well streamlined, non-throttled duct places virtually no obstruction in the field of the submerged jet, the duct inlet velocity profile is indistinguishable from the corresponding portion of the free jet profile. It is evident that the transition from the highly nonuniform inlet profile to a seemingly fully developed profile takes place in 4-5 diameters. It is interesting that the point at which the wall static pressure first peaks occurs somewhat before the apparent point at which the profile is fully



a. Low input impedance; turbulent flow; asymmetrical inlet profile.



b. Low input impedance; turbulent flow; symmetrical inlet profile.



c. High input impedance; laminar flow; asymmetrical inlet profile.

d. High input impedance; laminar flow; symmetrical inlet profile.

Fig. 3. Constant-Area Diffusion of Nonuniform Streams.

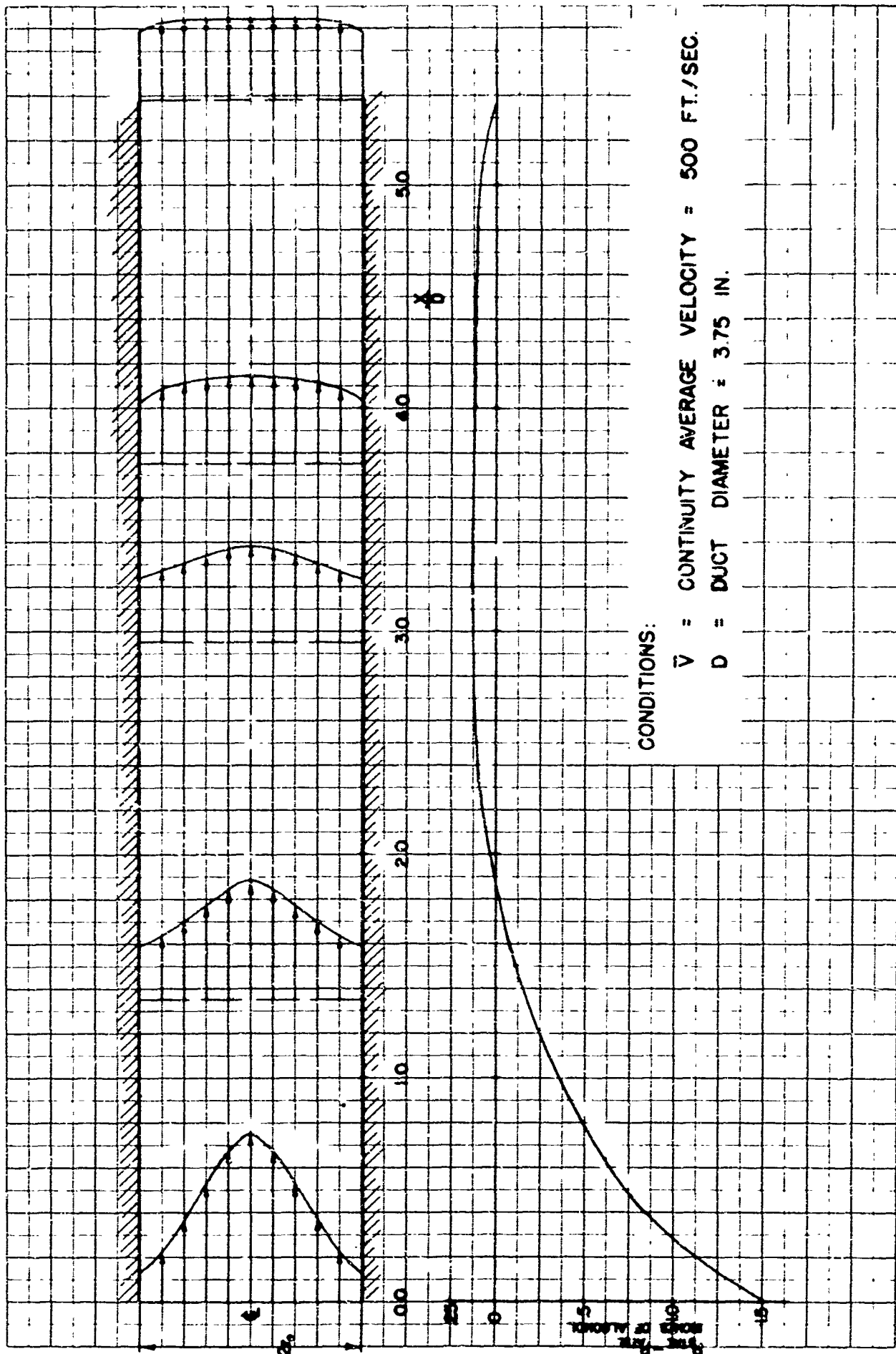


Fig. 4. Velocity Profile Development in a Circular Constant-Area Duct Displaced 15 Diameters from an Axially-Aligned Nozzle. (From data tabulated in Ref. 4)

developed. Furthermore, the static pressure data show the relative unimportance of the total integrated wall shear stress in the first 4 or 5 diameters of the duct. The important conclusion is the fact that the velocity profile smoothing, under the action of turbulent shear stresses, takes place much more rapidly than the profile "shaping" as a result of wall boundary layer growth. These data, although admittedly much too limited in scope, provide the basis for the previous hypotheses concerning the length of duct necessary to achieve a profile of high uniformity.

2.2.3. Empirical Approach to the Study of Constant-Area Turbulent Diffusion

It is entirely possible that jet modulator static performance can be predicted adequately by simplified means without ever really being concerned with the details of the diffusion processes. However, even if this ideal could be achieved, it is unlikely that there would exist a truly rational basis for optimization studies. Consequently, one seems justified in considering, insofar as is feasible, the details of the flow processes.

In establishing an analytical basis for optimizing the over-all diffusion process, it is necessary to have a knowledge of the velocity distribution in the diffuser passages. On seeking a solution to the constant area turbulent diffusion process, one is faced with the inadequacy of our understanding of even the most simple turbulent flow processes.

Truly no "exact" analytical solution to the basic equations of motion has ever been found for a turbulent flow problem. Nevertheless, the well-known semi-empirical hypotheses established by Prandtl, Reichardt, and Taylor have been applied with a reasonable degree of success in a number of important engineering problems and present some hope for the present problem. Of course, a solution to the turbulent diffusion problem would not be complete by itself. The truly useful solution must be applicable regardless of flow regime (i. e., turbulent, transition, or laminar). It seems unlikely that a single solution can be found that will be universally applicable. What is more probable is that two or more solutions can be "matched" judiciously!

The turbulent diffusion problem can now be stated as follows: Given the initial distribution of velocity and static pressure at a certain passage section (i. e., at the inlet section of the passage), what is velocity profile at another section downstream? Certainly a hint for a solution is offered by experimental evidence (Refs. 4 and 5) that the turbulent mixing process is far more rapid than the boundary layer growth. The success of Reichardt's inductive theory of turbulence when applied to submerged jets and other problems which have a principal flow direction, suggests that his theory may be applicable to the present problem. This theory has been applied with apparent success to problems of free jets, jets discharging parallel to a wall, and jets discharging at the center of a duct, by a group of investigators⁺ at the Engineering Experiment Station of the University of Illinois (Refs. 6 and 7). The technique developed to handle the case of a jet issuing at the center of the duct, as in a jet pump, is empirical in nature in that two constants must be determined experimentally. Such is typical for turbulent flow problems. An empirical expression is presented in Ref. 7 for the prediction of the transverse total momentum distribution at the various sections of the duct. Recently, R. Moissis and P. Griffith of M. I. T. successfully utilized the technique developed by the previous investigators for the "ducted jet", to predict the total momentum distribution in the wake of an air bubble in developing two-phase slug flow. (Ref. 8). The same general approach will be followed in the analysis below.

Consider now the steady, incompressible axially-symmetric turbulent flow in a constant-area circular passage. (The results of an analysis for a two-dimensional passage will follow the present development.) Boundary layer development at the walls is neglected. The theoretical reasoning of Reichardt's approach is discussed in Refs. 9 and 10. The theory is based on the momentum equation for the time-mean averages of the velocity in the principal direction of flow. Thus

⁺The PhD. thesis by H. L. Grimmer mentioned in Sec. 2.2.2. is part of this larger study.

$$\rho \left[\frac{\overline{\partial(u^2)}}{\partial x} + \frac{1}{r} \frac{\partial(ruv)}{\partial r} \right] = - \frac{\partial \bar{p}}{\partial x} \quad (3)$$

where

ρ = fluid mass density

u = instantaneous velocity in the x-direction

\bar{u} = time-mean-average velocity in the x-direction

v = instantaneous velocity in the r-direction

\bar{v} = time-mean-average velocity in the r-direction

x = distance along axis of cylindrical passage

r = radial position in cylindrical passage measured from axis of passage

P = static pressure; \bar{P} = mean static pressure

The second basic equation in Reichardt's theory is of an empirical nature and has the form

$$\overline{uv} = - \Lambda \frac{\overline{\partial(u^2)}}{\partial r} \quad (4)$$

The term \overline{uv} represents the turbulent shearing stress. The parameter Λ is called the "momentum transfer length." It has the dimensions of length and is assumed to be a function of x only. Equation (4) thus relates the turbulent shear stress to an easily measured mean flow quantity by means of a "hypothetical" transfer length. In words, Eq. (4) states that the flux of x-component of momentum which is transferred in a transverse direction is proportional to the transverse gradient of momentum.

Combining Eqs. (3) and (4) and rearranging yields

$$\frac{\partial \bar{p}}{\partial x} + \frac{\partial}{\partial x} (\overline{\rho u^2}) - \frac{1}{r} \Lambda \frac{\partial}{\partial r} \left[r \frac{\partial}{\partial r} (\overline{\rho u^2}) \right] = 0 \quad (5)$$

Assuming the pressure gradient in the transverse direction (i.e., $\partial \bar{p} / \partial r$) is of small order compared to the longitudinal gradient $\partial \bar{p} / \partial x$, $\partial \bar{p} / \partial r$ can be added to both sides of Eq. (5) without destroying its validity. Thus

$$\frac{\partial}{\partial x} (\bar{p} + \rho \overline{u^2}) - \frac{1}{r} \Lambda \frac{\partial}{\partial r} \left[r \frac{\partial}{\partial r} (\bar{p} + \rho \overline{u^2}) \right] = 0 \quad (6)$$

Defining $m = \bar{p} + \rho \overline{u^2}$ gives

$$\frac{\partial m}{\partial x} - \frac{1}{r} \Lambda \frac{\partial}{\partial r} \left[r \frac{\partial m}{\partial r} \right] = 0 \quad (7)$$

In order to simplify the boundary conditions, it is convenient to make the following definitions: $r^+ = 2r/D$, where $D =$ passage diameter and

$$M = (m - m_\infty)/m_0$$

where

$m_\infty = (\bar{p} + \rho \overline{u^2})$ at $x \rightarrow \infty$; taken as the fully developed turbulent flow total momentum

$m_0 = (\bar{p} + \rho \overline{u^2})$ at $x = 0$; $x = 0$ is the total momentum at the entrance of the passage and is assumed to be known.

Using these definitions, Eq. (7) can be written in dimensionless form as follows:

$$\frac{\partial M}{\partial x} - \frac{4}{r^+} \frac{\Lambda}{D^2} \frac{\partial}{\partial r^+} \left[r^+ \frac{\partial M}{\partial r^+} \right] = 0 \quad (8)$$

This is a linear, second-order partial differential equation in the variable M .

Four independent boundary conditions can be specified:

1. $(\partial M / \partial r^+)_{r^+ = 0} = 0$, from symmetry.
2. $(\partial M / \partial r^+)_{r^+ = 1} = 0$, since wall friction is neglected.
3. $(M)_{x \rightarrow \infty} = M_{fd}$, i. e., fully developed value of M is a useful reference. It can be calculated from an accepted power law profile.
4. $(M)_{x=0} = (m_0 - m_\infty)/m_0 = 1 - m_\infty/m_0 = f(r^+)$;

this value of M is assumed to be known.

Solution of Eq. (8) by separation of variables and subsequent substitution of the first two boundary conditions above yields the product solution.

$$M = \sum_{n=1}^{\infty} A_n J_0(a_n r^+) \exp \left[- \int_0^x \frac{4 \Lambda}{D^2} a_n^2 dx \right] \quad (9)$$

where

J_0 = Bessel function of zero-th order

J_1 = Bessel function of first order

a_n = n-th root of J_1

A_n = a constant

The function $\Lambda = \Lambda(x)$ which appears in the exponential (i. e., the momentum transfer length) must be determined empirically. Given a set of experimental values of M , the function $\Lambda(x)$ can be defined in such a manner that experimental and theoretical values of M are identical. Recalling the definition of M , it is obvious that measurements of velocity distribution and static pressure at various stations along the passage will yield the desired experimental values of M . Equipment has been designed and is now being constructed for the purpose of making measurements of this type. A pitot probe will be used for these measurements. Additional measurements will be made, using X-array hot-wire probes, of the actual turbulent shear stress distribution at various passage stations. These latter measurements will provide the additional information necessary for direct integration of the original equation of motion (i. e., Eq. (3)). The validity of the simplifying assumptions made in establishing Eq. (3) and, indeed, the whole of the Reichardt theory, can then be determined.

It would be highly desirable to establish an explicit relation for $\Lambda = \Lambda(x)$. The assumption has already been made that Λ is independent of r . This turns out to be a good assumption when the Reichardt hypothesis is used for free jet analyses. In contrast to free jets, Λ cannot grow indefinitely (as x increases) in a constant diameter passage. In the absence of wall friction, it seems reasonable that the presence of a wall should have no other effect on Λ than to place an upper limit on its growth. A purely

arbitrary function, suggested in Ref. 7, that reduces to the free jet relation for small x , but which imposes on Λ an upper limit which is a function of the passage diameter is

$$\Lambda = \frac{c^2 x}{2 \left(1 + \frac{bx}{D} \right)} \quad (10)$$

where c and b are arbitrary constants. By having such an arbitrary function, it would seem that one has a lot of latitude in correlating experimental data. It is to be expected that the form of Eq. (10) will be reasonable for a passage with little downstream throttling. In this case, the value of Λ at the entrance of the passage should be very nearly identical with that of the corresponding free jet. Whether Eq. (10) is of a reasonable form when there is considerable downstream throttling remains to be established.

Assuming the utility of Eq. (10), it is possible to carry the analysis further. Combining Eqs. (9) and (10) yields

$$M = \sum_{n=1}^{\infty} A_n J_0(a_n r^+) \exp \left\{ - \frac{2c^2 a_n^2}{b^2} \left[\frac{bx}{D} - \ln \left(1 + \frac{bx}{D} \right) \right] \right\} \quad (11)$$

The remaining two boundary conditions can now be utilized. These are

$$M \rightarrow 0 \quad \text{as } x \rightarrow \infty$$

and

$$M_0 = f(r^+).$$

The first condition is satisfied by the exponential term of Eq. (11) which tends toward zero as x increases without limit. The second condition yields

$$f(r^+) = \sum_{n=1}^{\infty} A_n J_0(a_n r^+) \quad (12)$$

By virtue of the orthogonality of the Bessel series

$$A_n = \frac{2}{\left[J_0'(a_n) \right]^2} \int_0^1 f(r^+) J_0(a_n r^+) r^+ dr^+ \quad (13)$$

provided the series is uniformly convergent. (Ref. 11) Now any arbitrary initial profile of the total momentum function, M_0 , can be imposed on A_n . Except for the case of little downstream throttling, a rational means for evaluating M_0 under all downstream load conditions does not exist presently. The earlier mentioned experimental program is aimed at providing this information.

There is as yet no known way to predict the values of the empirical constants, b and c , in Eq. (11). Resource must be made to judicious experiment. However, point by point application of Eq. (11) is not a satisfactory means of evaluating b and c from experimental data. It is possible, however, to greatly simplify the evaluation process by defining a one-dimensional function which is integrable in r^+ . The integral of M itself is not a suitable function since, by conservation of momentum, it is always zero. However, the integral of M^2 is not conserved, and may be used to define a one-dimensional function, I , as follows:

$$I = \int_0^1 M^2 \times 2\pi r^+ dr^+ \quad (14)$$

The function I appropriately may be termed the "mixing index."

For any set of values of b and c , an equation resulting from a combination of Eqs. (11), (13), and (14) yields an analytical expression for the variation of I as a function of x only. In addition, the value of I corresponding to any position x may be found by performing graphically the integration of Eq. (14). In the latter case, the values of M are obtained from experimental data. By trial-and-error the values of b and c can be chosen such that the "analytical" and "measured" values of I show good agreement. The success of this procedure awaits the results of the experimental program!

Consider now the case of constant-area turbulent diffusion in a two-dimensional passage. The momentum equation for the time-mean-averages of the velocity in the principal direction of flow becomes for this case

$$\rho \frac{\overline{\partial u^2}}{\partial x} + \rho \frac{\overline{\partial uv}}{\partial y} = - \frac{\partial \bar{p}}{\partial x}$$

where x is the coordinate in the principal flow direction and y is the coordinate in the transverse direction measured from the axis of flow.

Again, using Reichardt's hypothesis for the turbulent shear stress leads to the following partial differential equation

$$\frac{\partial M}{\partial x} = \frac{4 \Lambda}{h^2} \frac{\partial^2 M}{\partial y^2}$$

where h is the minimum transverse dimension of the passage and $y^+ = y/h$. The boundary conditions are of the same form as for the circular passage. Again making use of the separation of variables technique for solving partial differential equations, the following product solution for M is obtained

$$M = \sum_{n=1}^{\infty} c_n \exp \left[- \int_0^x \frac{4 \Lambda n^2 \pi^2}{h^2} dx \right] \sin n \pi y^+$$

From this point on, the same considerations hold as in the circular passage case.

2.2.4. Area-Change Diffuser Characteristics

The theoretical prediction of flow conditions in area-change diffusers has long been an unsolved problem in fluid mechanics. Researchers for over 50 years have relied almost totally on experimental techniques in the design of diffusers. Two basic problems have been studied extensively in connection with the design of straight-walled diffusers.

1. Prediction of optimum geometry for most efficient transformation of kinetic to potential energy, and

2. Prediction of impending flow separation and the flow regimes encountered with various degrees of separation.

Many basic problems remain unanswered, however. Nevertheless, considerable experimental data are available on the "efficiency" of circular, square, and rectangular diffusers having various area ratios, divergence angles, inlet boundary layer conditions, and Reynolds numbers. A brief bibliographical review of the literature is given by the writer in Ref. 2.

At the outset of the receiver-diffuser study, it was believed that considerable data existed which could be used directly in predicting performance of jet-modulator area-change diffusers. The results of a fairly comprehensive literature survey showed that considerable information is lacking. It is difficult to make direct comparisons of the available results of isolated studies since the experimental test conditions are not always well defined or even controlled. In addition, there is no common agreement in the literature on the most convenient definition of efficiency. Consequently, experimental results giving "efficiency" as a function of diffuser geometry and various operating conditions, is often extremely confusing. Even more important is the fact that, almost without exception, available diffuser performance data are restricted to relatively high diameter Reynolds numbers (say 10^4 and up). It is likely that in most future applications of jet modulators, Reynolds numbers between 1 and 10^4 will be encountered.

It is, of course, fortuitous that so much experimental data exist for the high Reynolds number range. The important trends and techniques established by the previous studies will be invaluable in the efficient planning of future experiments. Indeed, the hypotheses concerning optimum diffuser geometry discussed in Sec. 2.2.2. were based almost totally on available diffuser performance data. Since the available data are so important to the over-all goal of the static performance study, some of the best available pertinent diffuser data are reviewed below. Only the results of studies with conical diffusers will be discussed below. The interested reader is referred to Refs. 12, 13, and 14 for extensive discussions of diffusers of all shapes and forms.

Of the various efficiencies used in the literature, the most common and probably the most useful in the majority of situations is the "static pressure efficiency", or as sometimes termed, the "energy-conversion efficiency". This efficiency is defined as the ratio of the rate at which energy is transformed to the rate at which energy is supplied for transformation. Consider a passage which expands from an initial area A_1 to a final area A_2 . Let P be the static pressure, ρ the fluid mass density, u the component of velocity parallel to the axis of the passage, and w the absolute velocity at any point. Thus the actual energy-conversion or static pressure efficiency is

$$\eta_{ap} = \frac{A_2 \int P u dA - \int_{A_1} P u dA}{\int_{A_1} \frac{1}{2} \rho w^2 u dA - \int_{A_2} \frac{1}{2} \rho w^2 u dA} \quad (15)$$

If the flow is purely axial at sections 1 and 2, $w = u$ and P is a constant over the section (i. e., no streamline curvature). Then

$$\eta_{ap} = \frac{(P_2 - P_1) \bar{u}_1 A_1}{\int_{A_1} \frac{1}{2} \rho u^3 dA - \int_{A_2} \frac{1}{2} \rho u^3 dA} \quad (16)$$

where

$$\bar{u} = \frac{1}{A_1} \int_A u dA \quad (17)$$

Equation (16) can be simplified by defining a kinetic energy factor β as follows:

$$\beta = \frac{\int_{A_1} \frac{1}{2} \rho u^3 dA}{\frac{1}{2} \rho \bar{u}^3 A} \quad (18)$$

The kinetic energy factor is analogous to (but not equal to) the momentum factor α , defined in Section 2.2.3, in that it accounts for the nonuniformity of the velocity profile. Utilizing this definition and recognizing that continuity requires $u_1 A_1 = u_2 A_2$, the following expression is obtained:

$$\eta_{ap} = \frac{P_2 - P_1}{\frac{1}{2} \rho \bar{u}_1^2 \left[\beta_1 - \beta_2 \left(\frac{A_1}{A_2} \right)^2 \right]} \quad (19)$$

Many investigators have used a one-dimensional approximation to Eq. (19) as follows:

$$\eta_p = \frac{P_2 - P_1}{\frac{1}{2} \rho \bar{u}_1^2 \left[1 - \left(\frac{A_1}{A_2} \right)^2 \right]} \quad (20)$$

Equation (19) reduces to Eq. (20) if it is assumed that the velocity profiles at the entrance and exit sections are uniform (i.e., $\beta_1 = \beta_2 = 1.0$).

The efficiency depends on many factors, the most important of which is the rate of expansion of the flow. This is not surprising since it is this factor which determines the magnitude of the opposing pressure gradient. Some results of experiments on the flow between straight diverging walls (conical section only) by Gibson (Ref. 15) and Peters (Ref. 16) are summarized in Fig. 5. Efficiency, η_p , is plotted against 2θ , the included angle between the diverging walls. The efficiency is low at very small angles, rises to a peak in the vicinity of 5 - 8 degrees, rapidly falls as 2θ increases until a low point is reached in the vicinity of 60 degrees, and then slowly approaches the theoretical value given by Borda at $2\theta = 180^\circ$. The Borda limiting condition (i.e., a sudden expansion diffuser) is derived from simple continuity and momentum considerations; the following expression results:

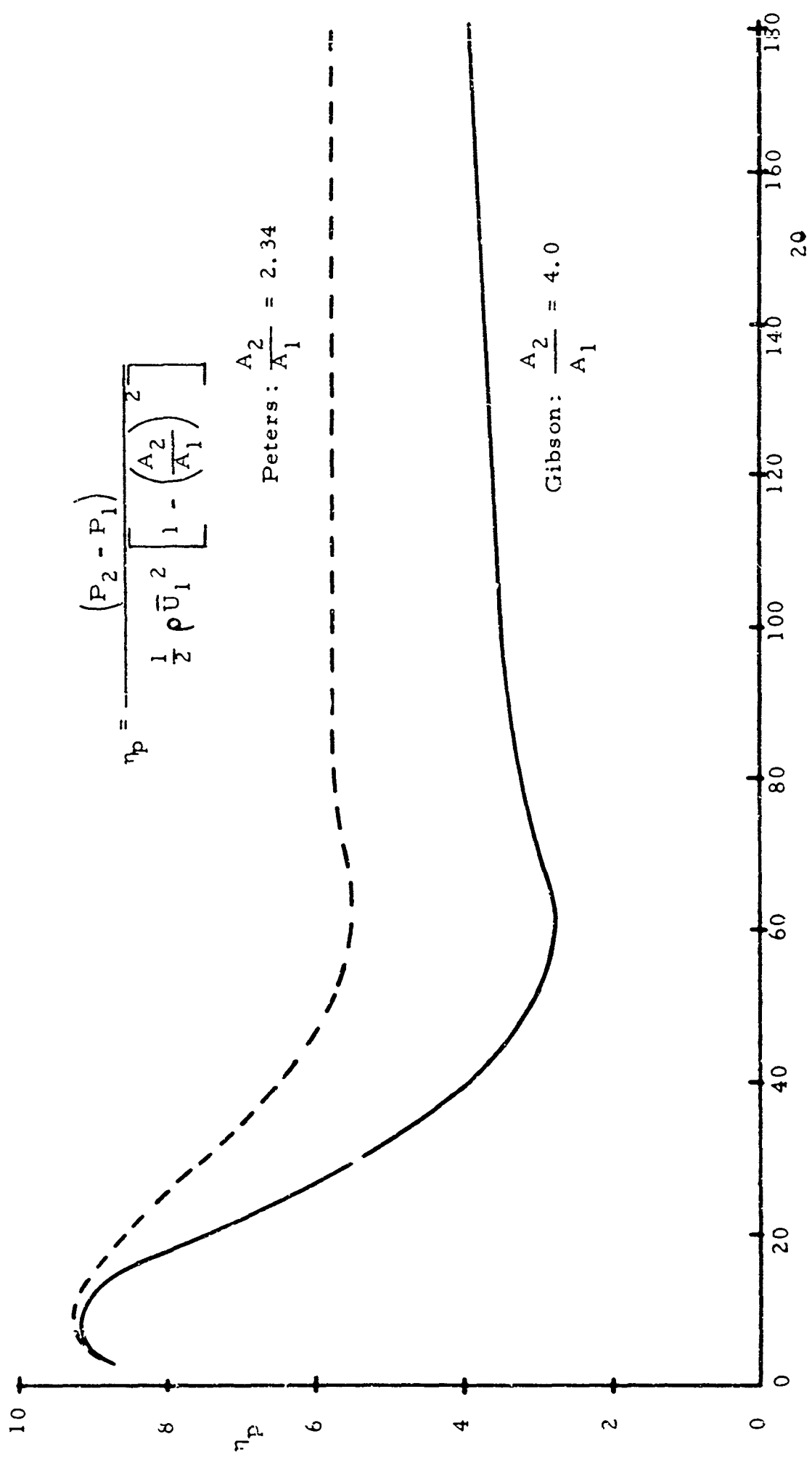


Fig. 5. Typical Pressure Efficiency for Area Change Diffusers.

$$\left(\eta_p \right)_{\text{sudden expansion}} = \frac{2}{1 + \frac{A_2}{A_1}} \quad (21)$$

Perhaps the most important feature of the results of Fig. 5 is that the efficiency reaches a peak value, which is quite high, in the vicinity of 5 - 8 degrees.

To understand the reason for the peak in the efficiency curve, consider a family of diffusers having identical area ratios ($A_2/A_1 = \text{const.}$). If the included angle is small (say $< 5^\circ$), the wall friction losses are large since the passage must be very long. However, the "separation" losses are extremely small. Conversely, if the included angle is large (say $> 15^\circ$), the passage length, and therefore the wall shear losses, are greatly minimized. The separation losses, though, are greatly increased as the included angle is increased. The peak efficiency condition then represents an optimum trade-off between wall shear and separation losses.

A factor which is often obscured in the presentation of diffuser performance data is the effect of inlet and exit velocity profile nonuniformity. Although efficiency calculations based on Eq. (19) take into account profile nonuniformity directly, most investigators have not bothered to make the additional (and tedious) measurements necessary to establish β_1 and β_2 . The approach used by most investigators (if they bothered at all) has been to study the effect of various inlet velocity profiles produced by using different lengths of constant diameter inlet pipe. For a very short inlet pipe, the value of β_1 is approximately equal to 1. As the inlet pipe length is increased to say 30 diameters, the value of β_1 is very nearly that of a fully developed turbulent flow profile ($\beta_1 \approx 1.05$, dependent on Reynolds number).

The percentage difference between the efficiencies calculated from Eqs. (19) and (20) may be as small as a few per cent or as large as 10 - 15 per cent. Even if the diffuser entrance profile is approximately uniform (i. e., $\beta_1 \approx 1.0$), the exit profile normally is quite nonuniform ($\beta_2 > 1.0$). Figure 6 is illustrative of typical flow conditions associated with a conical diffuser having "near optimum" geometry.

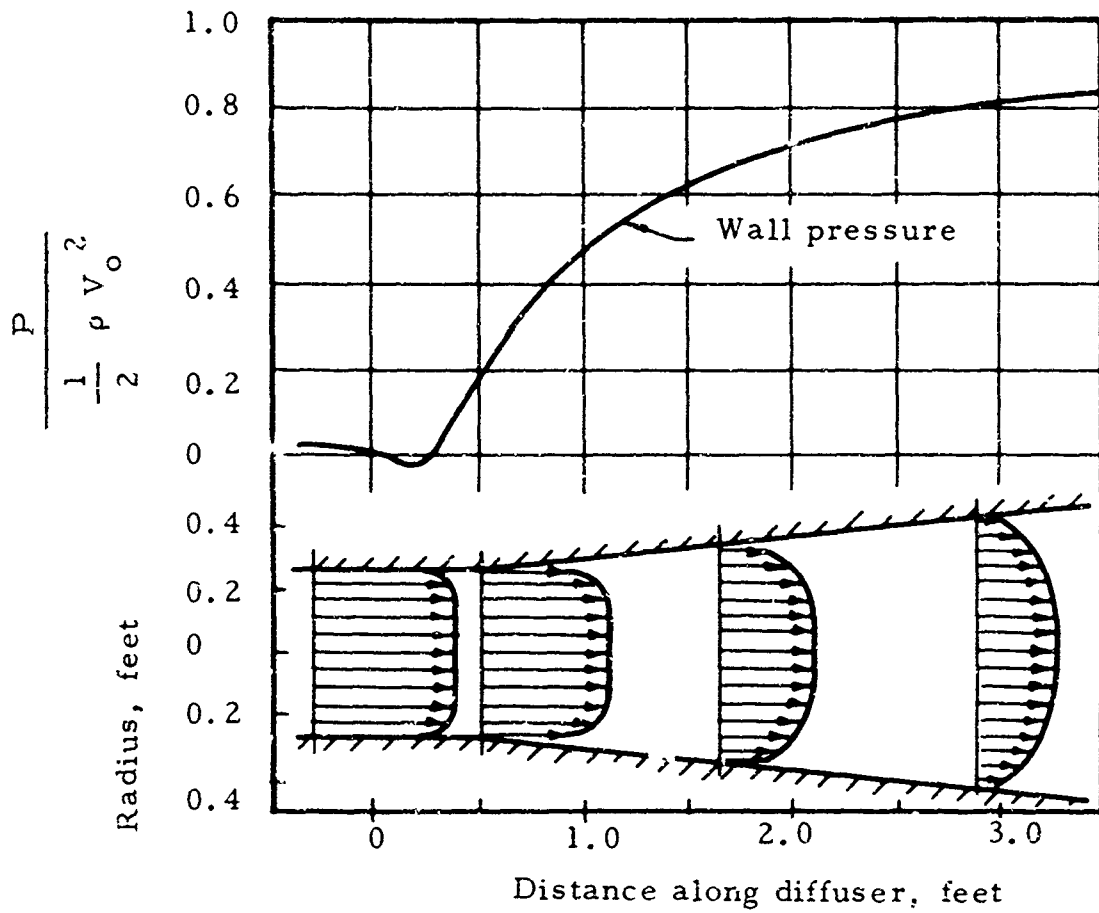


Fig. 6. Flow Conditions in a 7.5° Diffuser with Five Diameters of Entry Length; Reynolds No. = 2×10^6 (Ref. 25)

Due to the fact that the diffuser outlet velocity profile is typically quite nonuniform, the addition of a constant diameter mixing section downstream of the exit section may have an important effect on the diffuser efficiency. A diffuser with constant diameter inlet and outlet sections is shown in Fig. 7a. If the velocity profile at the diffuser exit is more nonuniform than a fully developed profile (and in most cases it is), the profile becomes progressively smoother in the discharge section which follows. As a result, the static pressure continues to rise in the discharge section until a position is reached at which the static pressure is a maximum. From that point on, the pressure decreases due to wall shear. Peters (Ref. 16) has found that the velocity profile at the point of maximum static pressure is very nearly the same as the fully-developed profile. Results obtained by Peters showing the point of maximum static pressure recovery as a function of diffuser included angle and entrance section length are given in Fig. 7b. The importance of the discharge length on diffuser efficiency is obvious. In fact, modified definitions of efficiency are suggested which utilize the static pressure at the point of maximum recovery rather than at the exit plane of the area change section. A one-dimensional relation which corresponds to Eq. (20) is

$$\eta_p' = \frac{P_2' - P_1}{\frac{1}{2} \rho \bar{u}_1^2 \left[1 - \left(\frac{A_1}{A_2} \right)^2 \right]} \quad (22)$$

Similarly P_2' can be substituted into Eq. (19) for the true efficiency in place of P_2 . Therefore, the difference between η_p and η_p' is a measure of the effect of the addition of adequate length of discharge section.

The difference between the true or actual efficiency between two sections and the corresponding one-dimensional approximation is a measure of the nearness to unity of the values of β at the two sections. Figure 8 shows an interesting comparison between the actual efficiency between sections (1) and (2), the approximate efficiency between (1) and (2), and the approximate efficiency between (1) and (2'). The actual efficiency between sections (1) and (2') is not shown but could be inferred quite easily.

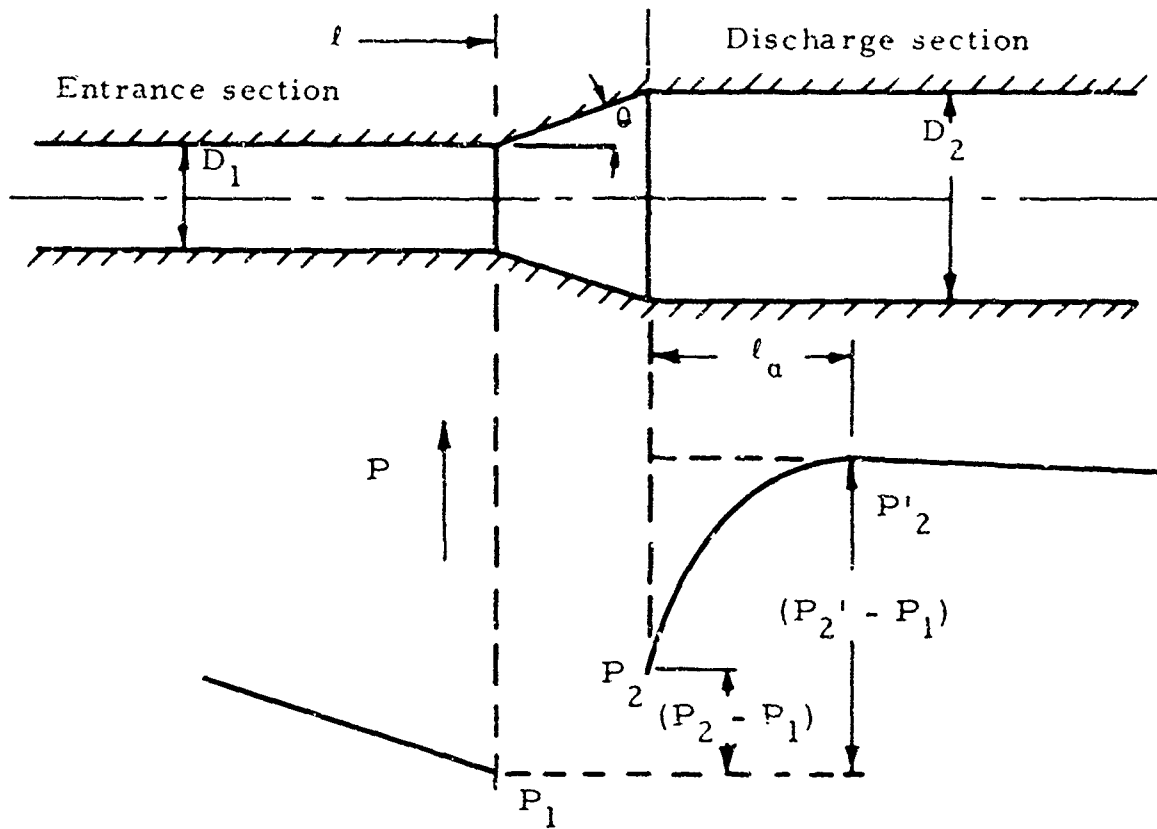


Fig. 7a. Definition of Diffuser Variables

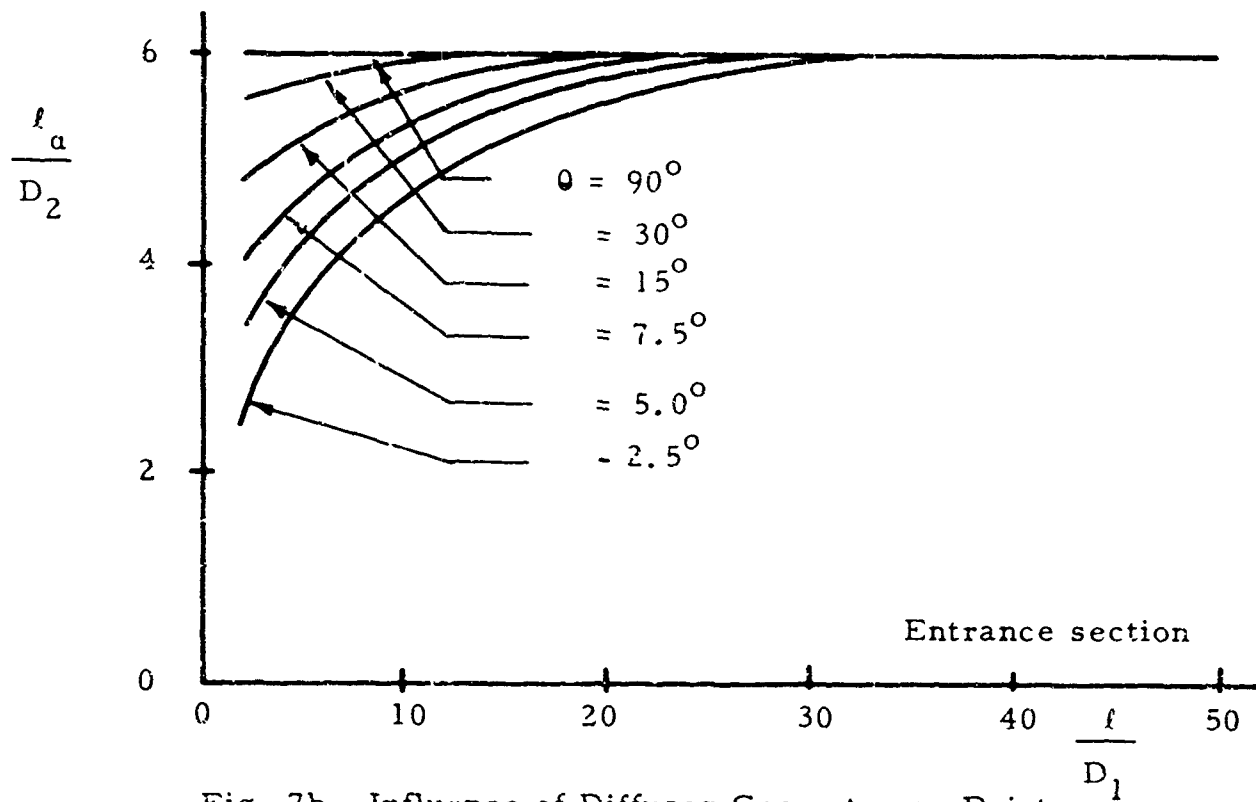


Fig. 7b. Influence of Diffuser Geometry on Point of Maximum Static Pressure Recovery.

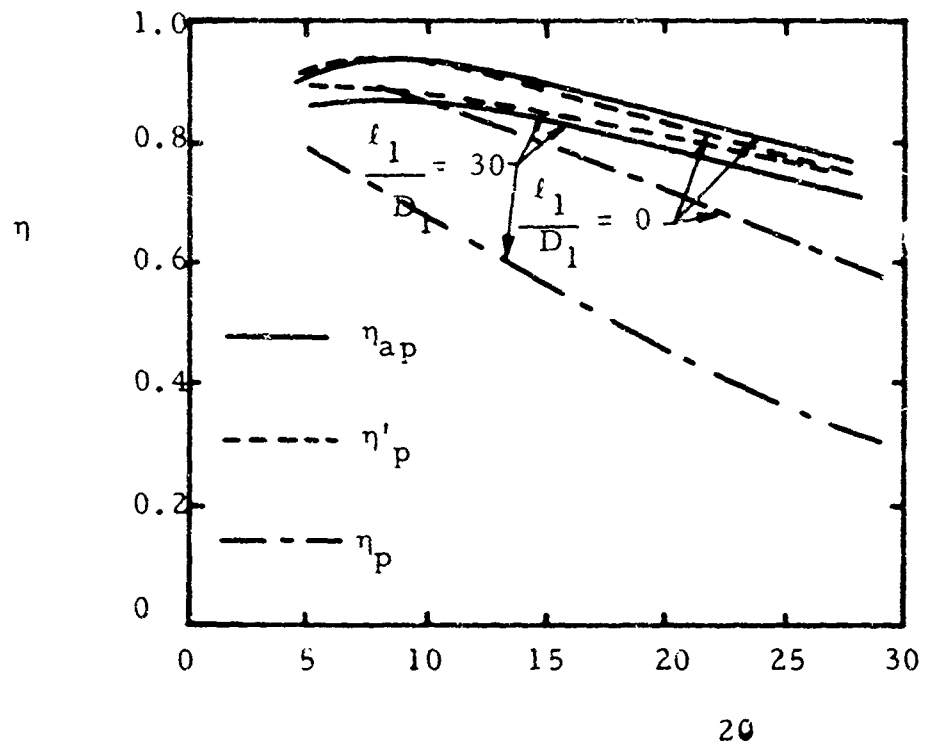


Fig. 8. Effect of Entrance and Exit Section Length on Diffuser Pressure Efficiency (Ref. 16)

Generally speaking, the one-dimensional approximation leads to significant errors (and often misleading results) when there is appreciable nonuniformity in the inlet and exit velocity profiles. What is most important about these results is the significance of even a seemingly uniform profile (i. e., fully developed) on the value of the efficiency. If the submerged jet of a jet modulator were to be diffused directly by an area change diffuser, the corresponding efficiency would be quite low (even for so-called optimum geometries) because of the high nonuniformity of the inlet velocity profile. It was this belief that led to the hypotheses of Sec. 2.2.2. A careful study of the available literature and past experience with jet-pipe valves leads the writer to believe that:

1. the most efficient receiver-diffuser for a specified "degree of diffusion" (i. e., total area change) is one having in succession a constant-area mixing section, a "short" . . . 8 degree diverging section, and finally a sudden expansion section.
2. the most linear pressure-flow characteristics of a three way, axially symmetric, axially aligned jet-receiver-diffuser will result with a short, constant - diameter mixing section followed by a sudden expansion section.

The discussion above gives only a sample of the factors which must be considered in the efficient design of area-change diffusers. Much remains to be done in properly evaluating and extending the existing diffuser performance data. A more detailed discussion of diffuser performance will be presented in the writer's ScD. thesis (summer 1964).

2.2.5. Orifice Characteristics

In many applications of jet modulators (i. e., a "four-way" jet-pipe valve or jet amplifier), fluid may flow out of the receiver-diffuser into a reservoir or plenum under certain conditions of downstream loading. In such situations, the receiver-diffuser flow is "reversed", so to speak, and the flow characteristics would be expected to be radically different. Indeed they are. If the receiver-diffuser consists of a constant-diameter mixing

section followed by an area-change section, then the reversed flow situation is that of flow through a "short-tube" orifice with a converging or "sudden contraction" entry section. Curiously enough, the flow characteristics of orifices of this type are not very well established, especially in the low Reynolds number range. A cursory discussion of the available literature on short-tube orifices is given by the writer in Ref. 3.

The writer reported the results of a recent M.I.T. study of sharp-edged short-tube hydraulic orifices in Ref. 17. This study was carried out by D. J. Tapparo, an S.M. thesis student, under the supervision of the writer. The results of the study have led to an empirical means of predicting the discharge coefficient for sharp-edged short-tube orifices within the following limitations:

$$2 \leq \frac{L}{D} \leq 6, 100 < Re_d < 1000$$

and $4000 \leq Re_d \leq 25,000$ (where L = orifice length, D = orifice diameter, and Re_d = diameter Reynolds number). It is expected that these results, even though somewhat limited, will be extremely useful to the writer in establishing a means for predicting over-all static performance of receiver-diffusers.

Also expected to be of considerable value are the results of a study of the friction factor in the laminar entry region of a smooth tube by Shapiro et al several years ago. These results are valid for a short-tube with a bell-mouth and for $Re_x < 5 \times 10^5$ (where Re_x is the Reynolds number based on length along the tube). With rather easily defended assumptions, the orifice discharge coefficient can be shown to be a function of the integrated apparent friction factor multiplied by the L/D ratio.

2.2.6. Experimental Study of an Axially-Aligned, Axi-Symmetric, Three-Way Jet Modulator

It is anticipated that results of studies discussed in previous sections will eventually yield techniques useful in predicting over-all static performance of jet modulators based on empirically derived characteristics of sub-parts. Consequently, an experimental study has been initiated to provide a means for evaluating these techniques. A large-scale model of an axi-symmetric, axially-aligned three-way jet modulator has been designed and fabricated. Preliminary tests have been conducted at relatively high Reynolds numbers and with a few geometrical variations. These results are presented in an S. B. thesis by H. Leibowitz (Ref. 18). The apparatus was designed so that a systematic study can be made of the over-all diffusion process for a wide number of internal and external receiver-diffuser geometries. Provisions have been made in the apparatus for varying the nozzle-to-receiver spacing, the length of constant-area mixing section, and the included angle and area ratio of the area change diffuser section (by using a series of molded plastic diffusers). A schematic of the experimental apparatus is shown in Fig. 9. The apparatus is sufficiently flexible so that radically different geometries could be incorporated if desired.

Illustrative of the preliminary experimental results are the pressure-flow data shown in Fig. 10. These data show the effect of variation of included angle of the area change diffuser. The significant increase of maximum power recovery ($Q_a \times P_a$) by use of a low angle diffuser is evident.

A comprehensive experimental study is planned which will cover a wide Reynolds number range and incorporate a large number of geometrical variations. Air (or water) and hydraulic oil will be used as working fluids. Results will be presented when they become available.

2.3. Jet-Receiver Dynamic Interaction Studies

2.3.1. Preliminary Measurements of Source Dynamic Characteristics

In the previous annual report on this contract (Ref. 1), an experiment involving a simple axi-symmetric nozzle-receiver was outlined.

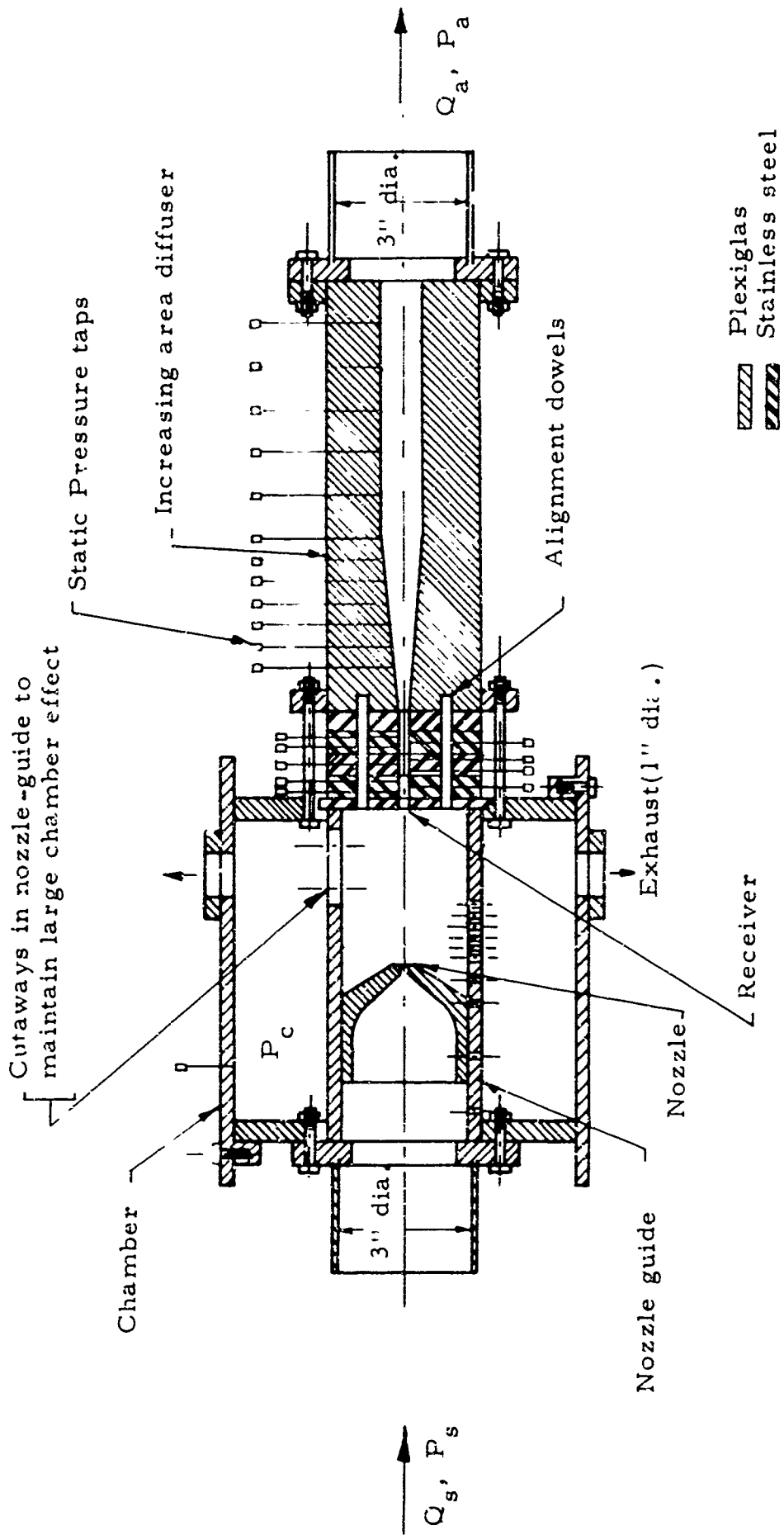


Fig. 9. Schematic of Apparatus for Studying Steady-State Characteristics of a Three-Way Jet Modulator.

	2θ	s/D_r	L/D_r
○	5°	2	2
△	14°	2	2
□	180°	2.5	2

Conditions:
 $D_r = 0.25$ in.
 $D_n = 0.187$ in.
 $Re_n = 16.7 \times 10^3$

Nomenclature:

- D_r = Receiver diameter
- D_n = Nozzle diameter
- S = Nozzle-receiver spacing
- L = Diffuser mixing section length
- 2θ = Diffuser included angle
- P_c = Chamber pressure
- Re_n = Reynolds number based on nozzle diameter

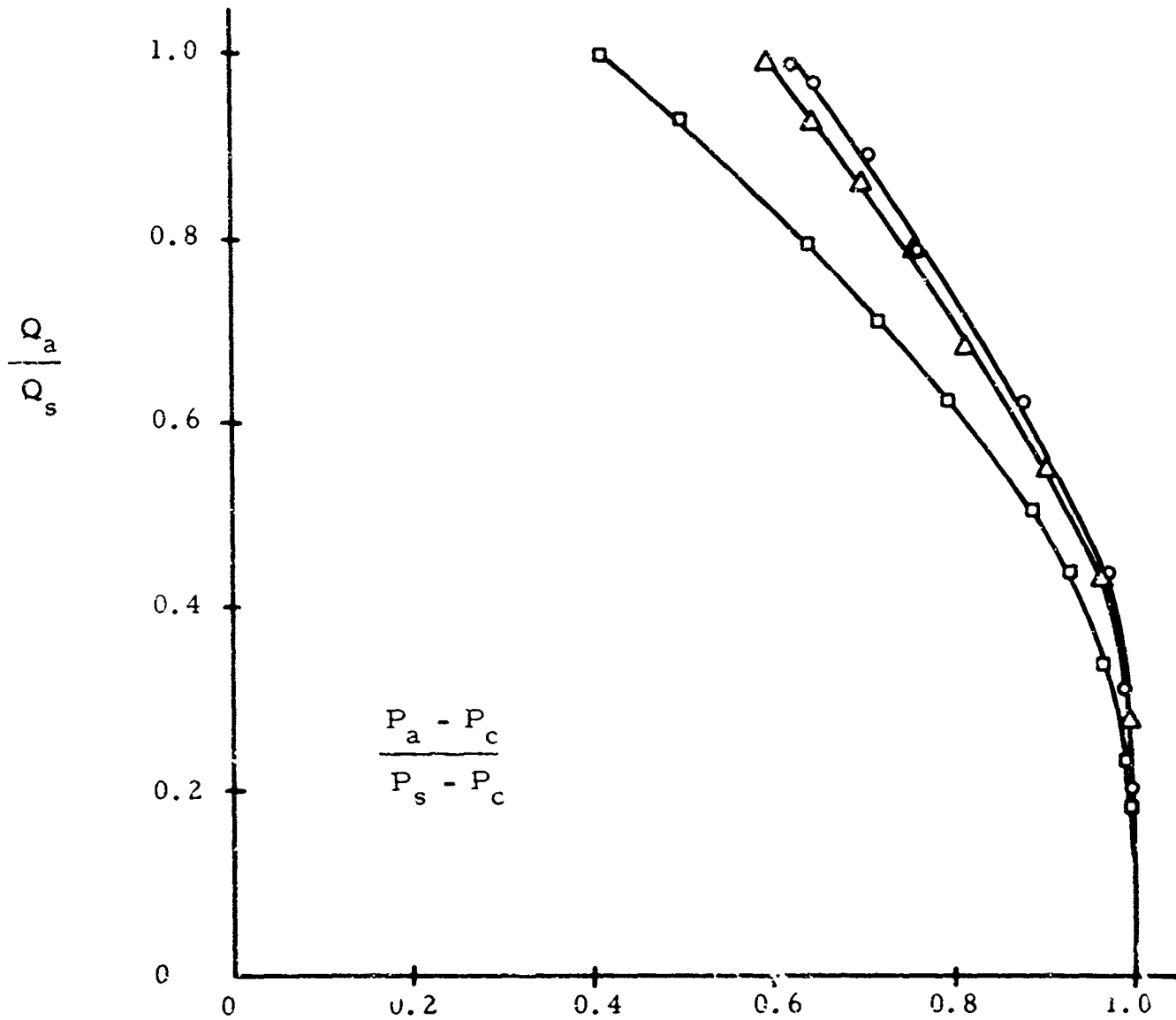


Fig. 10. Pressure-Flow Characteristics of a Three-Way Jet Modulator

The experiment was designed to measure the dynamic characteristics of the jet-receiver interaction region (termed the "source") as viewed from a point downstream in the receiver. Provisions were made for introducing a pressure pulse at a point downstream in the receiver, measuring the pressure associated with the incident and reflected waves, and damping out all extraneous waves. The experiment thus constituted a pulse or step response of the interaction region. Having obtained a dynamic characterization of the source, stability of systems incorporating this source could be investigated.

Since the last writing, measurements have been made which indicate that the reflection of a pulse or step from the source terminal can be characterized simply by a "reflection coefficient" for frequencies up to at least several hundred cycles per second. This implies that for low frequencies, the steady-state pressure-flow characteristics are adequate to predict the interaction region phenomena. Measurement techniques and typical steady-state characteristics are discussed in Sec. 2.3.3.

2.3.2. "Creation" of an Active Source

Before a study of the dynamic or static characteristics of the interaction region could be made, it was necessary to establish means for "creating" an active source, i. e., a source which "feeds" an impending oscillation. Certainly, past experience with jet modulators of various types is sufficient to give one confidence that a sustained pressure oscillation in the receiver can be produced! It will be recalled that the axi-symmetric nozzle-receiver-transmission line-load apparatus was constructed to eliminate all unnecessary solid boundaries in the interaction region and all potential receiver cross-coupling effects. With the apparatus so constructed, the influence of various types of nearby bounding surfaces can be studied in a systematic manner.

Consequently, the apparatus was arranged to have a source driving a transmission line blocked at its downstream end, since a sustained pressure oscillation is most likely to occur in such a system. Then, various solid boundaries were placed in the interaction region in an effort

to create a "large" amplitude pressure oscillation in the line. The configurations, shown in Fig. 11, were found to produce the desired oscillation. Case (a) typifies the phenomena observed.

By proper placement of the wall in the jet, the jet is caused to attach and follow the wall until the point is reached where an adverse pressure gradient causes it to separate. Placement of the receiver mouth near the separation point results in a sustained pressure oscillation in the transmission line and a corresponding oscillation of the jet. The nature and cause of the oscillation can be explained qualitatively as follows: As the jet is "turned on", the pressure begins to rise in the receiver as a result of simple charging of the associated capacitance; the pressure in the separation region also rises above its "equilibrium" value because of the high resistance to flow introduced by the wall-to-receiver mouth restriction; the pressure in the separation region finally becomes large enough (but not necessarily above atmospheric) that the jet is caused to separate further up the wall and thus partially miss the receiver; the receiver and separation region pressures then tend to decrease until the original separation point is restored, at which point the process is repeated again and again. Of course, wave motion in the receiver-line plays an important role in this phenomena. As the jet is turned on, a compression wave travels down the line and is reflected from the blocked end as a compression wave. When this wave returns to the receiver mouth, it causes the separation region pressure to increase rapidly and the jet to suddenly flip away from the wall. The motion of the jet causes a sudden decrease in the pressure at the receiver entry and, as a consequence, causes a rarefaction wave to travel down the line. This wave is reflected from the blocked end in like sense, and on its return to the receiver mouth, reduces the separation region pressure enough so that the jet can re-attach at the original point of attachment. The receiver pressure oscillation is very nearly triangular in shape.

It is important to note that it is not necessary to have a wave-like element (i. e., a transmission line) connected to the source in order to observe a sustained oscillation. If a tank (simple capacitance) is substituted for the transmission line, the tank pressure will oscillate as well.

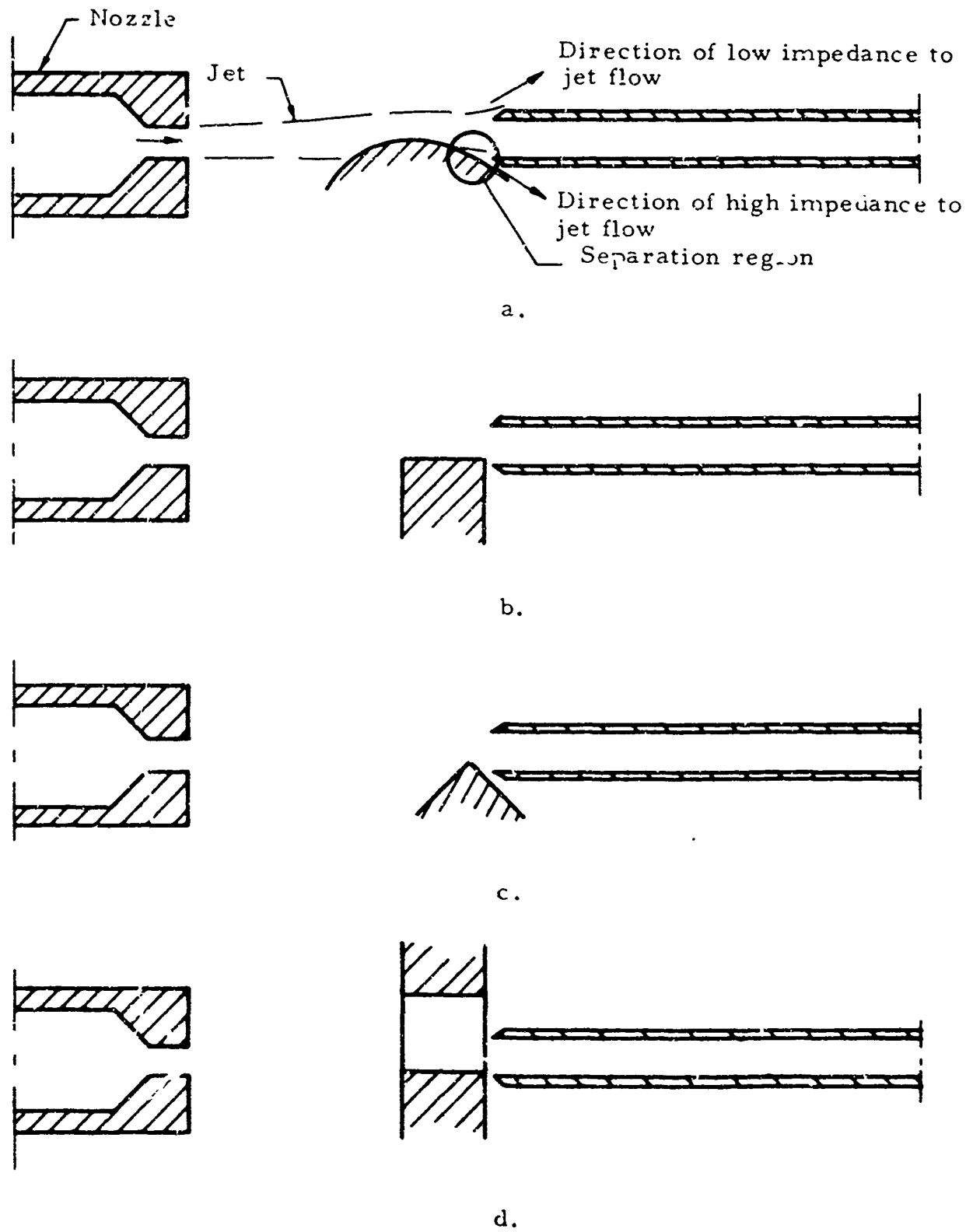


Fig. 11. Demonstrated "Active" Sources.

In this case, the oscillation is characterized by an exponential rise followed by an exponential decay, i. e., a direct result of the inherent RC characteristics of the receiver-tank combination. The charging and discharging time constants usually are different, the discharging time constant generally being the smaller of the two.

The explanation of the oscillation phenomena given above applies qualitatively to Cases (b), (c), and (d) of Fig. 11 as well. The most important features of the potentially unstable configuration seem to be: (1) a boundary be present onto which the jet can attach, and, (2) the boundary be placed slightly into the jet and near the receiver mouth so as to create a semi-enclosed separation region.

2.3.3. Conceptual Representation of a Single-Receiver Jet-Modulator System

It is convenient to represent the system being studied by a chain of four terminal elements as shown in the block diagram of Fig. 12, where the W's are mass flow rates and the P's are static pressures. The "source" includes the nozzle, jet, and receiver-diffuser. The "line", if one exists, includes any reasonably long constant diameter passage⁺ which connects the source to the load, and along which wave motion effects are important. The "load" includes all active and passive elements attached to the line or directly to the source, i. e., tanks, orifices (laminar or square law), jet-modulator control ports, etc.

A characterization of the source involves establishing the functional relationship $W_a = f(P_a, \text{geometry})$.

2.3.4. Measurement of Steady-State Characteristics of an Active Source

Reasonably early in the study, physical intuition and reasoning led to the conclusion that the steady-state source characteristic for a potentially unstable geometrical configuration was probably S-shaped. Such is true for most dynamic systems which exhibit a tendency toward self-excited oscillations. A sketch of the "anticipated" active source characteristic is shown in Fig. 13 along with a typical passive characteristic.

⁺ The line may also be made up of several lengths of piping, each having a different diameter.

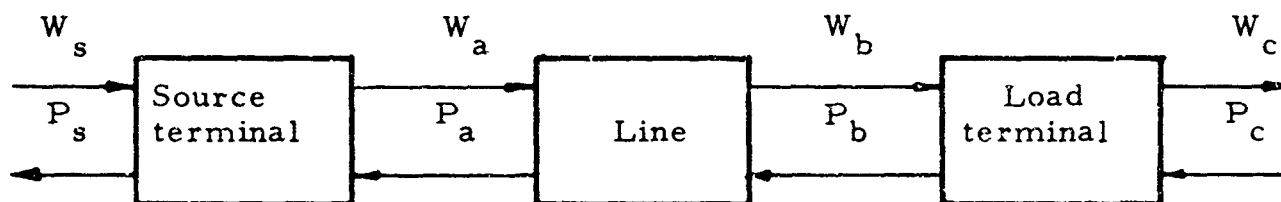


Fig. 12. Block Diagram of Single-Receiver Jet-Modulator System.

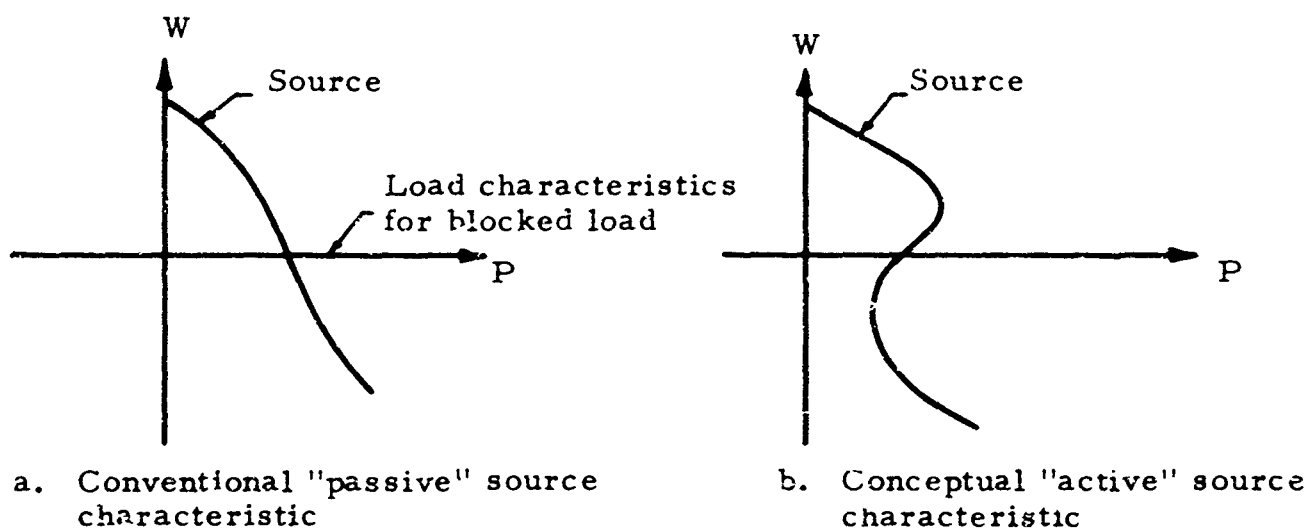


Fig. 13. Typical Passive and Active Source Characteristics.

It is well known that instability is most often associated with a blocked load condition. Furthermore, if sufficient fluid is allowed to flow from the load, the system may be stabilized. Considering a system consisting of a source plus a resistive load, a blocked load (i. e., an infinite load) characteristic superimposed on the source characteristic consists of the zero-flow axis, as shown in Fig. 13. The point of intersection is, of course, the simultaneous "solution" or the equilibrium condition (if one exists). To better understand the relationship which must exist between load and source resistances in order to produce an instability, it is helpful to refer to Fig. 14. Three typical cases are shown for example only. This in no way presents a complete picture of system stability, as will become evident in the following section. In each of the cases shown in Fig. 14, only the region of intersection of the two characteristics is shown. Stability "in-the-small" may be determined by considering the consequences of a small positive pressure disturbance relative to the apparent equilibrium condition. Below each W versus P plot is a schematic of a small control volume supposed to be situated between the source and load. The source flow enters the control volume and the load flow leaves the control volume; equilibrium requires that these two flows be equal. The length of arrow is indicative of the relative magnitude of the corresponding flows entering and leaving as a result of the pressure disturbance.

Both cases (a) and (b) represent stable systems since a positive pressure disturbance leads to a load flow demand which is greater than the source can provide, thereby causing the pressure to decrease once again. In contrast, Case (c) represents a situation where the positive pressure disturbance leads to a load flow demand which is smaller than the source supplies. As a result, the pressure increases even further until eventually some mechanism places a limit on its magnitude. This is a static type of instability. It will be seen in Sec. 2.3.5 that three types of instabilities can be identified, one of which is a static instability.

The conventional technique for measuring the portion of the characteristic curve in the first quadrant for a passive source involves varying the load resistance from zero (vertical line) to infinity (horizontal

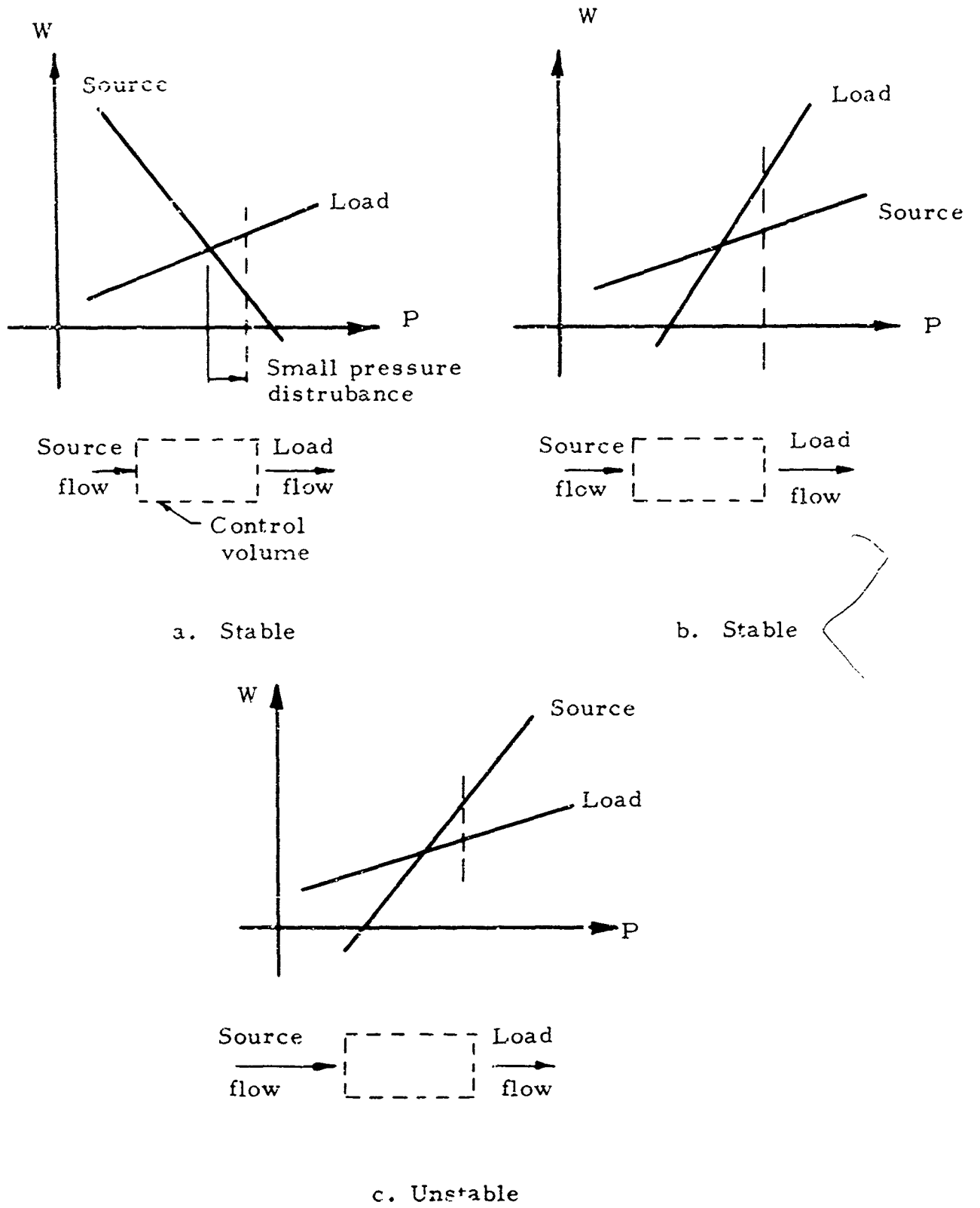


Fig. 14. Concept of Static Stability "In-the-Small".

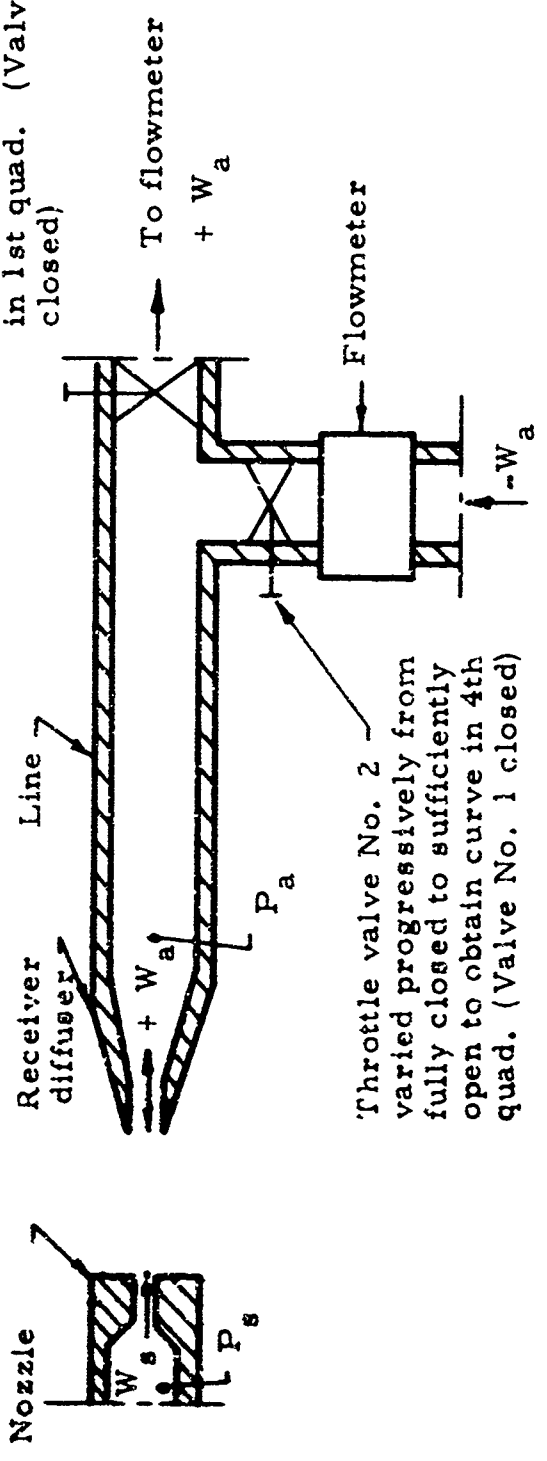
line), in such a way that the resistance is always positive. To measure the portion of the curve in the fourth quadrant, it is necessary to vary the load curve slope from a large negative value to a small negative value. The negative slope load is produced by supplying flow from an external source. In all cases, the load curve passes through the origin of the coordinates. Figure 15 illustrates schematically the experimental technique. Notice that there are two throttle valves, one of which is generally always closed (although this is not necessary).

Obviously the technique employed to measure the characteristic of a passive source would lead to a static instability in the case of an active source (i. e., see Fig. 14c). If, however, a family of load characteristic curves can be generated which all have a relatively low resistance (i. e., large change in flow for a small change in pressure) in the vicinity of their point of intersection with the source curve, stable operation can be achieved (i. e., see Fig. 14 b). A possible set of load curves is shown superimposed on a source curve in Fig. 16. It is not necessary that all the curves have the same slope, only that the slopes be very near zero in the region of potential static instability. In contrast to the passive source measurement technique, it is not possible for all the load curves to pass through the origin.

An experimental technique which can be used to obtain the active source characteristic curve is shown schematically in Fig. 17.

The critical flowmeter is a simple orifice in which the flow is always choked. Choked flow is insured if the supply pressure to the orifice is maintained always at least twice the downstream pressure. Constant flow is achieved by maintaining the upstream pressure constant at a reasonably large value compared to the maximum expected value of the downstream pressure. The flow rate to be determined, W_a , is equal to the total flow as indicated by the downstream rotameter minus the constant flow from the external source. In the first quadrant, W_a is positive and the rotameter flow is greater than the flow from the constant flow source. In the fourth quadrant W_a is negative and the rotameter flow is less than the flow from the constant flow source. It is evident that if the flow from the constant flow source is adjusted properly, the flow rate W_a can be made to undergo

Load Valve No. 1 - varied progressively from wide open to fully closed to obtain curve in 1st quad. (Valve No. 2 closed)



Throttle valve No. 2 varied progressively from fully closed to sufficiently open to obtain curve in 4th quad. (Valve No. 1 closed)

From high pressure source

Fig. 15. Experimental Technique for Determining the Characteristic Curve of a Passive Source.

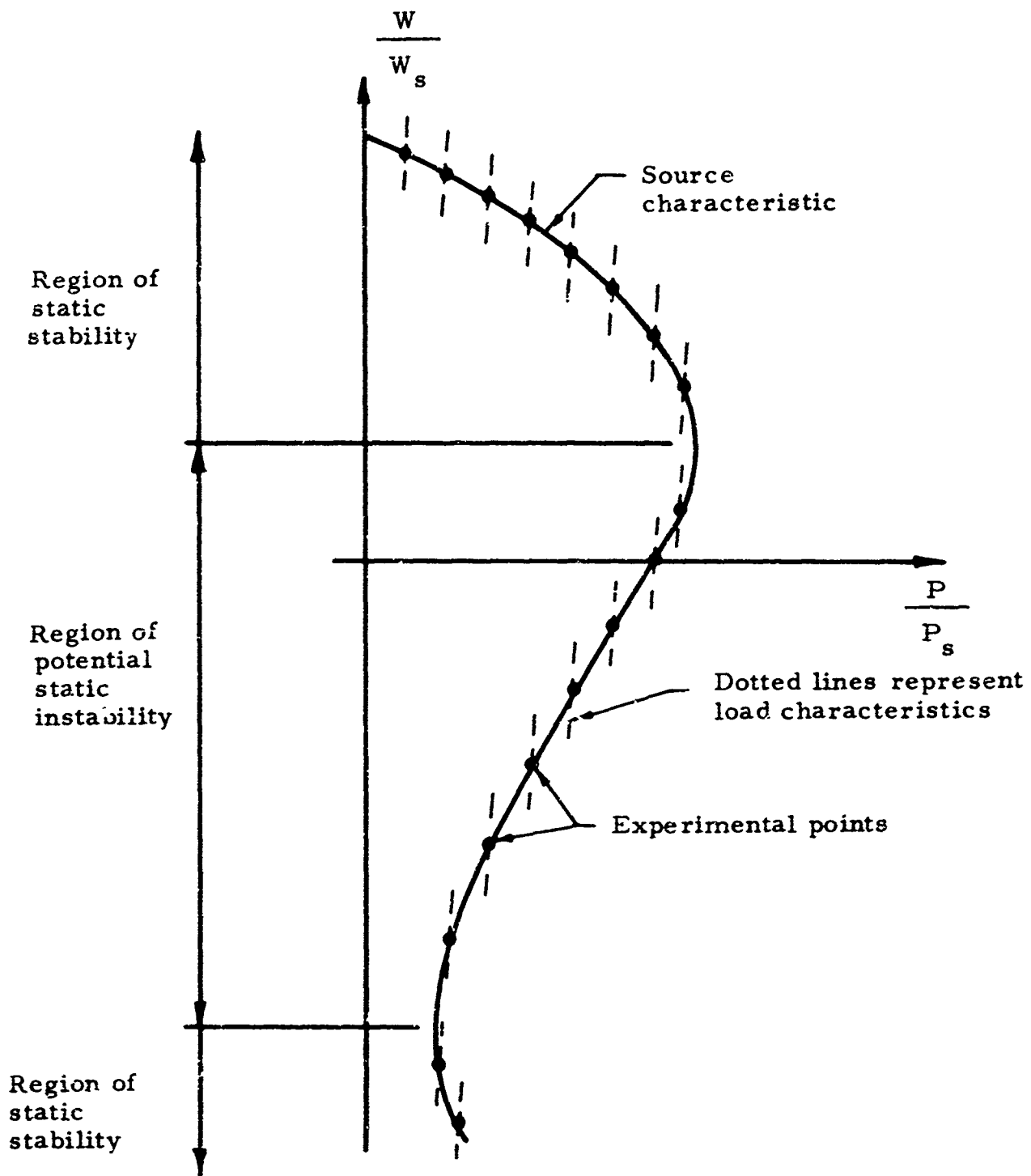


Fig. 16. Concept of Point-By-Point Measurement of an Active Source Characteristic.

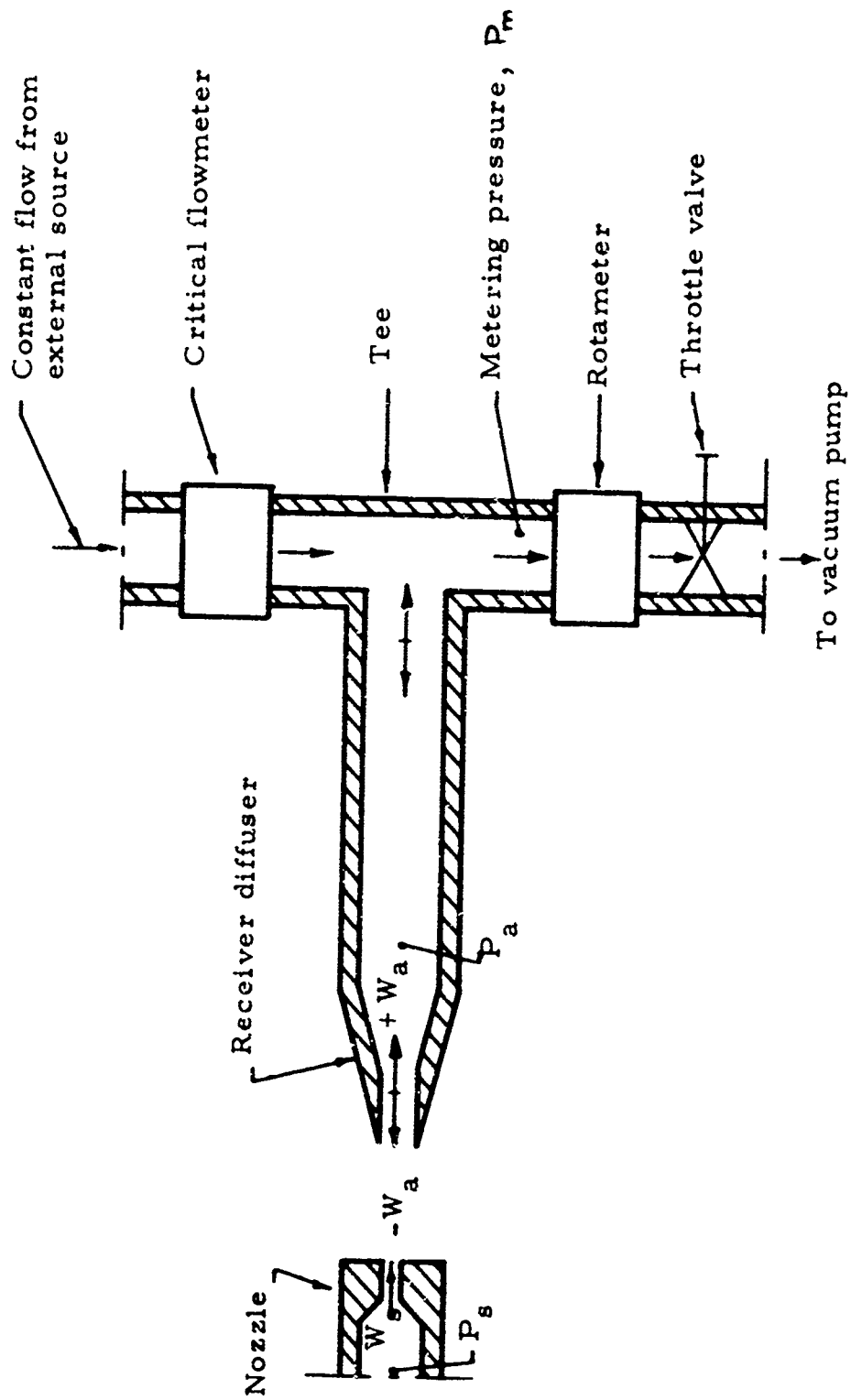


Fig. 17. Experimental Technique for determining the Static Characteristic of an Active Source.

large changes while the metering pressure P_m undergoes only small changes. The progressive variation from one load characteristic curve to another is accomplished simply by varying the amount of downstream throttling. Notice, for example, that the load curve which intersects the source curve at $W_a = 0$ is obtained by setting the downstream throttle such that $P_a = P_m = P_{\text{ambient}}$. In this case, the rotameter flow exactly equals the flow from the constant flow source.

The measurement technique outlined above has been used successfully to measure steady-state source characteristics for one particular active source. There are, of course, other techniques which could be used. For example, one promising technique involves the use of a very long line connected to the source and/or a terminal load attached to the end of the line having an impedance equal to the line surge impedance. Any pressure waves would then be damped due to friction and/or absorbed by the "perfectly matched" terminal. Although a reasonably successful attempt was made to construct a "perfectly matched" load terminal, this technique was abandoned in favor of the other technique because of superior performance and simplicity of the latter. A typical measured characteristic is plotted in dimensionless form in Fig. 18. The source geometry was chosen such that, when coupled with a load, a high degree of instability existed. It was the purpose of this preliminary experiment to demonstrate technique only. A systematic study of the effect of geometrical variations on the character of the source is expected to be carried out in the future by another investigator.

2.3.5. Analytical Prediction of "Stability-in-the Small"

Consider, as before, the single-receiver jet-modulator system consisting of an active source coupled to an active or passive load terminal by means of a simple transmission line. In the discussion to follow, the concept of "load" will be broadened to include all elements coupled to the source. For the particular case being considered here, the "load" includes the transmission line and the load terminal. Such a system is interesting as well as practical in that it serves as a potential building block for more complicated systems.

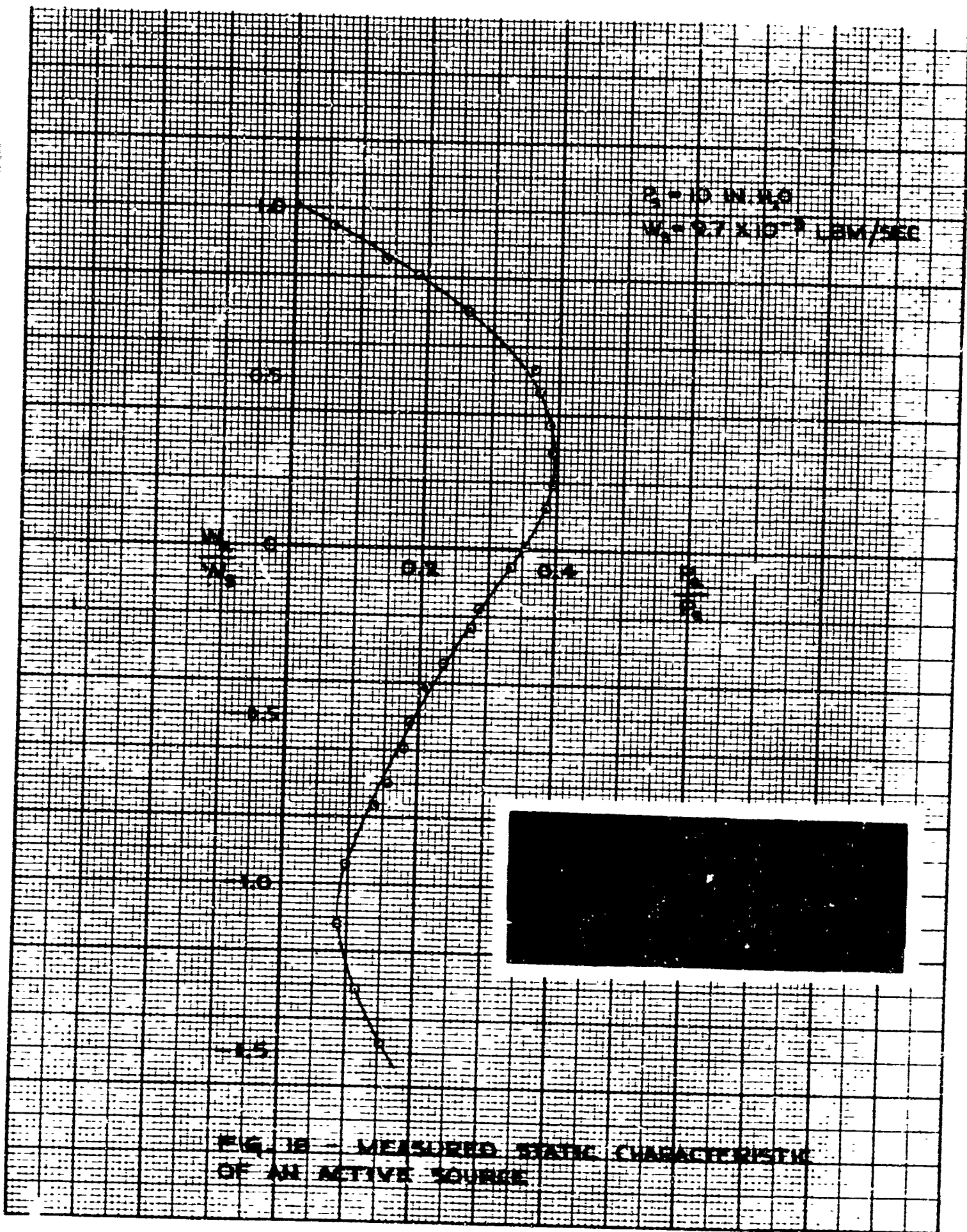


FIG. 18 - MEASURED STATIC CHARACTERISTIC OF AN ACTIVE SOURCE.

Fig. 18. Active source characteristic.

The presence of the "wave-like" element (transmission line) in the system suggests that consideration be given to system dynamic stability as well as the static stability discussed in the previous section. Professor F. T. Brown has suggested that the absolute stability "in-the-small" of such a system be classified according to the character of the load. The following types of stability (or instability) are then identifiable: Static, wave, and surge. These three types of stability arise on considering the effect of the length of the transmission line coupling the source and load. Static stability is obviously associated with a system containing an extremely short line. Referring again to the discussion of static stability in the previous section and, in particular, to the sketches in Fig. 14, it is possible to establish a simple criterion for static stability "in-the-small" (i. e., for small disturbances). The system is stable in the vicinity of the equilibrium point (i. e., point of intersection of the source and load curves) if the source impedance, Z_s , and load impedance, Z_l , are related by the inequality

$$\frac{1}{Z_s} + \frac{1}{Z_l} > 0 \quad (23)$$

Notice that a positive value of source impedance implies a negative slope on the W versus P plot, whereas a positive value of the load impedance implies a positive slope on the W versus P plot. This is merely a result of sign convention for the flow, i. e., positive flow is defined as flow from the source to the load.

If the source-to-load capacitance is also very small, the static instability will result in a very high frequency oscillation. In such a case, the concept of static stability based on the measured steady-state characteristic curve for the source may lose its meaning because of the inadequacy of this characteristic at high frequencies. For this case, the source dynamic characteristics must be considered and it is appropriate to speak of the corresponding dynamic stability (as distinct from wave and surge types of dynamic stabilities associated with transmission lines).

If the line attached to the source is very long, pressure waves take a considerable time to travel down the line and then return again.

Over the period of the round-trip of a wave, the effective load impedance seen by the source is the "surge" or "characteristic" impedance of the line rather than the impedance of the load terminal. The idealized⁺ characteristic impedance of a line of cross-sectional area A, in terms of a ratio of pressure to mass flow rate at a point in the line, is given simply by $Z_c = c/A$, where c is the speed of sound in the medium. The stability criterion given by Eq. (23) applies to this surge situation if Z_l is replaced simply by Z_c . Thus the system is surge-wise stable if the following inequality is satisfied

$$\frac{i}{Z_s} + \frac{1}{Z_c} > 0 \quad (24)$$

The oscillation frequency associated with a static or surge-type instability is characteristically quite high. The very high frequency noise associated with most jet-modulator systems is undoubtedly a manifestation of the surge-type instability.

Since the surge impedance only represents the true load impedance seen by the source for relatively short periods of time, it is necessary to consider wave motion effects if stability over longer periods of time is of interest (and it most often is of prime interest). Wave motion effects obviously have their greatest importance for intermediate length lines. Here, consideration of the reflection of waves from both ends of the transmission line leads to the concept of "wave stability."

The ratio of the pressure amplitude of a wave reflected from the termination of a line to the pressure amplitude of the incident wave producing the reflection is known as the "reflection coefficient". An expression was derived from first principles in the previous report (Ref. 1) which relates the reflection coefficient to the terminal and line characteristic impedance as follows:

$$\frac{P_-}{P_+} = r = \frac{Z_t - Z_c}{Z_t + Z_c} \quad (25)$$

⁺ neglecting wall shear

where Z_t is the terminal impedance. A close examination of Eq. (25) reveals that the reflection coefficient, r , may be positive or negative, must be equal to or less than unity if the terminal is passive, and is unbounded if the termination is active.

Consider now a "lossless" transmission line having two terminals, a source and a load. For the sake of generality, let the associated terminal impedances be denoted as Z_1 and Z_2 , without specification as to which refers to the source and which to the load. If a wave reflects first off of one terminal and then the other, that is, undergoes one complete cycle returning to its initial position and direction of motion, its new amplitude is $r_1 r_2$ times its initial amplitude. The product $r_1 r_2$ may be positive or negative and equal to, less than, or greater than unity. If $|r_1 r_2| > 1$, then the wave has picked up energy (from an active source and/or load) and the system is unstable. Such a result was clearly evident in the limited data (oscilloscope pictures) presented in the previous report. One of two types of instabilities may exist. If $r_1 r_2 > +1$, the instability is "exponential" in-the-small (Type I) whereas if $r_1 r_2 < -1$, the instability is oscillatory (Type II). This follows directly from consideration of more than one complete cycle of travel of a given wave.

The criterion for wave-type absolute stability is therefore

$$\left| r_1 r_2 \right| < 1 \quad (26)$$

A condition of marginal stability exists when

$$\left| r_1 r_2 \right| = 1$$

Combining Eqs. (25) and (26) gives the criterion for absolute stability in terms of the surge and two terminal impedances. Thus

$$\left| r_1 r_2 \right| = \left| \left(\frac{Z_1 - Z_c}{Z_1 + Z_c} \right) \left(\frac{Z_2 - Z_c}{Z_2 + Z_c} \right) \right| < 1. \quad (27)$$

Consider again the two types of instability. For Type I, Eq. (27) shows that for absolute stability

$$Z_1 + Z_2 < 0, \text{ if } Z_2(\text{or } Z_1) < Z_c < Z_1 (\text{or } Z_2)$$

$$Z_1 + Z_2 > 0, \text{ if } Z_c > Z_1 \text{ and } Z_2,$$

and for marginal stability, $Z_1 + Z_2 = 0$.

For Type II, Eq. (27) shows that for absolute stability

$$Z_1 Z_2 + Z_c^2 < 0, \text{ if } Z_c > Z_1 \text{ and } Z_2$$

$$Z_1 Z_2 + Z_c^2 > 0, \text{ if } Z_c < Z_1 \text{ or } Z_2 \text{ but not both.}$$

and for marginal stability,

$$Z_1 Z_2 + Z_c^2 = 0.$$

A summary of the stability types and criteria for all possible permutations of real terminal impedances (resistances) is given in Table I. This summary was originally prepared by F. T. Brown and is reproduced from Ref. (19). The reader interested in a detailed treatment of stability considerations in "two-line" systems should refer to Ref. 19. In that reference, coupling between receivers and/or loads is also considered.

2.3.6. Graphical Techniques for Prediction of System Relative Stability

The stability criteria developed in the previous section are particularly useful when information concerning the absolute stability of a system is desired; that is, is the system stable or unstable "in-the-small?" Nothing can be inferred from these criteria concerning the relative stability of the system. In addition, these or similar criteria are difficult to apply in cases involving non-real terminal impedances. Very often, a knowledge of the frequency and amplitude of a pressure

Table 1

Z ₁ and Z ₂		Wave Stability		Surge Stability	Static Stability
		Stable	Type		
-∞	∞			$\frac{1}{Z} + \frac{1}{Z_c} > 0$	$\frac{1}{Z_1} + \frac{1}{Z_2} > 0$
✓✓		No	Non-oscillatory	Yes	No
✓		No	Oscillatory	No	No
		No	Non-oscillatory	No	No
✓	✓	when $Z_1 Z_2 + Z_c^2 < 0$	Oscillatory	Yes	Yes
✓	✓	when $Z_1 + Z_2 < 0$	Non-oscillatory	Yes	when $Z_1 + Z_2 \leq 0$
	✓	when $Z_1 + Z_2 > 0$	Non-oscillatory	No	when $Z_1 + Z_2 \leq 0$
	✓	when $Z_1 Z_2 + Z_c^2 > 0$	Oscillatory	No	No
	✓✓	Yes	--	Yes	Yes
	✓	Yes	--	Yes	Yes
	✓✓	Yes	--	Yes	Yes

oscillation is required. For example, such information is vital in the design of oscillators. As another example, consider a system which exhibits an instability. The over-all performance of the system may not be impaired significantly providing the oscillation frequency is high enough and the amplitude is low enough; again a knowledge of the detailed character of the oscillation is required before its effect can be fully evaluated.

The suitability of graphical techniques such as the method of characteristics (Ref. 20) and slope-line integration (Refs. 21 and 22) for dealing with transient phenomena in systems incorporating simple nonlinearities, wave-like elements, and other simple active and passive elements, is well known. It follows, therefore, that these graphical techniques should be extremely useful in studying the relative stability of simple jet-modulator systems comprising a single source, transmission line, and load. As will become evident in the discussion which follows, these graphical techniques afford an amazingly accurate and rapid approach to the study of jet-modulator system stability. As a demonstration of the utility of these techniques, three interesting examples are discussed below. In each case, the analysis is semi-empirical in that experimentally derived (or otherwise known) source and load pressure-flow characteristics are utilized. The solutions presented are, therefore, limited to the range of frequencies for which the steady-state source and load characteristics are valid. In all cases, the basic equations describing system behavior are presented in finite difference form, since the graphical techniques involve a type of numerical step-by-step solution.

Example 1 - Active source coupled to a uniform rigid transmission line blocked at its downstream end. A schematic of the system under consideration is shown in Fig. 19. The solution sought is as follows: given a small disturbance in the load end pressure, P_b , what is the resulting variation of P_b with time, i. e., does the disturbance die out or does the presence of the active source lead to a wave instability. Furthermore, the detailed nature of any limit cycle is to be determined.

Before proceeding with the example a slight digression to consider pertinent details of the transmission line portion of the system only is deemed

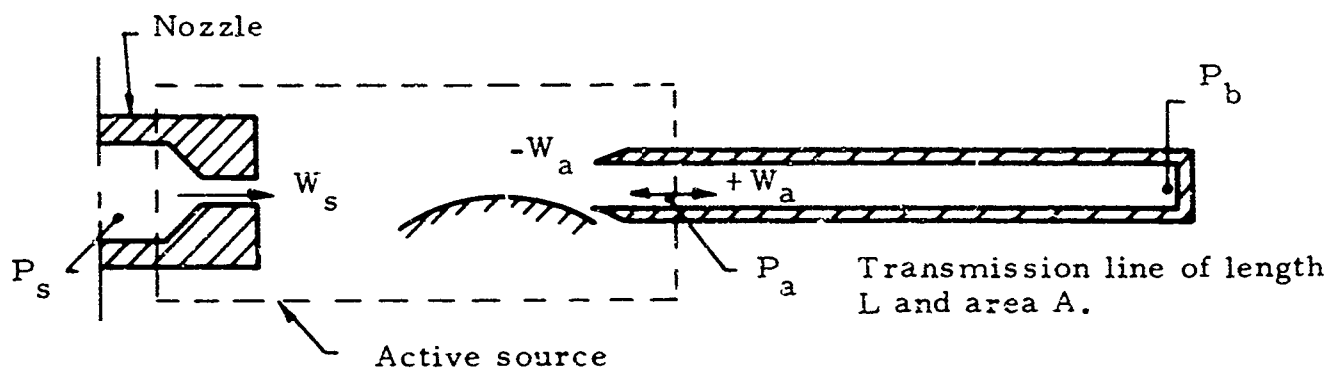


Fig. 19. Active Source Coupled to a Transmission Line Blocked at its Downstream End.

necessary. The line may be considered as a distributed parameter system but only small amplitude waves are admitted. It is further assumed that the gross fluid velocity is very small compared to the speed of sound in the medium and that wave dispersion effects are unimportant. The assumptions permit use of the well-known linearized form of the wave equations. Of the various forms of the solution, the most convenient is that given in terms of the conditions at the ends of the line as follows:

$$\begin{bmatrix} P_b \\ W_b \end{bmatrix} = \begin{bmatrix} \cosh \Gamma & -Z_c \sinh \Gamma \\ -\frac{1}{Z_c} \sinh \Gamma & \cosh \Gamma \end{bmatrix} \cdot \begin{bmatrix} P_a \\ W_a \end{bmatrix} \quad (28)$$

where

$\Gamma \equiv$ propagation operator

$Z_c \equiv$ characteristic impedance of the line; defined as the complex ratio of the instantaneous pressure to the instantaneous flow rate at a given point in the line.

Both Γ and Z_c are, in general, frequency dependent properties. In terms of the physical characteristics of the line,

$$\Gamma(s) = L \sqrt{Y(s) \cdot Z(s)}$$

and

$$Z_c(s) = \sqrt{\frac{Z(s)}{Y(s)}}$$

where

$L =$ distance separating two stations,

$Y =$ line shunt admittance per unit length,

$Z =$ line series impedance per unit length, and

$s =$ Laplace operator.

Brown (Ref. 23) has shown that, for the case of uniform attenuation (i. e., no dispersion), the propagation operator can be approximated as follows:

$$\Gamma = -a + \Gamma s \quad (29)$$

where

T = characteristic time of the line,
 $e^{-\alpha}$ = the attenuation factor; α is termed the attenuation constant.

For the special case of an ideal, lossless pneumatic line it follows that

$$\Gamma = Ts$$
$$Z_c = \frac{c_o}{A} = Z_{co}$$

where

c_o \equiv acoustic speed of sound; and
 A \equiv cross-sectional area of the line.

Experiment and analysis shows, however, that line friction is important even in seemingly short lines. As will become evident in Sec. 2.3.9, reasonable correlation between theory and experiment requires consideration of the effects of line friction (and corresponding attenuation).

Two convenient techniques are available for determination of the characteristic parameters Γ and Z_c ; the constant R-L-C model and a more rigorous and exact model based on the direct solution of the continuity, momentum, and energy equations which describe the process. Although considerably more complex, the "exact" model is generally superior since it includes varying velocity profile and heat transfer effects. Nevertheless, in certain cases the two models yield very nearly the same results and the simpler R-L-C model is adequate. Brief summaries of the techniques available for computation of the characteristic parameters are given below.

Constant R-L-C model (Refs. 23, and 26)

The series impedance and shunt admittance are given by

$$Z = ID + R$$

and

$$Y = CD$$

where

- I = inertance per unit length of line,
- C = capacitance per unit length of line,
- R = resistance to flow in line per unit length
- D = d/dt

Thus

$$\Gamma = L\sqrt{IC D^2 + RCD}$$

$$Z_c \approx \sqrt{\frac{Z}{Y}} \approx \sqrt{\frac{I}{C}} \sqrt{1 + \frac{R}{ID}}$$

But if R is sufficiently small (as it usually is) or if $R/I\omega \ll 1$, where ω is the lowest frequency component of interest, then

$$\Gamma = -\alpha + TD \approx \frac{LR}{2} \sqrt{\frac{C}{I}} + L\sqrt{CI} D$$

$$Z_c \approx \frac{I}{C} \left(1 + \frac{R}{2ID}\right)$$

For sinusoidal excitation the following limiting forms are useful:

$$\frac{R}{\omega I} \ll 1$$

$$\frac{R}{\omega I} \gg 1$$

$$Z_c \approx \sqrt{\frac{I}{C}}$$

$$Z_c \approx \sqrt{\frac{R}{j\omega C}}$$

$$\Gamma \approx L \frac{R}{2} \sqrt{\frac{C}{I}} + jL\sqrt{IC} \omega$$

$$\Gamma \approx L\sqrt{\frac{RC\omega}{2}} + jL\sqrt{\frac{RC\omega}{2}}$$

Thus, for uniform attenuation, the attenuation constant is

$$\alpha = -\frac{LR}{2} \sqrt{\frac{C}{I}} \quad \text{for} \quad \frac{R}{\omega I} \ll 1$$

and

$$\alpha = -L \sqrt{\frac{RC\omega}{2}} \quad \text{for} \quad \frac{R}{\omega I} \gg 1$$

If it is assumed that the flow is fully developed and laminar and that the line friction is the same as for steady flow, the attenuation constant can be expressed in terms of line and fluid properties⁺ as follows:

$$\alpha = -\frac{4Lv}{a^2 c_o} \quad \text{for} \quad \frac{8v}{a^2 \omega} \ll 1$$

$$\alpha = -\frac{2L}{ac_o} \sqrt{v\omega} \quad \text{for} \quad \frac{8v}{a^2 \omega} \gg 1$$

The assumption that the resistance is the same as for steady, fully developed laminar flow, can only be defended for cases where the frequency is low and the line length-to-diameter ratio is large. At the higher frequencies the unsteadiness of the flow results in an effectively higher value of the resistance. Rohmann and Grogran (Ref. 26) suggest that R be increased by 20 per cent over the calculated value. Equally important is the fact that in many practical situations (and perhaps the majority) the line length-to-diameter ratio is not large enough to discount the effect of increased resistance to developing flow, i. e., the apparent friction factor (and therefore the resistance) is significantly greater in the "entry length" of a tube than in the fully developed region many diameters

⁺ ν = kinematic viscosity
 a = line radius
 ω = frequency

downstream. Resistance estimates based on the friction factor correlations summarized by Shapiro, et al (Ref. 27) should provide corrections which are adequate for most engineering purposes. These correlations allow computation of the integrated apparent friction factor in the laminar entry of a tube as a function of diameter Reynolds number and the tube L/D ratio. The resistance R is computed easily from friction factor information.

"Exact" Model. - Derivations for the propagation operator and characteristic impedance are given by Brown (Ref. 24). The model assumes: cylindrical tube, one-dimensional flow, isothermal walls, small amplitude laminar disturbances, and continuous medium. Results pertinent to the present study have been extended in range and replotted in Figs. 20 and 21. Attenuation factors as a function of line and fluid properties may be obtained from Fig. 20. Since dispersive effects are neglected in the present example, only the magnitude of the characteristic impedance need be considered. Figure 21 may be used to obtain a correction to the nominal value of the characteristic impedance (i.e., $Z_{c0} = c_0/A$).

Having established means of computing Γ and Z_c it is necessary now to rewrite the line equations in a form suitable for step-by-step graphical or numerical solution. The method of solution requires that the equations be written in time difference form. By noting that

$$\cosh \Gamma = \frac{e^{\Gamma} + e^{-\Gamma}}{2} \quad ; \quad \sinh \Gamma = \frac{e^{\Gamma} - e^{-\Gamma}}{2}$$

and

$$e^{\text{TD}} F(t) = F(t + T)$$

a combination of Eqs. (28) and (29) yields the following two equations:

$$\frac{P_b(t+2T)}{P_s} - e^{2\alpha} \cdot \frac{P_b(t)}{P_s} = \frac{Z_c W_s}{P_s} \left[2e^{\alpha} \frac{W_a(t+T)}{W_s} - \frac{W_b(t+2T)}{W_s} \right. \\ \left. - e^{2\alpha} \frac{W_b(t)}{W_s} \right] \quad (30)$$

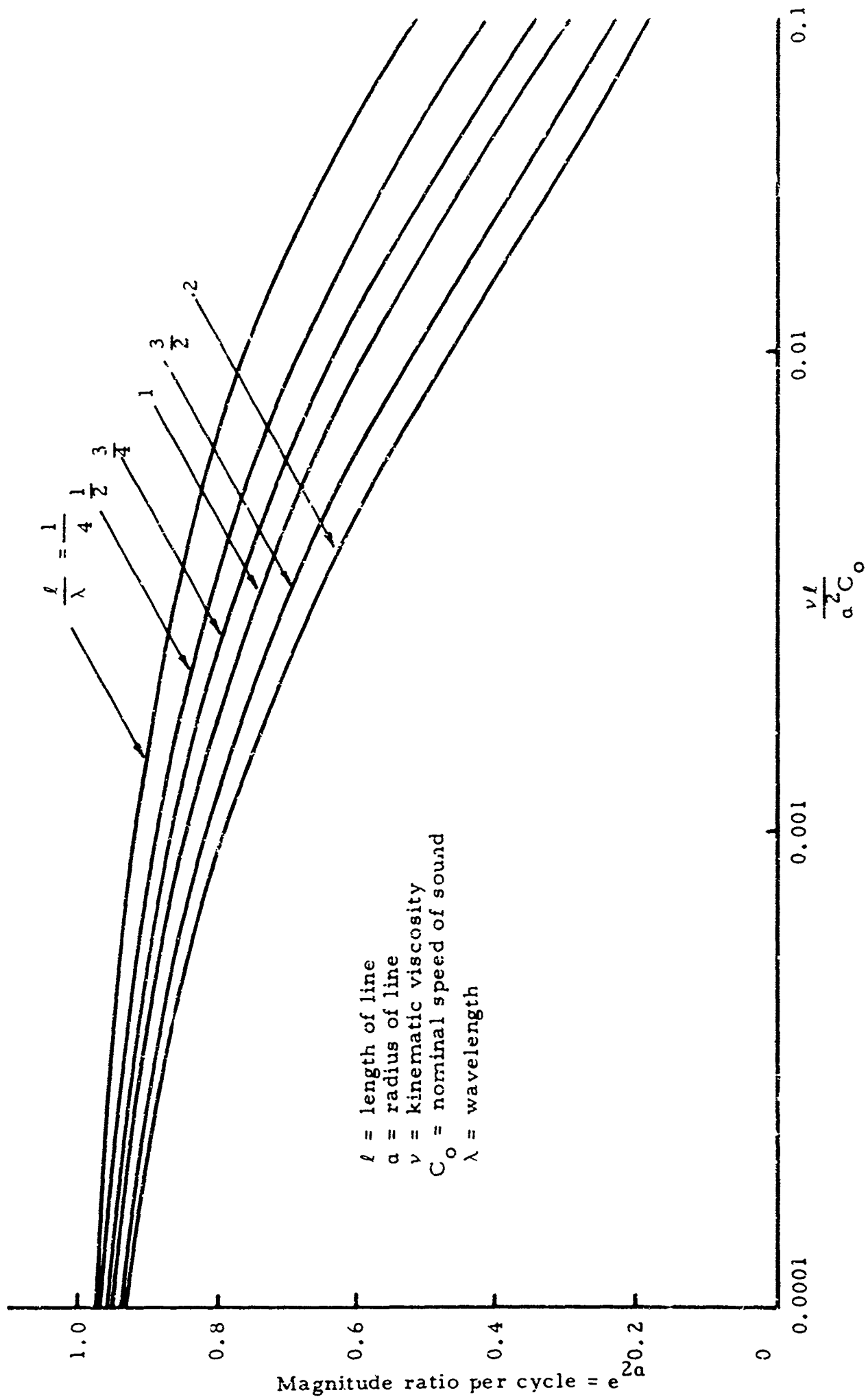


Fig. 20. Attenuation per Cycle of Small Amplitude Sine Waves in Rigid, Isothermal Wall, Laminar-Flow, Circular Air Line.

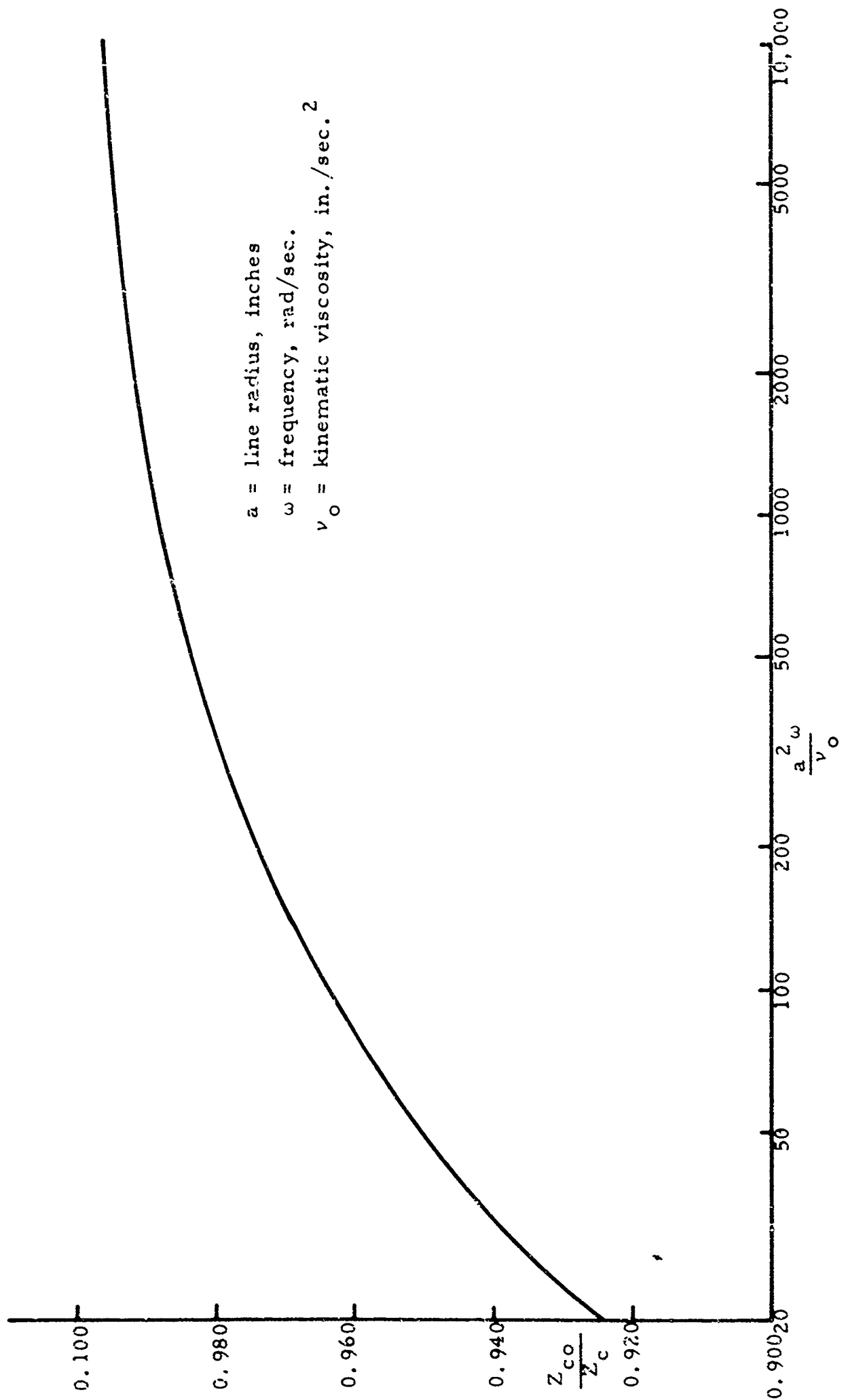


Fig. 21. Magnitude of Line Characteristic Impedance.

$$\frac{P_b(t + 2T)}{P_s} + e^{2\alpha} \frac{P_b(t)}{P_s} = 2c^a \frac{P_a(t + T)}{P_s} - \frac{Z_c W_s}{P_s} \left[\frac{W_b(t + 2T)}{W_s} - e^{2\alpha} \frac{W_b(t)}{W_s} \right] \quad (31)$$

where

- t = time variable
- T = L/c_o = characteristic time of the line,
- c_o = acoustic speed of sound in the fluid medium,
- Z_c = characteristic impedance of the line,
- W_s = nozzle mass flow rate, and
- P_s = nozzle supply pressure.

It is seen that events occur in increments of the characteristic time of the line T, that is, the time required for a wave to travel from one end of the line to the other. One period is equal to 2T.

Returning now to consideration of the entire system of Fig. 19, the describing equations in addition to the line equations are

Source:

$$\frac{W_a}{W_s} = f\left(\frac{P_a}{P_s}, \text{ geometry}\right) \quad (32)$$

Load:

$$\frac{W_b}{W_s} = 0; Z_l = \infty \quad (33)$$

The required solution is then a simultaneous solution of Eqs. (30) through (33).

Consider first the special case of a lossless line for which $e^{\alpha} = 1$. If the solution is assumed to "start" at an arbitrary non-equilibrium condition at $t = 0$, a combination of Eqs. (30), (31) and (33) yields:

$$\left(\delta \frac{P_b}{P_s} \right)_1 = \frac{P_a(T)}{P_s} - \frac{P_b(0)}{P_s} = \frac{Z_c W_s}{P_s} \frac{W_a(T)}{W_s} \quad (34)$$

for the period $t = 0$ to $t = T$, whereas

$$\left(\delta \frac{P_b}{P_s} \right)_2 = \frac{P_b(2T)}{P_s} - \frac{P_a(T)}{P_s} = \frac{Z_c W_s}{P_s} \frac{W_a(T)}{W_s} \quad (35)$$

for the period $t = T$ to $t = 2T$.

Analogous results for the more general case (i.e., $e^{\alpha} \neq 1$) are:

$$\left(\delta \frac{P_b}{P_s} \right)_1 = \frac{P_a(T)}{P_s} - \frac{P_b(0)}{P_s} = \frac{Z_c W_s}{P_s} e^{-\alpha} \frac{W_a(T)}{W_s} + (1 - e^{-\alpha}) \frac{P_a(T)}{P_s} \quad (36)$$

and

$$\left(\delta \frac{P_b}{P_s} \right)_2 = \frac{P_b(2T)}{P_s} - \frac{P_a(T)}{P_s} = \frac{Z_c W_s}{P_s} e^{\alpha} \frac{W_a(T)}{W_s} + (e^{\alpha} - 1) \frac{P_a(T)}{P_s} \quad (37)$$

Although Eqs. (34) and (35) for the lossless case admit simple graphical interpretation, Eqs. (36) and (37) do not. Since the usual case is such that $-\alpha \ll 1$, Eqs. (36) and (37) may be approximated by the following more tractable equations:

$$\left(\delta \frac{P_b}{P_s} \right)_1 = \frac{P_a(T)}{P_s} - \frac{P_b(0)}{P_s} \approx \frac{Z_c W_s}{P_s} e^{-a} \frac{W_a(T)}{W_s} \quad (38)$$

$$\left(\delta \frac{P_b}{P_s} \right)_2 = \frac{P_b(2T)}{P_s} - \frac{P_b(0)}{P_s} \approx \frac{Z_c W_s}{P_s} e^a \frac{W_a(T)}{W_s} \quad (39)$$

A simple graphical interpretation of the various system equations is presented in Fig. 22. The limiting case for which $e^a = 1$ is shown by the dotted line solution. The line equations may be rewritten to cover the time period $t = 2T$ to $t = 4T$. The graphical solution is continued in the same fashion as for the previous period of time. A complete solution for the case of a "lossless" line is carried out using an actual measured source characteristic in Fig. 23a. These results are presented in terms of a phase-plane plot of P_b/P_s versus W_a/W_s . The corresponding plot of P_b/P_s versus t/T is shown in Fig. 23b. It is evident that an exponential wave instability exists but that the nonlinearity associated with the source characteristic places an upper bound on the oscillation amplitude. Thus a "limit cycle" or "standing wave" exists whose frequency is the quarterwave frequency of the line and whose amplitude is equal to 3.84 times the nozzle supply pressure for the case of a supply pressure equal to 10 inches of H_2O . A complete solution showing the effect of line friction in a 3 foot line (0.518 inch in diameter) is shown in Fig. 24 for comparison. It is clearly evident that line friction is significant even in a comparatively short line. The resulting limit cycle amplitude is reduced to $P_b/P_s = 1.94$, whereas the oscillation frequency remains the quarter wave frequency as expected. The accuracy[†] of the graphical method of solution as presented here, depends mainly on the validity of the assumption that $-a \ll 1$.

[†] The term accuracy here refers to the method of solution of the describing equations and not to the quantitative comparison of the results with actual experiment.

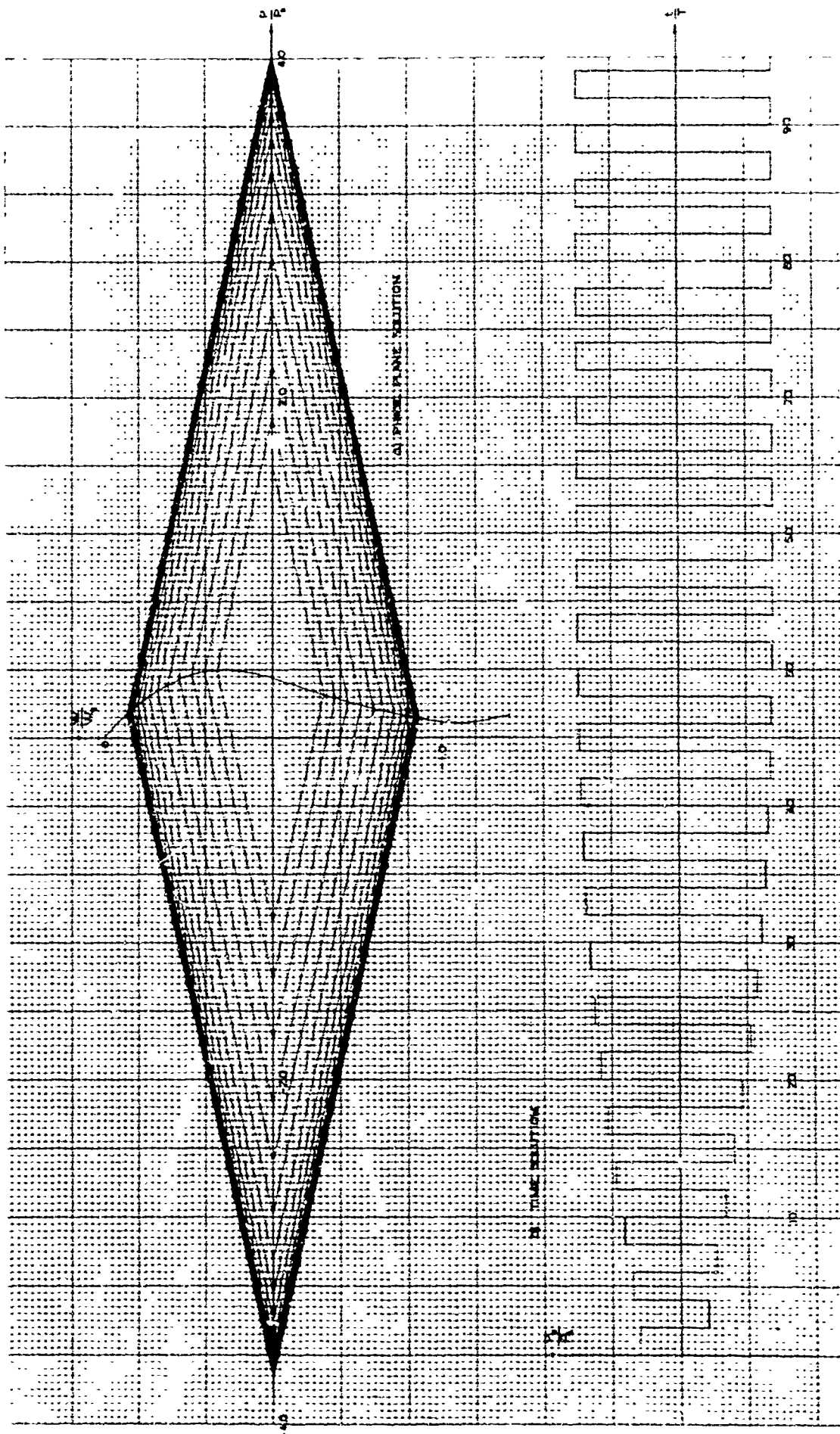


Fig. 23. Graphical Stability Analysis of an Active Source Coupled to a Lossless Transmission Line.

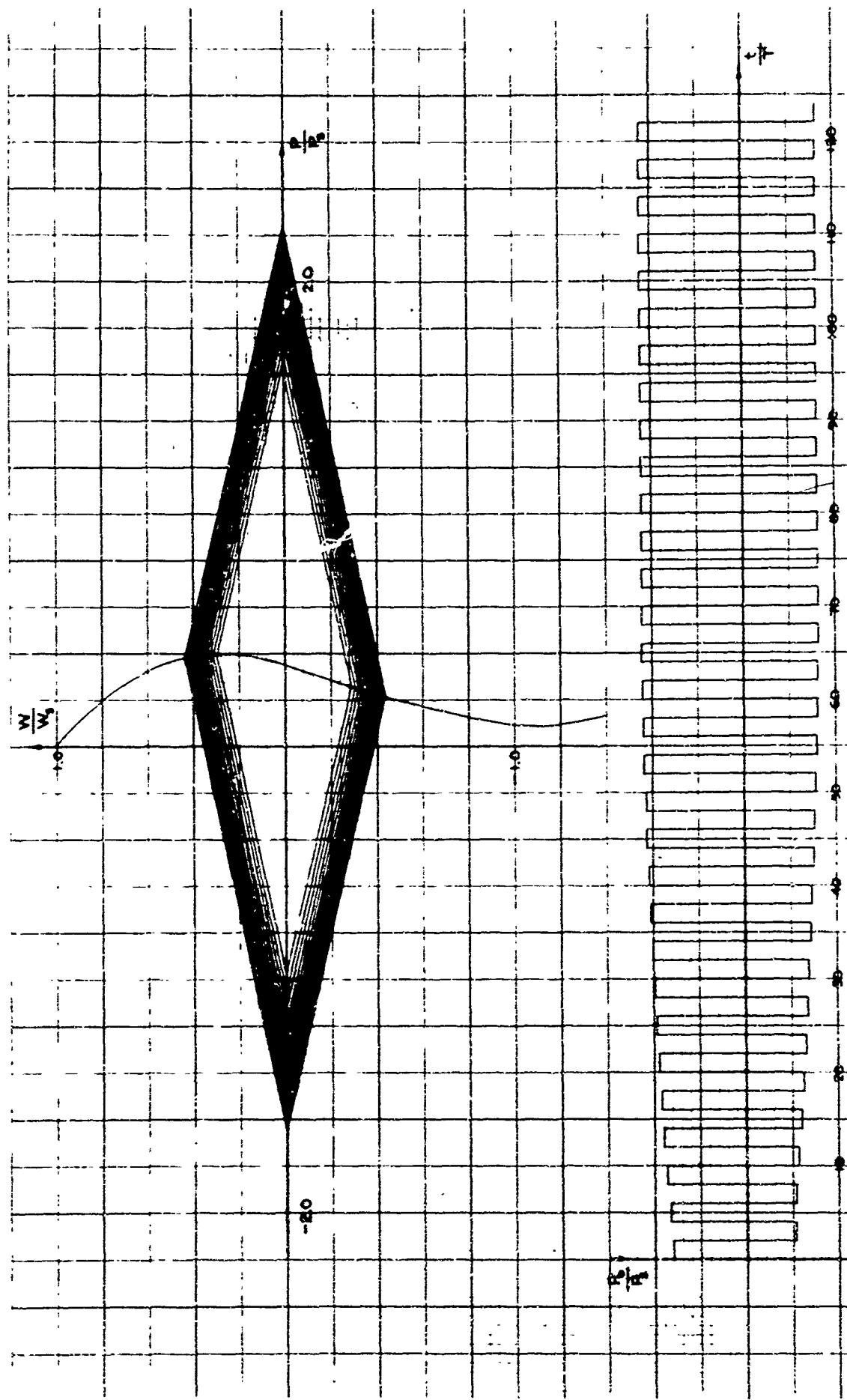


Fig. 24. Graphical Stability Analysis of an Active Source Transmission Line System Including Effects of Line Friction.

For the sake of generality, the solutions of Figs. 23 and 24 were carried out on a nondimensional basis. However, although the dimensionless source curve (for the particular geometry tested) is relatively independent of nozzle supply pressure over the range investigated ($5 \leq P_s \leq 20$ inch H_2O), the corresponding dimensionless characteristic impedance of the line is not. The dimensionless characteristic impedance is defined as

$$\bar{Z}_c = \frac{Z_c W_s}{P_s}$$

Thus the only way in which \bar{Z}_c can be independent of P_s is if $W_s/P_s = \text{constant}$, that is, the nozzle is a laminar flow resistance. In most practical cases, the nozzle is more nearly a square-law resistance. For the nozzle used in the experiments, the following relation can be established from the nozzle calibration data:

$$\bar{Z}_c = \frac{14.6}{(P_s)^{0.515}}$$

where P_s is given in inches of H_2O .

Solutions showing the dependence of the predicted limit cycle amplitude on the value of the dimensionless characteristic impedance are presented in Sec. 2.3.9.

The graphical technique demonstrated here is, of course, not limited to an infinite load terminal impedance. Solutions may be carried out for any real finite load terminal impedance, whether it be passive or active. It is interesting that a relatively small bleed orifice placed at the end of the line can completely eliminate the limit cycle instability.

Example 2 - Active source coupled to a load chamber (lumped compliance) with and without flow out of the chamber; no transmission line. A schematic drawing of the system considered is shown in Fig. 25.

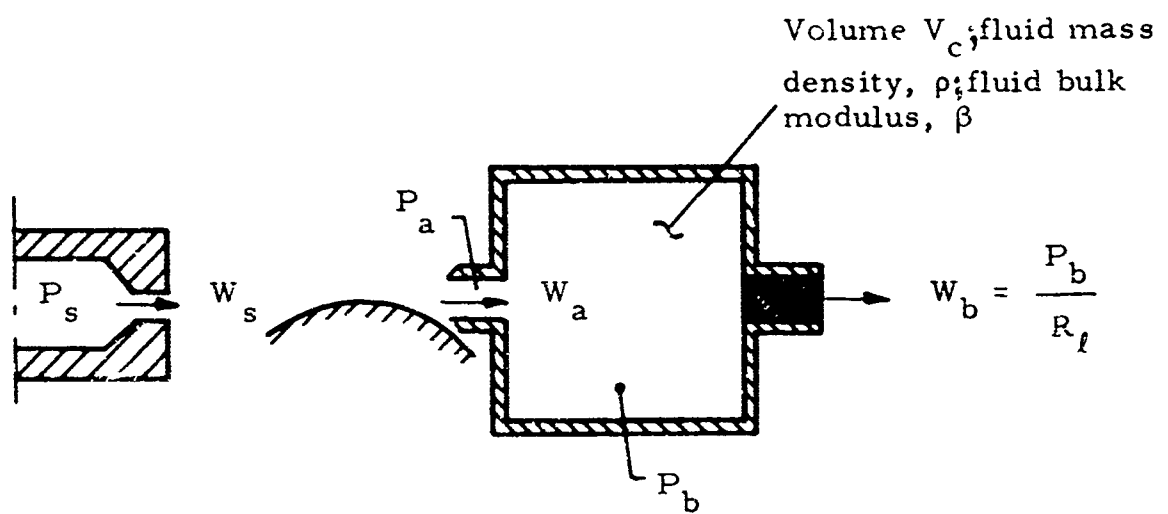


Fig. 25. Active Source Coupled to a Load Chamber.

The basic nondimensional equations which describe the system behavior include

Source:

$$\frac{W_a}{W_s} = f\left(\frac{P_a}{P_s}, \text{geometry}\right) \quad (40)$$

Chamber:

$$\frac{W_a}{W_s} - \frac{W_b}{W_s} = \frac{\rho V_c P_s}{\beta W_s} \frac{d\left(\frac{P_b}{P_s}\right)}{dt} = \frac{d\left(\frac{P_b}{P_s}\right)}{d\tau} \quad (41)$$

or in finite difference form

$$\delta\left(\frac{P_b}{P_s}\right) \approx \delta\tau \left[\frac{W_a}{W_s} - \frac{W_b}{W_s} \right]_{\text{ave}} \quad (42)$$

Load resistance (assumed to be linear):

$$\frac{W_b}{W_s} = \frac{P_s}{R_\ell W_s} \frac{P_b}{P_s} \quad (43)$$

where τ is the dimensionless time variable. These three equations contain four unknowns, so one additional equation is required. Consideration of energy, momentum, and continuity for the sudden expansion from section a to b leads to the conclusion that $P_a/P_s = f(P_b/P_s, W_a/W_s, A_a/A_b)$ where A_a = cross-sectional area of inlet and A_b = cross-sectional area of chamber. This functional relationship follows directly from the earlier discussion of "sudden expansion diffusers." If, for the purposes of this example only, it is assumed that $A_b \gg A_a$, then it follows that $P_a/P_s \approx P_b/P_s$. Therefore, Eq. (40) for the source characteristic can be written

$$\frac{W_a}{W_s} = f\left(\frac{P_b}{P_s}, \text{ geometry}\right) \quad (44)$$

and the original measured characteristic (W_a versus P_a) would still apply. Equations (42), (43), and (44) may be interpreted graphically (for the first increment in dimensionless time), as shown in Fig. 26.

Figure 27 shows complete graphical solutions for three selected values of the load resistance. A limit cycle is seen to exist for the cases where the load resistance is high; for low enough values of load resistance the system is totally stable. The limit cycle frequency is easily determined from the plots.

Since the method of solution requires the use of an approximate finite difference equation to represent the original first order differential equation, the solution is expected to be approximate. Accuracy is generally assured if the slope of the "slope line" ($1:\delta\tau/2$) is maintained sufficiently large. In other words, since the parameter $\delta\tau$ contains both t (the time variable) and V_c (the chamber volume) it suffices to always maintain Δt small compared to the integrating time constant (i.e., $\rho VP_s/\beta W_s$). If the solution is carried out using dimensionless parameters the actual oscillation frequency or period for a given volume V_c is simple determined by appropriately interpreting the oscillation period obtained in terms of τ .

Consideration of the limiting case for which $R_l = \infty$ and $V \rightarrow 0$ yields interesting results. As the volume approaches zero, $\delta\tau/2 \rightarrow 0$ (i.e., the "slope line" approaches a vertical line). It is then obvious that the limiting condition results in an infinite frequency limit cycle bounded by the "knees" of the source characteristic. (See the dotted line in Fig. 26). This result is, of course, impossible and therefore of academic interest. Certainly the source dynamics must become significant long before the theoretical limiting case is approached.

Actually the mathematical formulation presented above is oversimplified for some practical cases. It is not necessarily valid to assume that the dynamic behavior of the system is governed entirely by the charging

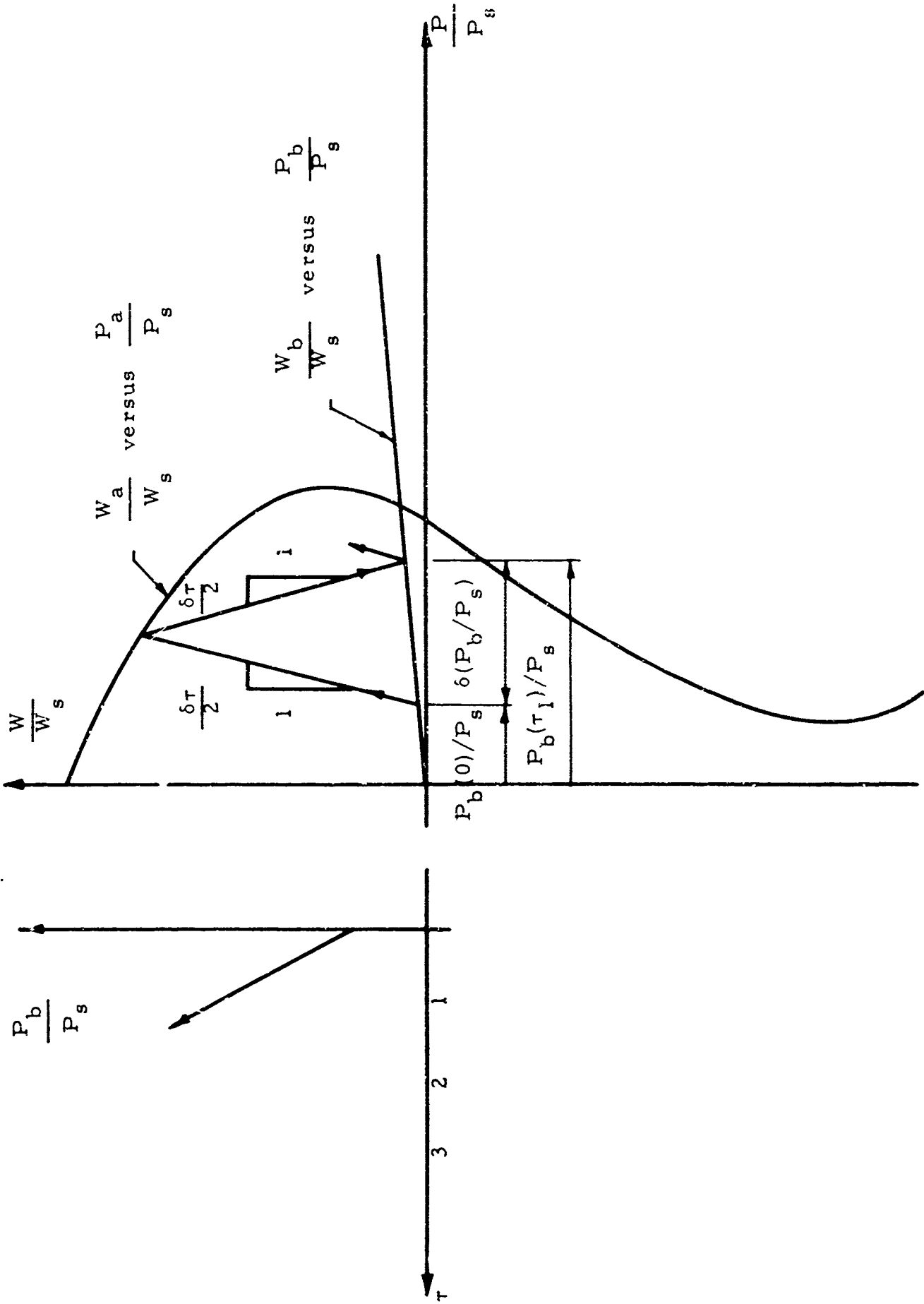


Fig. 26. Graphical Interpretation of Eqs. (40), (42), and (43).

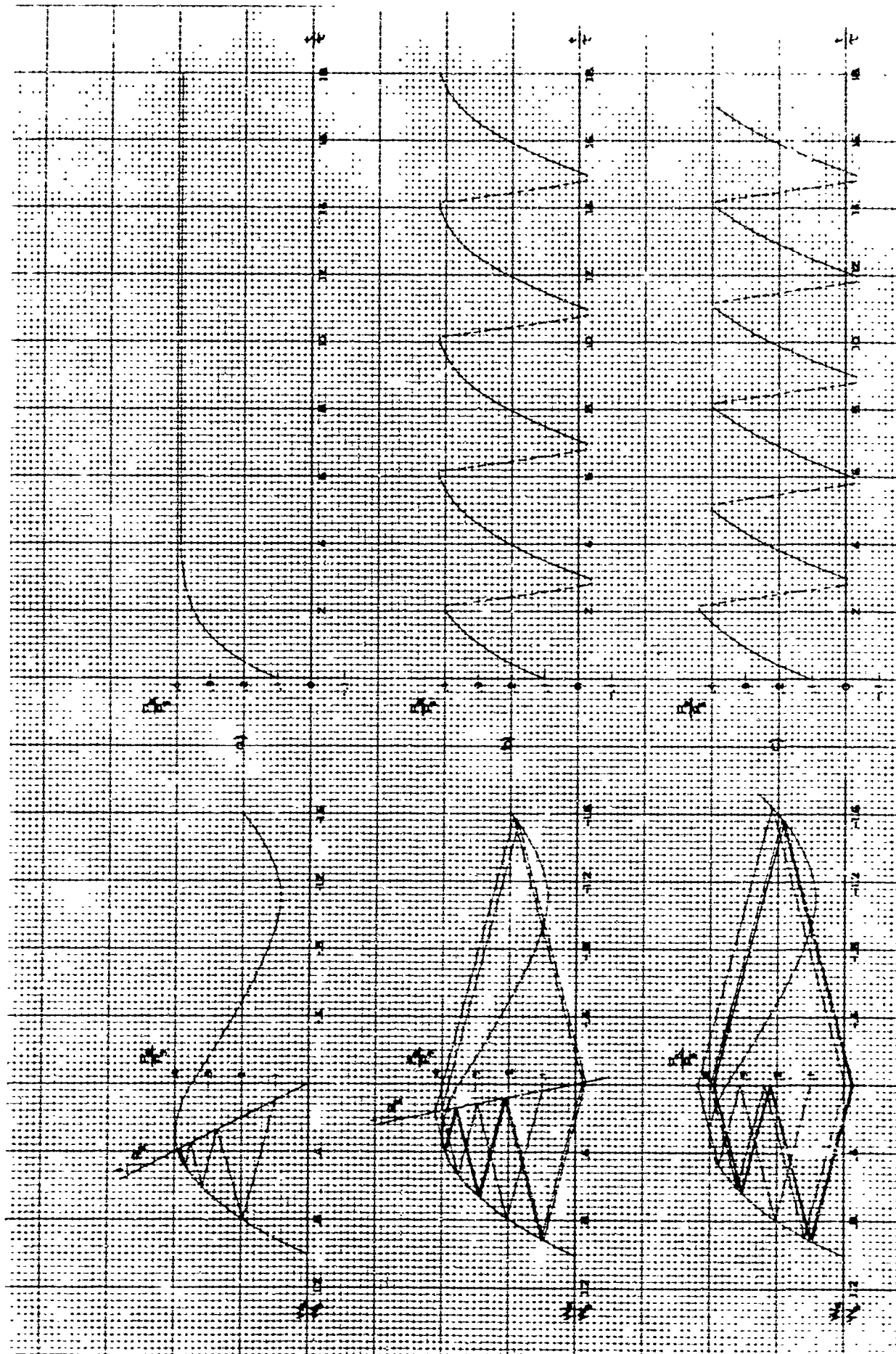


Fig. 27. Graphical Solutions for an Active Source Coupled to a Capacitive Plus Resistive Load.

and discharging of the lumped capacitance. Even though no line precedes the pure capacitance, there may be a significant inertial effect at the entrance due to the acoustic impedance of the entrance aperture. In fact, it can be shown(Ref. 28) that the "effective" length of a sharp-edged orifice is $1.7a$ where a is the radius of the orifice. The effect of the presence of a line preceding the lumped capacitance is treated in Example 3.

Example 3 - Active source coupled to a transmission line terminated by a load chamber and load resistance. Figure 28 shows a schematic of the system considered.

The describing time-difference equations are given below:

Source:

$$\frac{W_a}{W_s} = f\left(\frac{P_a}{P_s}, \text{ geometry}\right) \quad (45)$$

Line: (A lumped parameter model could be used to accurately model the line for frequencies which are small compared to the fundamental natural frequency of the line (See Sec. 2.3.8)

$$\begin{aligned} \frac{W_b(t+2T)}{W_s} - e^{2\alpha} \frac{W_b(t)}{W_s} &= \frac{1}{\bar{Z}_c} \left[2e^{\alpha} \frac{P_a(t+T)}{P_s} \right. \\ &\quad \left. - e^{2\alpha} \frac{P_a(t)}{P_s} - \frac{P_b(t+2T)}{P_s} \right] \end{aligned} \quad (46)$$

$$\frac{W_b(t+2T)}{W_s} + e^{2\alpha} \frac{W_b(t)}{W_s} = 2e^{\alpha} \frac{W_a(t+T)}{W_s} -$$

$$\frac{1}{\bar{Z}_c} \left[\frac{P_b(t+2T)}{P_s} - e^{2\alpha} \frac{P_b(t)}{P_s} \right] \quad (47)$$

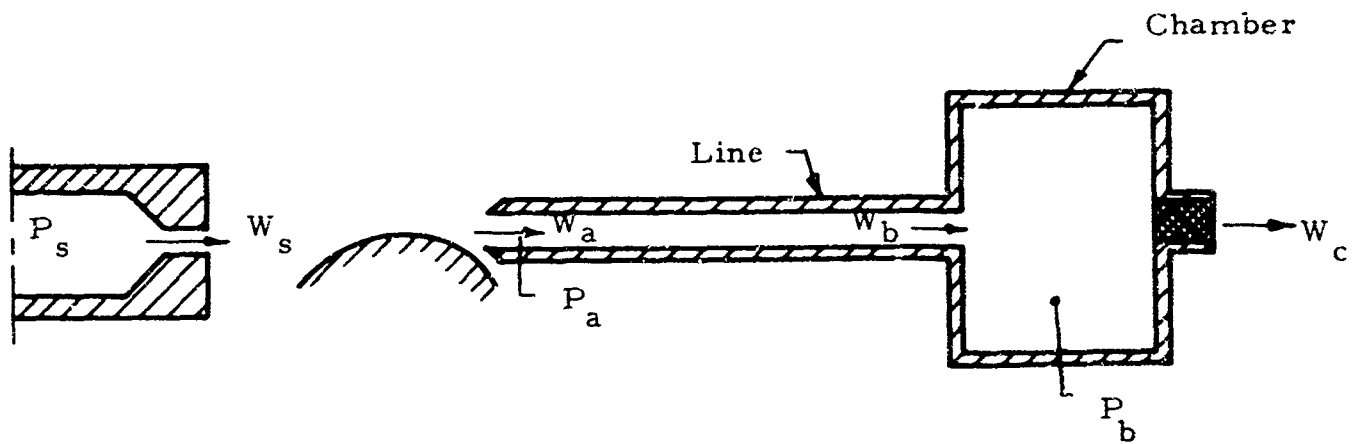


Fig. 28. Active Source Coupled to a Transmission Line Terminated by a Load Chamber and Resistance.

Chamber (See Example 2):

$$\delta \left(\frac{P_b}{P_s} \right) \approx \delta \tau \left[\frac{W_b}{W_s} - \frac{W_c}{W_s} \right]_{ave} \quad (48)$$

where

$$\tau = \frac{tW_s}{K_1 P_s} ; \quad K_1 = \frac{\rho V_c}{\beta}$$

Load Resistance:

$$\frac{W_c}{W_s} = \frac{P_s}{R_f W_s} \frac{P_b}{P_s} \quad (49)$$

The graphical technique involves a simultaneous solution of the describing equations as in the previous examples. There is, however, a fundamental difference between this example and the previous ones. Only one "dynamic" element was present in the systems of Examples 1 and 2. In the present example, there are two coupled "dynamic" elements - the line and the chamber. Consequently, two graphical solutions must be carried on simultaneously, with the resulting "common point of intersection" being the "answer". A graphical interpretation of the technique is given in Fig. 29. It is evident that the minimum value allowed for $\delta\tau/2$ is TW_s/K_1P_s .

A typical complete graphical solution for the lossless line case is shown in Fig. 30. For the particular conditions chosen, it is seen that a limit cycle instability exists.

The limit cycle or "surge" frequency can be determined directly from the plot by counting the number of time increments required to complete one encirclement on the phase plane plot, or more easily, by observing the

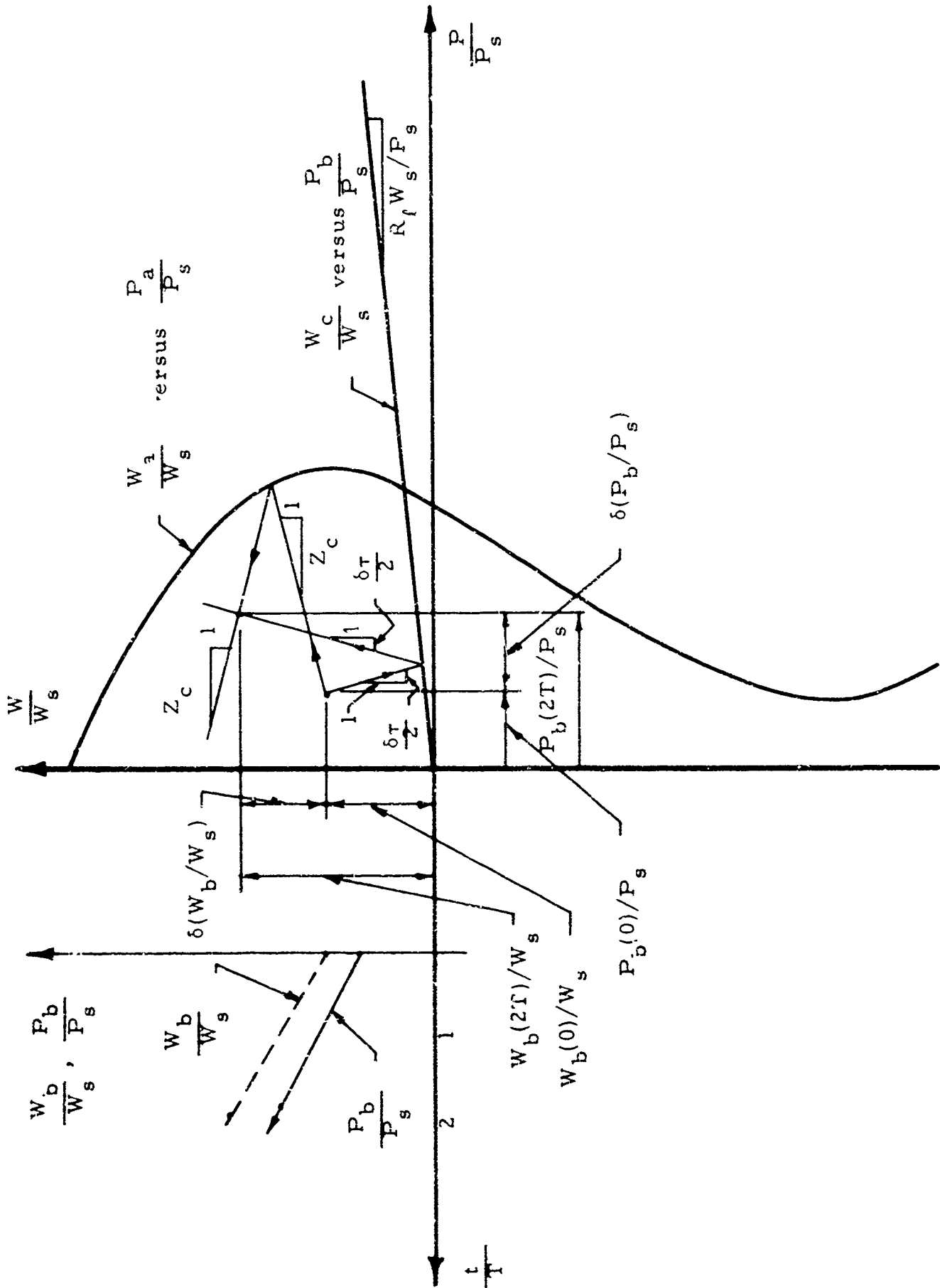


Fig. 29. Graphical Interpretation of Eqs. (45), (46), (47), (48) and (49).

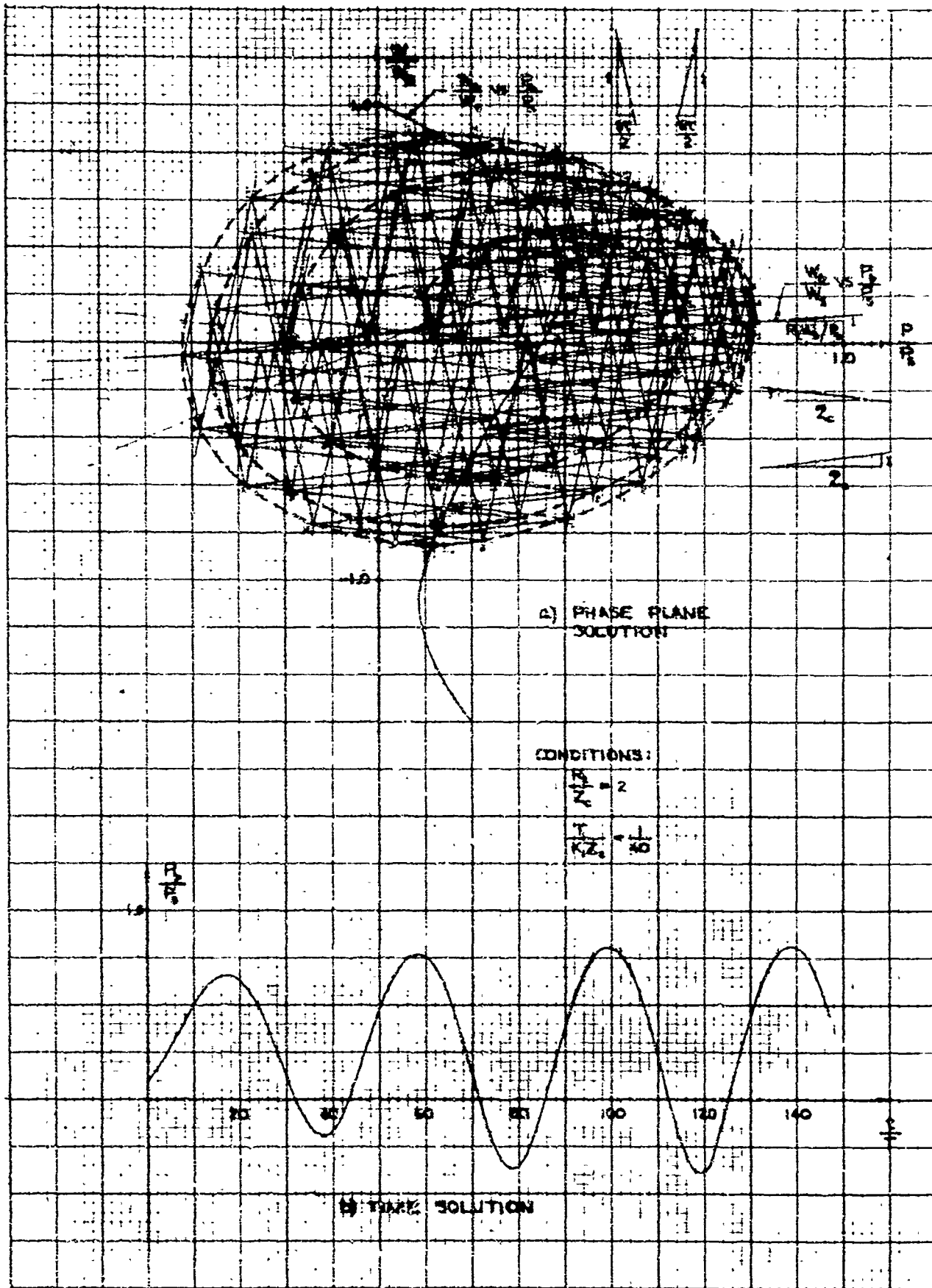


Fig. 20. Graphical Stability Analysis of an Active Source Coupled to a Lossless Transmission Line Terminated by Capacitive Plus Resistive Load.

period on the time plot. The parameters which determine the limit cycle frequency and amplitude for a given source characteristic are obviously the line length and characteristic impedance, the chamber volume, and the terminal impedance. The nature of the solution in normalized form reduces the "free" parameters to the following pair of ratios

$$\frac{R_t}{Z_c} \quad \text{and} \quad \frac{\beta T}{\rho V_c Z_c} \equiv \frac{V}{V_c}$$

Simple analytical means for computing the "surge" or limit cycle frequency for the special case of $R_t = \infty$ are presented in Sec. 2.3.8. Unfortunately, accuracy of solution using this particular technique is not assured in all cases. Since the system contains a single delay element, (i.e., the transmission line) computations yield results only at the points in actual time represented by $t = 2T, 4T, 6T, \dots$ etc. As in Example 2, good accuracy requires that the slope $1:\delta\tau/2$ be large. However, in contrast to the previous example, there is now an important restraint placed on the minimum size of $\delta\tau/2$ due to the presence of the line. It easily is shown that unless V_t/V_c is very small compared to unity, that the slope $1:\delta\tau/2$ may be too small (or $1:\bar{Z}_c$ may be too large) to insure adequate accuracy of solution. Obviously simple scaling manipulations on the abscissa and ordinate do not help. What is actually required is the introduction of an artifice that will effectively reduce the minimum relative value of $\delta\tau/2$. Such an artifice is achieved simply by dividing the uniform transmission line into n -sections, each having a length $L' = L/n$ and a characteristic time $T' = T/n$. The chamber "slope lines" are increased in number and slope by the factor n . For example, suppose the line is divided into 4 equal sections as shown in Fig. 31. Equations identical to Eqs. (46) and (47) except for obvious changes in subscripts, can be written for each section. The chamber slope lines have a slope $1:\delta\tau/8$. It is possible now to compute the values of all the state variables of interest at points in actual time represented by $t = 2T', 4T', 6T' \dots$ etc. This, of course, requires that the state variables at the line points 1, 2, and 3 also be computed every $2T'$. A graphical interpretation of the solution technique is shown in Fig. 32

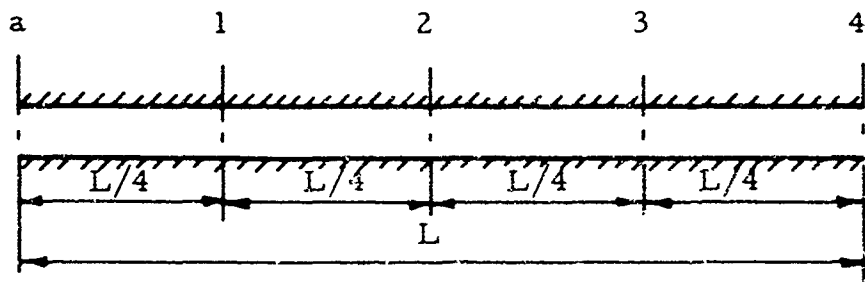


Fig. 31. Transmission Line Divided into 4-Sections.

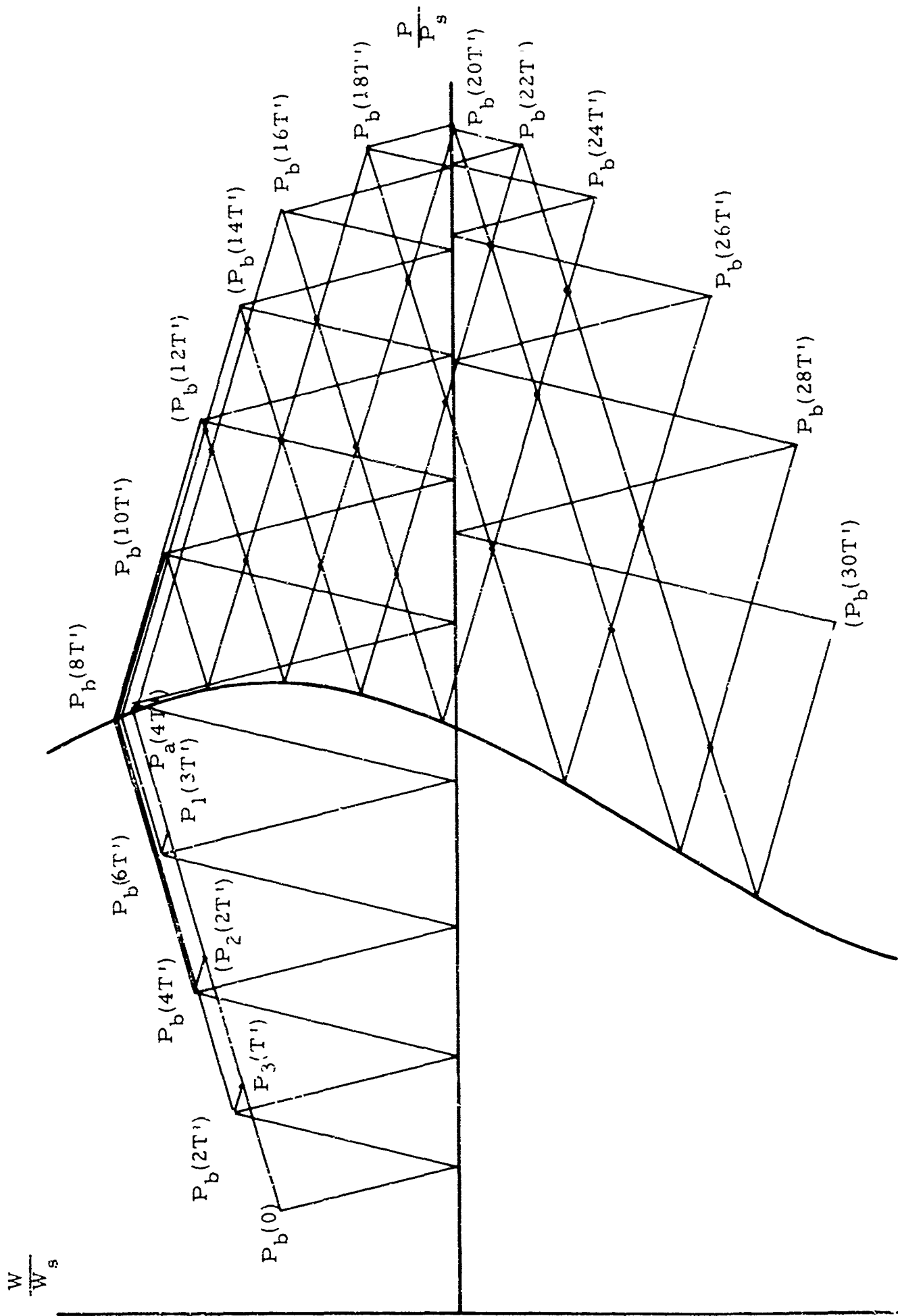


Fig. 32. Graphical Interpretation of Example 3 for a Line Divided into Four Sections

for the case of $n = 4$. It is interesting that the technique yields the values of the state variables at points 1, 2, and 3 rather "Automatically"; in the numerical solution to be discussed in Sec. 2.3.7 these values must each be computed individually as time progresses.

2.3.7. Computer-Aided Numerical Prediction of System Relative Stability

The elegance and general utility of the graphical techniques presented in the previous section are obvious. These techniques provide insight into problem formulation and solution which is exceedingly difficult to realize with other numerical methods. Nevertheless, for detailed design studies involving extensive computations, only machine computation affords the necessary speed and over-all flexibility. Techniques for solving the previous three example problems numerically with the aid of a digital computer, are demonstrated below. Results of actual computations are given in Sec. 2.3.9. Fortran program's for each of the Examples are available from the writer and are to be presented in the writer's ScD. thesis (Summer 1964).

Example 1 - Active source coupled to a transmission line blocked at its downstream end. Equations (30) through (33) fully describe the behavior of this simplified system. The source characteristic written in functional form in Eq. (32), is experimental in nature and therefore may be presented in graphical or tabular form. Tabular representation is preferred (and assumed) here.

The results of the previous graphical solutions indicate that events occur in increments of the characteristic time of the line, T . Accordingly, the simultaneous solution of the governing equations⁺ is most easily realized by "computing" changes every $2T$ units of time. If it is assumed that the state of the system is known at time $t = 0$, then subtraction and addition of Eqs. (30) and (31) yield the following two relations ($W_b/W_s = 0$).

⁺ The "exact" form of the line equations may be used here with no increase in difficulty.

$$\frac{P_b(t)}{P_s} = e^{-a} \frac{P_a(t+T)}{P_s} - e^{-a} \bar{Z}_c \frac{W_a(t+T)}{W_s} \quad (50)$$

$$\frac{P_b(t+2T)}{P_s} = e^a \frac{P_a(t+T)}{P_s} + e^a \bar{Z}_c \frac{W_a(t+T)}{W_s} \quad (51)$$

It is seen that the pressure at the downstream end of the line at time t and $t + 2T$ is related to the pressure and flow at the upstream (source) end at time $t + T$. The source characteristic is, of course, good for all time. Thus from Eq. (32) we have

$$\frac{W_a(t+T)}{W_s} = f \left[\frac{P_a(t+T)}{P_s} \right] \quad (32a)$$

Starting with a given set of initial conditions (i. e., at $t = 0$), the solution involves: 1) simultaneous solution of Eqs. (32a) and (50) to obtain $P_a(T)/P_s$ and $W_a(T)/W_s$, and then 2) solution of Eq. (51) to obtain $P_b(2T)/P_s$. The solution for each succeeding increment in time $2T$ follows in exactly the same way. Due to the nature of the source characteristic, it is obvious that the simultaneous solution of Eqs. (32a) and (50) involves iteration and interpolation (unless, of course, an algebraic relation is established for the source characteristic). A useful and completely general approach is as follows:

1. From Eq. (50) define a new function, WP , such that

$$WP = \bar{Z}_c \frac{W_a(t+T)}{W_s} - \frac{P_a(t+T)}{P_s} + e^a \frac{P_b(t)}{P_s}$$

Thus, an exact simultaneous solution of Eqs. (32a) and (50) would give $WP = 0$.

2. Starting with the first entry in a table of values representing the source characteristic, compute WP for successive points, noting that $P_b(t)/P_s$ is known and $W_a(t + T)/W_s$ and $P_a(t + T)/P_s$ are the values from the table. The two points in the table which bracket the exact solution is found by noting the change in sign of WP .
3. Employ any standard random or systematic iteration technique to find the unknown point within an acceptable tolerance. One useful and efficient iteration technique⁺ involves successively halving the interval, computing W_a/W_s , interpolating to find P_a/P_s , computing WP , and testing WP against an acceptable tolerance B . The process is repeated (usually 6 or 7 times for a reasonable tolerance) until $|WP| \leq B$. For the step involving interpolation, the well-known parabolic interpolation technique (Ref. 29) should be adequate for most purposes. The final results of the above iteration can then be utilized in Eq. (51) to obtain $P_b(2T)$. Then the entire process can be repeated in steps of $2T$ until the complete solution is obtained.

Example 2 - Active source coupled to a load chamber. The approach is fundamentally the same as in Example 1; however, the governing equations are different and a slight modification is necessary in the source characteristic searching procedure. Equation (42) describing the charging process for the chamber can be rewritten, and subdivided into two parts as follows:

⁺ The table is conveniently arranged so that the column of W_a/W_s changes in equal increments.

$$\frac{P_b(k+1)}{P_s} - \frac{P_b(k)}{P_s} \approx \frac{\delta\tau}{2} \left[\frac{W_a(k+1)}{W_s} - \frac{W_b(k)}{W_s} \right] \quad (52)$$

$$\frac{P_b(k+2)}{P_s} - \frac{P_b(k+1)}{P_s} \approx \frac{\delta\tau}{2} \left[\frac{W_a(k+1)}{W_s} - \frac{W_b(k+2)}{W_s} \right] \quad (53)$$

The source and load characteristics become

$$\frac{W_a(k+1)}{W_s} = f \left[\frac{P_a(k+1)}{P_s} \right] = f \left[\frac{P_b(k+1)}{P_s} \right] \quad (54)$$

and

$$\frac{W_b(k)}{W_s} = \frac{P_s}{R_l W_s} \frac{P_b(k)}{P_s} \quad (55a)$$

$$\frac{W_b(k+2)}{W_s} = \frac{P_s}{R_l W_s} \frac{P_b(k+2)}{P_s} \quad (55b)$$

Starting with a set of initial conditions ($k = 0$), the solution involves:

1) simultaneous solution of Eqs. (52), (54), and (55a) to obtain $P_b(1)/P_s$ and $W_a(1)/W_s$, and 2) solution of Eqs. (53), and (55b) to obtain $P_b(2)/P_s$.

The solution for each succeeding value of k follows in exactly the same way. An examination of the graphical solution of this particular problem indicates that a range exists for which the "slope line" crosses the source curve in three places; thus three solutions are possible but only one is the desired solution. The same logic which leads to a selection of the correct value when employing the graphical technique, must obviously be incorporated into the numerical solution. The general approach is as follows:

1. From Eq. (52) define a function, WP, such that

$$WP = \frac{\delta\tau}{2} \left[\frac{W_a(k+1)}{W_s} \right] + \left[1 - \left(\frac{\delta\tau}{2} \right) \frac{P_s}{R_l W_s} \right] \frac{P_b(k)}{P_s} - \frac{P_b(k+1)}{P_s}$$

2. Starting with the first entry in the table of values representing the source characteristic, compute WP for successive points until the first "knee" of the curve is exceeded. Care should be taken to stop before the second "knee" is reached. A change in sign of WP indicates the bracket about the desired solution. If a change in sign is not found, start with the last entry in the table and proceed backwards through the table computing WP for each point.
3. Employ the earlier mentioned iteration and interpolation routine to find the desired point within acceptable tolerance.
4. For the next complete computation reverse the procedure in step (2) above.

In Step (3) of the above procedure, logic decisions must be employed which indicate at which end of the table the computations are being made. Furthermore, certain of the basic formula must be appropriately changed to account for the direction of travel and placement in the table.

Example 3 - Active source coupled to a transmission line terminated by a load chamber and load resistance. Here the most interesting and useful solution is the one which allows the division of the line into n-sections. The solution proceeds in much the same manner as for the previous Examples except that it is more lengthy and does not involve any possible triple value results as in Example 2. Again it is necessary to start with a set of initial conditions for all state variables and then proceed with a simultaneous solution of the governing equations. The procedure involves the following successive steps:

1. Define a function, WP, such that

$$WP = \frac{Z_c W_s}{P_s} \left[\frac{W_a(t+T)}{W_s} - \frac{W_b(t)}{W_s} \right] + \frac{P_b(t)}{P_s} - \frac{P_a(t+T)}{P_s}$$

2. Starting with the first entry in the table, compute WP for each successive entry and find the points in the table which bracket the desired point, i. e., $W_a(nT')$ and $P_a(nT')$. Note that $T' = T/n$.
3. Knowing the initial values of the $n-1$ intermediate state variables, compute in succession $P_1[(n+1)T']$, $P_2[(nT')]$, $P_3[(n-1)T']$, ..., $P_{n-1}[(3T')]$.
4. Compute $P_b(2T')$ and $W_b(2T')$.
5. Return to step (2) to find $W_a[(n+2)T']$ and $P_a[(n+2)T']$ and then continue on in the same manner to find successive values of P_b and W_b .

2.3.8. Analytical Prediction of Surge Frequency for a Transmission Line Terminated by a Chamber.

Of the three examples presented in the previous sections, Example 3 represents the general case. Examples 1 and 2 are merely limiting cases of Example 3. It is possible, without carrying out any graphical or numerical solutions, to predict the surge frequency of the system in Example 3 for two important special cases: 1) $R_\ell = \infty$ and 2) $R_\ell = 0$. The surge frequency is the lowest natural frequency of the system and is the frequency at which the limit cycle is most likely to exist. Consider the first case of infinite load terminal impedance. Two approaches are available, depending on the nature of the model for the line. Either the lumped or distributed parameter model may be used.

Distributed Parameter Solution. Assume that the line is lossless and that the effective bulk modulus of the fluid in the line is equal to that in the chamber. The governing equations for the lossless line are:

$$P_b = \left[\cosh TD \right] P_a - Z_c \left[\sinh TD \right] W_a \quad (56)$$

and

$$W_b = \frac{1}{Z_c} \left[\sinh TD \right] P_a + \left[\cosh TD \right] W_a \quad (57)$$

Considering the terminating chamber as a pure capacitance gives

$$W_b = \frac{V_c}{\beta} DP_b \quad (58)$$

Combining Eqs. (56), (57), and (58) and eliminating W_a and W_b gives

$$\frac{P_b}{P_a} = \frac{\frac{1}{Z_c \sinh TD}}{\frac{jV_c \omega}{\beta} + \frac{1}{jZ_c \tan \omega \tau}} \quad (59)$$

where

$$\begin{aligned} \omega &= \text{frequency} \\ j &= \sqrt{-1} \end{aligned}$$

The surge frequency can be determined by setting the characteristic equation of the above transfer function equal to zero. Thus

$$\frac{\beta T}{V_c Z_c} = \omega T \tan \omega T \quad (60)$$

Since

$$T = \ell \sqrt{\frac{\rho}{\beta}} \quad \text{and} \quad Z_c = \sqrt{\frac{\rho \beta}{A}}$$

we find that

$$\frac{V_\ell}{V_c} = \eta \tan \eta \quad (61)$$

where

$$V_l = \text{volume of line} \equiv A l$$

$$\eta = \text{dimensionless surge frequency} = \omega T$$

By noting that the fundamental natural frequency of the line with zero terminating volume is

$$\Omega_l = \frac{\text{speed of sound}}{4l} = \frac{1}{4T}$$

and setting $\omega = 2\pi\Omega_{cl}$, we obtain

$$\frac{\Omega_{cl}}{\Omega_l} = \frac{2}{\pi} \eta \quad (62)$$

Equations (61) and (62) relate the dimensionless surge frequency to the line-to-chamber volume ratio. The resulting relation for the fundamental is plotted in Fig. 33. For the case when $R_1 = 0$, it is necessary to consider the multi-valued character of Eq. (61)

Lumped Parameter Solution. When the surge frequency is small compared to the fundamental natural frequency of the line alone, a simple lumped parameter model of the line-tank system is adequate. For example, consider the line as a "pure" inertance (no capacitance),

$$P_a - P_b = \frac{l}{A} \frac{dW_b}{dt} \quad (63)$$

Combining Eqs. (58) and (63), and solving the resulting characteristic equation for the surge frequency gives

$$\Omega_{cl} = \frac{1}{2\pi} \sqrt{\frac{\beta A}{\rho l V_c}} \quad (64)$$

from which follows

$$\frac{\Omega_{cl}}{\Omega_l} = \frac{1}{2\pi} \sqrt{\frac{V_l}{V_c}}$$

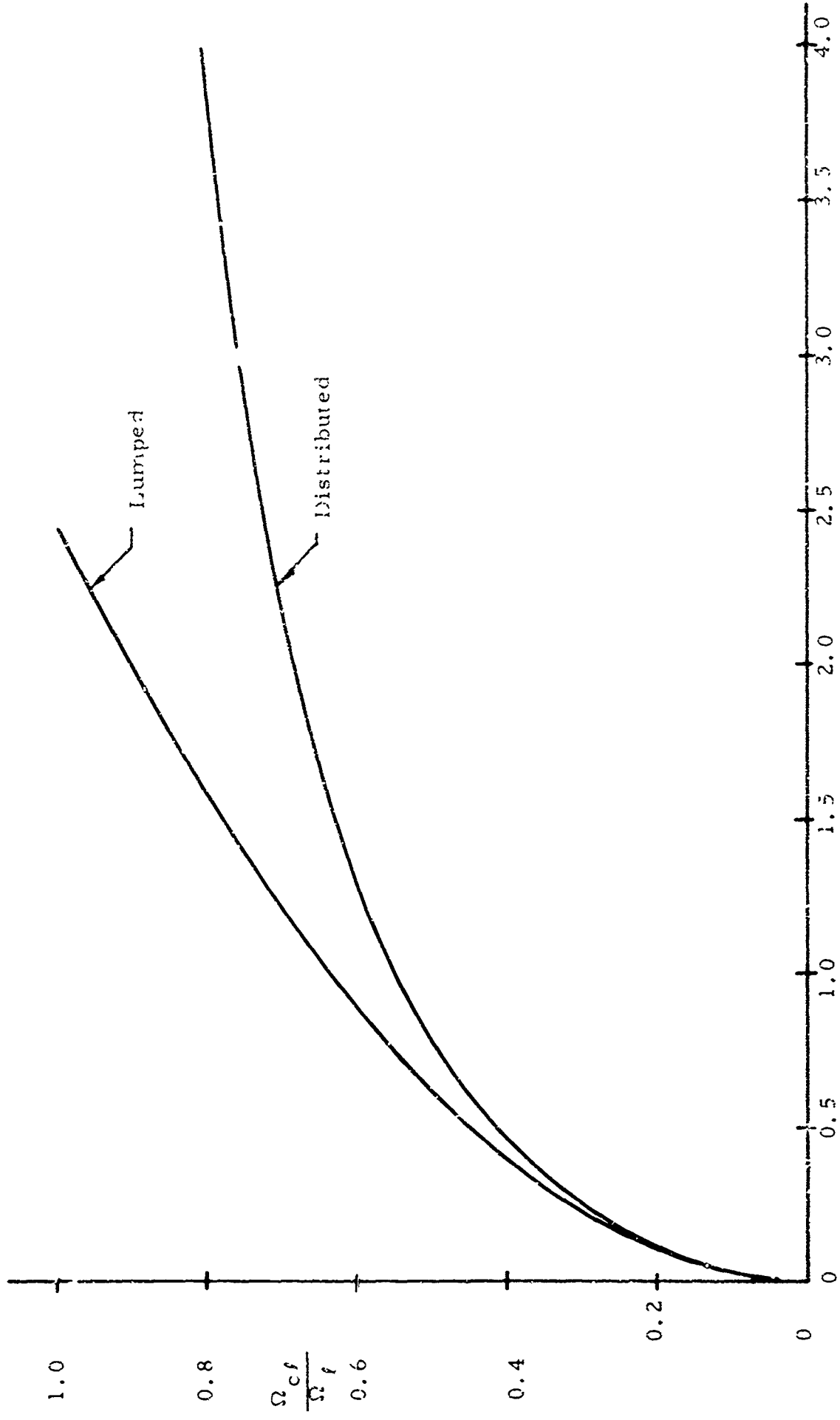


Fig. 33. Surge Frequency of a Lossless Transmission Line Terminated by a Simple Tank.

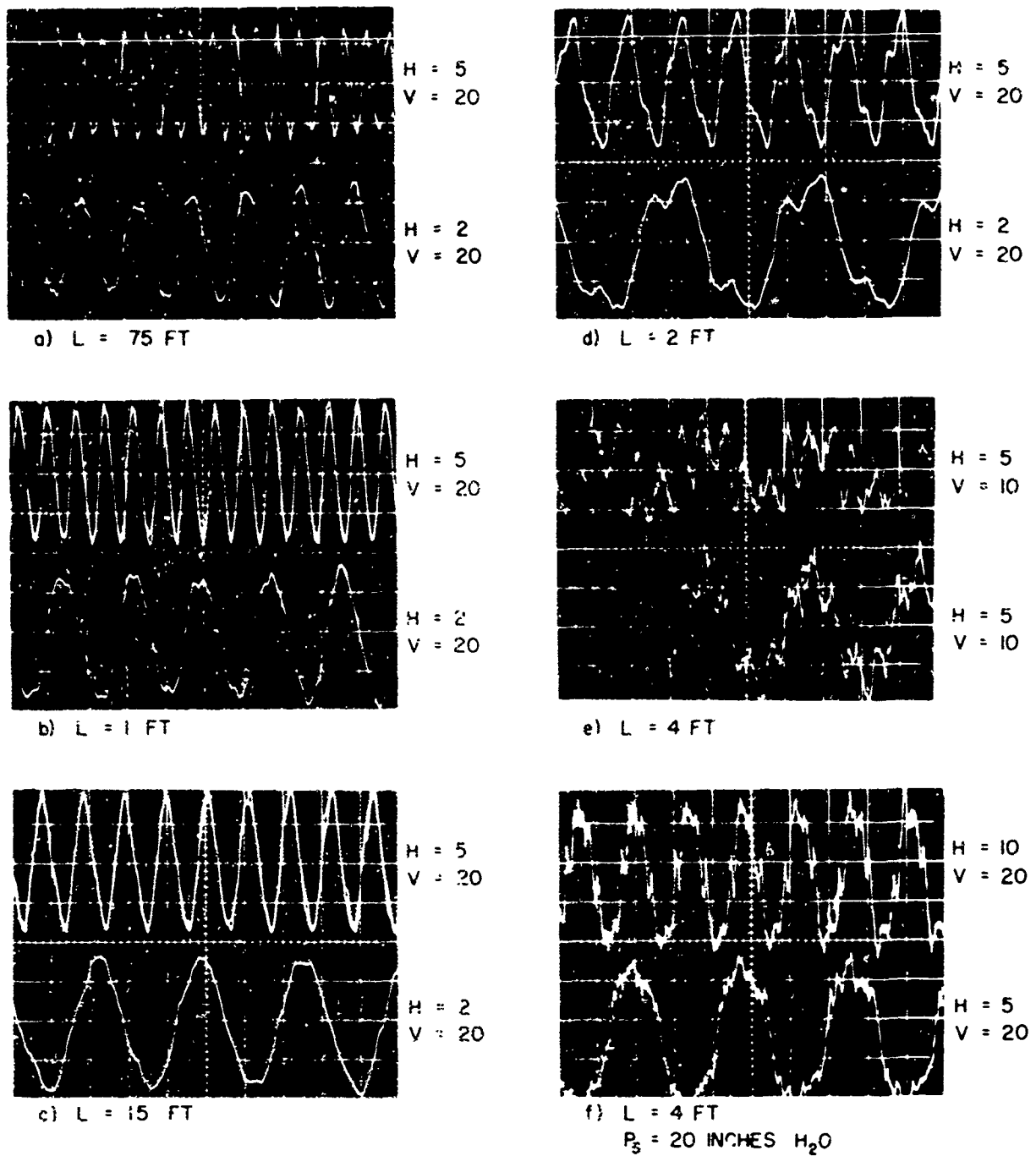
This expression is compared to the distributed parameter solution in Fig. 33.

2.3.9. Comparison of Analytical and Empirical Predictions With Experimental Measurements

In order to demonstrate the validity of the graphical and numerical solution techniques presented in Secs. 2.3.6 and 2.3.7, results of a representative set of digital computer solutions and experimental measurements are presented below.

Example 1 - Active source coupled to a transmission line blocked at its downstream end. Two types of experimental measurements were made: 1) pressure oscillation amplitude at the downstream end (point of maximum pressure for the standing wave), and 2) oscillation frequency and waveform characteristics. Figure 34 shows a set of oscilloscope traces which indicate the character of the waveform. If there were no wave dispersion and line friction effects, the waveform would be a square wave since all odd numbered harmonics must be present; this follows directly from the multivalued character of the line equations. Higher harmonics are seen to be present in the pictures of Fig. 34, but they are highly attenuated because of friction and dispersion. Oscillation frequency estimated from the apparent fundamental in the pictures compares very well with the expected quarter-wave frequency.

Oscillation amplitude measurements were particularly difficult for this system because of the sporadic presence of higher harmonics and a very low frequency modulation. It is not immediately clear, in fact, what amplitude should be measured. A single frequency spectrum analysis was carried out which indicated the presence of 3rd and 5th harmonics with approximately the expected amplitudes. This suggested that the most meaningful measurement would be the amplitude of the fundamental. A square wave having an amplitude $\pi/4$ times this fundamental should compare with the predicted "square-wave" solution within the validity of the original model. However, instrumentation was not available which could be used for making this measurement accurately. If no dispersive effects were present, a measurement of the true rms amplitude of the waveform would yield the amplitude of the desired square wave. Since a true rms voltmeter was available, measurements were carried out in this manner. A few spot



Legend:

V = vertical scale in inches H_2O /division (approx.)

H = horizontal scale in milliseconds/division

L = Line length in feet

P_s = nozzle supply pressure = 10 inches H_2O for pictures (a) through (e).

D = line diameter = 0.518 inch

Fig. 34. Pressure Oscillations at the Blocked End (Downstream) of a Constant Diameter Transmission Line Coupled to an Active Source. (Conf. 3).

checks with a wave analyzer indicated that the difference between $\pi/4$ times the fundamental amplitude and the true rms amplitude was easily within 5 per cent. Figure 35 shows the results of the rms amplitude measurements. The results of digital computer predictions which included the friction correction from Fig. 20, are shown for comparison in Fig. 35b. Although the comparison appears generally poor, several important results are apparent. The model is adequate to predict the qualitative behavior for the longer length lines; however, the friction correction seems too severe to provide good quantitative comparison. The solution is highly sensitive to the friction factor; for example, e^{α} for the one foot, line is 0.977 which results in a factor of two reduction of the amplitude as compared with the results of the lossless solution.

Frequency limitation in the static source characteristic is, perhaps, a contributing factor to the poor correlation at the higher frequencies (i. e., shorter lines). Several of the basic assumptions underlying the line equations are open to some question for the shorter lines. The inclusion of dispersive effects might improve the correlation. Nevertheless, the correlation is not actually very bad considering the particular difficulties of experimental measurement and the extreme sensitivity to the value of the attenuation factor. Several improvements in the model which would lead to better correlation with experiment, are presently under study.

Example 2 - Active source coupled to a simple chamber. All measurements were made with line lengths greater than 6 inches preceding the chamber. Pertinent experimental results are presented in connection with Example 3. The apparent transition between the systems of Examples 2 and 3 will be explored in more detail in the writer's ScD. thesis.

Example 3 - Active source coupled to a transmission line terminated by a chamber and load resistance. It was established earlier that the pertinent free parameters are V_f/V_c and R_f/Z_c . Only the infinite resistance case ($R_f = \infty$) is considered here. Figures 36 and 37 show typical waveforms for various values of V_f/V_c . Unlike the results for Example 1 the waveforms are very nearly sinusoidal. The chamber coupled to the line introduces a type of "filtering" effect, such that the higher harmonics do not generally

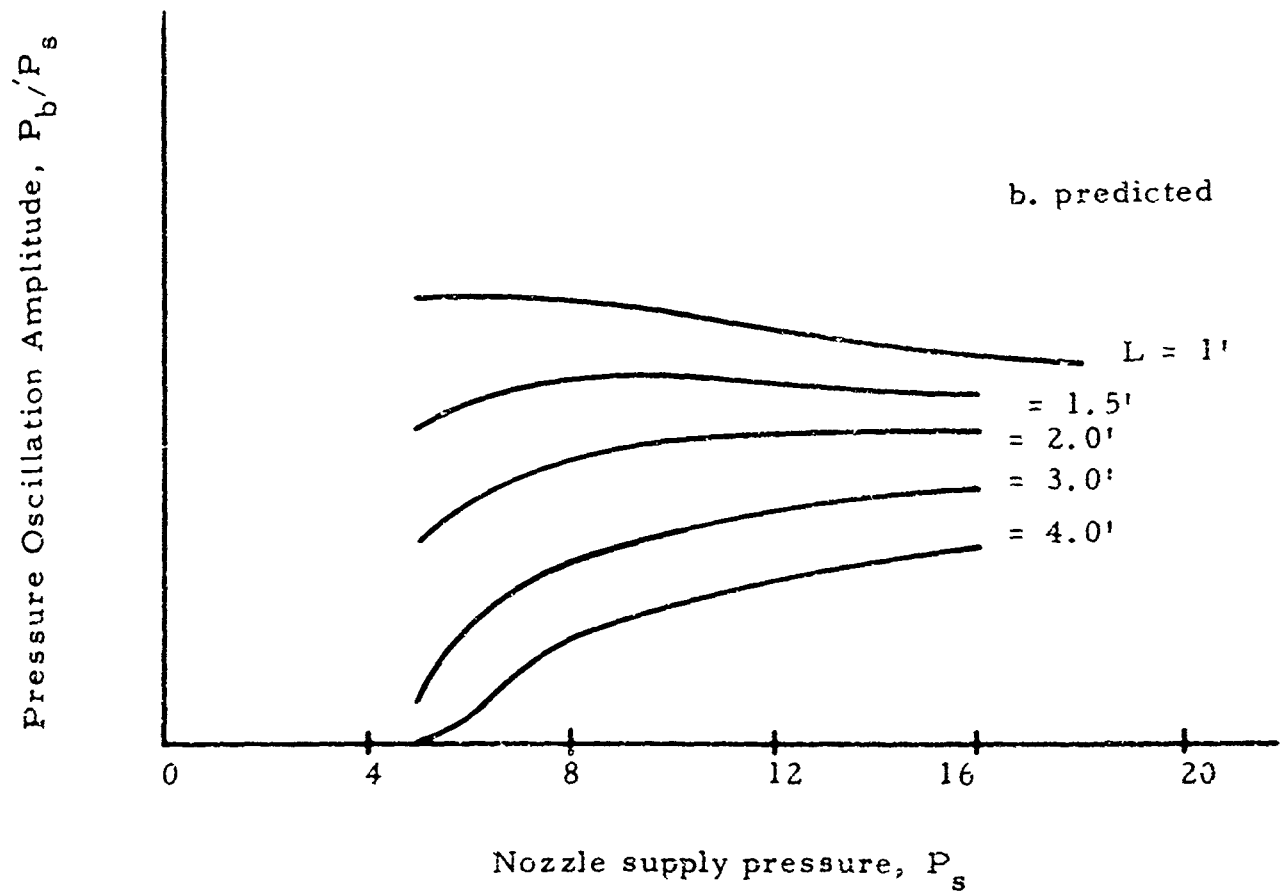
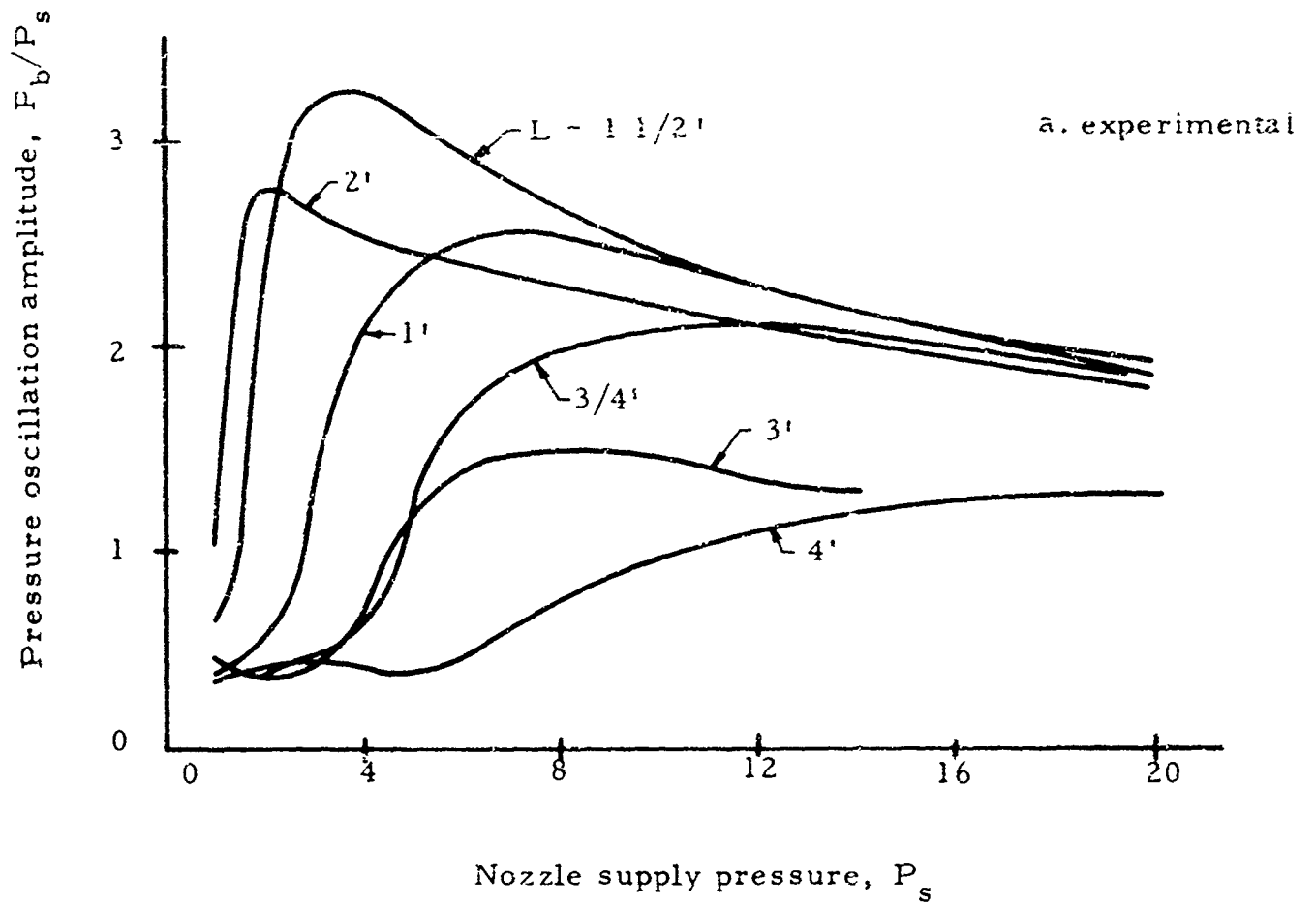
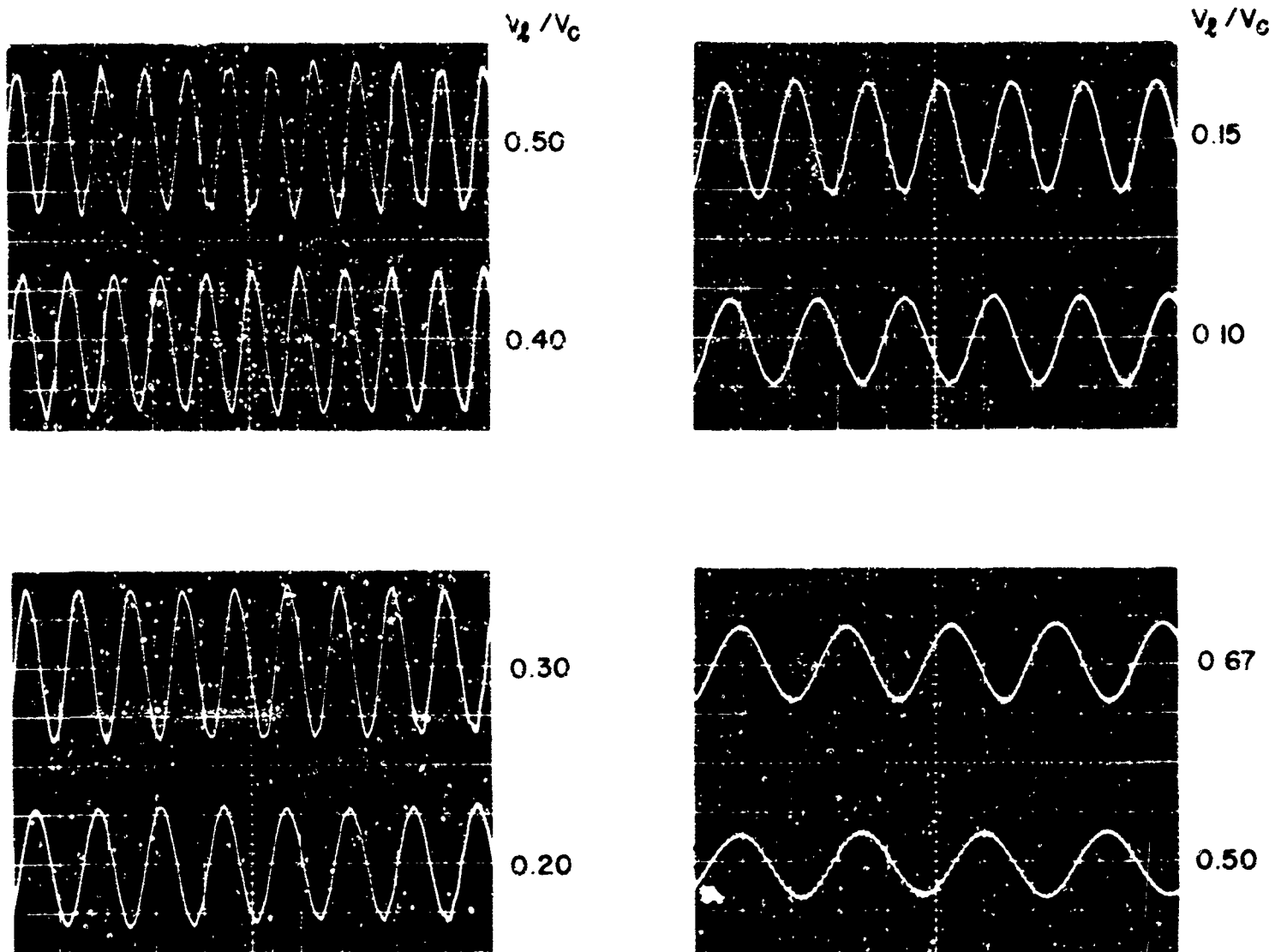


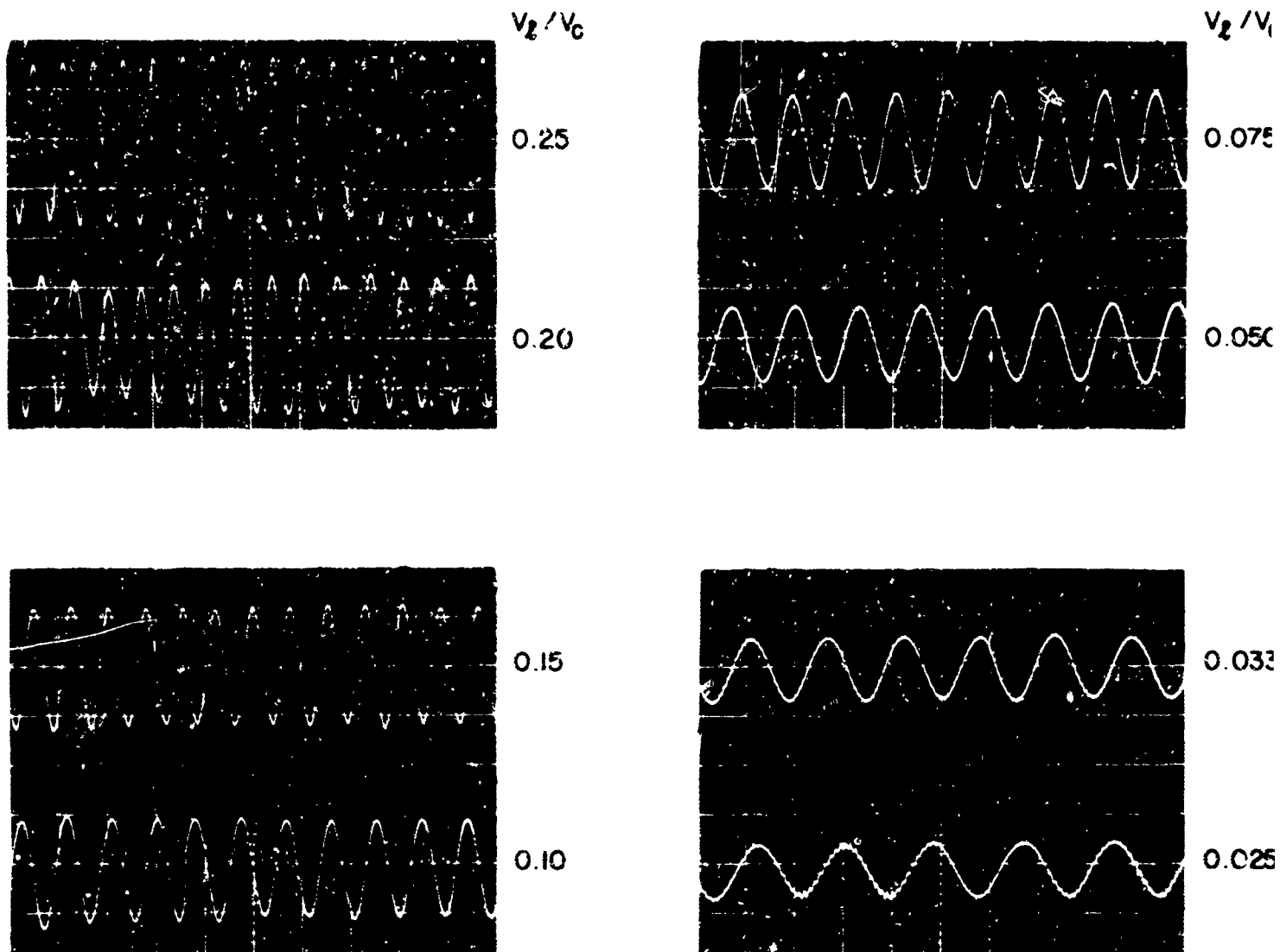
Fig. 35. Comparison of Predicted and Experimental Measurements of Pressure Oscillation Amplitude for an Active Source Coupled to a Transmission Line.



All Pictures:

Vertical scale = 10.2 inches H_2O /division
 Horizontal scale = 10 milliseconds/division
 Nozzle supply pressure = 10 inches H_2O
 Line length = 12 inches
 Line diameter = 0.518 inch
 V_l/V_c = Line-to-chamber volume ration

Fig. 36. Pressure Oscillations in a Blocked Chamber Coupled to an Active Source (Conf. 3).



All Pictures:

Vertical scale = 10.2 inches H_2O /division
 Horizontal scale = 10 milliseconds/division
 Nozzle supply pressure = 10 inches H_2O
 Line length = 6 inches
 Line diameter = 0.518 inch
 V_l/V_c = Line-to-chamber volume ratio

Fig. 37. Pressure Oscillations in a Blocked Chamber Coupled to an Active Source (Conf. 3).

appear. As V_f/V_c becomes very small the situation of Example 1 is approached and higher harmonics begin to appear. For longer lines the waveforms become less sinusoidal and higher harmonics begin to be more apparent. A comparison of measured and theoretical limit cycle frequencies is given in Fig. 38. The comparison is remarkably good even for such short lines, thereby showing the validity of the mathematical formulation for the range of conditions considered.

Oscillation amplitude measurements were carried out using the true rms voltmeter. In this case the rms value and the amplitude of the fundamental are assumed to be the same. Typical measured results are shown in Fig. 39. As expected, the amplitude decreases with increases in both chamber size and supply pressure. The decrease in amplitude with supply pressure is a result of an increase in the stiffness of the jet with supply pressure increase.

A typical comparison of predicted and measured results is shown in Fig. 40. The correlation is remarkably good considering the difficulties of measurement and the sensitivity of the solution to the friction correction. Since the frequencies were low compared to the natural frequency of the line alone, the attenuation factor was computed from the lumped parameter approximation (see Sec. 2.3.6). A minor improvement (in the favorable direction) could be achieved by using the more exact values, but this requires lengthy computation. Typical values of the attenuation factor are: $e^{\alpha} = 0.9988$ for $L = 1$ ft. and $e^{\alpha} = 0.9953$ for $L = 4$ ft. Sensitivity to changes in the fourth digit are apparent!

Conclusions - It is believed that the experimental measurements conducted to date adequately demonstrate the importance, general usefulness, and limitations of the prediction models. Certain refinements are needed in the models, but, for the majority of practical cases, the predictions are in remarkably good agreement with the experiments.

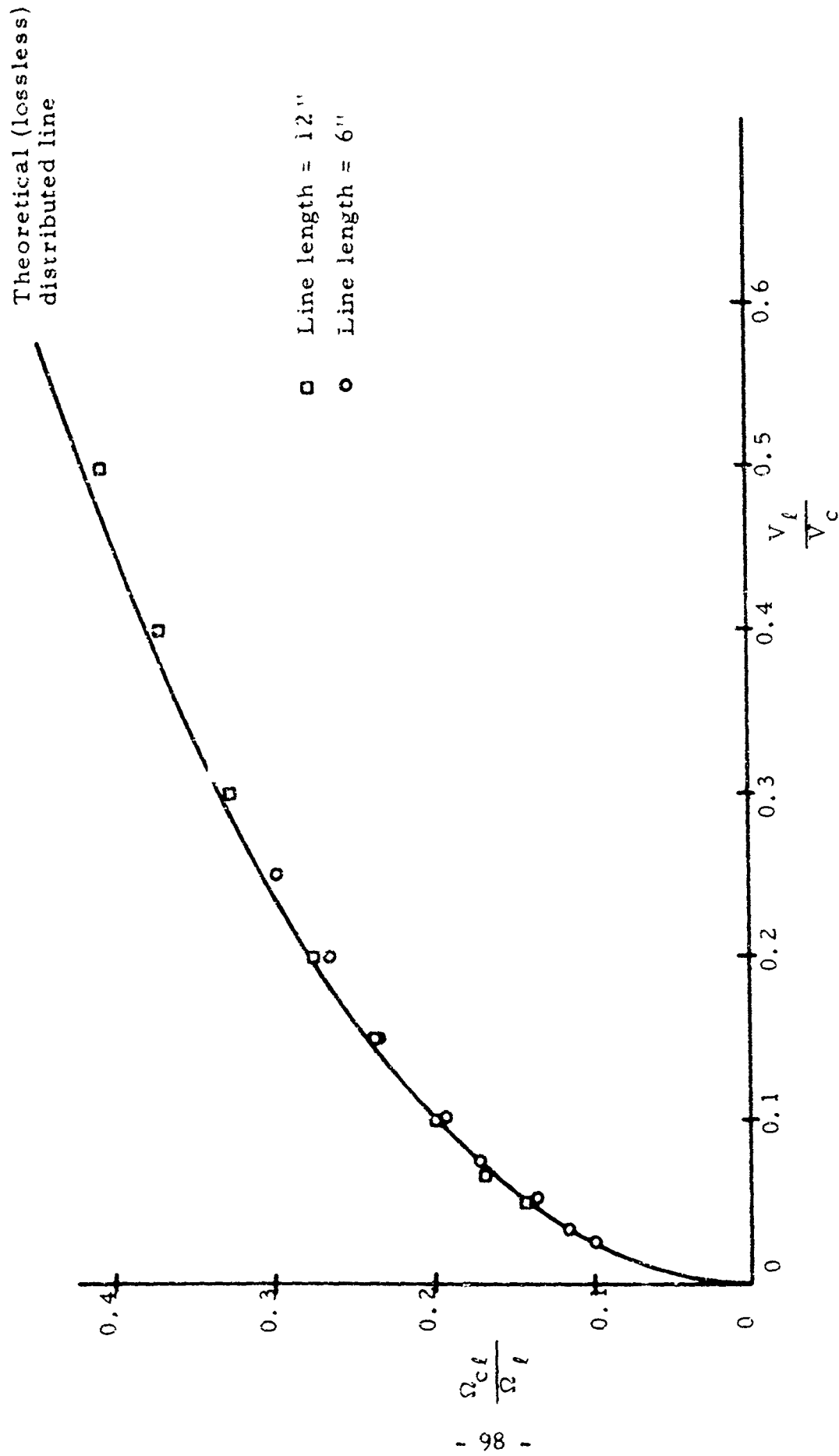


Fig. 38. Comparison of Theoretical and Experimental Surge Frequencies of a Transmission Line Terminated by a Simple Chamber.

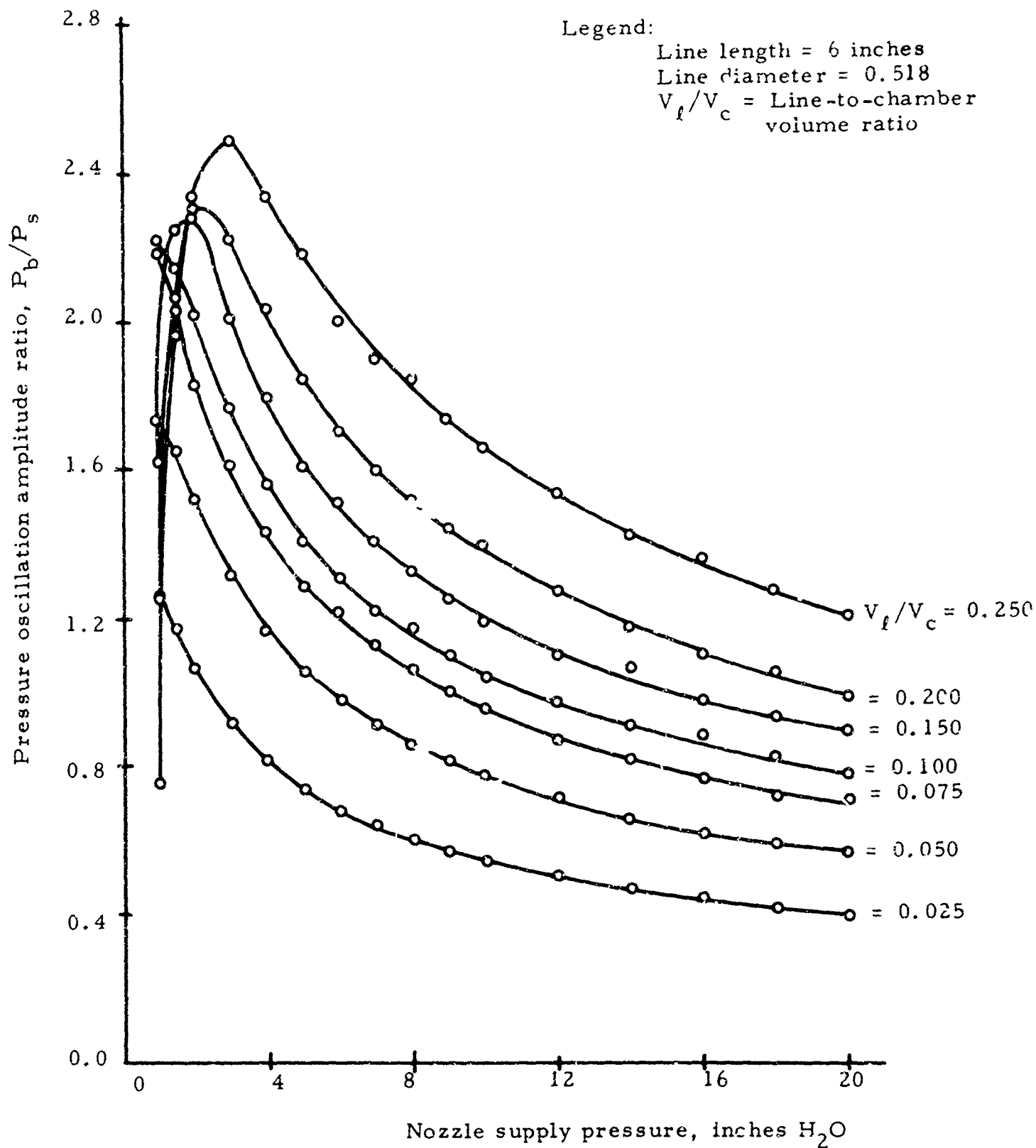


Fig. 39. Experimental Measurements of Pressure Oscillation Amplitude in a Chamber Coupled to an Active Source by Means of a Six-inch Line.

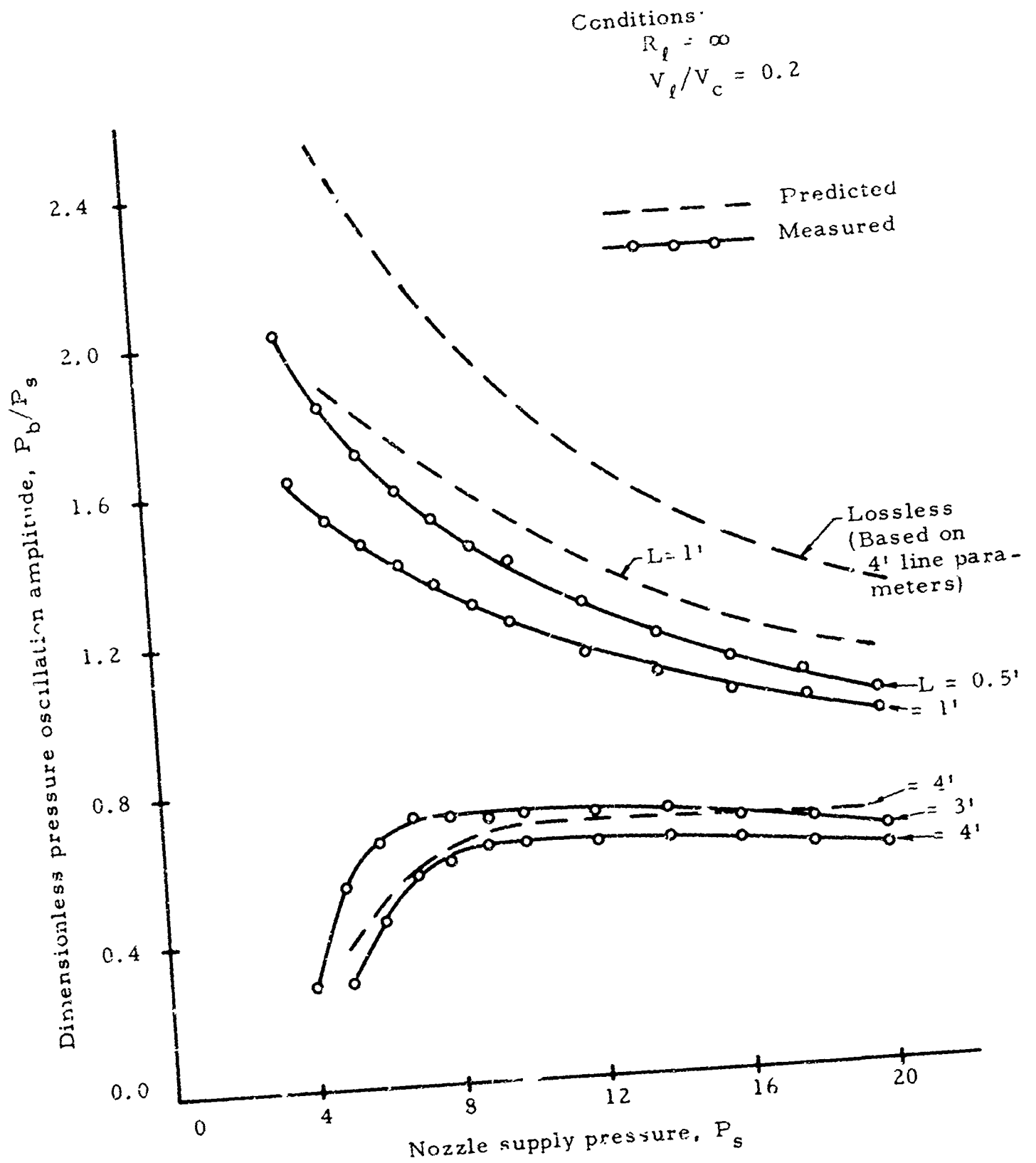


Fig. 40. Comparison of Predictions and Experimental Measurements of Pressure Oscillation Amplitude for an Active Source Coupled to a Transmission Line Terminated by a Chamber.

3. DYNAMIC ANALYSIS OF CONTROLLED JET DEFLECTION

3.1. LaPlace Transform Solution of the Jet Equations

In an earlier report, Ref. 1, the equations describing the motion of the jet were written directly in terms of the values of variables at discrete points. These equations in actuality assumed certain types of approximations for the space derivatives of the transverse jet velocity and position. There was no standard solution against which could be compared the digitally computed solution and consequently no way of knowing which derivative approximations would give the best results. The purpose of this section is to compare the solution of the jet equations using various space derivative approximations against two exact solutions.

3.1.1. Rederivation of Jet Equations

Consider a segment of the jet with stagnant fluid around it as in Fig. 41.

The momentum equation gives:

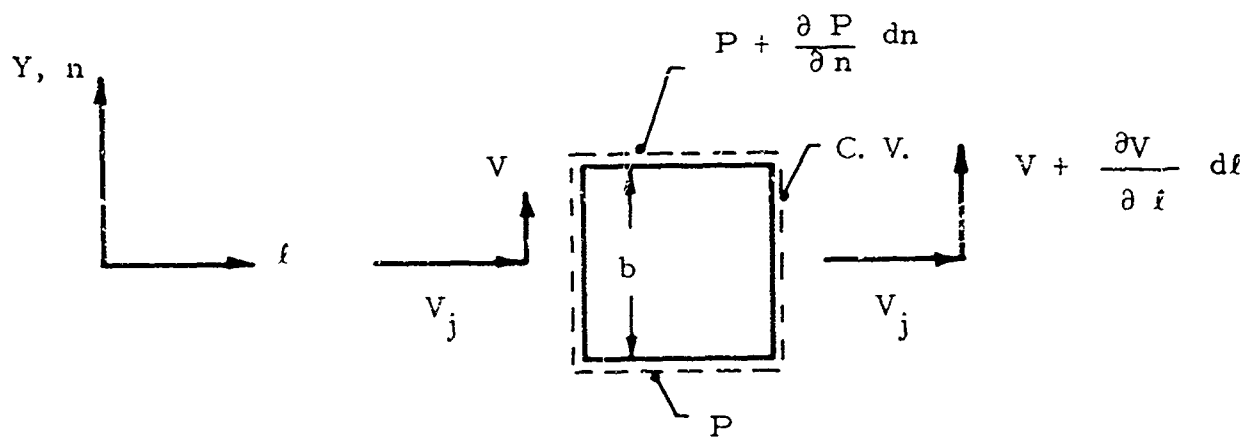
$$\rho h d\ell - \left(P + \frac{\partial P}{\partial n} dn \right) h d\ell = \frac{\partial}{\partial t} (\rho h d\ell dn V)$$

$$+ \left(V + \frac{\partial V}{\partial \ell} d\ell \right) V_j \rho h dn - V V_j \rho h dn \quad (65)$$

$$- \frac{\partial P}{\partial n} = \rho \frac{\partial V}{\partial t} + \rho V_j \frac{\partial V}{\partial \ell} \quad (66)$$

The appropriate nondimensionalized variables are:

$$\bar{V} = \frac{V}{V_j}$$



$h = \text{depth}$
 $\rho = \text{density}$
 $V_j = \text{axial jet velocity}$
 $V = \text{transverse jet velocity}$
 $P = \text{pressure}$

Fig. 41. Control Volume Around a Segment of Jet.

$$\bar{P} = \frac{P}{\frac{1}{2} \rho V_j^2}$$

(67)

$$\bar{Y} = \frac{Y}{b}$$

$$\bar{t} = \frac{V_j t}{b}$$

The quantity $1/\bar{t}$ can be defined as the Strouhal number for the modulator. Equation (66) becomes

$$\frac{\partial \bar{V}}{\partial \bar{t}} = - \frac{\partial \bar{V}}{\partial \bar{l}} - \frac{1}{2} \frac{\partial \bar{P}}{\partial \bar{n}} \quad (68)$$

The jet position equation is (Ref. 1):

$$\frac{\partial \bar{Y}}{\partial \bar{t}} = - \frac{\partial \bar{Y}}{\partial \bar{l}} + \bar{V} \quad (69)$$

We can combine Eqs. (68) and (69) and obtain (dropping the ($\bar{\quad}$) notation):

$$\frac{\partial^2 Y}{\partial t^2} + 2 \frac{\partial^2 Y}{\partial t \partial l} + \frac{\partial^2 Y}{\partial l^2} = - \frac{1}{2} \frac{\partial P}{\partial n} \quad (70)$$

This is a second-order partial differential equation of the parabolic type.

The forcing term of Eq. (70) can be evaluated as follows:

$$-\frac{1}{2} \frac{\partial P}{\partial n} \approx -\frac{1}{2} \frac{\Delta P}{\Delta n} = -\frac{1}{2} \frac{\Delta P}{b} = -\frac{1}{2} \frac{P_a - P}{b} = \frac{1}{2} \left(\frac{P - P_a}{b} \right) \equiv F \quad (71)$$

where

P = bubble pressure

P_a = atmospheric pressure

Thus Eq. (70) becomes

$$\frac{\partial^2 Y}{\partial t^2} + 2 \frac{\partial^2 Y}{\partial t \partial l} + \frac{\partial^2 Y}{\partial l^2} = F \quad (72)$$

3.1.2. Step Change in Pressure Across Jet

Consider a step change in F which acts over a finite length l_0 of jet as shown in Fig. 42.

The expression for F is:

$$F = F_0 U_s(t) (V_s(l) - U_s(l - l_0)) \quad (73)$$

where U_s is the unit step function. The LaPlace Transform with respect to l of Eq. (72) with Eq. (73) inserted, is:

$$\frac{d^2 Y}{dt^2} + 2q \frac{dY}{dt} + q^2 Y = F_0 U_s(t) \left(\frac{1}{q} - \frac{e^{-l_0 q}}{q} \right) = F_0 U_s(t) \frac{Q}{q} \quad (74)$$

where

$$Q \equiv (1 - e^{-l_0 q}) \quad (75)$$

Equation (74) is now an ordinary differential equation which can be solved in a straightforward manner by finding the homogeneous and particular solutions, then superposing the results, and evaluating the arbitrary constants.

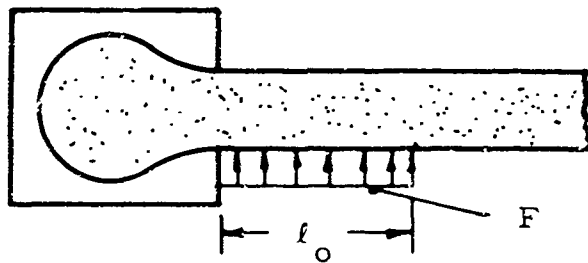


Fig. 42. Step Change in Pressure Over a Finite Distance.

Particular Solution

$$Y_p = \frac{F_o U_s(t) Q}{q^3} \quad (76)$$

Homogeneous Solution

The roots are equal, hence:

$$Y_h = A_1 e^{-qt} + A_2 t e^{-qt} \quad (77)$$

Total Solution

$$Y = A_1 e^{-qt} + A_2 t e^{-qt} + \frac{F_o U_s(t) Q}{q^3} \quad (78)$$

Initial Conditions

$$Y = 0 \text{ at } t = 0$$

$$\frac{dY}{dt} = 0 \text{ at } t = 0$$

Thus

$$A_1 = -\frac{F_o U_s(t) Q}{q^3}; \quad A_2 = \frac{F_o U_s(t) Q}{q^2} .$$

$$\frac{Y}{F_o} = U_s(t) \left(-\frac{1}{q^3} e^{-qt} - \frac{1}{q^2} e^{-qt} + \frac{1}{q^3} \right) Q \quad (79)$$

The inverse Laplace Transform of Eq. (79) is:

$$\frac{Y}{F_o} = U_s(t) \left(i - e^{-l_o} \frac{d}{dt} \right) \left[U_s(t) \frac{t^2}{2} - U_s(t-t) \left(\frac{t^2}{2} - \frac{t^2}{2} \right) \right] \quad (80)$$

or

$$\frac{Y}{F_o} = \left[U_s(l) \frac{l^2}{2} - U_s(l-t) \left(\frac{l^2}{2} - \frac{t^2}{2} \right) \right]$$

$$- \left[U_s(l-l_o) \frac{(l-l_o)^2}{2} - U_s(l-l_o-t) \left(\frac{(l-l_o)^2}{2} - \frac{t^2}{2} \right) \right] \quad (81)$$

In addition we can obtain V by using Eq. (69).

$$\frac{V}{F_o} = U_s(l) [l] + U_s(l-t) [t-l] - U_s(l-l_o) [l-l_o]$$

$$+ U_s(l-l_o-t) [l-l_o-t] \quad (82)$$

Both Y and V are shown in Fig. 43.

3.1.3. Exponential Change in Pressure Across Jet

It is apparent from an earlier report (Ref. 1, page 13) that the control region pressure looks like the step response of a simple first-order system with a two unit time constant. The step response of such a system is a simple exponential function of time which can be easily generated for the purpose of separately testing the jet equations. The simple first-order response will be a good test input since it is reasonable to expect that the bubble pressure will always be describable by a first or higher-order differential equation. The jet equations are solvable with this type of input. The step response as derived in Sec. 3.1.2 is the special case where the time constant of the forcing function is zero.

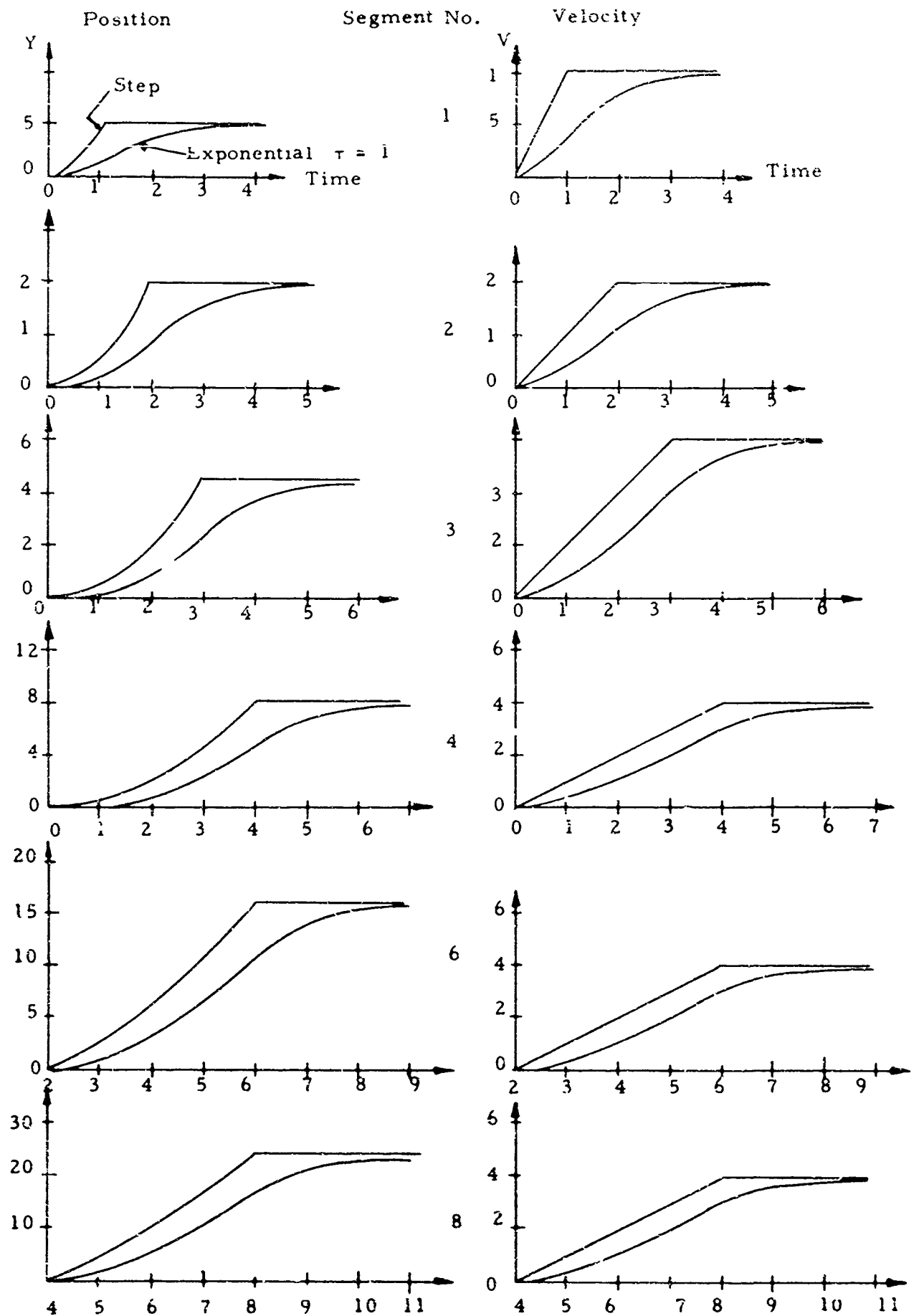


Fig. 43. Response of Jet Equations to Step and Exponential Inputs.

The forcing function is

$$F = F_o U_s(t) (1 - e^{-\frac{t}{\tau}}) (U_s(l) - U_s(l - l_o)) \quad (83)$$

The LaPlace Transformed jet equation is

$$\frac{d^2 Y}{dt^2} + 2q \frac{dY}{dt} + q^2 Y = F_o U_s(t) (1 - e^{-\frac{t}{\tau}}) \frac{Q}{q} \quad (84)$$

Particular Solution

$$Y_p = \frac{F_o U_s(t) Q}{q^3} - \frac{F_o U_s(t) Q}{q \left(\frac{1}{\tau} - q\right)^2} \quad (85)$$

The homogeneous solution is the same as Eq. (77)

Total Solution

$$Y = A_1 e^{-qt} + A_2 t e^{-qt} + \frac{F_o U_s(t) Q}{q^3} - \frac{F_o U_s(t) Q}{q \left(\frac{1}{\tau} - q\right)^2} \quad (86)$$

With the initial conditions as before, the arbitrary constants are:

$$A_1 = - F_o Q \left(\frac{1}{q^3} - \frac{1}{q \left(\frac{1}{\tau} - q\right)^2} \right);$$

$$A_2 = - F_o Q \left(\frac{1}{q^2} - \frac{1}{q \left(\frac{1}{\tau} - q\right)^2} + \frac{1}{q \tau \left(\frac{1}{\tau} - q\right)^2} \right).$$

The solution can be obtained by inserting the expressions for A_1 and A_2 in Eq. (86) and then taking the inverse LaPlace transform. The resulting expression for Y/F_0 is long and is best presented in parts for the various possibilities of l and t . The velocity V is also included.

$$\underline{l < l_0}$$

$$\underline{t < l}$$

$$\frac{Y}{F_0} = U_s(t) \left[\frac{t^2}{2} - \tau^2 e^{-\frac{t}{\tau}} - \tau(t - \tau) \right]$$

$$\frac{V}{F_0} = U_s(t) \left[t - \tau \left(1 - e^{-\frac{t}{\tau}} \right) \right]$$

$$\underline{t > l}$$

$$\frac{Y}{F_0} = U_s(t) \left[\frac{l^2}{2} - \tau^2 e^{-\frac{t}{\tau}} + \tau(\tau - l) e^{-\frac{(t-l)}{\tau}} \right]$$

$$\frac{V}{F_0} = U_s(t) \left[l - \tau \left(e^{-\frac{l}{\tau}} - 1 \right) e^{-\frac{t-l}{\tau}} \right]$$

$$\underline{l_0 < l < l_0 + t}$$

$$\underline{t < l}$$

$$\frac{Y}{F_0} = U_s(t) \left[\frac{t^2}{2} - \frac{(l - l_0)^2}{2} + \tau(\tau - t) \right] \text{ (con't.)}$$

$$- \tau (\tau - l + l_0) e^{\frac{(l - l_0 - t)}{\tau}}$$

$$\frac{V}{F_0} = U_s(t) \left[(t - \tau) - (l - l_0) + \tau e^{\frac{(l - l_0 - t)}{\tau}} \right]$$

$$\underline{t > l}$$

$$\frac{Y}{F_0} = U_s(t) \left[\frac{l^2 - (l - l_0)^2}{2} + \tau \left((\tau - l) \left(1 - e^{-\frac{l_0}{\tau}} \right) - l_0 e^{-\frac{l_0}{\tau}} \right) e^{-\frac{(l-t)}{\tau}} \right]$$

$$\frac{V}{F_0} = U_s(t) \left[l_0 - \tau \left(1 - e^{-\frac{l_0}{\tau}} \right) e^{-\frac{(l-t)}{\tau}} \right]$$

$$\underline{l > l_0 + t}$$

$$\frac{Y}{F_0} = \frac{V}{F_0} = 0 \tag{87}$$

Both Y and V are shown in Fig. 43 1.

3.2. Solution of the Jet Equations Using Various Finite Difference Approximations to the Space Derivatives

The space derivatives, $\partial V/\partial l$ and $\partial Y/\partial l$, in Eqs. (68) and (69) can be approximated at a fixed point in space by a finite difference expression of the form

$$\left. \frac{df}{dl} \right|_k \approx \sum_{i=1}^n a_i f_i; \quad 1 \leq k \leq n \quad (88)$$

The coefficients of the differentiation formula, Eq. (88) can be obtained from almost any numerical analysis text, (Ref. 30 and 31) though often not directly. A digital computer program has been written which calculates these coefficients for any n and all k 's.

In the following cases, the space increment, Δl , is unity. The jet is divided into 8 segments; the first four of which experience the driving force, F , and the last four, no driving force. Both V and Y are computed, and, in the three representative cases, compared with the theoretical response by means of a graph.

Case I - Fig. 44 - Step Input

Derivative formulae:

$$\frac{dY_k}{dl} = Y_k - Y_{k-1} \quad (89)$$

$$\frac{dV_k}{dl} = V_k - V_{k-1} \quad (90)$$

Comments:

1. Gives correct steady-state for V .
2. Does not give the correct steady-state for Y .
3. Computed response leads the theoretical response for segments 5 - 8.

Case II - Step Input

Derivative formulae:

$$\frac{dY_k}{dl} = 0.5 Y_{k+1} - 0.5 Y_{k-1} \quad (91)$$

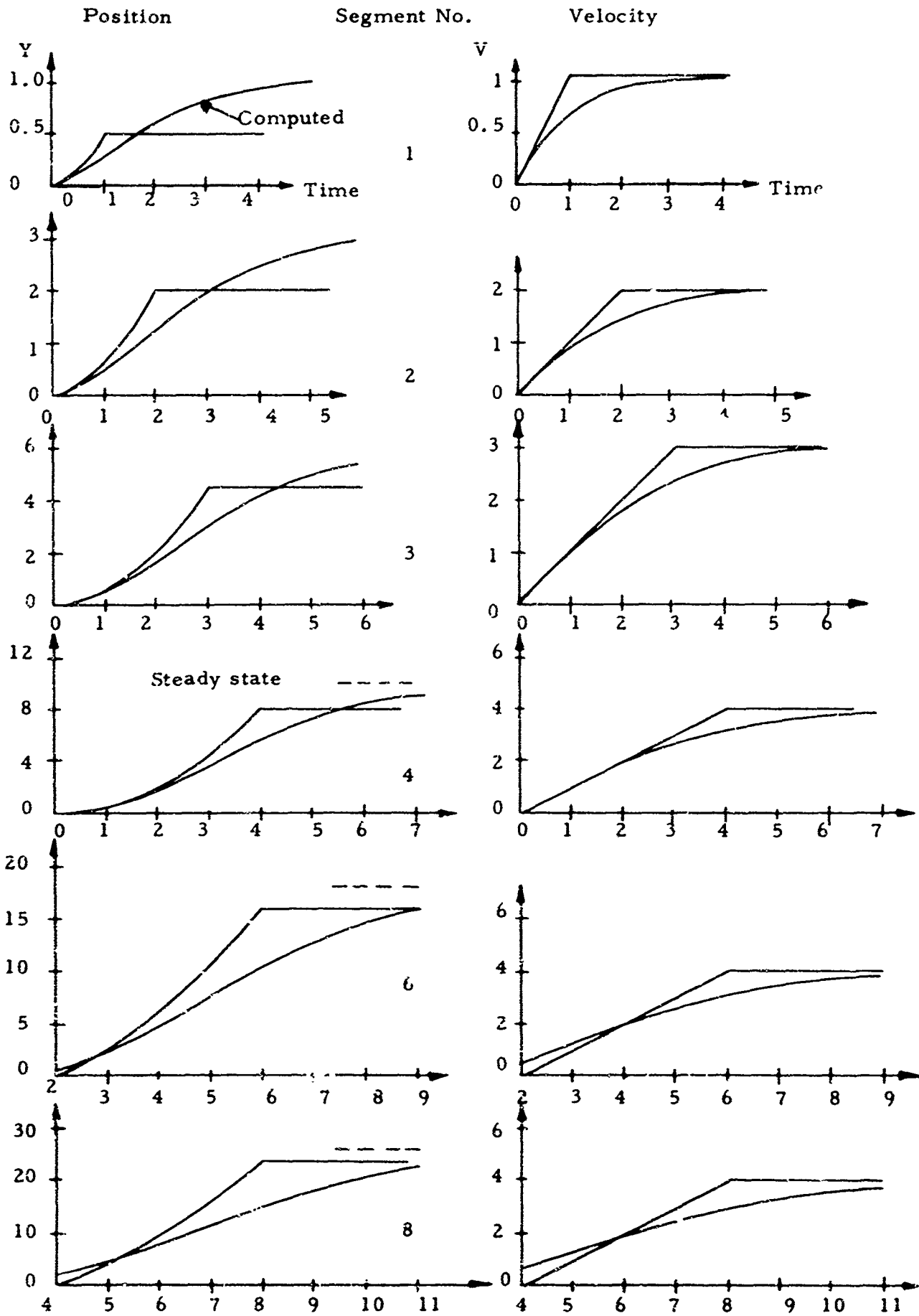


Fig. 44. Computed Jet Equation Response - Case I - Step Input.

$$\frac{dV_k}{dt} = 0.5 V_{k+1} - 0.5 V_{k-1} \quad (92)$$

Terminating Conditions:

Same as Eqs. (89) and (90)

Comments:

1. Very little damping, Damping is introduced only by the terminating conditions.

Case III - Step Input

Derivative formulae:

$$\frac{dY_k}{dt} = 1.5Y_k - 2Y_{k-1} + 0.5Y_{k-2} \quad (93)$$

$$\frac{dV_k}{dt} = 1.5V_k - 2V_{k-1} + 0.5V_{k-2} \quad (94)$$

Starting conditions:

$$Y_{-1} = Y_1 \quad (95)$$

$$V_{-1} = V_1 \quad (96)$$

Comments:

1. Steady state is not correct for either Y or V.
2. Computed response leads the theoretical response for segments 5 - 8.

Case IV - Step Input

Derivative formulae:

$$\frac{dY_1}{dt} = Y_1 - Y_0$$

$$\frac{dY_2}{dt} = 1.5Y_2 - 2Y_1 + 0.5Y_0$$

·
·
·

$$\frac{dY_k}{dt} = \sum_{i=0}^k a_i Y_i \quad (97)$$

Same for V

Comments:

Same as for Case II.

Case V - Fig. 45) - Step Input

Derivative formulae:

for

$$Y_k, \text{ Eq. (93)}$$

for

$$V_k, \text{ Eq. (90)}$$

Comments:

1. Gives correct steady state for Y and V.
2. Computed response leads for segments 5 - 8.

Case VI - Fig. 46 - Exponential Input

Derivative formulae:

Same as for Case V.

Comments:

Same as for Case V.

Conclusions:

Only the derivative formulae used in Case V give the correct steady state. The derivative formula for V is a two-point linear type. It is reasonable to expect that the formula for Y should be a three-point parabolic type. However, it is also seen that the computer response is too slow, especially for Y. Lead action still occurs for segments 5 - 8.

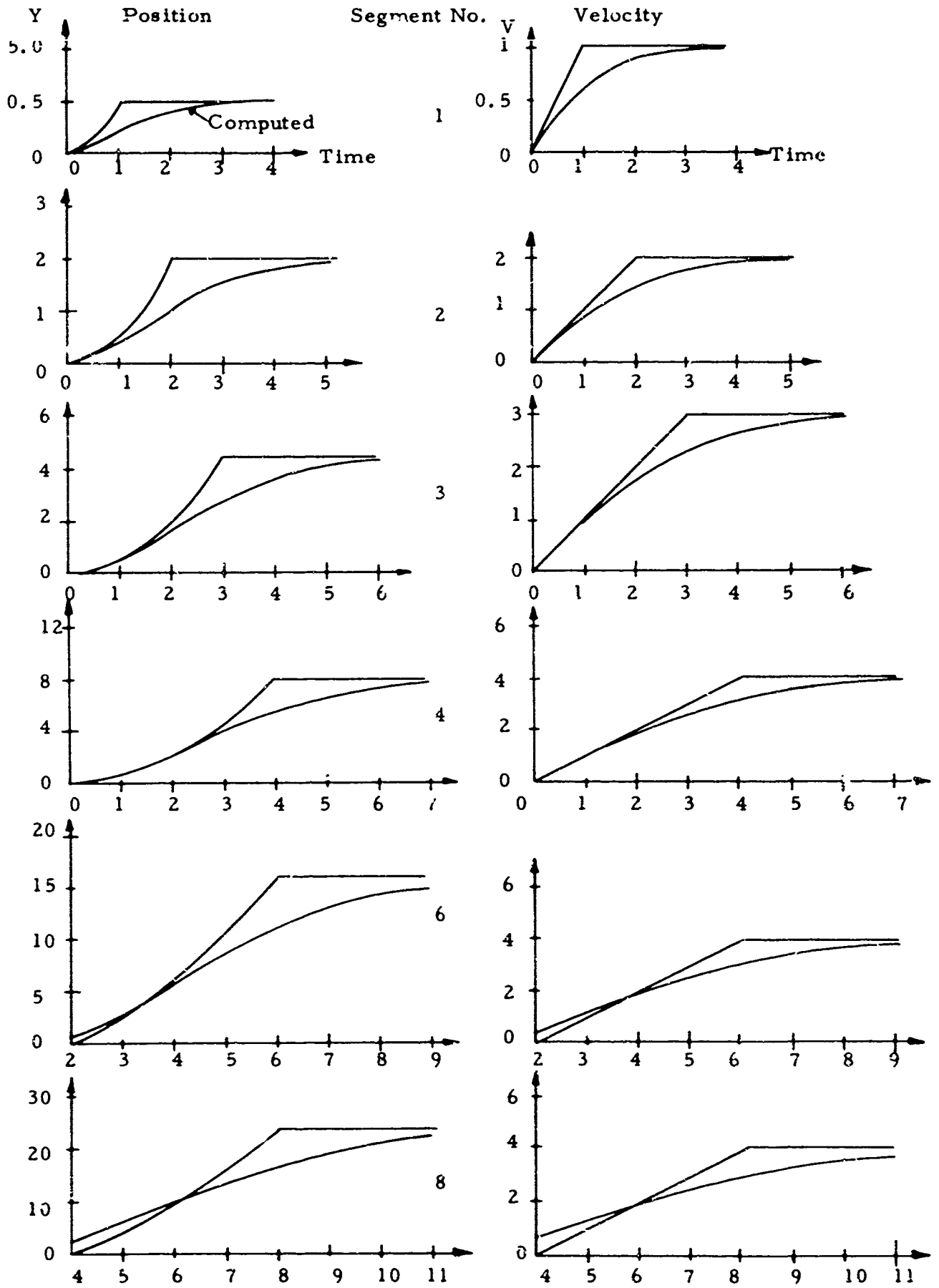


Fig. 45. Computed Jet Equation Response - Case V - Step Input.

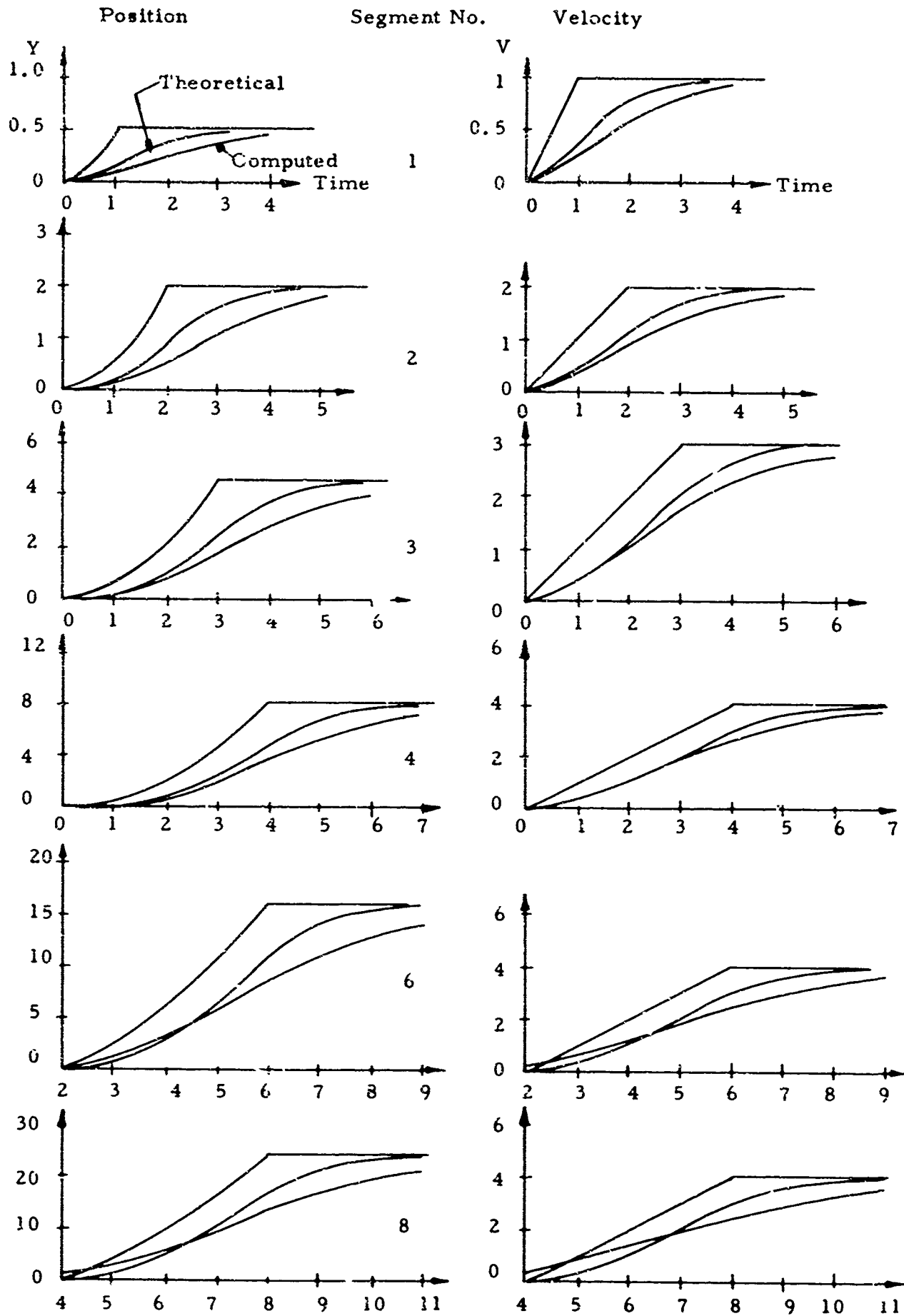


Fig. 46. Computed Jet Equation Response - Case V - Exponential Input.

This is to be expected because a pure transport delay is impossible to approximate with a finite set of continuous differential equations.

The general conclusion is that none of these approximations work very well. A good approximation should at least produce a correct steady state and a transient which is a reasonable facsimile of the theoretical one.

3.3. Characteristic Curves of Partial Differential Equations

3.3.1. Significance of Characteristic Curves

Certain types of partial differential equations possess what are called characteristic curves. (Refs. 29 and 32). As an example, consider the wave equation,

$$v^2 \frac{\partial^2 P}{\partial l^2} - \frac{\partial^2 P}{\partial t^2} = 0 \quad (98)$$

where $P = f(l)$ and $P_t = 0$ at $t = 0$. The solution is known to be of the form

$$P(l,t) = \frac{1}{2} \left[f(l - Vt) + f(l + Vt) \right] \quad (99)$$

which can be represented as in Fig. 47. The value of P at point C depends only on the values of P at A and B . Furthermore, every point within the shaded area is determined by a pair of points on the l axis in the interval AB . The two lines, AC and BC , are called "characteristic curves". Disturbances at A and B propagate along these curves and combine to form the value of P at point C . The shaded area is called the "region of determination" of point C .

Another region of determination, (Ref. 32), DEC , can be defined in Fig. 48 when Eq. (98) is converted into a difference equation. The value of P at point C is now determined by the values of P on the last two horizontal lines.

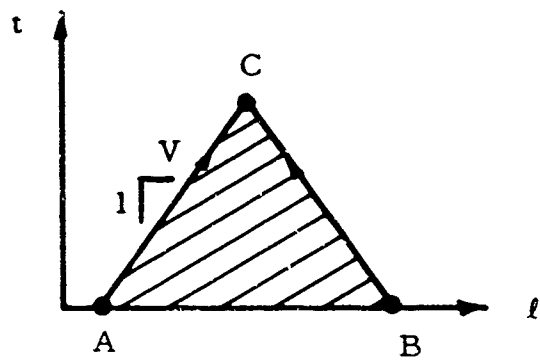


Fig. 47. Characteristic Curves for Wave Equation.

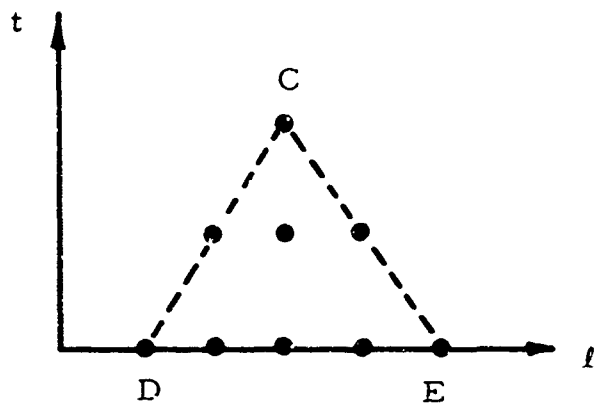


Fig. 48. Finite Difference Solution of Wave Equation.

If the solution to the difference equations is to converge to the true solution then the region of determination for the difference equations must include or coincide with that of the differential equations. Thus DE must be greater than AB. If DE were smaller than AB then the values of P at points A and B would not influence the value of P at point C; in which case the solution does not converge to the true solution when the mesh spacing shrinks to zero.

3.3.2. Characteristic Curves for the Jet Equation

The characteristic curves of Eq. (72) can be obtained from the quadratic: (Ref. 29).

$$adl^2 - b\,dt\,dl + cdt^2 = 0 \quad (100)$$

where a, b, and c correspond to the first, second, and third coefficients of Eq. (72) respectively. With $a = c = 1$, and $b = 2$, Eq. (100) becomes:

$$(dl - dt)^2 = 0 \quad (101)$$

Hence,

$$\frac{dt}{dl} = 1 \quad (102)$$

The single characteristic curve for the jet equation is shown in Fig. 49. The value of Y at B is determined by the value of Y an equal number of space and time units previous. With $F = 0$, the solution to Eq. (72) is:

$$Y(l, t) = Y(l - \Delta, t - \Delta) \quad (103)$$

where Δ is a constant. If F is not zero it would appear that Eq. (103) is in need of an additional term on its right side. This term should represent the cumulative effect of F on the jet over the intervals $(l - \Delta) \rightarrow l$ and $(t - \Delta) \rightarrow t$.

All of the above indicates that the jet equation should be solved by a technique which accumulates the effects of F and uses the values of Y only at previous t's and l's.

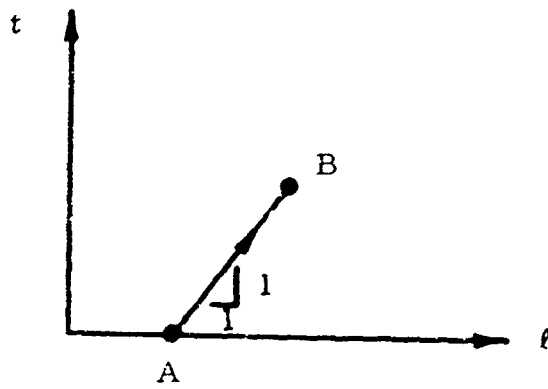


Fig. 49. Characteristic Curve for Jet Equation.

3.4. Generalized Transmission Processes

3.4.1. Definition of a Transmitter

The two equations,

$$\frac{\partial P}{\partial x} = - \frac{\partial q}{\partial t} \quad \text{and} \quad (104)$$

$$\frac{\partial q}{\partial x} = - \frac{\partial P}{\partial t} , \quad (105)$$

can be combined to obtain the well-known wave equation in terms of P or q:

$$\frac{\partial^2 P}{\partial x^2} = \frac{\partial^2 P}{\partial t^2} , \quad (106)$$

or

$$\frac{\partial^2 q}{\partial x^2} = \frac{\partial^2 q}{\partial t^2} . \quad (107)$$

One can write Eqs. (104) and (105) in a convenient matrix form after defining the operator

$$D = \frac{\partial}{\partial t} . \quad (108)$$

Thus

$$\frac{d}{dx} \begin{bmatrix} P \\ q \end{bmatrix} = \begin{bmatrix} 0 & -D \\ -D & 0 \end{bmatrix} \begin{bmatrix} P \\ q \end{bmatrix} \quad (109)$$

or

$$\frac{dS}{dx} = NS . \quad (110)$$

The variables, P and q, are called state variables, and S, a state vector. Processes which can be described by Eq. (109) are wavelike or diffusive in nature. Thus Eq. (110) describes the generalized transmission process. (Ref. 33).

Equation (104) is the result of applying the momentum equation. If body forces are present, then an additional term is necessary.

$$\frac{\partial P}{\partial x} = - \frac{\partial q}{\partial t} + F_b . \quad (111)$$

Equation (105) is the result of applying the continuity equation. Likewise, if sources or leaks are present then:

$$\frac{\partial q}{\partial x} = - \frac{\partial P}{\partial t} + Q . \quad (112)$$

Thus Eq. (110) becomes

$$\frac{d S}{dx} = NS + F . \quad (113)$$

where F is a vector containing F_b and Q . Thus Eq. (112) describes the generalized transmission process with external forcing.

3.4.2. Solution of the Generalized Transmitter Differential Equations

The assumed form of solution to Eq. (113) is:

$$S_x = N S_o + G F_o , \quad (114)$$

where M and G are square matrices. Differentiating Eq. (114)

$$\frac{d S_x}{dx} = \frac{d M}{dx} S_o + \frac{d G}{dx} F_o , \quad (115)$$

and substituting into Eq. (113) gives:

$$\frac{d M}{dx} S_o + \frac{d G}{dx} F_o = N M S_o + N G F_o + F_o \quad (116)$$

Collecting terms;

$$\left(\frac{dM}{dx} - NM \right) S_o + \left(\frac{dG}{dx} - NG \right) F_o = F \quad (117)$$

If F is assumed constant over the interval of space, x , (though not time) then

$$\left(\frac{dM}{dx} - NM \right) S_o + \left(\frac{dG}{dx} - NG - \text{II} \right) F_o = 0 \quad (118)$$

Since, in general, S_o and F_o are not equal to zero, then it must be that

$$\frac{dM}{dx} - NM = 0, \quad (119)$$

and

$$\frac{dG}{dx} - NG = \text{II}. \quad (120)$$

The solution to Eq. (119) is the well-known exponential given by

$$M = e^{N x} M_o \quad (121)$$

The solution to Eq. (120) contains two parts:

Homogeneous Solution

$$G_n = e^{N x} G_o \quad (122)$$

Particular Solution

$$G_p = - N^{-1} \quad (123)$$

Total Solution

$$G = e^{N x} G_0 - N^{-1} \quad (124)$$

The matrices M_0 and G_0 can be determined from initial conditions. At $x = 0$, it is obvious that

$$S_x \longrightarrow S_0 \quad (125)$$

Therefore, from Eq. (114) it follows that

$$S_0 = M S_0 + G F_0 \quad (126)$$

which demands that

$$M = \mathbb{I} \quad \text{and} \quad G = 0 \quad (127)$$

Hence, it follows that

$$M_0 = \mathbb{I} \quad \text{and} \quad G_0 = N^{-1} \quad (128)$$

Equation (114) becomes

$$S_x = e^{N x} S_0 + \left(e^{N x} - \mathbb{I} \right) N^{-1} F_0 \quad (129)$$

which is a familiar result (see page 11, Ref. 1).

3.4.3. Application to the Jet Equations

Equations (69) and (68) can be rewritten as

$$\frac{dY}{dx} = -DY + V, \quad (130)$$

and

$$\frac{dV}{dx} = -DV + F. \quad (131)$$

The matrix equation is

$$\frac{d}{dx} \begin{bmatrix} Y \\ V \end{bmatrix} = \begin{bmatrix} -D & 1 \\ 0 & -D \end{bmatrix} \begin{bmatrix} Y \\ V \end{bmatrix} + \begin{bmatrix} 0 \\ F \end{bmatrix} \quad (132)$$

Thus

$$N = \begin{bmatrix} -D & 1 \\ 0 & -D \end{bmatrix}, \quad (133)$$

$$e^{N x} = \begin{bmatrix} e^{-xD} & x e^{-xD} \\ 0 & e^{-xD} \end{bmatrix}, \quad (134)$$

$$N^{-1} = \begin{bmatrix} -\frac{1}{D} & -\frac{1}{D^2} \\ 0 & -\frac{1}{D} \end{bmatrix}, \quad (135)$$

and

$$(e^{N x} - \mathbf{I}) N^{-1} = \begin{bmatrix} \frac{1}{D} (1 - e^{-xD}) & \frac{(1 - e^{-xD})}{D^2} - \frac{x e^{-xD}}{D} \\ 0 & \frac{1}{D} (1 - e^{-xD}) \end{bmatrix} \quad (136)$$

The solution for Y and V are:

$$Y(x) = e^{-xD} (Y_0 + xV_0) + \left(\frac{(1 - e^{-xD})}{D^2} - \frac{x e^{-xD}}{D} \right) F, \quad (137)$$

$$V(x) = e^{-xD} V_0 + \left(\frac{1 - e^{-xD}}{D} \right) F. \quad (138)$$

Making use of the fact that e^{-xD} is the time delay operator and replacing x by Δx the above equations become,

$$Y_{x+\Delta x, t+\Delta x} = (Y + \Delta x V)_{x, t} + \left(\frac{(1 - e^{-\Delta x D})}{D^2} - \frac{\Delta x e^{-\Delta x D}}{D} \right) F, \quad (139)$$

$$V_{x+\Delta x, t+\Delta x} = V_{x, t} + \left(\frac{1 - e^{-\Delta x D}}{D} \right) F, \quad (140)$$

By comparing with Eq. (103) it is seen that indeed Eqs. (139) and (140) do represent the desired form of the solution. The right-most portions of Eqs. (139) and (140) represent the integrated effects of F over the space interval $x \rightarrow x + \Delta x$ and time interval $t \rightarrow t + \Delta x$.

Equations (139) and (140) are of a mixed form involving both difference and differential (or integral) equations. Both types of equations are easily solved by means of a digital computer. The method of solution of the portions of Eqs. (139) and (140) due to F is discussed in the next section.

3.5. Monotone Processes

3.5.1. Definition

Monotone dynamic processes are best described by Paynter, (Ref. 33, pp. 280 - 286), of which a small section is reproduced below.

"A large number of fluid, thermal, chemical and other industrial and organic processes are characterized by a step response which is monotonic nondecreasing in time as indicated. (See Fig. 50)

The corresponding frequency response, at least for most continuous processes, would have a non-increasing amplitude and non-decreasing phase lag with increasing frequency as follows: (See Fig. 51)

All linear systems giving to such response can be called monotone processes.

Monotone response is manifested through:

- (a) Time delay or dead time.
- (b) Dispersion or rise time.

In physical processes, time delay is usually associated with propagation or transport phenomena as measured by the ratio of travel distance to propagation or transport velocity. The dispersion in any process can

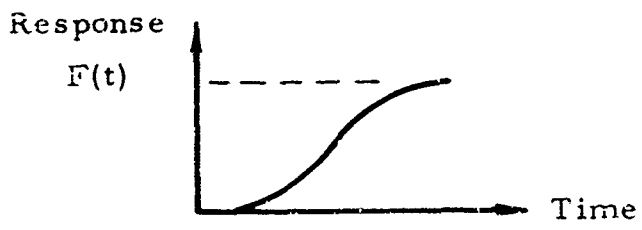


Fig. 50. Step Response of a Monotone.

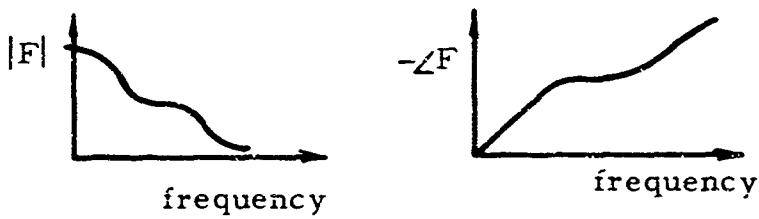


Fig. 51. Frequency Response of a Monotone.

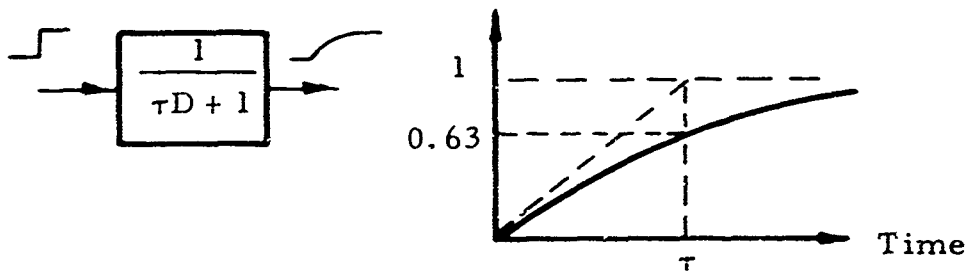


Fig. 52. Step Response of a Simple Lag.

ultimately be attributed to the law of increasing entropy, whereby the distributed resistances in any system cause an attenuation increasing with frequency. Such scattering action is reduced by isolation and relaying methods, but is always present to some degree.

Oscillatory processes, characterized by the presence of complementary energy storage elements, will have monotonic response whenever the energy dissipated per cycle becomes sufficiently large compared to the energy stored in each mode."

By way of an example, it is seen that the simple first-order lag is a monotone and is dynamically characterized by a single number, the time constant. (See Fig. 52).

It is possible to determine a transfer characteristic of the form: (Ref. 34).

$$G(D) = \frac{1}{1 + b_1 D + b_2 D^2 + \dots} = \frac{1}{\sum_k b_k D^k} ; b_0 \equiv 1 \quad (141)$$

which will adequately represent a monotone process over a desired range of frequencies. In order to determine the coefficients of the polynomial it is necessary to have a representative step response E , of the process from which can be calculated the time moments which are defined as:

$$a_0 = \int_{-\infty}^{+\infty} dE(t), \text{ (usually normalized to unity)}$$

$$\vdots$$

$$a_k = \int_{-\infty}^{+\infty} t^k dE(t). \quad (142)$$

The moments and the polynomial coefficients are related by the determinant: (Ref. 34).

$$\begin{array}{c}
 a_n = n! \\
 \left| \begin{array}{cccccc}
 b_1 & b_0 & 0 & \dots & 0 \\
 b_2 & b_1 & b_0 & \dots & 0 \\
 \dots & \dots & \dots & \dots & \dots \\
 b_{n-1} & b_{n-2} & b_{n-3} & \dots & b_0 \\
 b_n & b_{n-1} & b_{n-2} & \dots & b_1
 \end{array} \right| \cdot
 \end{array} \quad (143)$$

If the step response is the result of a transfer characteristic of the form given by Eq. (141), then indeed one will obtain an exact representation. However, if the step response exhibits discontinuities then probably the process contains time delays and consequently cannot be exactly represented by Eq. (141). The resulting representation in this case, though not exact, should still prove adequate for most applications. A word of caution is appropriate at this point. It may seem that a better approximation is always possible by taking more terms in the polynomial. However, some of the higher order coefficients (b_k), may be negative, resulting in an unstable representation, which is generally useless.

3.5.2. Application to the Jet Equations

Let us consider the contributions to Y and V caused by F in Eqs. (139) and (140):

$$G_1 \equiv \frac{Y}{F} = \frac{(1 - e^{-\Delta x D})}{D^2} - \frac{\Delta x e^{-\Delta x D}}{D}, \quad (144)$$

and

$$G_2 \equiv \frac{V}{F} = \frac{(1 - e^{-\Delta x D})}{D} \quad (145)$$

One can immediately write the solutions to these equations for a step change in F:

$$\frac{Y}{F} = \frac{1}{2} t^2 - U_s(t - \Delta x) \left[\frac{1}{2} (t - \Delta x)^2 - \Delta x(t - \Delta x) \right], \quad (146)$$

and

$$\frac{V}{F} = t - U_s(t - \Delta x) \left[(t - \Delta x) \right]. \quad (147)$$

These responses are shown in Fig. 53. It is now apparent that G_1 and G_2 represent monotones with discontinuities. Therefore, it is not possible to find exact representations in the form of Eq. (141) for G_1 and G_2 .

The moments for G_2 can be easily calculated with the aid of Eq. (142). In this case Δx is taken as unity. They are:

$$a_0 = 1, a_1 = \frac{1}{2}, \dots, a_k = \frac{1}{k+1}. \quad (148)$$

From these and Eq. (143) it is now possible to obtain the b_k :

$$\begin{aligned} b_0 &= 1 \\ b_1 &= \frac{1}{2} \\ b_2 &= \frac{1}{12} \\ b_3 &= 0 \\ b_4 &= -\frac{1}{720} \\ &\vdots \\ &\vdots \\ &\vdots \end{aligned} \quad (149)$$

Therefore, the best approximation to G_2 is

$$G_2' = \frac{1}{1 + \frac{1}{2} D + \frac{1}{12} D^2} \quad (150)$$

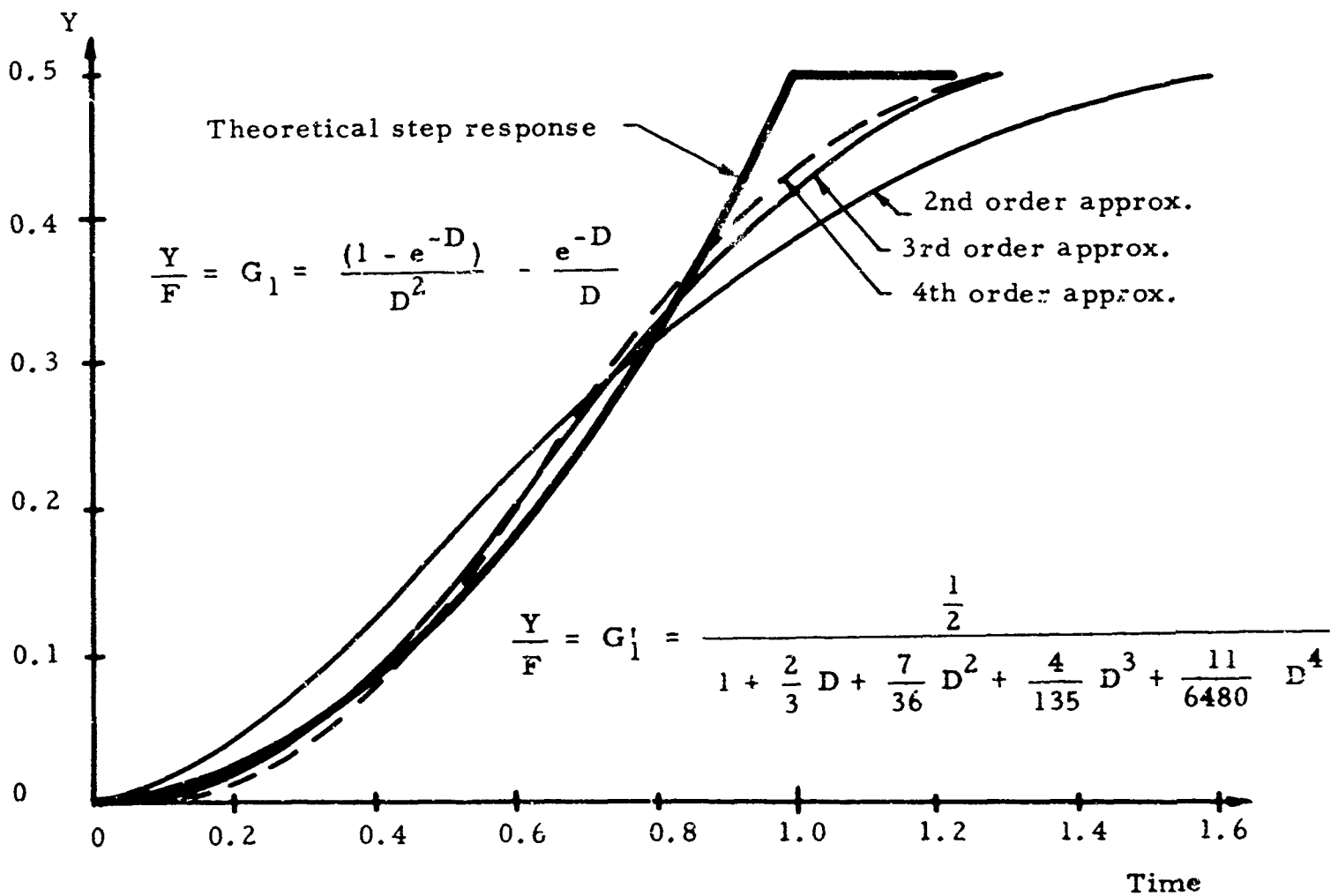
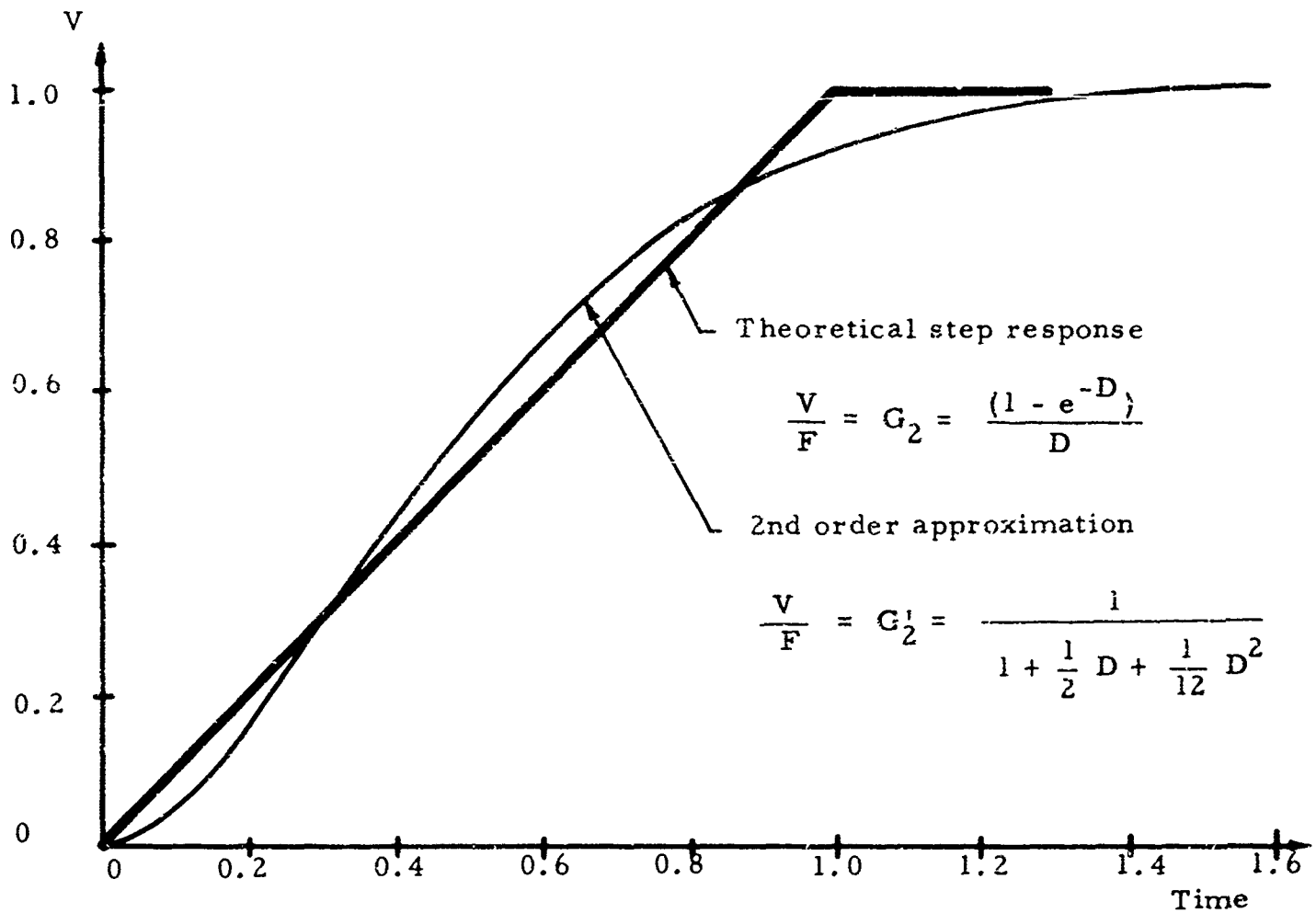


Fig. 53. Monotone Approximations for Jet Equations.

The step response of G_2' is compared to that of G_2 in Fig. 53.

The steady-state value of the unit step response of G_1 is $1/2$. It is usually more convenient to normalize this to unity for the purpose of calculating the b_k . The steady-state gain of the resulting transfer characteristic can then be modified very easily.

Proceeding as before, one finds that for G_2 the a_k are:

$$a_0 = 1, a_1 = \frac{2}{3}, \dots, a_k = \frac{2}{k+2}. \quad (151)$$

and that

$$\begin{aligned} b_0 &= 1 \\ b_1 &= \frac{2}{3} \\ b_2 &= \frac{7}{36} \\ b_3 &= \frac{4}{135} \\ b_4 &= \frac{11}{6480} \\ b_5 &= -\frac{39}{51,030} \\ &\vdots \\ &\vdots \\ &\vdots \end{aligned} \quad (152)$$

The best approximation to G_1 is

$$G_1' = \frac{\frac{1}{2}}{1 + \frac{2}{3} D + \frac{7}{36} D^2 + \frac{4}{135} D^3 + \frac{11}{6480} D^4} \quad (153)$$

where the " $1/2$ " is the correction for the steady-state gain. The step response of G_1' for the 2nd, 3rd, and 4th order cases is compared to that of G_1 in Fig. 53.

The approximations that ultimately will be used for G_1 and G_2 depend on two factors:

1. The expected frequency content of F , and
2. Computer storage and time.

It was seen in Sec. 3.1.3, that the bubble region pressure looks like the response of a simple first-order system with a time constant of about 2 units. The bubble region pressure is the force, F , in Eqs. (144) and (145). The harmonic content of the bubble pressure signal is therefore small at frequencies above the break frequency, $1/\tau \approx 0.5$ rad/unit. The natural frequency of G_2' , Eq. (150), for example, is $\omega_n = 3.46$ rad/unit which is comfortably above 0.5. Since G_2' is a good approximation to G_2 up to frequencies of 3.46 rad/unit then it follows that it also should be sufficiently accurate when driven by the bubble pressure. Similar considerations apply to G_1' .

Using higher-order approximations for G_1 and G_2 without justification is wasteful of computer storage and time. If a jet is modeled by 8 segments, a 2nd-order approximation for G_2 , and a 3rd-order approximation for G_1 , then it becomes necessary to operate on 40×40 matrices. A minimum number of three such matrices necessitates 4,800 words of computer storage.

3.6. A Possible Model for the Fluid Jet Modulator

From the results of the preceding sections it is now possible to propose a simplified model for a single control port fluid jet modulator. A non-functional block diagram is shown in Fig. 54.

The input to the system is the control pressure applied upstream of the control port restriction. The resulting control flow combines with the flow being demanded of the bubble region by the jet. The excess flow, resulting from this combination, then causes the bubble region pressure to "charge-up" to a new level because of the compliance (compressibility) of the fluid in the bubble.

The bubble pressure then causes the jet to accelerate to a new position. The change in position of the jet at the knife-edge affects the demand characteristics. The characteristics are also influenced by the

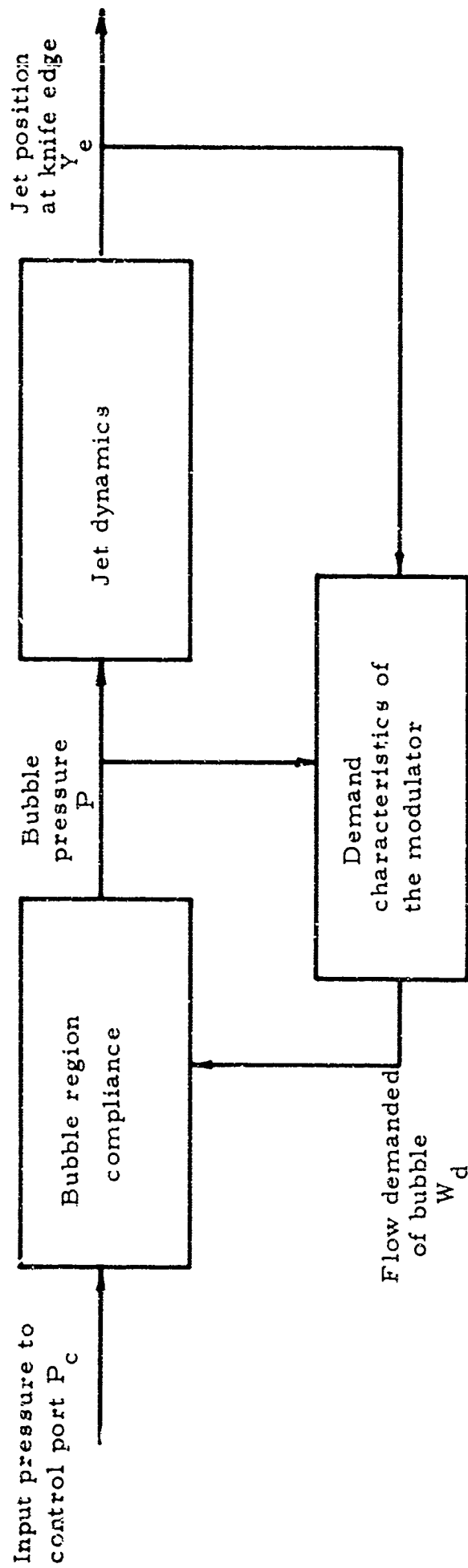


Fig. 54. Non-Functional Block Diagram of a Pressure Controlled Fluid Jet Modulator.

bubble pressure. The resulting change in the demand flow then affects the bubble region pressure thus closing the loop in the diagram.

Figure 55 shows a functional diagram of the same system. The checked enclosures indicate the correspondence with Fig. 54.

The difference between the control and bubble pressures is multiplied by the control port conductance, G , to produce the control flow, W_c . This flow is being supplied to the bubble region. The flow being demanded of the bubble region is then subtracted off. When the system is in steady state this difference is zero. An excess of one over the other causes a rate of change of bubble pressure, and consequently, a transient. This pressure rate is integrated to produce the bubble pressure. The bubble pressure is fed back thus closing a loop.

The net pressure across the jet, $(P - P_a)$ is applied to a transfer characteristic similar to Eq. (153) which determines the position of the jet in the region of the knife edge.

The atmospheric flow is computed as a product of two distinct functions. It is postulated that this flow passes through some effective area which is a function of Y_e and the lateral setback of the knife edge and is described by a static function, ϕ_2 . The effective pressure driving this flow is a function of $(P - P_a)$, or its negative, and is described by ϕ_1 . The simplest possible functions that seem appropriate are:

$$\phi_1 \propto \sqrt{(P_a - P)}$$

$$\phi_2 \propto (Y_o - Y_e - \frac{b}{2})$$

where Y_o is the lateral setback of the knife edge and b is jet width at the knife edge. The atmospheric flow would be

$$W_a \propto (Y_o - Y_e - \frac{b}{2}) \sqrt{(P_a - P)}$$

which is recognized as the form of the simple orifice equation.

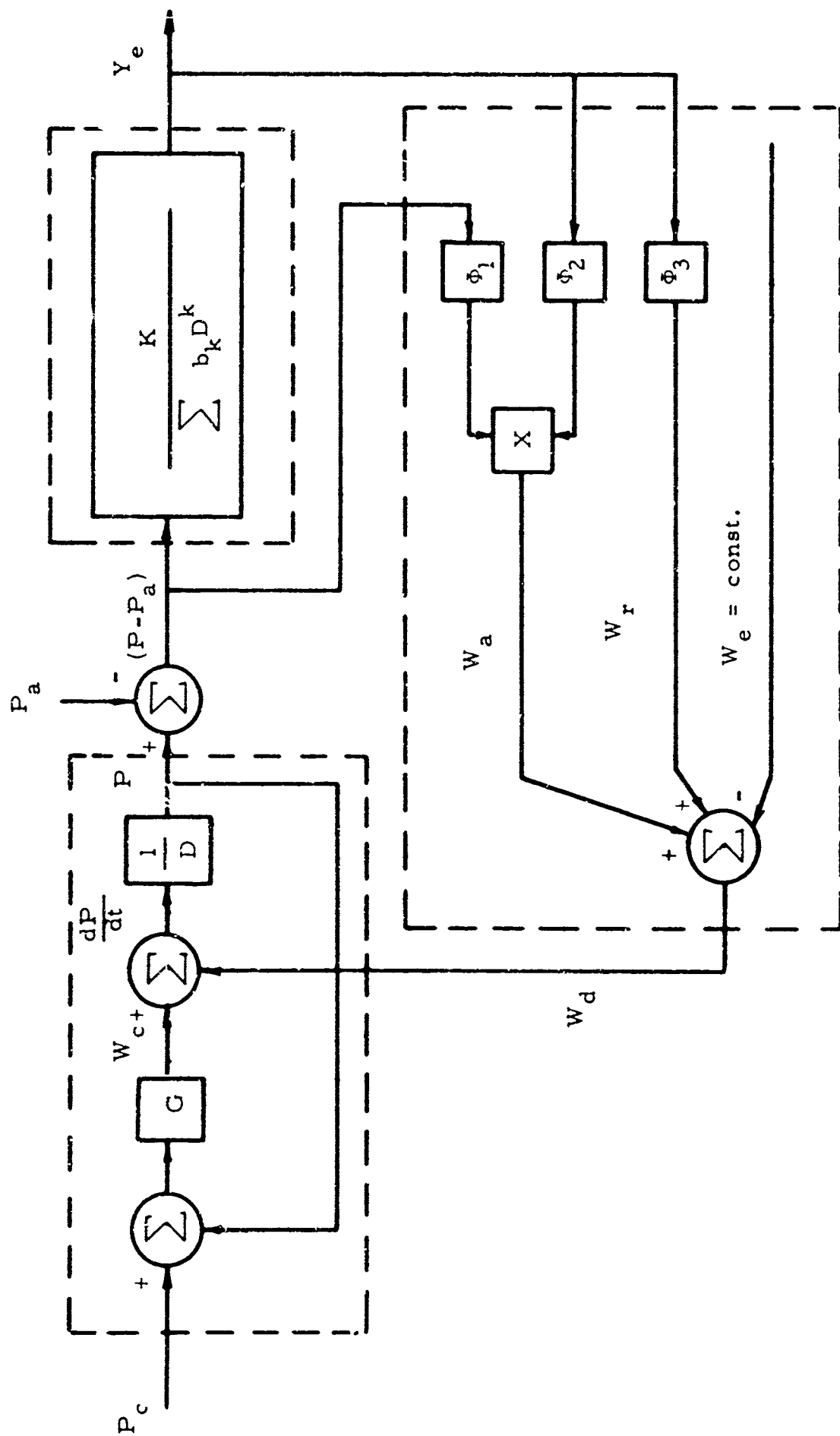


Fig. 55. Functional Block Diagram of a Pressure Controlled Fluid Jet Modulator.

The return flow is computed as a function of the jet position only. The simplest possible reticulation of ϕ_3 would be

$$W_r = 0; \quad Y_e + \frac{b}{2} + \delta \leq Y_o$$

$$W_r \propto (Y_e + \frac{b}{2} + \delta - Y_o); \quad Y_e + \frac{b}{2} + \delta \geq Y_o$$

where δ is a constant which allows the $W_r = 0$ point to fall within or without the non-zero range of W_a

The entrained flow, W_e , is assumed constant although this is probably not strictly true.

The combination of these three flows then combine to produce the demand flow thus closing the loop.

The above model assumes that the jet equations derived in Sec. 3.5.2. are valid (at least dynamically) and that the demand characteristics can be reticulated as indicated in this section. Both assumptions must be verified by experiment.

4. THE DYNAMICS OF SYSTEMS

4.1. The Transmission of Waves in Lines

Viscosity and heat transfer disperse the wave-fronts in fluid lines. LaPlace operators for the propagation and characteristic impedance functions have been derived by the author (Ref. 24) for liquid and perfect-gas filled lines, and the frequency response and parts of the step responses were calculated. Following the suggestions of the author (Ref. 35), S. E. Nelson found the complete families of the step responses of liquid-filled lines. This work is presented in a thesis (Ref. 36); a professional paper is planned. All of the above work assumed small disturbances in rigid cylindrical lines with laminar flow.

D. M. Auslander is presently finishing his S.M. thesis in which he makes theoretical predictions for the frequency responses of liquid flow in cylindrical rigid lines with a gross turbulent flow. The predicted attenuation is much greater than for laminar flow. Both smooth-walled and rough-walled pipes are considered.

None of the above work was supported by the present contract.

A question of frequent importance is the effect of bends on the transmission of waves in lines. A rather simple answer can be provided when the wave-lengths of interest are much longer than the dimensions of the bend, and the disturbance is small. Under these conditions the steady-flow characteristics of the bend apply, producing a pressure drop proportional to the square of the flow. The proportionality factor, which depends on the sharpness of the bend, is given for several geometries in even elementary fluid-mechanics texts. The small disturbance assumption allows an incremental linear resistance to be found. This resistance is an increasing function of the gross flow; it is zero for zero gross flow.

Thus the bend acts like a friction joint in a straight pipe. An incident wave is partly reflected and partly transmitted; if R is the linearized resistance for small disturbances about a gross flow in a line with characteristic impedance Z_0 (roughly equal to the speed of sound divided by the area of the line), the reflection and refraction operators (coefficients in simple cases) are respectively,

reflection operator:

$$\frac{R}{2 Z_o + R} \quad (154)$$

refraction operator:

$$\frac{2\sqrt{Z_o (Z_o + R)}}{2 Z_o + R} \quad (155)$$

4.2. The Stability of Fluid Systems

Fluid systems, especially those containing proportional fluid amplifiers with no moving parts, often display little understood bistable or cyclic instabilities. The author has prepared a paper on this subject (Ref. 37) which will be widely available before the present report; the present contract is therein credited with the support for the work. Therefore, the substance of this work omitted herein.

Two general criteria for small-disturbance stability are presented, with simple illustrations involving amplifiers, lines, and volumes. Application of the criteria to real systems is based on separate measurements of certain static and dynamic properties of the more complicated elements and analysis of the separate properties of the other elements.

5. STALL CELL SENSOR

5.1. Introduction

The concept and test results on the first model of a stall-cell sensor are described in Sec. 3.2 of the first annual report. Analytical work of both a theoretical and experimental nature has continued. A static stability analysis has been completed which should result in useful design formulae. The experimental study was continued, utilizing a new test model, and although results are mostly of qualitative value, some quantitative data is presented.

5.2. Bistable Jet Amplification

Fluid jet amplifiers are classed as analog (proportional) and digital (bi- and tri-stable) depending on the stable operating positions of the jet. A bistable jet is unstable in the center position and stable only in its two extreme positions. The mechanism of bistable jet amplification is explained as follows.

While a free jet is inherently statically stable, a jet which is not permitted to blow freely into the environment may be rendered statically unstable through proper design of the discharge region. Consider a jet discharging to a region such as that shown in Fig. 56. In passing through the discharge region, the jet entrains flow, w_e . The flow entrained is relatively unaffected by control port pressure differences and jet curvature and hence remains constant on each side. The entrained flow removed from the control port is equal to the flow into this region from the environment, w_a . Then, on the side in the direction of jet curvature, the velocity of the flow passing through the area between the projection and the edge of the jet increases. Due to increased frictional losses, the pressure on that side (P_1) decreases. The pressure on the opposite side (P_2) increases. A pressure force is then seen to act on the jet in the direction of curvature. If the pressure force accompanying a "small" deflection of the jet exceeds the force due to the accompanying Y-component of momentum reaction, static instability results - the jet curvature will then increase until the jet attaches to the projecting edge. In the case of a two-sided amplifier, such as the one shown, this is referred to as bistable operation.

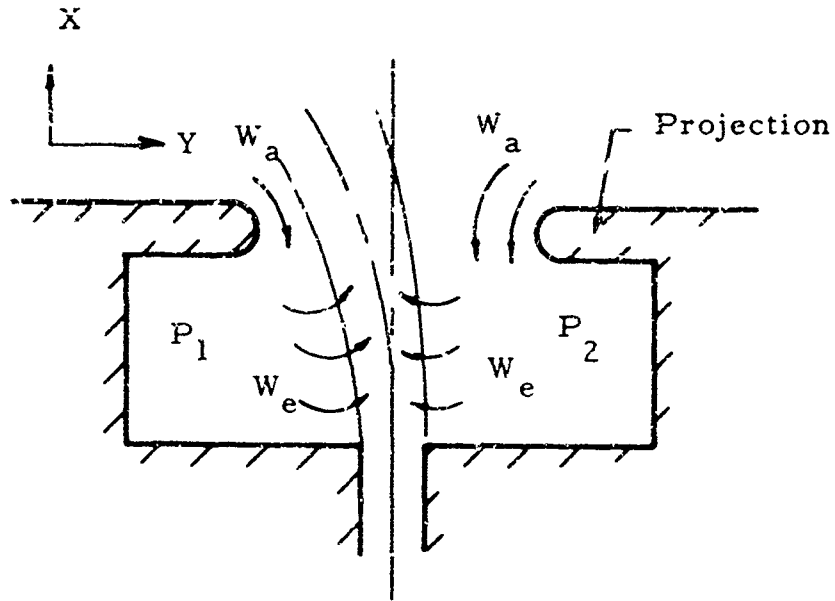


Fig. 56. Discharge Region Giving Static Instability.

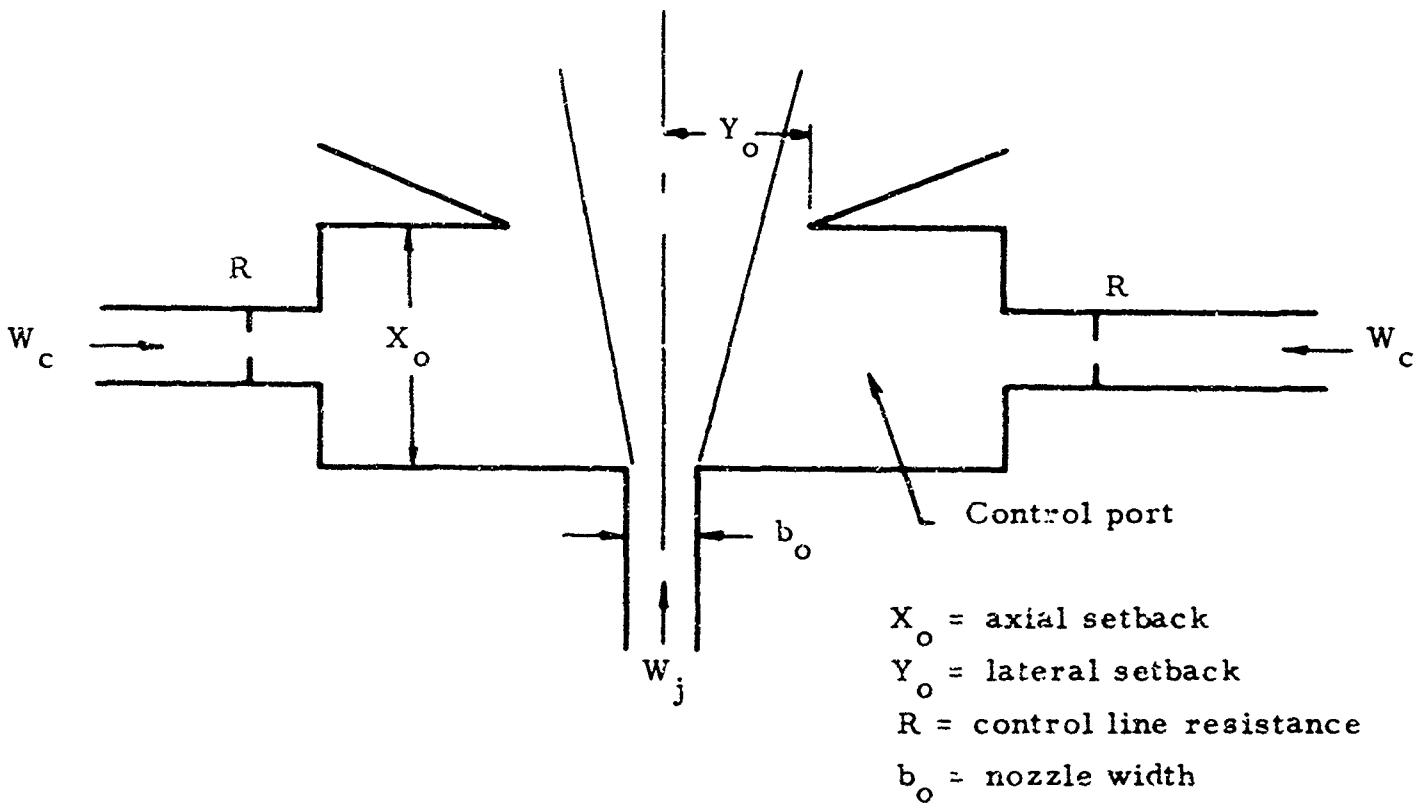


Fig. 57. Discharge Region With Control Lines Added.

Curvature of a bistable jet can be effected by adding control lines to each side of the discharge region. This is shown in Fig. 57 along with nomenclature that will be of use. By increasing the control flow on the side of attachment, decreasing control flow on the unattached side, or both, the jet can be flipped from one side to the other. The ability of the power jet to flip quickly in response to an alternating signal transmitted to the control port led to the proposed application. A schematic of the stall sensing arrangement is shown in Fig. 58 (see also Fig. 20 of Ref. 38). In Fig. 59c a possible packaging arrangement is shown.

5.3. Theoretical Study

5.3.1. Static Stability Analysis

Brown has presented a criterion for static and surge stability of the center position of the power jet, based on experimental measures of the characteristics of the device as measured at the control ports. Van Koevering has generalized this to include non-center jet positions and configurational asymmetries. Brown and Simson have reported criteria for the wave (organ pipe) stability using some of the same results, and in Sec. 4.2. of this report, Brown discusses a generalized approach to the stability and response of linear systems.

The stability analysis for the center position of the jet is herein interpreted analytically in terms of the jet model given by Simson (Ref. 39) plus one added assumption, reducing greatly the requirement for experimental data. The analysis is for a symmetrical amplifier, assumes no feedback effects of the receiver ports, and neglects the dynamic head of the control flow which enters through a very large passage. In addition, the "return flow, w_r ", is assumed zero for the center position of a jet, a condition which is approximately necessary for bistability. The flow entrained into the jet, w_e , is assumed to be unaffected by small deflections of the jet. Thus the changes in the control flow w_e are equal to minus the changes in the flow w_a which enters the control region from the environment by passing between the knife edge and the jet. Brown's criterion for center-position stability then becomes (See Ref. 40)

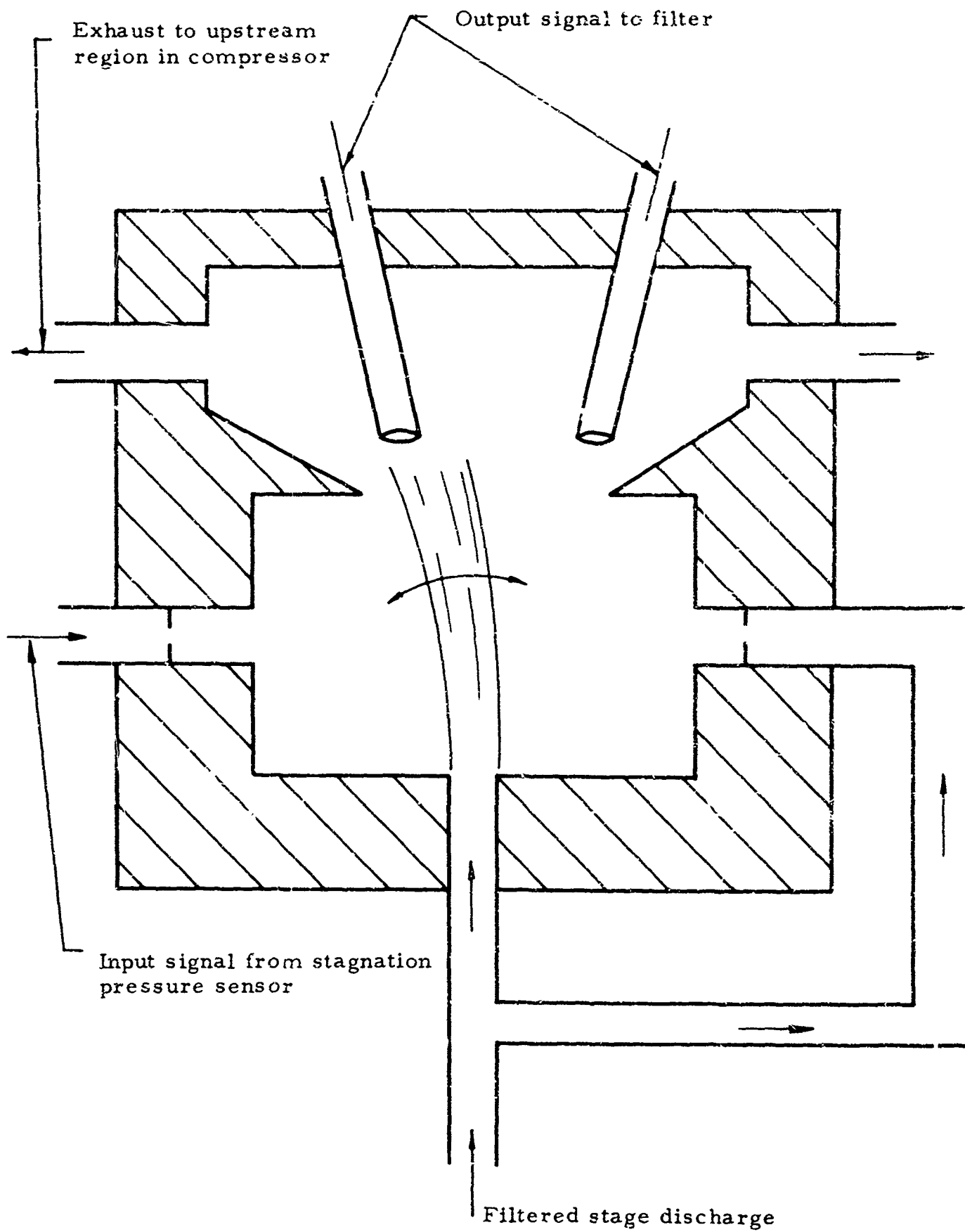
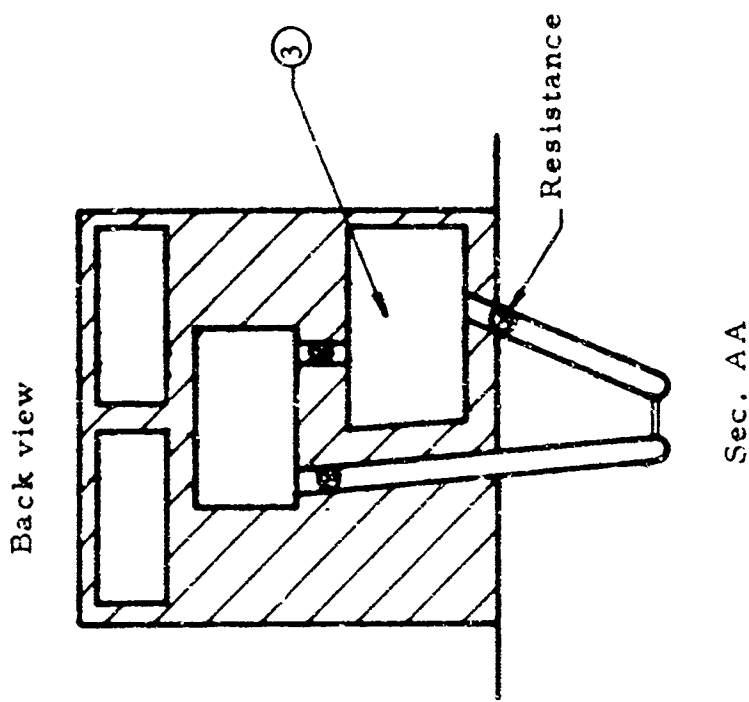
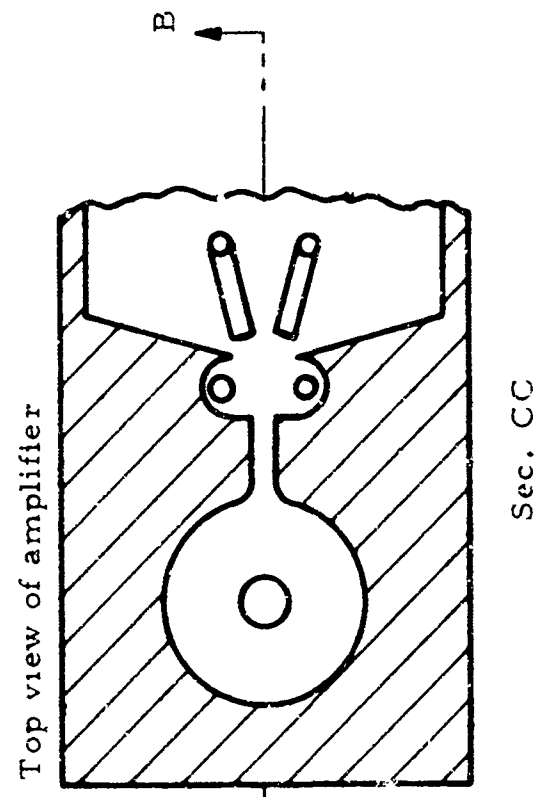
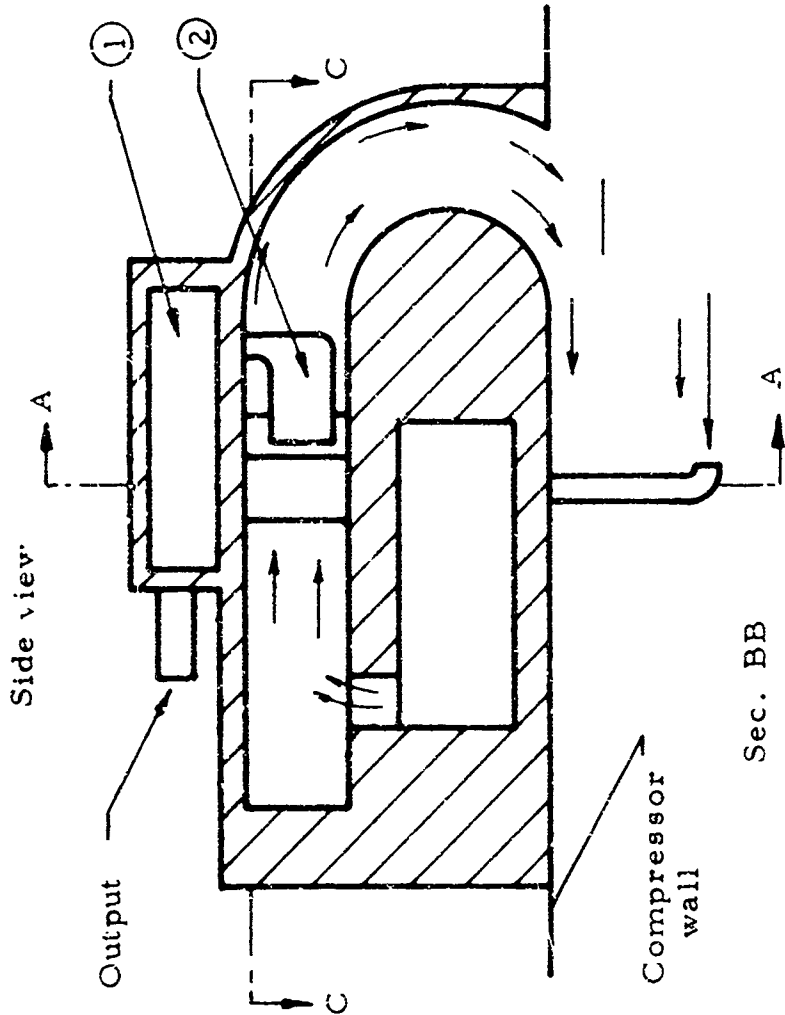


Fig. 58. Proposed Stall Sensing Arrangement.



- (1) Output filter
- (2) Pitot tube to output filter
- (3) Nozzle and reference port supply filter

Fig. 59. Stall Sensor Unit.

$$\frac{1}{(R)_{Y_1=0}} > \left[\frac{\partial w_{a1}}{\partial P_1} \right]_{Y_1=0, P_1=\text{const.}} - 2 \left[\frac{\partial w_{a1}}{\partial (P_2 - P_1)} \right]_{P_1=\text{const.}, P_2=P_1} \quad (156)$$

in which the subscripts 1 and 2 refer to the two control regions, Y_1 is the deflection of the jet as shown in Fig. 60, and R is the resistance of the upstream restriction. The resistance R can be assigned either steady state or surge values.

The deflection of the jet, for small pressure gradients, is very nearly

$$Y_1 = \frac{X_o^2 (P_a - P_1)}{2 \rho b_o V_j^2} \quad (157)$$

an assumption based on the uniformity of the pressure gradient across the jet and the conservation of the momentum of the jet. The nozzle width is b_o , and the jet mean velocity V_j .

The most critical assumption is the modelling of the flow w_a

$$w_{a1} = C_d Y_{a1} t \sqrt{2 \rho (-P_1)} \quad (158)$$

where t is the depth of the model. This is, of course, the classical adaption of Bernoulli's equation to flow through an orifice. The orifice here is assumed bounded by the "edge" of the jet. The atmospheric flow is assumed to be into the control port, a condition necessary for bistability. For positive control flow, this imposes the requirement $w_c < w_e$.

The substitution of Eqs. (157) and (158) into Eq. (156), noting that $dY_{a1} = -dY_1$, gives the condition for stability

$$\frac{w_{ao}}{\rho (C_d Y_{ao} t)^2} \frac{1}{(R)_{Y_1=0}} > -1 + \frac{X_o^2 w_{ao}^2}{\rho^2 b_o C_d^2 Y_{ao}^3 t^2 V_j^2} \quad (159)$$

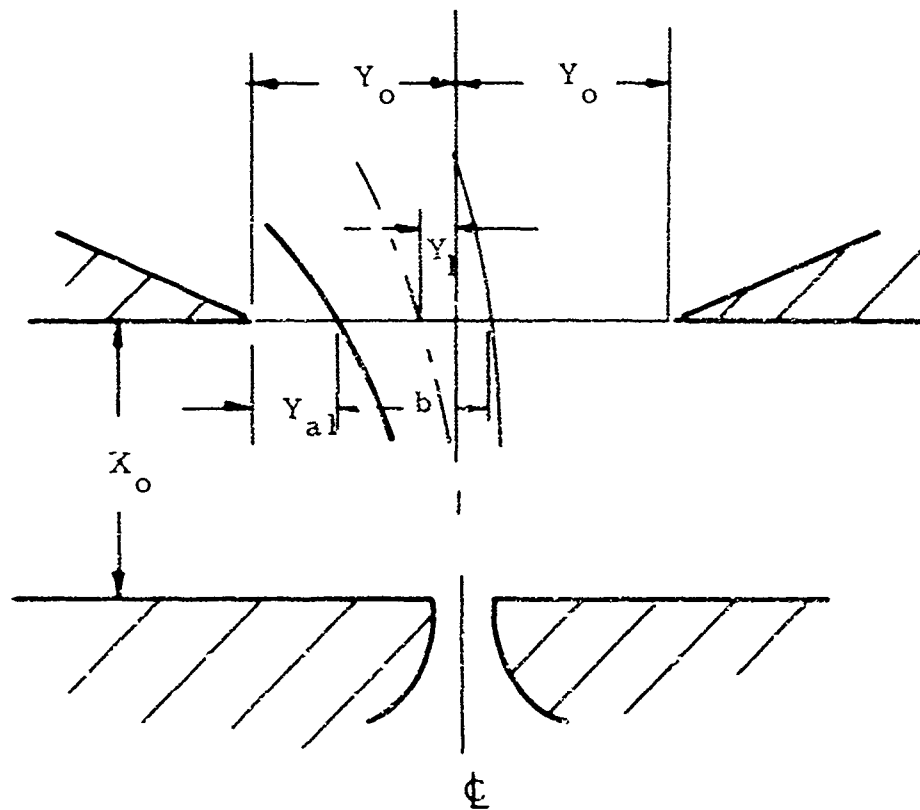


Fig. 60. Jet In Vicinity of Knife Edge.

The remaining steps are to put w_{ao} and Y_{ao} into more convenient forms. Using Simson's model for a jet, and assuming that the knife edge is within a distance of 5.2 nozzle widths from the nozzle,

$$Y_{ao} = Y_o - 0.169 X_o - 0.5 b_o \quad (160)$$

The flow w_{ao} is the difference between the entrained and control flows; using Simson's model for the former and w_c for the latter,

$$w_{ao} = 0.035 \rho X_o t V_j - w_{co} \quad (161)$$

For the general case of finite resistance and w_c , Eq. (159) with the condition of Eq. (161) results in the following criteria for bistable operation:

$$\begin{aligned} & \left(\frac{1}{R} \right)_{Y_1=0} (P_c - \bar{P}) \left[\rho b_o Y_{ao} V_j^2 + (P_c - \bar{P}) X_o^2 \right] \\ & - \left(\frac{1}{R} \right)_{Y_1=0} \left[0.035 \rho X_o t V_j \left\{ \rho b_o Y_{ao} V_j^2 + 2 (P_c - \bar{P}) X_o^2 \right\} \right] \\ & - (\rho t V_j)^2 \left[b_o C_d^2 Y_{ao}^3 - (0.035)^2 X_o^4 \right] \geq 0 \end{aligned}$$

for linear resistance

$$\left(\frac{1}{R} \right)_{Y_1=0} = \frac{w_{co}}{P_c - \bar{P}} \quad (162)$$

$$\begin{aligned} & \left(\frac{1}{R} \right)_{Y_1=0}^2 (P_c - \bar{P}) \left[2 \rho b_o Y_{ao} V_j^2 + 4 (P_c - \bar{P}) X_o^2 \right] \\ & - \left(\frac{1}{R} \right)_{Y_1=0} \left[0.035 \rho X_o t V_j \left\{ \rho b_o Y_{ao} V_j^2 + 4 (P_c - \bar{P}) X_o^2 \right\} \right] \end{aligned} \quad (163)$$

$$- (\rho t V_j)^2 \left[P_o C_d^2 Y_{ao}^3 - (0.035)^2 X_o^4 \right] \geq 0$$

for square-law resistance,

(163)

$$\left(\frac{1}{R} \right)_{Y_1=0} = \frac{w_{co}}{2(P_c - P)}$$

where P_c is the control line supply pressure, P is the average control port pressure ($= P_1 + P_2)/2$), and Y_{ao} is given by Eq. (160). These results enable a theoretical prediction, for example, of the optimum control line resistance for a particular configuration.

For the special case of blocked control passages ($R = \infty$), Eqs. (160), (162), and (163) reduce to

$$Y_o < 0.169 X_o + 0.5 b_o + \sqrt[3]{\frac{(0.035)^2 X_o^4}{C_d^2 b_o}} \quad (164)$$

For the case of finite R , this relation represents a necessary (although not sufficient) condition for bistability on which dimensional choices can be based.

The upper limit imposed on Y_o by Eq. (164) represents the transition from bistable to tristable operation. By reducing the control line resistance sufficiently, the operation can then become continuous. The lower bistability limit is approximately the point where the return flow becomes finite for a center-positioned jet. This limit represents a transition from bistable to continuous operation, and may be estimated from Eq. (160), by setting $Y_{ao} = 0$. The dimensional limits for bistability given by Eqs. (160) and (164) are plotted in Fig. 61.

5.3.2. Atmospheric Flow Coefficient

Continuing the analogy of orifice-type flow for the atmospheric flow component, it is shown by dimensional analysis that the loss coefficient C_d has the following functional relationship (neglecting the effect of variations in control port shape)

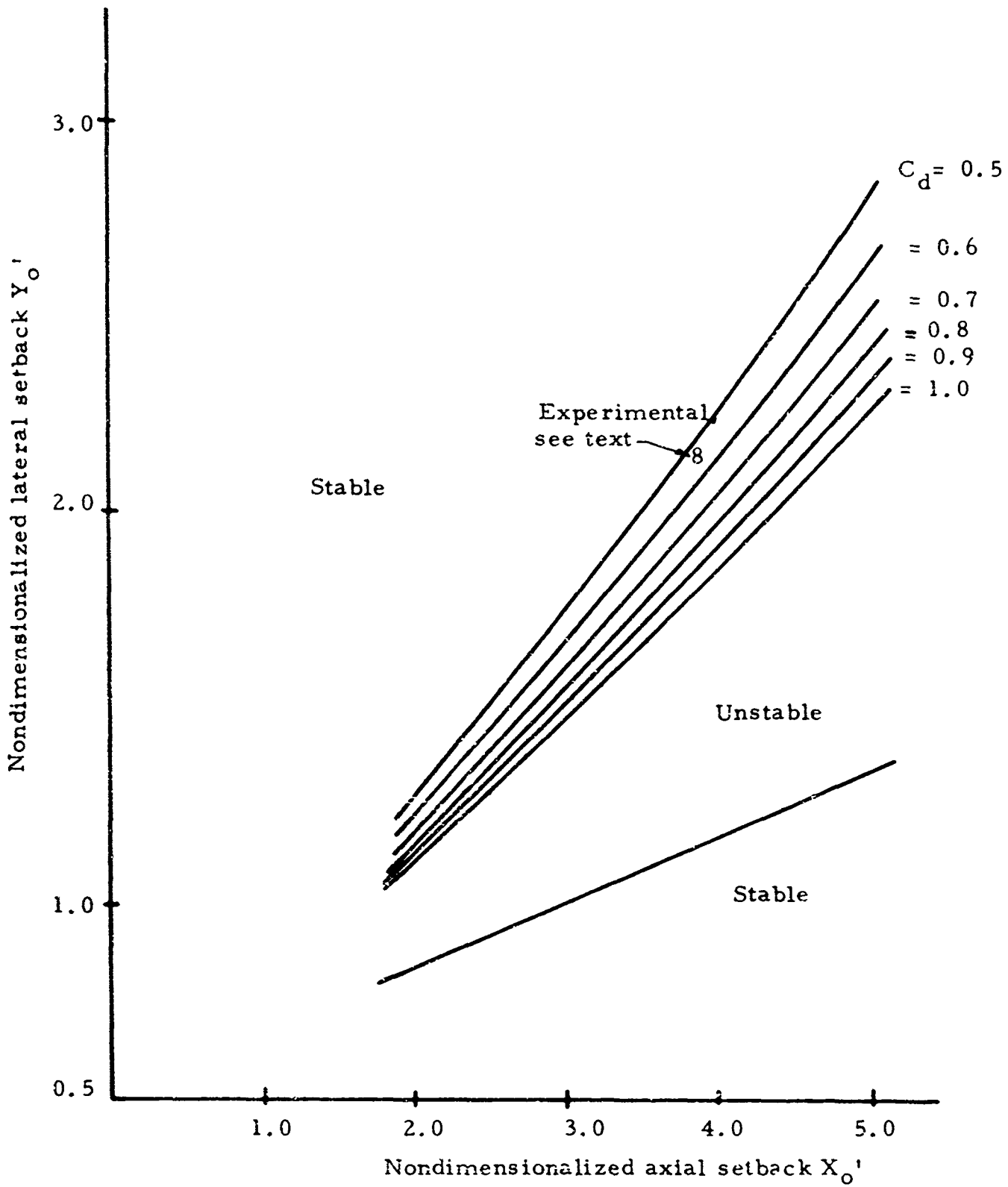


Fig. 61. Dimensional Limits for Bistable Operation.

$$C_d = \phi \left(\frac{Y_{ao}}{t}, Re_a \right) \quad (165)$$

where Re_a is the Reynold's number associated with the atmospheric flow.

Taking the characteristic velocity as the bulk mean velocity of the atmospheric flow and the characteristic length as Y_{ao} , the Reynold's number can be expressed as

$$Re_a = \frac{w_{ao}}{\mu t} \quad (166)$$

From Eqs. (158) and (161)

$$C_d = \frac{w_{ao}}{Y_{ao} t \sqrt{2\rho(-\bar{P})}} \quad (167)$$

$$w_{ao} = 0.035 X_o t \sqrt{2\rho(P_s - \bar{P}) - w_{co}} \quad (161)$$

so that the desired functional relation for C_d is determined experimentally by measuring P_s , w_{co} and \bar{P} .

Data of this type has been extracted from a load-flow diagram presented by VanKoevering (Ref. 41, Fig. 5.8[†]) and is presented graphically in Fig. 62. This plot is for fixed Y_{ao}/t ; C_d is seen to vary moderately with Reynolds number over this range. The latest test model (described in Sec. 5.4.1) was tested with Y_{ao}/t ranging from 0.39 to 0.58 and Reynold's number on the order of 4000. C_d had values ranging from 0.2 to 0.3 and was a moderate function of Y_{ao}/t and weak function of Reynold's number. Leakage resulting in a large control port pressure asymmetry limited the quantitative value of the data.

5.3.3. General Application of Theory

The procedure for applying the proposed theory in designing for optimum bistable operation is outlined below. This is for the most general situation, where C_d is a function of Reynold's number in the range of interest.

[†]The value of R' on VanKoevering's Fig. 5.8 should be 6.75. The corrected value is computed from p. 98 of his thesis.

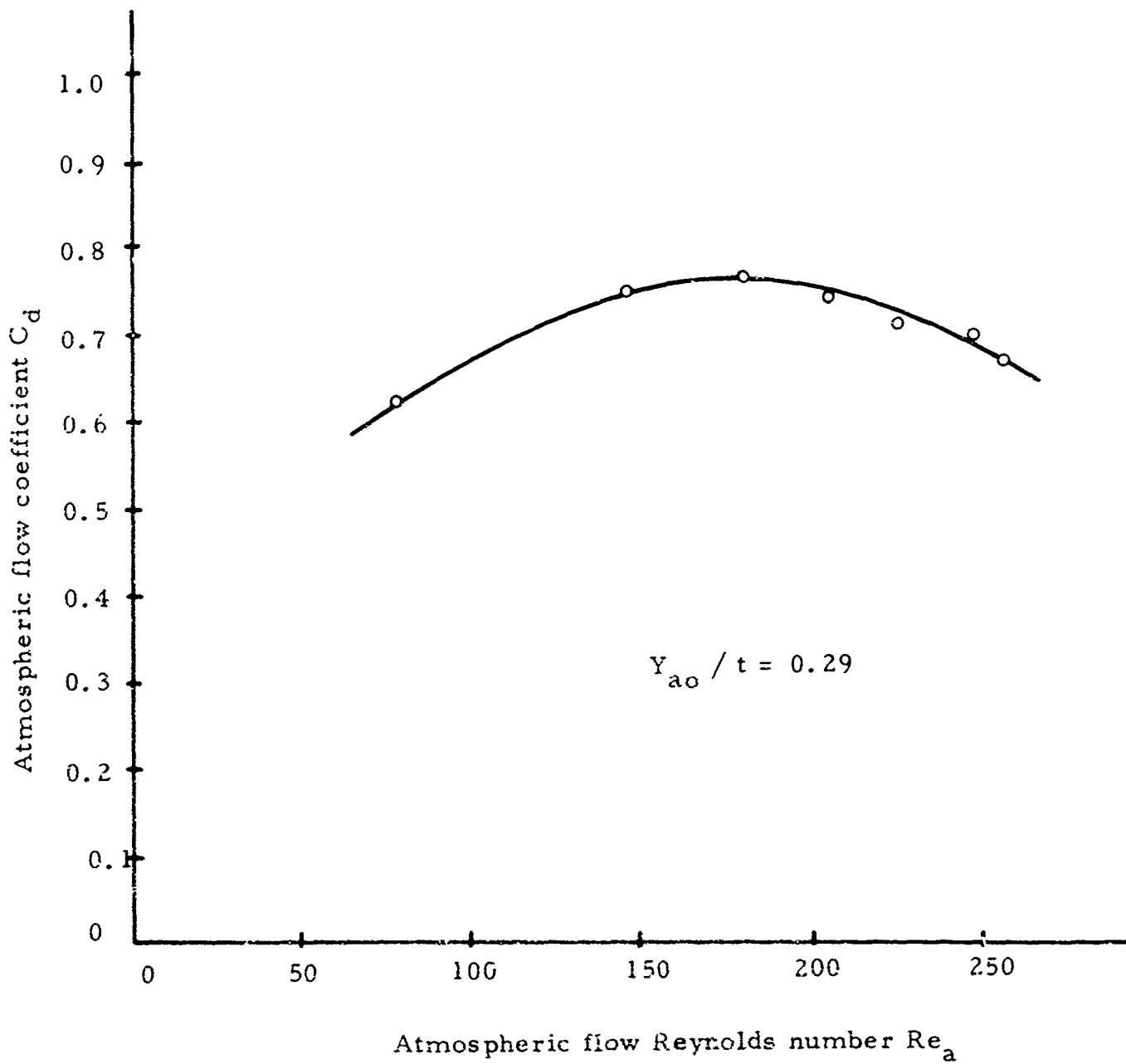


Fig. 62. Atmospheric Flow Coefficient from VanKoevering Data.

1. Determine Y_{ao}/t . Approximating $\bar{P} = w_{co} = 0$, determine Re_a from Eqs. (166) and (161), the control line resistance being known.
2. From experimental data of the type presented in Fig. 62, determine C_d .
3. Solve Eqs. (162) or (163) for the control line resistance, still approximating $\bar{P} = 0$.
4. From Eqs. (158), (160), and (161) solve for w_{co} and \bar{P} .
5. Using these values of w_{co} and \bar{P} determine the new Re_a and corresponding C_d . Solve Eq. (162) or (163) again, etc. until the process converges. Better initial assumptions should lead to faster convergence.

5.3.4. Application of Theory to Stall Sensing Amplifier

For the application at hand, with square-law control line resistance and equal supply and control port pressures, Eq. (162) simplifies to

$$d_o^4 - \frac{0.035 X_o t (b_o Y_{ao} + 2X_o^2)}{C_o \frac{\pi}{4} (b_o Y_{ao} + X_o^2)} d_o^2 - \frac{t^2 [b_o C_d^2 Y_{ao}^3 - (0.035)^2 X_o^4]}{\left(C_o \frac{\pi}{4}\right)^2 (b_o Y_{ao} + X_o^2)} = 0 \quad (168)$$

where d_o and C_o are the control line orifice diameter and flow coefficient, respectively. For control flow Reynold's number

$$R_c = \frac{2vd_o}{v} > 260$$

where v is the average velocity through a sharp-edged orifice, C_o can be assumed constant at about 0.625 (Ref. 42, p. 183). This Reynold's is easily exceeded in the present application.

Brown's graphical source-load matching technique was applied to the load flow curve corresponding to Fig. 62. A value for optimum control line orifice diameter of 0.0319 inch was predicted at an operating point for which the atmospheric flow Reynolds number is determined to be approximately 105. From Fig. 62 this corresponds to a flow coefficient of 0.66. The appropriate dimensions and $d_o = 0.0319$ inch in Eq. (168) give $C_d = 0.566$ in fair agreement. The variation in d_o for these two values of C_d is about 30 per cent.

Using the dimensions of the new test model; $X_o = 0.253$ inch, $b_o = 0.058$ inch, $t = 0.175$ inch, Eq. (168) was solved for d_o in terms of Y_o' ($= Y_o/b_o$). Two positive real roots were always obtained but a consideration of the direction of inequality ruled out the larger (as they indicated that orifices larger than the optimum favor bistability). The results are plotted in Fig. 63 ($AR = \text{Aspect Ratio} = b/t$).

5.4. Experimental Study

5.4.1. Test Apparatus

The test amplifier, shown in Fig. 64, is a modification of several earlier models which presented difficulties due to (1) Control port resonance, (2) Knife-edge reattachment, (3) Pressure asymmetry.

The first problem arises from wave phenomena in the control regions. It is in part due to low frequency standing waves and the effect is best minimized by making the control ports as small as possible. Small control ports also favor dynamic response.

In order to minimize hysteresis, sharp knife edges are employed. This presents a problem due to the formation of a separation pocket downstream of the knife edges (see Fig. 65). A deficiency of flow from the environment into this region can cause the jet to reattach downstream of the edge of the knife resulting in a large increase in hysteresis. Data summarized by Simson (Ref. 39, p. 131) predicted reattachment at larger lateral setbacks (hence small β - see Fig. 65) with the present test model for all but impractical knife-edge lengths. An alternative solution involved placing large holes in the face plates in the region of the separation pockets.

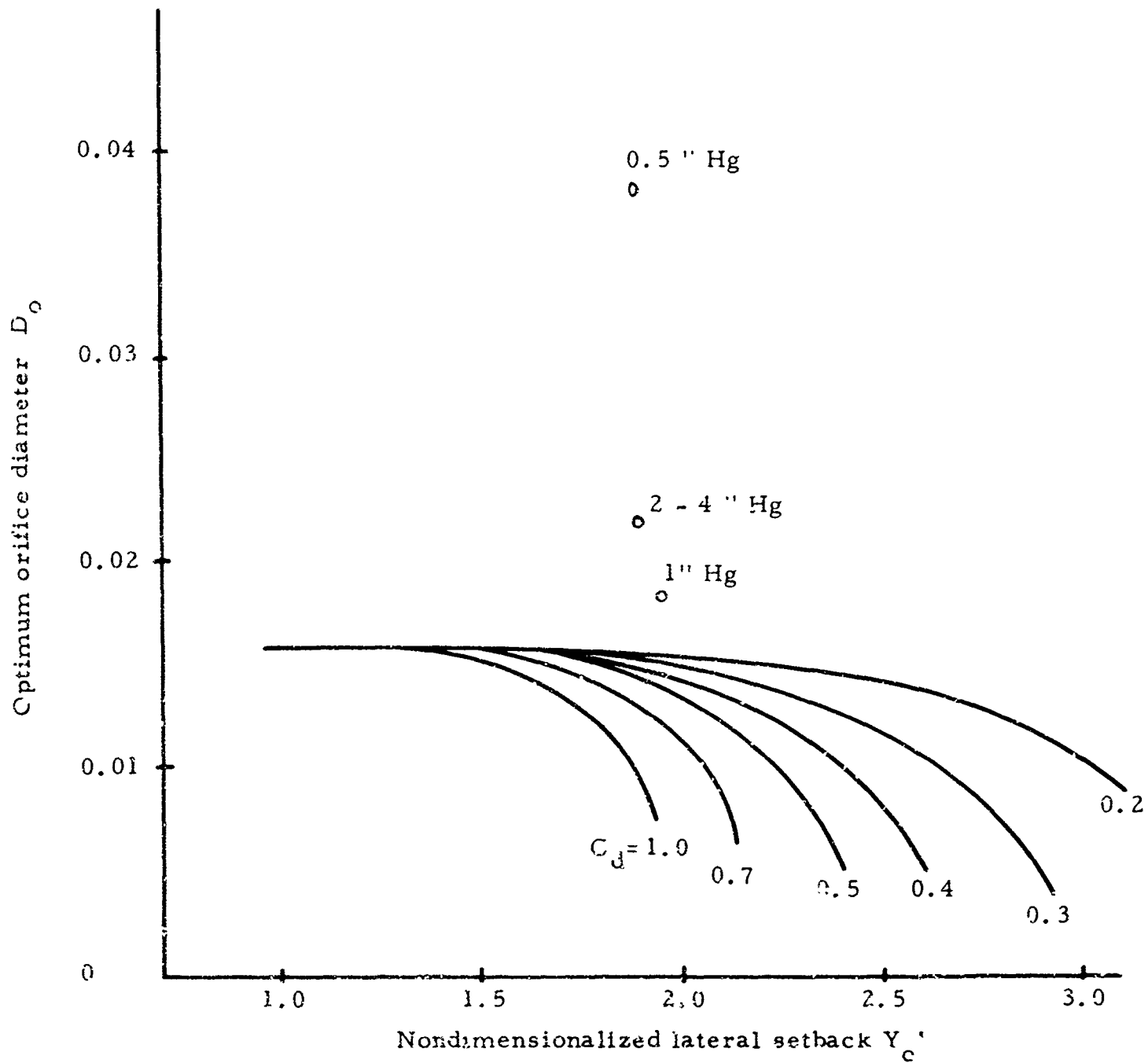


Fig. 63. Solution of Eq. (168) for $X_o' = 4.36$, $AR = 3.02$.

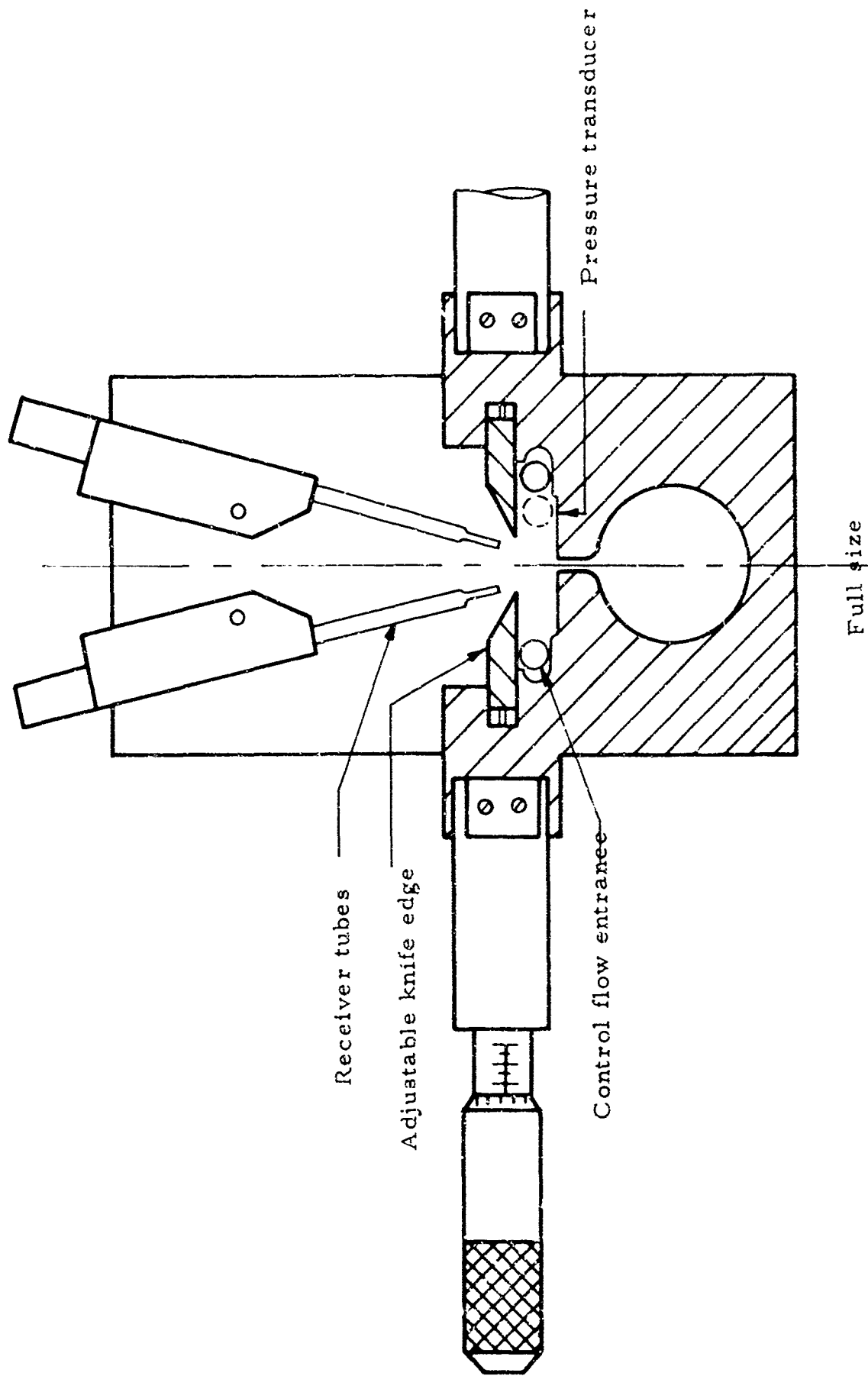


Fig. 64. Test Model With Receiver Tubes Installed.

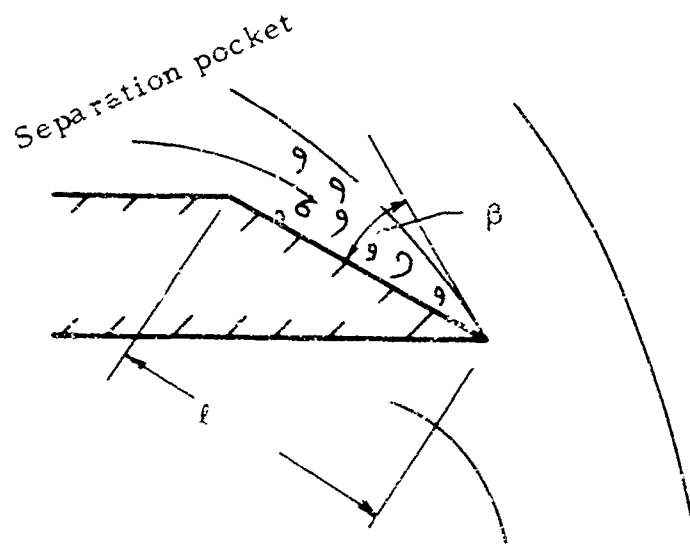


Fig. 65. Separation Pocket Formed With Attached Jet.
 Small β and Large l Favor Reattachment.

The third problem, and the most difficult to cope with, results from small dimensional misalignments and leakage. The extreme sensitivity of setback tolerance on operating characteristics led to a micrometer adjustment permitting easy changes to 0.001 inch accuracy. The problem of leakage was particularly perplexing because the desired free movement of the knife edges prevented adequate sealing.

The dynamic test arrangement (Figs. 66 and 67) is similar to that of the first annual report. To eliminate control line dynamics, the control lines are almost negligibly short, although they were initially long enough to insert piezoelectric pressure transducers. During static testing and while adjusting the signal line supply pressure for dynamic testing, a manometer is added to the signal control line. The test model has dimensions given in Sec. 5.3.4.

5.4.2. Static Test Results

A large amount of experimental data has been taken using the present and earlier test models. Unfortunately, dimensional misalignment and leakage problems limited the quantitative value of most of the results.

The upper instability limit (for $R = \infty$) as given by Eq. (164) is plotted in Fig. 61. Setbacks are nondimensionalized with respect to nozzle width. The results of two test runs at a supply pressure of 3.45 psia[†] and with $X_0' = 3.89$ are shown in Fig. 61. The smallest possible setback used in practice to decrease the hysteresis band of the control, increasing the gains.

From Eq. (168), d_0 is plotted versus Y_0' and C_d in Fig. 63, for the dimensions of the present test model. The experimentally determined optimum orifice diameters for $Y_0' = 2.07$ are plotted. Agreement is fair within the range of validity of the theory (i. e., incompressible flow - $P_g < 2$ in. Hg). Data points further up in the compressible range (6 to 10 in. Hg) are off the graph. A sudden jump between 4 and 5 in Hg was observed.

[†] 3.45 psi is the average stall-free pressure ratio across a single compressor stage as determined in the first annual report.

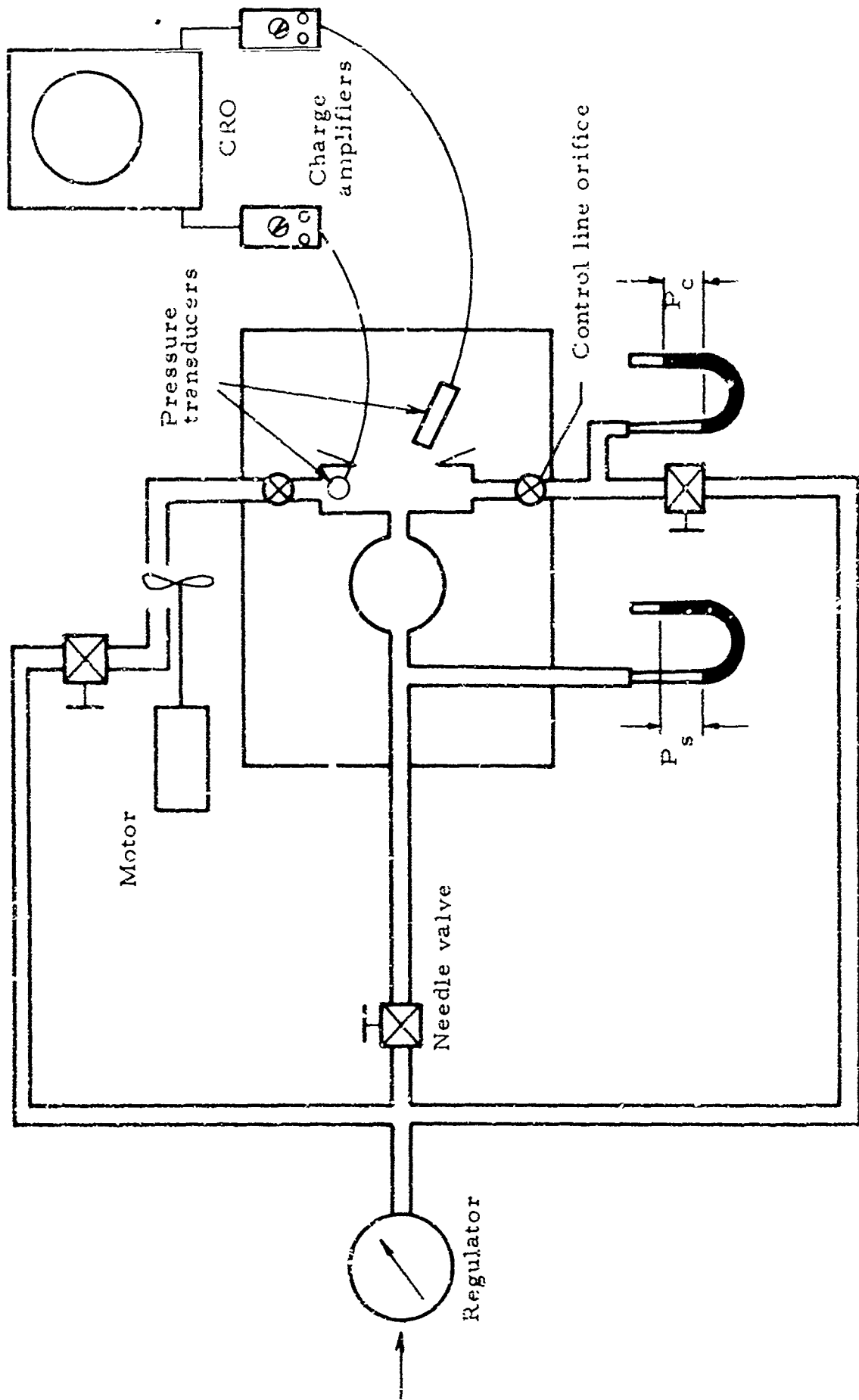


Fig. 66. Schematic of Dynamic Test Set Up.

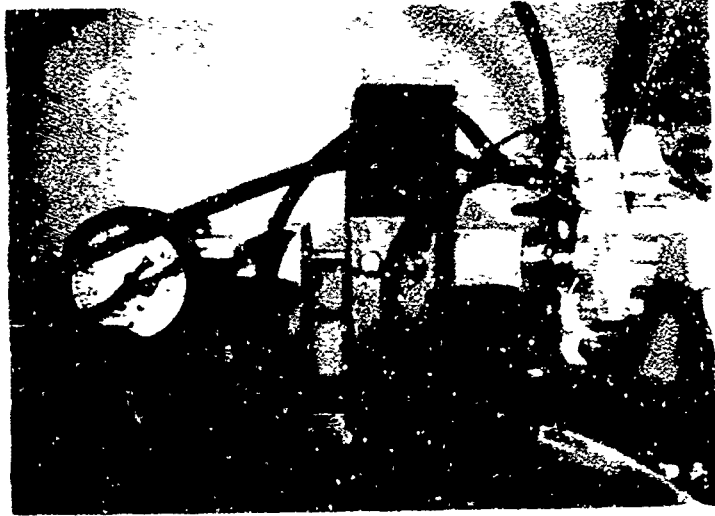


Fig. 67. Dynamic Test Apparatus.

One of the principal objectives of the experimental study was to determine if the hysteresis could be reduced sufficiently to permit bi-stable operation with the available pressure swing ($P_{MAX} - P_{MIN} < 0.1$ psi). This was done successfully and reported in the First Annual Report (see Fig. 21). With the new test model, operation with very small hysteresis was difficult due to control port noise of the same order of magnitude as the hysteresis. The signal (slightly filtered) from a piezoelectric in one control port is shown in Fig. 68. Control port resonance caused random flipping of the jet, the large jump indicating jet movement. The increase in noise is possibly due to the sharp knife edge. Tilting the knives at an angle less than 90° would probably reduce the noise.

Defining Gain as Supply Pressure times Recovery Ratio divided by Hysteresis; with a recovery of 70 per cent, hysteresis within 0.1 psi, supply pressure of 3.4 psi, the gain would be slightly greater than 24.

5.4.3. Dynamic Test Results

A primary purpose of the experimental study was to determine the frequency response characteristics of the amplifier. In Sec. 3.2.1 of the First Annual Report, it was established that the amplifier must have a frequency response better than 400 cps at 5 per cent modulation, corresponding to a rise time of 0.125 millisecond. The test results reported in the first report indicated a maximum frequency response of 260 cps at 37 per cent modulation and only 60 cps at 8 per cent modulation. This corresponds to a rise time of about 1.4 milliseconds. For the nozzle supply pressure of 2.94 (pressure ratio = 1.2) the nozzle flow velocity is 598 ft/sec. Then with the lateral setback = 0.06 inch, the transport time defined as $2X_o/V_n$ is 0.0167 millisecond. Thus the response time is greater than 80 transport times which is much larger than the results of Sec. 2.1.5. in the first report would indicate. The discrepancy was attributed to dynamics associated with the long control line.

In the new test model the control line was virtually eliminated. The control ports however, were larger than before to permit instrumenting each control port with a piezoelectric pressure transducer.

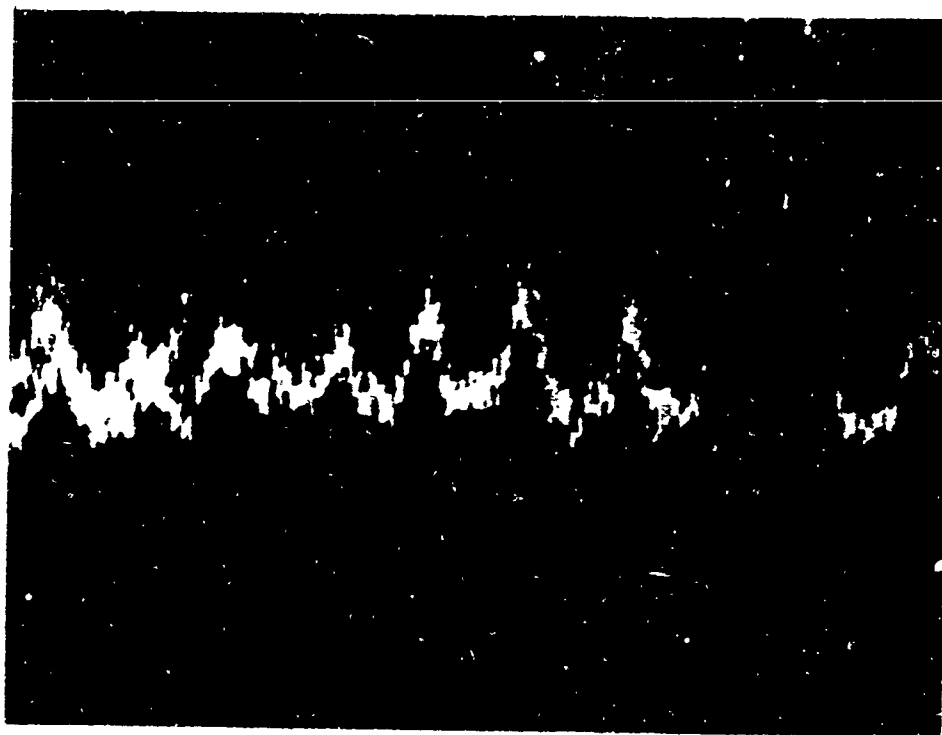


Fig. 68. Random Flipping of Jet Due to Control Port Noise.

The stall cell signals are shown in Fig. 20b of the first report. The means of modulating the input signal did not permit exact simulation of the stall signal, the minimum pressure being lower than in the actual case. The experimental input signal is shown in Fig. 69. The rise time associated with the signal increase should closely simulate the rise time with the actual signal.

Dynamic test results are shown in Fig. 70. The lower trace is from the piezoelectric in the signal control port and the upper trace from a piezoelectric placed downstream of the knife-edge as in the first report. The modulation is approximately 25 per cent.

The asymmetry in the input signal is evident in the lower trace, the rise time in one direction being much greater than in the other. The effect on the upper trace is to lengthen the output pulse width. At 455 cps, the control port transducer indicates sharp response to the larger decreasing pressure signal.

5.5. Conclusions

Experimental data enabling an assessment of the theoretical stability criteria is incomplete. To avoid the dimensional asymmetry and leakage problems a large scale test model should be constructed. With such a model these extraneous effects would have less consequence.

The dynamic test results demonstrate the strong dependence of response on pressure swing. A reduction in size of the control ports could increase the response significantly. With the larger pressure swing it appears that the response is adequate. By staging amplifiers, using proportional devices in all but the last stage, the stall cell signal could be amplified to the necessary pressure swing.

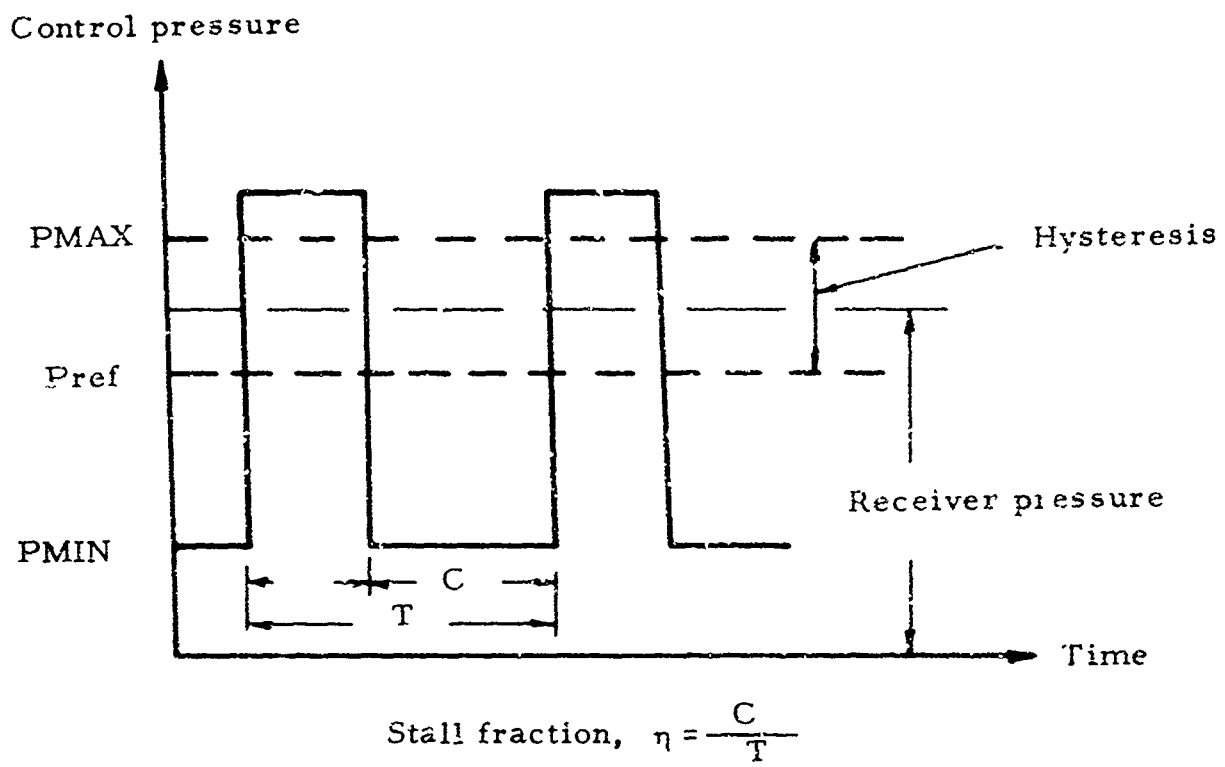
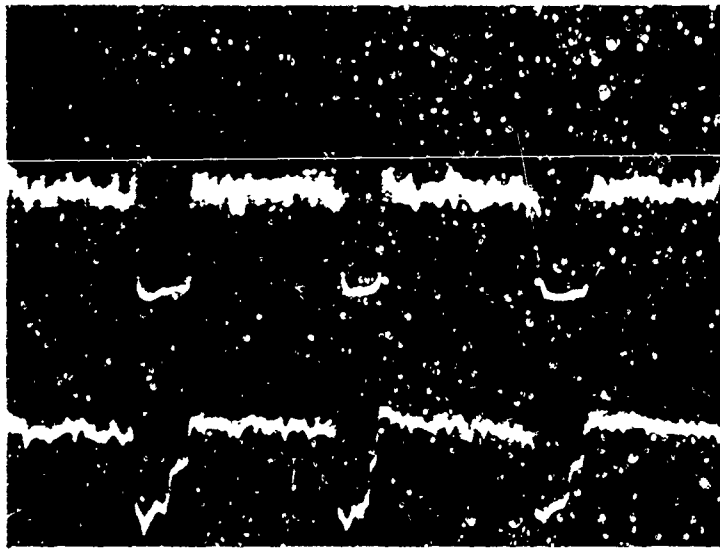
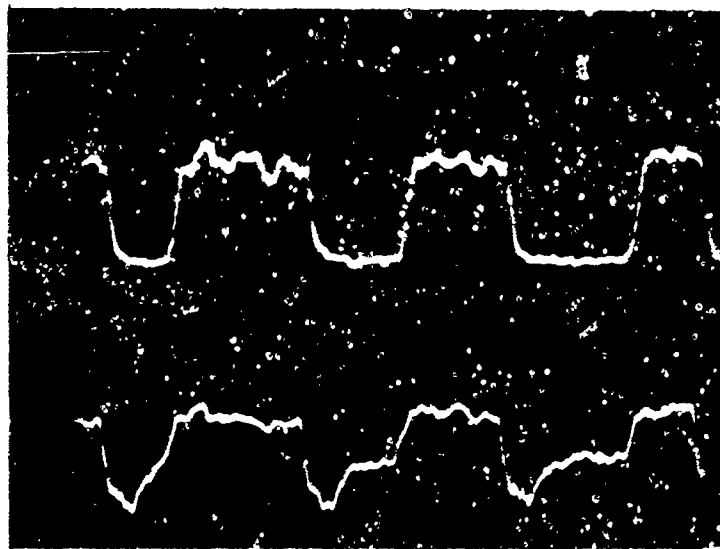


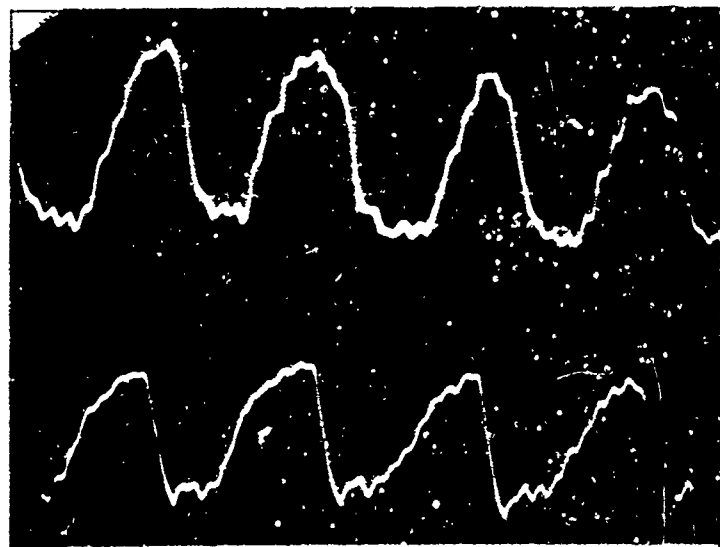
Fig. 69. Pulse-Width-Modulator Input Signal.



18.5 cps



60.6 cps



455 cps

Fig. 70. Dynamic Test Results with 25 per cent Modulation.

6. DESIGN OF A TEMPERATURE-INSENSITIVE PNEUMATIC OSCILLATOR

6.1. Introduction

A constant-frequency pneumatic oscillator is a necessary element in pneumatic logic systems and could form part of the basis of temperature-measuring and speed-measuring devices. The frequency of a really useful oscillator should be insensitive to the temperature and pressure of the fluid. The objective of this report has been the development of a fixed-frequency pneumatic oscillator which requires no temperature control and only the pressure control of a common regulator.

A very simple oscillator consists of a pneumatic jet amplifier with transmission lines connected to its control ports in such a way as to cause a dynamic instability. See Fig. 71. Since the velocity of sound varies as the square root of the absolute temperature, the lengths of the transmission lines would have to be automatically adjusted over a large range, and the adjustment would have to be very precise. The lengths would also have to be adjusted for pressure changes, since the entrainment of flow and the velocity of the jet significantly affect the frequency of oscillation.

Another oscillator is one in which a linear mechanical spring-mass system (essentially a tuning fork) controls the frequency. Since the damping is small, the frequency is limited to the vicinity of the natural frequency of the spring-mass system; compensation for changes in pressure and temperature are smaller and need not be so precise. For this reason, only oscillators controlled by spring-mass systems have been considered, although an oscillator with a pneumatic resonator might be satisfactory for some purposes.

To meet the requirement of pressure insensitivity, the goal has been driving pressure forces which are as nearly as possible in phase with the velocity of the mass so that they subtract from the damping forces but neither add to nor subtract from the spring forces. Then the phasing of the pressure forces would be independent of both temperature and pressure except to the extent that the modulus of elasticity of the spring and the dimensions of the vibrating system vary with temperature. The amplitude

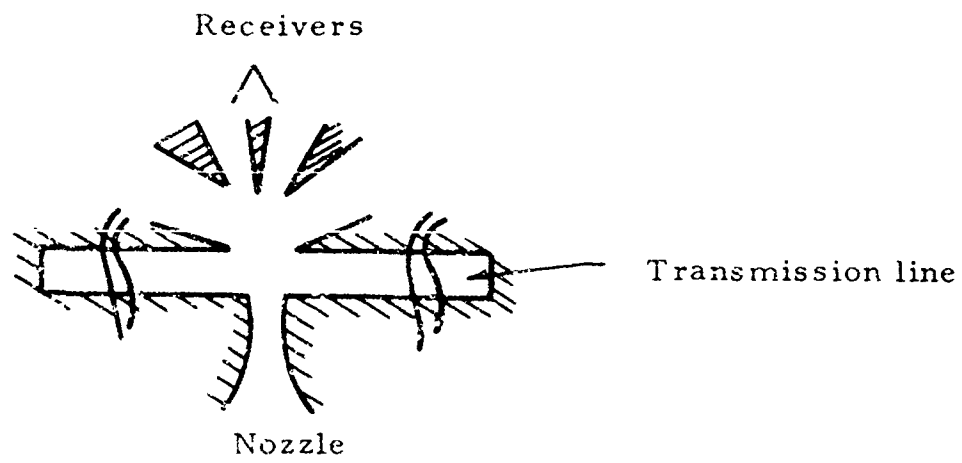


Fig. 71. Jet Amplifier-Oscillator.

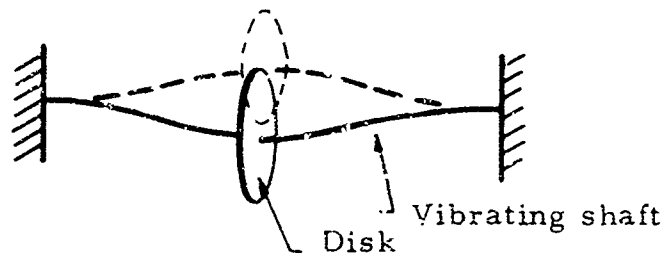


Fig. 72. Vibrating Shaft and Disk.

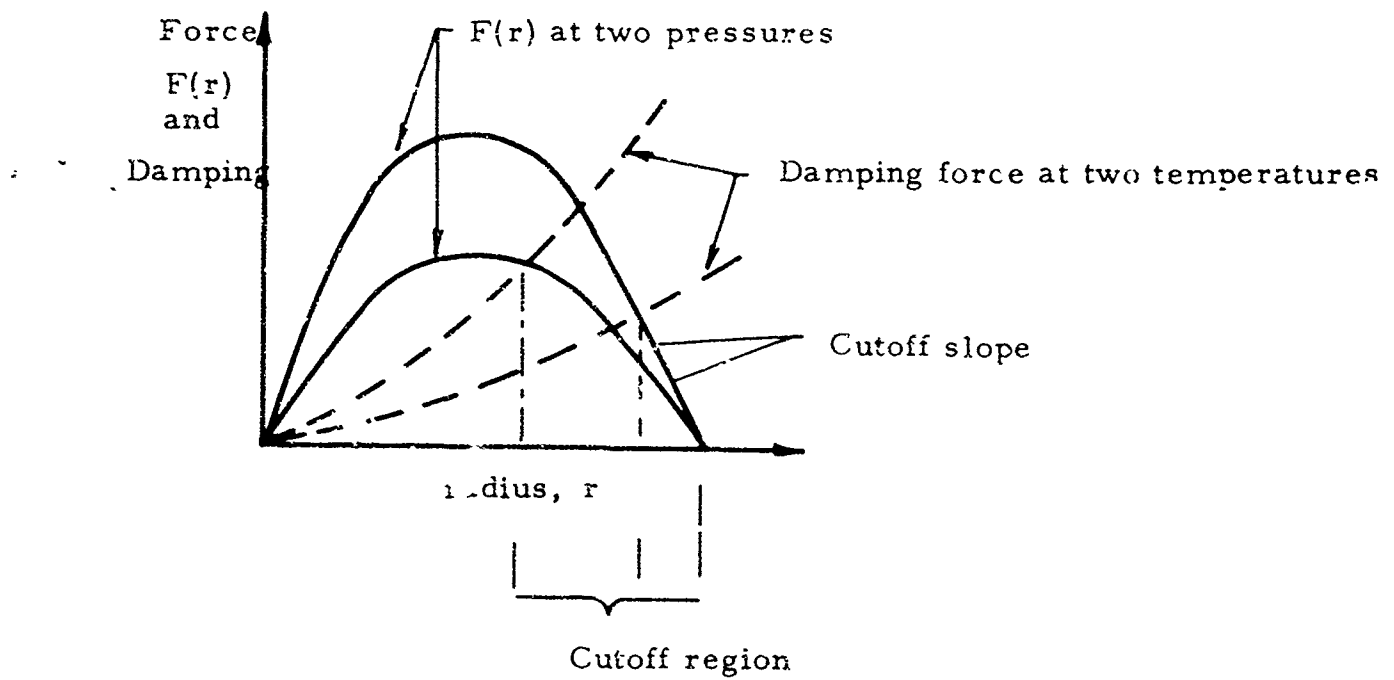


Fig. 73. A Suggested Driving-Force Versus Radius Curve.

of motion would change with pressure, however, requiring some non-critical control to increase the range of pressures over which the device would operate usefully.

6.2. Circular-Motion Oscillator

A disk on a shaft of negligible mass can be made to vibrate (without rotation) in a circular path. This motion can be considered as the superposition of two mutually perpendicular lateral vibrations with equal amplitudes and a ninety degree phase difference. See Fig. 72.

From steady-state circular motion, the conditions for equilibrium are

$$mr\omega^2 = kr + G \quad (169)$$

in radial direction

$$Br\omega = F \quad (170)$$

in the tangential direction where

m = mass of the disk

ω = the angular frequency of vibration

r = the displacement from the center position

k = the lateral stiffness of the shaft

G and F = forcing functions

Notice that if $G = 0$, then $\omega = \sqrt{k/m}$. F might be a function of r , $F(r)$. Thus, if a configuration can be found which will provide a driving force which is perpendicular to the displacement at all points of the cycle and of constant magnitude for any given amplitude, then the frequency of oscillation will be the undamped natural frequency of the disk-shaft system. $F(r)$ might be a function of pressure and temperature, but only the amplitude of oscillation is affected by changes in pressure and temperature.

The relationship $F(r)$ might have a sharp cutoff at a certain amplitude, r , as shown in Fig. 73. The equilibrium amplitude is determined by the intersection of the damping force and the $F(r)$ curves.

6.3. Problems Affecting the Configuration

Two problems greatly affect the configuration and limit the usefulness of the circular motion oscillator. One is the minimization of the radial flow and pressure forces which affect the effective spring constant. This will be discussed in detail later.

The second problem is that of the stability of the circular-motion equilibrium. It may be desirable to substitute for the ideal $F(r)$ another $F(r, \theta)$, where θ is the angle or $\int \omega dt$. For example, in the shaded portion of Fig. 74a, $F(r, \theta)$ might be zero. Now the intersection of the damping force and the driving force curves has no meaning except in a qualitative way, and equilibrium motion is not strictly harmonic, although perhaps very nearly so.

Assuming harmonic motion, it can be seen that the circular equilibrium motion might be unstable. A slight increase in the amplitude in the X-direction would, because of the slope of the $F(r, \theta)$ curve, result in a decrease in the Y direction driving force and, consequently, the Y-direction amplitude. By similar argument the X-direction amplitude would increase some more, and the final steady-state motion would be elliptical.

For certain applications, an elliptical motion would be acceptable, but more often, circular motion is desired. If the number of regions of positive driving force (shaded areas in Fig. 74b) is increased, then $F(r, \theta)$ approaches an ideal, continuous $F(r)$. For this case, a more careful analysis is required to determine the stability of the circular motion. Such an analysis was motivated by initial experimental observations of sharply elliptical rather than the desired circular motion.

6.4. Stability Analysis for Continuous $F(r)$.

In this analysis the motion of the end support is taken into account. It is assumed that the movable end support of Fig. 75 moves up and down without sidewise or rotational motion and that its motion is directly proportional to the motion of the vibrating disk. (We assume that the wire is stiff axially). The result is that the effective mass, spring, and damping constants for vibration in the radial direction are different, generally, from those for vibration in the tangential direction. (For purely circular motion of the disk, the end support does not move at all).

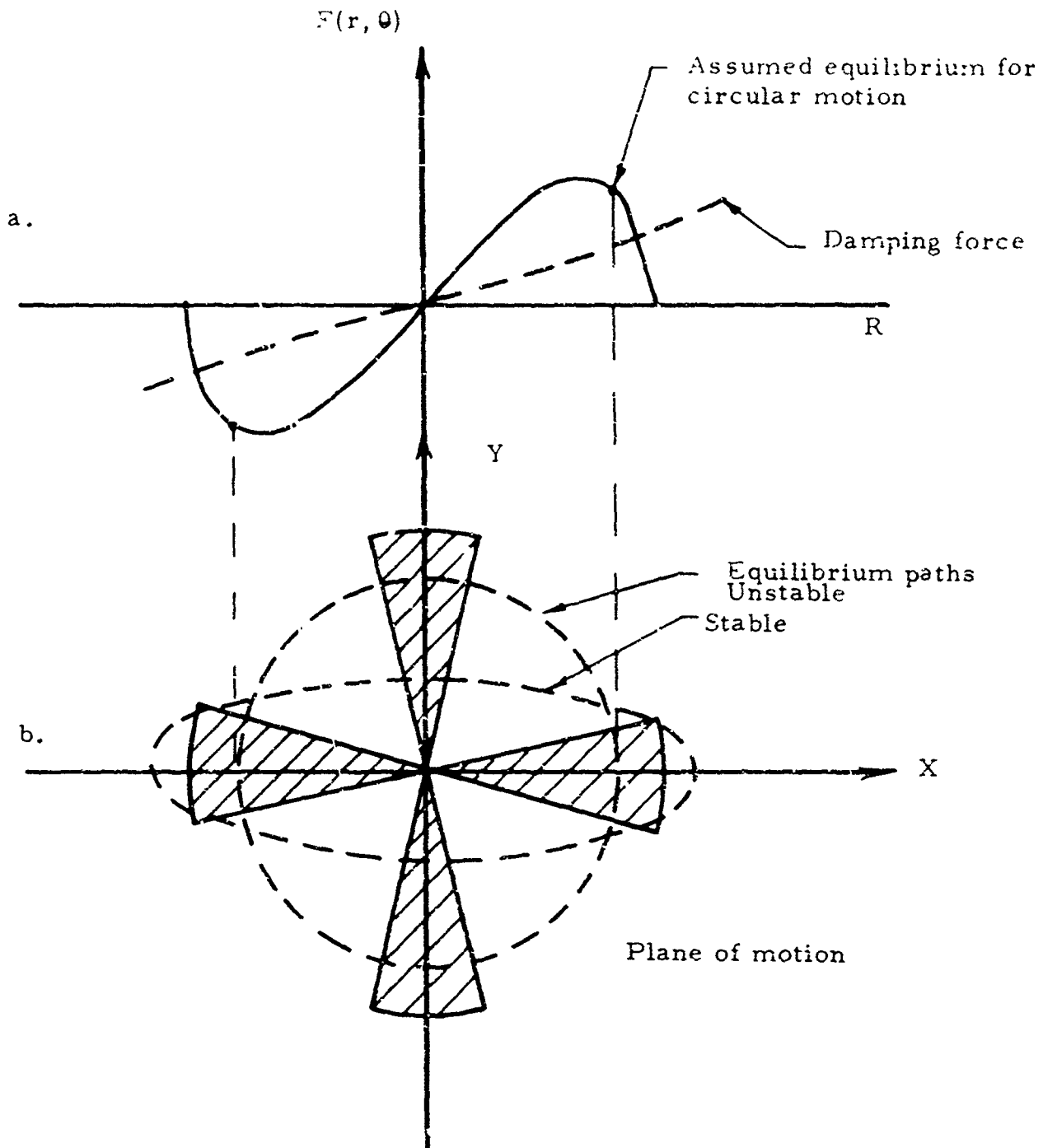


Fig.74. Stability of an Oscillator with a Discontinuous Driving Force.

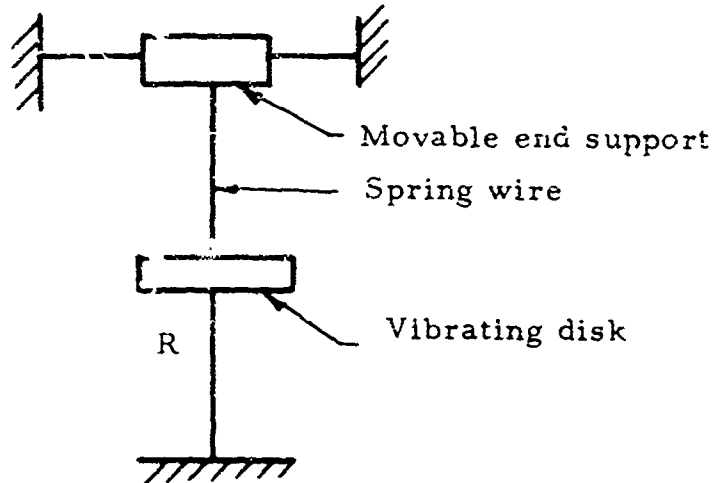


Fig. 75. General Oscillator Configuration for the Stability Analysis.

The kinematic equations are:

$$\text{Displacement} = r \bar{u}_r \quad (171)$$

$$\text{Velocity} = \dot{r} \bar{u}_r + r \dot{\theta} \bar{u}_\theta \quad (172)$$

$$\text{Acceleration} = \left[\ddot{r} - r \dot{\theta}^2 \right] \bar{u}_r + \left[2\dot{r}\dot{\theta} + r \ddot{\theta} \right] \bar{u}_\theta \quad (173)$$

where \bar{u}_r is a unit radial vector, \bar{u}_θ is a unit tangential vector, and r and θ are polar coordinates in the system whose center is the neutral position of the disk.

Next, using only the radial acceleration, velocity and displacement and assuming linear damping, the dynamic equation for the radial direction is written.

$$m_r \left[\ddot{r} - r \dot{\theta}^2 \right] + B_r \dot{r} + K_r r = 0 \quad (174)$$

where r -subscripts refer to the radial direction.

Let

$$\omega_r^2 \equiv \frac{K_r}{m_r} ; \quad 2\zeta_r \omega_r \equiv \frac{B_r}{m_r} ; \quad (175)$$

then

$$(\ddot{r} - r \dot{\theta}^2) + 2\zeta_r \omega_r \dot{r} + \omega_r^2 r = 0 \quad (176)$$

The dynamic equation for the tangential direction is

$$m_\theta \left[r \ddot{\theta} + 2\dot{r}\dot{\theta} \right] + B_\theta r \dot{\theta} - F(r) = 0 \quad (177)$$

where θ -subscripts refer to the tangential direction.

Define

$$\omega_\theta^2 \equiv \frac{K_\theta}{m_\theta} , \quad 2\zeta_\theta \omega_\theta \equiv \frac{B_\theta}{m_\theta} , \quad \text{and } f(r) = \frac{F(r)}{m_\theta} \quad (178)$$

where $F(r)$ is the continuous driving force;
then

$$(r\ddot{\theta} + 2\dot{r}\dot{\theta}) + 2\zeta_r \omega_r \dot{\theta} - f(r) = 0. \quad (179)$$

In analyzing the stability of circular motion, we can linearize equations (176) and (177) and investigate the effect of a small departure from equilibrium. Equation (176) becomes

$$\Delta\dot{r} - 2r\dot{\theta}\Delta\dot{\theta} - \dot{\theta}^2 \Delta r + 2\zeta_r \omega_r \Delta\dot{r} + \omega_r^2 \Delta r = 0 \quad (180)$$

Now

$$\Delta f(r) = \frac{df}{dr} \Delta r = f' \Delta r, \quad (181)$$

so Eq. (179) becomes

$$\ddot{\theta} \Delta r + r\ddot{\Delta\theta} + 2\dot{r}\Delta\dot{\theta} + 2\dot{\theta}\Delta\dot{r} + 2\zeta_r \omega_r \dot{\theta} \Delta r + 2\zeta_r \omega_r r\Delta\dot{\theta} - f' \Delta r = 0 \quad (182)$$

For the equilibrium condition under investigation,

r is constant

$$\begin{aligned} \dot{r} &= \ddot{r} = 0 \\ \dot{\theta} &= \omega_\theta \\ \ddot{\theta} &= 0 \end{aligned} \quad (183)$$

so that Eqs. (180) and (182) become

$$\Delta\dot{r} + 2\zeta_r \omega_r \Delta\dot{r} + (\omega_r^2 - \omega_\theta^2) \Delta r - 2r\omega_\theta \Delta\dot{\theta} = 0 \quad (184)$$

$$r\Delta\ddot{\theta} + 2\omega_\theta \Delta\dot{r} + 2\zeta_r \omega_r \omega_\theta \Delta r + 2\zeta_r \omega_r r\Delta\dot{\theta} - f' \Delta r = 0 \quad (185)$$

When the Eqs. (184) and (185) are combined and the $\Delta\theta$ terms eliminated (one differentiation involved), the result is

$$\Delta\ddot{r} + 2\omega_r(\zeta_r + \zeta_\theta)\Delta\dot{r} + \left[\omega_r^2(1 + 4\zeta_r\zeta_\theta) + 3\omega_\theta^2 \right] \Delta\dot{r} + \left[2\zeta_\theta\omega_r(\omega_r^2 + \omega_\theta^2) - 2\omega_\theta f' \right] \Delta r = 0 \quad (186)$$

The stability of several situations might be investigated. The simplest one is that for which

$$\omega_r = \omega_\theta, \quad \zeta_r = \zeta_\theta \quad (187)$$

(end supports rigid, supporting wire stretchable) and

$$\zeta_r \zeta_\theta \ll 1 \quad (188)$$

(a very reasonable assumption in any case of interest here). We now get

$$(D^3 + 4\zeta_\theta\omega_\theta D^2 + 4\omega_\theta^2 D + 4\zeta\omega_\theta) \Delta r = 2\omega_\theta f' \Delta r \quad (189)$$

where

$$D \equiv \frac{d}{dr} \quad (190)$$

Figure 76 is a polar plot of the left-hand side of Eq. (189) with D replaced by $j\omega$. The Nyquist stability criterion for this inverse Nyquist plot requires, for a stable circular motion, that $2\omega_\theta f'$ have a value of the real axis within the curve; for stability,

$$-6\zeta_\theta\omega_\theta^2 < f' < 2\zeta\omega_\theta^2 \quad (191)$$

This result is expressed graphically in Fig. 77. The lower limit for the cutoff slope, $-6\zeta_\theta\omega_\theta^2$, is the one of interest. Physically, an instability

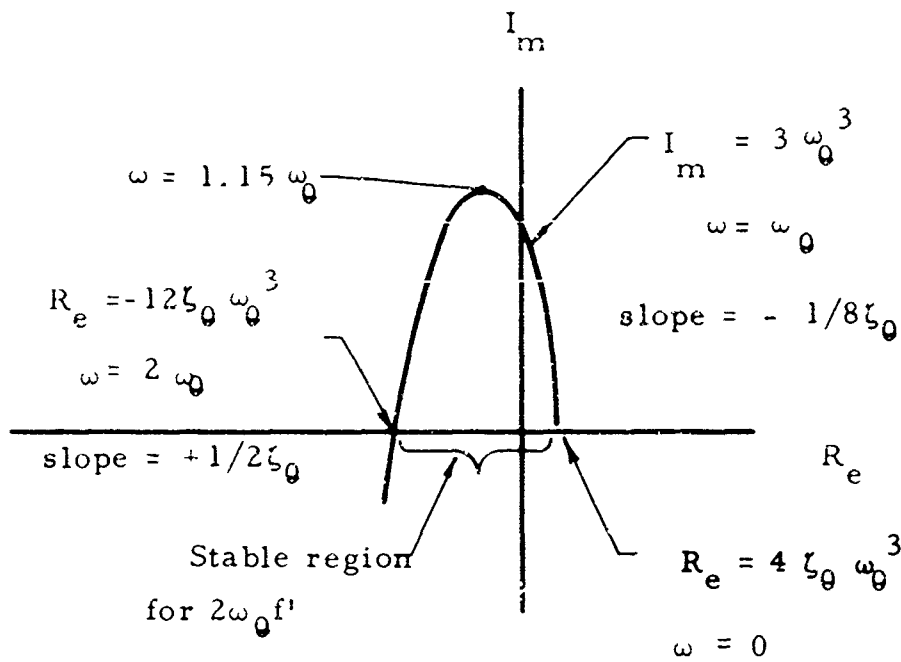


Fig. 76. Inverse Nyquist Plot for System Without Lead or Lag.

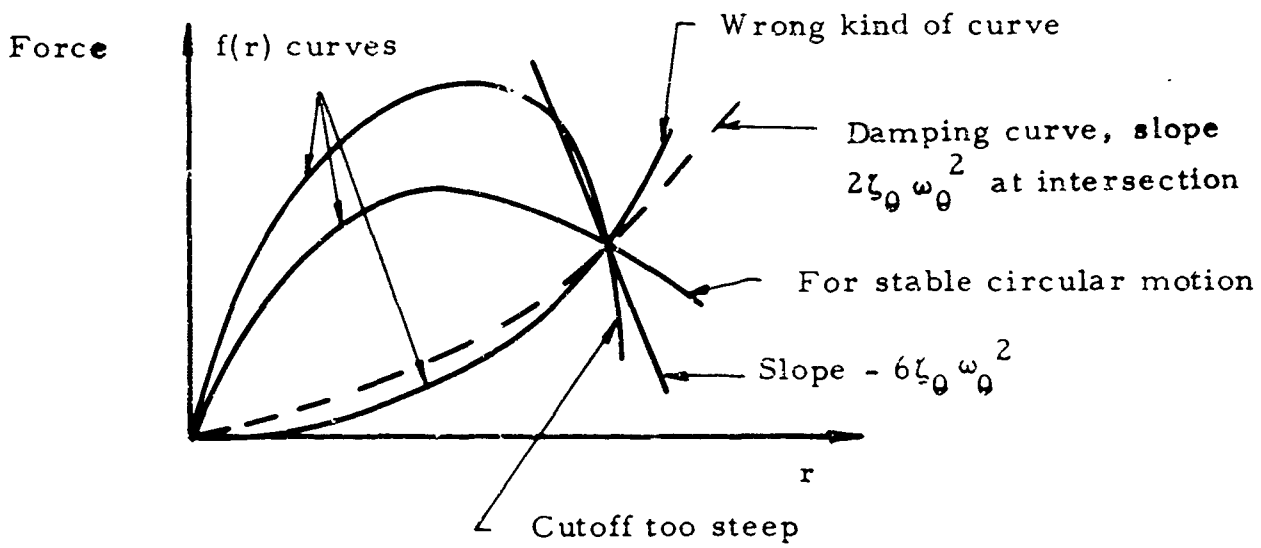


Fig. 77. Interpretation of Stability Analysis.

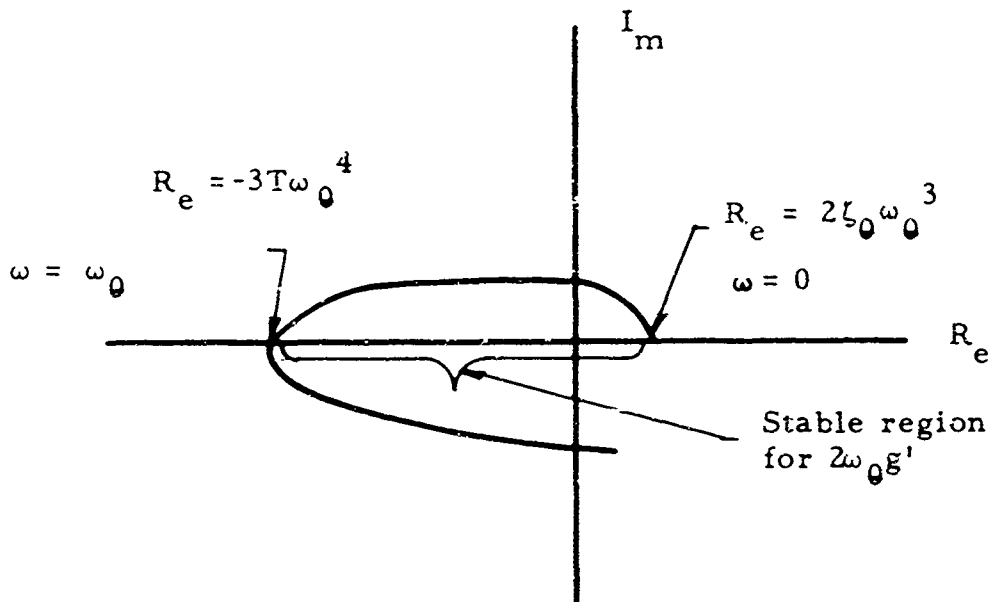


Fig. 78. Inverse Nyquist Plot for System With Lag.

at this slope is not very spectacular; the path of motion merely begins to become elliptical. Note, from the polar plot, that the frequency for oscillations of Δr about the equilibrium radius is $2\omega_0$.

The range of permissible cutoff slopes can be increased by introducing a lag into the driving function. At the operating radius, we use

$$\frac{\Delta f}{\Delta r} = \frac{g'}{(TD + 1)} \quad (192)$$

to replace the f' previously used. Physically, this means that changes in the driving force are related to changes in the radius at an earlier time, i.e., at an earlier angle, θ , in the motion. If the lag angle is almost ninety degrees, then an increase on the amplitude in, say, the X-direction will result in a decrease in the driving force in the same (X) direction, but ninety degrees later.

To find the effect of this lag upon the stability, the left-hand side of Eq. (189) and the polar plot of Fig. 74 are multiplied by $(jT\omega + 1)$. If $T\omega \gg 1$ at $\omega = \omega_0$, the $\omega = \omega_0$ point will be rotated counterclockwise almost ninety degrees, and the magnitude at $\omega = \omega_0$ will be multiplied by $T\omega_0$. The new polar plot is shown in Fig. 78. We find that, for stability,

$$-\frac{3}{2} T \omega_0^3 < g' < 2\zeta_0 \omega_0^2 \quad (193)$$

and

$$\frac{g'_{\min}}{f'_{\min}} = \frac{-\frac{3}{2} T \omega_0^3}{-6\zeta_0 \omega_0^2} = \frac{T \omega_0}{4\zeta_0} \quad (194)$$

where

$$T \omega_0 \gg 1 \quad \text{and} \quad \zeta_0 \ll 1, \text{ probably.} \quad (195)$$

Of course,

$$\frac{g'_{\max}}{f'_{\max}} = 1. \quad (196)$$

The optimum lag is actually slightly less than ninety degrees and rotates the point of maximum amplitude at $\omega = 1.15\omega_0$ to the negative real axis. If the g' cutoff slope is too steep, the resulting "instability" has an oscillation frequency $\omega \approx \omega_0$. This means that the motion is not elliptical but epicyclic.

Although the use of the lag provides for a much steeper allowable cutoff slope and consequently a greater pressure range for satisfactory operation, its use increases the complexity of the oscillator. For this reason, the oscillators built and tested all lacked the lag.

A lead could also be used and would be even more successful than a lag, although it would make a still more complex system. In this case

$$\frac{\Delta f}{\Delta r} = h' (TD + 1) \quad (197)$$

would be used to replace f' in Eq. (89). The polar plot would be divided by $(jT\omega + 1)$. The result (See Fig. 79) would be a stable system for all cutoff slopes and all pressures.

A physical interpretation of these results is now given with the aid of Fig. 80, which shows a hypothetical disk motion in which r_a is large. The simplest system senses the error in r_a and corrects r_b by correcting F_a . If r_b is reduced, r_c in turn becomes elongated, r_c reduced, and the motion becomes elliptical. The system with a ninety degree lag corrects r_c . If r_c is reduced, r_a is consequently increased more, and the motion becomes eccentric. In the system with a lead, r_a itself, rather than its innocent complements, is corrected.

Now suppose that $\omega_0 \neq \omega_r$, but that $\zeta_0 \approx \zeta_r$. Assume a system like that of Fig. 81. If the amplitude of radial vibration of the disk is δ , then the amplitude of vertical vibration of the top support is approximately δ^2/L . The effective mass of the support as seen at the disk is

$$\frac{\delta^2}{L} M = \frac{\delta}{L} M, \quad (198)$$

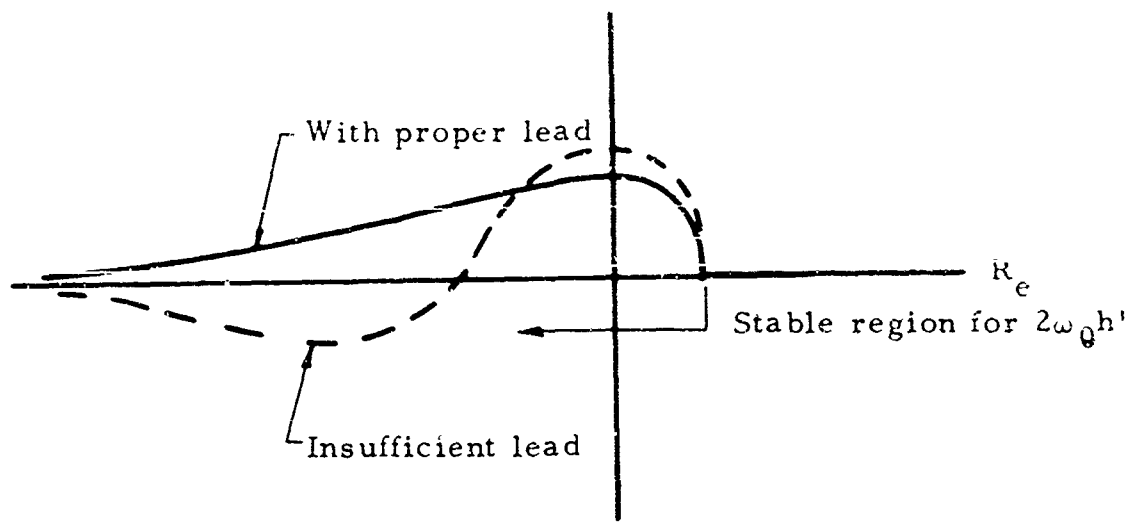


Fig. 79. Inverse Nyquist Plot for System with Load.

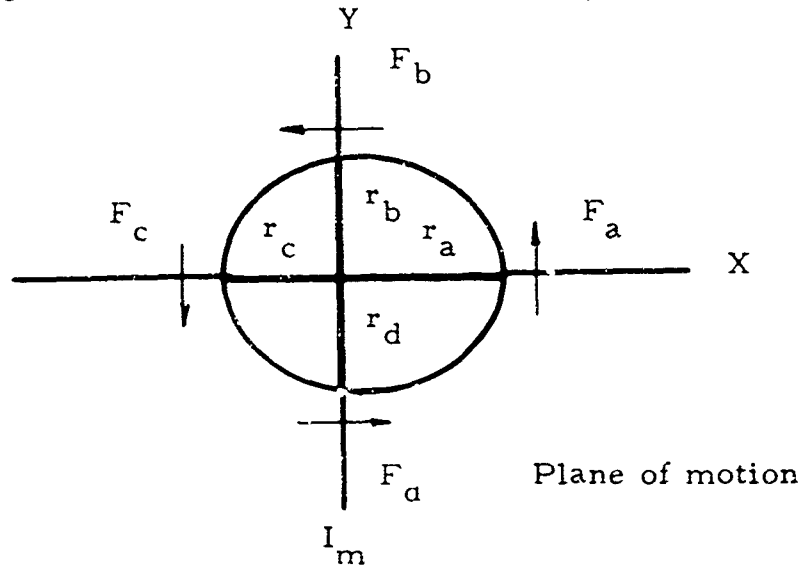


Fig. 80. Hypothetical Disk Motion.

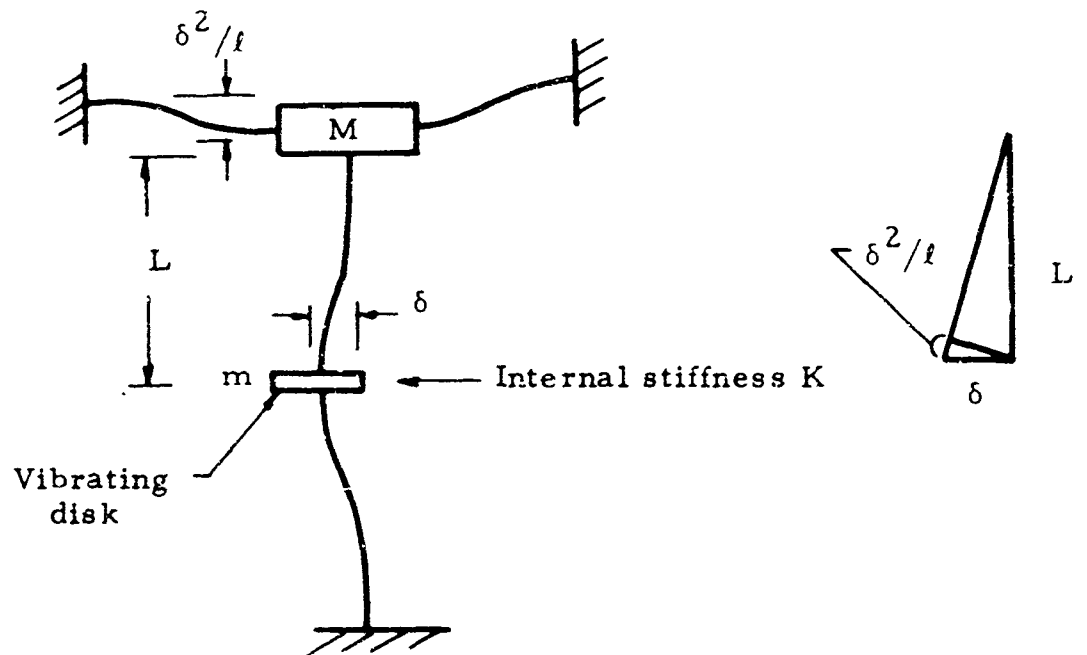


Fig. 81. Notation for Analysis of Oscillator with Movable End Support.

and the natural radial frequency is

$$\omega_r = \sqrt{\frac{K}{m + \frac{\delta}{L} M}} \quad (199)$$

If the disk is vibrating in a circular path, the top support will not move at all, so the tangential natural frequency is

$$\omega_\theta = \sqrt{\frac{K}{m}} \quad (200)$$

Routh's stability criterion applied to Eq. (175) yields, for the lower limit of stability,

$$f' = \frac{\omega_r}{\omega_\theta} \zeta_\theta (\omega_r^2 + \omega_\theta^2) - \frac{\omega_r}{\omega_\theta} (\zeta_r + \zeta_\theta) \left[\omega_r^2 (1 + 4\zeta_r \zeta_\theta) + 3\omega_\theta^2 \right] \quad (201)$$

Assuming $\zeta_r \zeta_\theta \ll 1$, this becomes

$$f' = \frac{\omega_r}{\omega_\theta} (-\zeta_r \omega_r^2 - 3\zeta_r \omega_\theta^2 - 2\zeta_\theta \omega_\theta^2) \quad (202)$$

Now, with hindsight not yet available to the reader, we assume that $\delta/L = 0.02$ and $M = 20m$. As a result, $\omega_r = \omega_\theta/1.4$.

An application of Routh's criterion, Eq. (202), shows that for stability, the steepest allowable cutoff slope is $-3.94\zeta_\theta \omega_\theta^2$ compared to $6\zeta_\theta \omega_\theta^2$ for rigid end supports and stretchable spring wires, or, equivalently, zero support mass. This indicates that it is necessary to minimize the movable support mass.

Extra damping might be given the vertical motion of the support. If we assume that $\zeta_r = 10\zeta_\theta$, Eq. (202) shows that $f'_{\min} = -26.5\zeta_\theta \omega_\theta^2$. The additional damping seems to be desirable.

6.5. Temperature Compensation

The frequency of the ideal circular-motion oscillator is not affected by changes in the physical properties of the gas flowing through it. Changes in temperature will, however, change in the size and the stiffness of the mechanical parts.

Changes in stiffness dominate changes in size. According to simple beam theory, the lateral stiffness, K of a shaft is proportional to EI/L^3 where I is the second area moment of the cross-section, E is the modulus of elasticity in tension, and L is the length. I is proportional to L^4 at all temperatures, so K is proportional to EI . Figure 82 (Ref. 43) shows the variation in E with temperature for some steels. Along the linear portion of the curves,

$$\frac{\Delta E}{E\Delta T} = - \frac{2.13 \times 10^{-4}}{^{\circ}\text{F}} \quad (203)$$

From any materials handbook, a typical value for the coefficient of linear expansion of steel is

$$\frac{\Delta L}{L\Delta T} = \frac{6.7 \times 10^{-6}}{^{\circ}\text{F}} \quad (204)$$

For purposes of analysis, the change in size will be neglected. Fine adjustment of an actual oscillator can overcome this neglect.

Now we have

$$\frac{\Delta K}{K\Delta T} = \frac{\Delta E}{E\Delta T} \approx \frac{2 \times 10^{-4}}{^{\circ}\text{F}} \quad (205)$$

If $\Delta T = 1000^{\circ}\text{F}$, then $\Delta K/K \approx 20$ per cent. This number will be kept in mind henceforth. Notice that linearity is here assumed.

Of several possible mechanisms investigated for temperature compensation, the only one that seems really satisfactory for such a large-scale compensation is the varying of the axial compression or

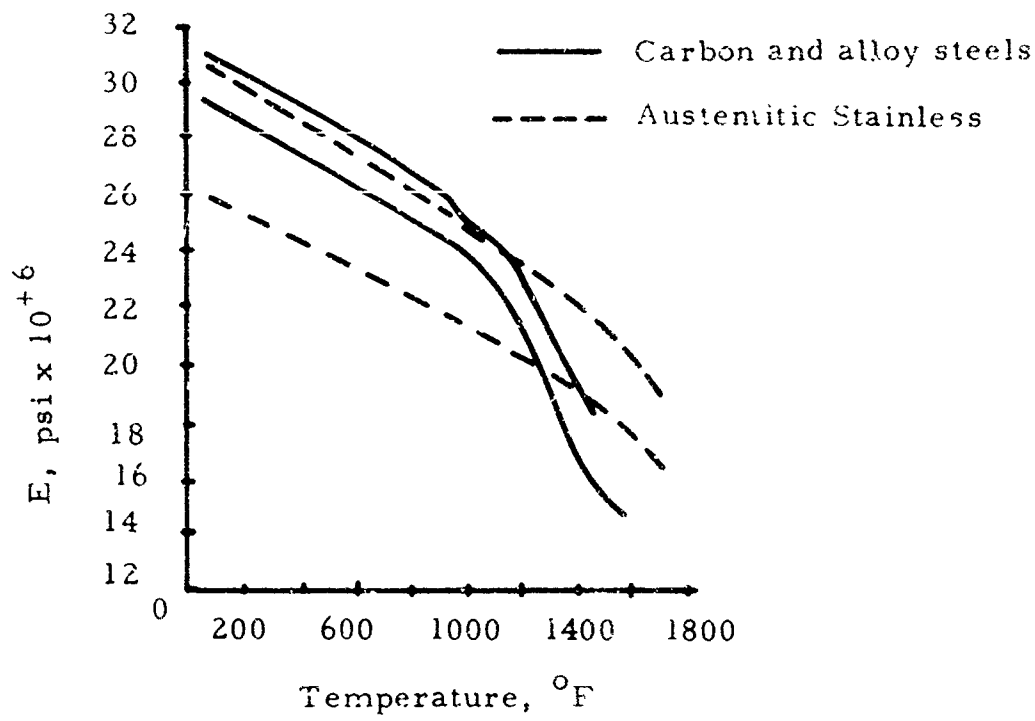


Fig. 82. Variation of Modulus of Elasticity with Temperature.

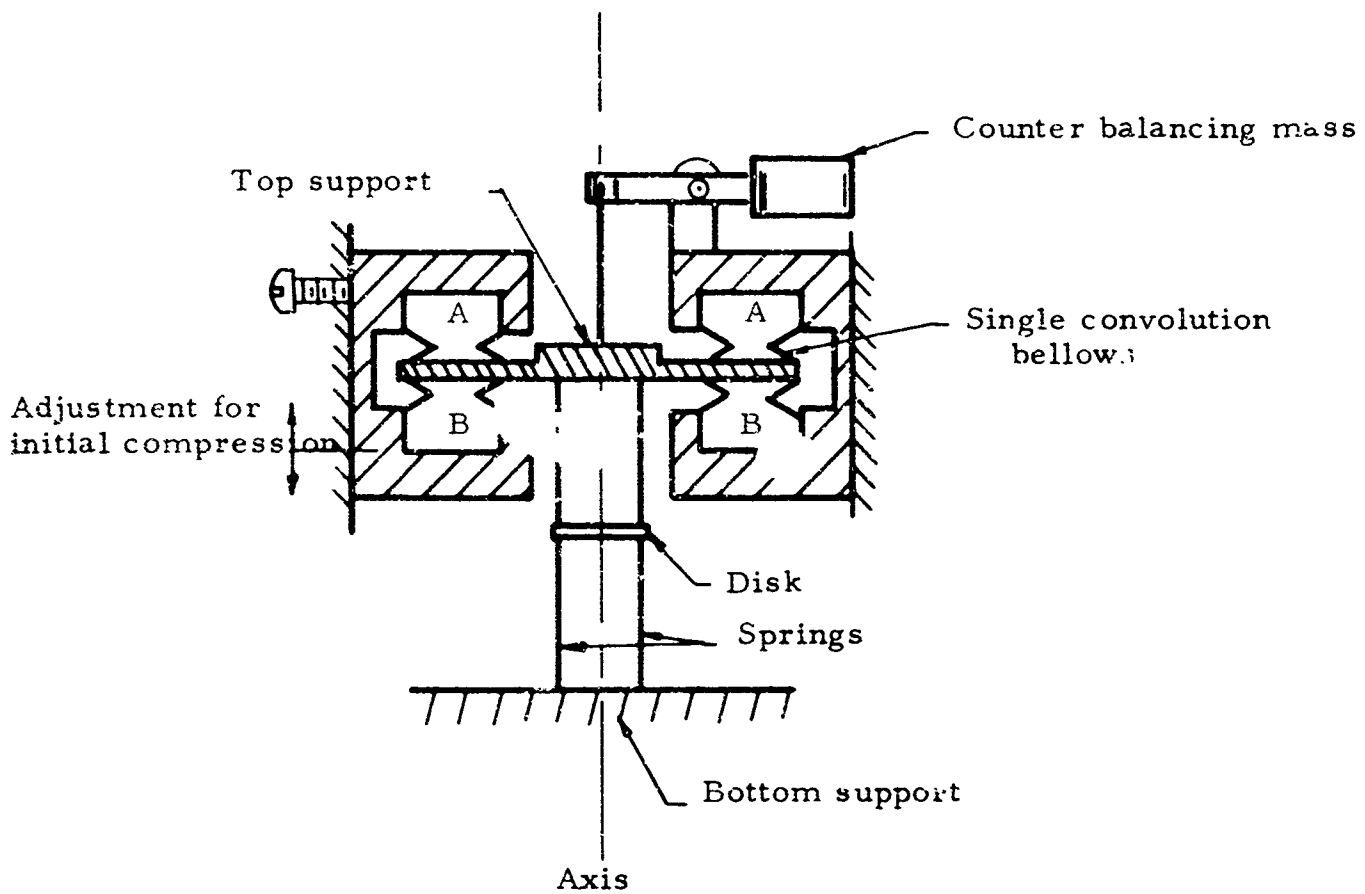


Fig. 83. Temperature-Compensating Oscillator.

tension of the supporting wires by means of a sealed bellows. With this mechanism, one end support can be made non-rigid, as required for linearity of the vibrating spring, and the actual compensating motion can be kept very small, although the force changes by a substantial amount.

Figure 83 shows schematically the oscillator with the bellows temperature compensator. The bellows are designed to be flexible in the axial direction and stiff in the lateral direction. The vibrating disk is supported for by four wire springs. Because of the parallelogram action of the four wires, the net moment felt by the movable end support is small, and the only force to be resisted is the lateral force.

Sealed chambers A and B encircle the axis. The gas in chamber B is at a higher pressure than in chamber A. The pressure difference applied to the movable support is proportional to the absolute temperature of the gas in chambers A and B. With the spring of the bellows or with a separate spring, the wires can be given an initial compression. As temperature increases, the stress in the wires changes from compressive to zero to tensile. Since the fatigue resistance of the metal becomes less at high temperature, the adjustment should be such that the compressive stresses become zero at the highest temperature.

The use of two chambers, A and B, eliminates the influence of changes in the environmental pressure. In some applications, one chamber might be omitted. If the oscillator is subjected to acceleration, the counterbalancing mechanism shown in Fig. 81 is necessary in order that the oscillator be insensitive to acceleration in the axial direction. The oscillator will still be sensitive to accelerations and vibrations in the lateral direction to a degree depending upon its mass and spring constants. Because of the sensitivity to forces in the axial direction, the oscillator driving and porting mechanism at the vibrating disk must be designed so that the axial pressure forces, as well as the radial flow forces, are kept very small.

6.6. Lateral Stiffness of the Springs as a Function of the Compression

For the cantilever beam shown in Fig. 84 the maximum deflection is given by (Ref. 44).

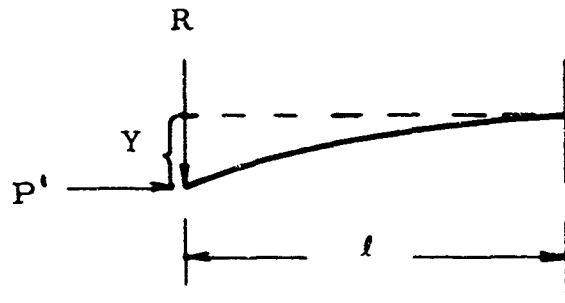


Fig. 84. Cantilever Beam with Lateral and Axial End Loads.

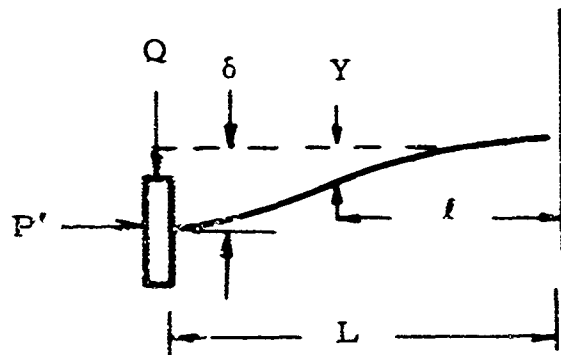


Fig. 85. Modification of Fig. 84.

$$Y = - \frac{R}{P'} \left(\sqrt{\frac{EI}{P'}} \tan \sqrt{\frac{P' l^2}{EI}} - l \right) \quad (206)$$

This can be modified for the case of Fig. 85:

$$\delta = \frac{2Q}{P'} \left(\sqrt{\frac{EI}{P'}} \tan \sqrt{\frac{P' L^2}{4EI}} - \frac{L}{2} \right) \quad (207)$$

Equation (207) can be put into the form (Ref. 45)

$$\frac{1}{K_{lat}} = \frac{\delta}{Q} = \frac{L^3}{4EI} \left(\frac{\tan \alpha - \alpha}{\alpha^3} \right) \quad (208)$$

where

$$\alpha = \sqrt{\frac{P' L^2}{4EI}} \quad (209)$$

For $P' = 0$, $(K_{lat})_{P'=0}$ is $12EI/L^3$ from simple beam theory or by reducing of Eq. (208). Then

$$\frac{K_{lat}}{(K_{lat})_{P=0}} = \frac{\alpha^3}{\tan \alpha - \alpha} \quad (210)$$

Den Hartog then expands this in an infinite series:

$$\begin{aligned} \frac{K_{lat}}{(K_{lat})_{P'=0}} &= 1 - \frac{\pi^2}{10} \frac{P'}{P'_{crit}} - \frac{1}{525} \left(\frac{\pi^2}{4} \right)^2 \frac{P'^2}{P'_{crit}} - \dots \\ &= 1 - 0.987 \frac{P'}{P'_{crit}} - 0.012 \left(\frac{P'}{P'_{crit}} \right)^2 - 0.001 \frac{P'}{P'_{crit}}^3 - \dots \end{aligned} \quad (211)$$

where $P'_{crit} = \pi^2 EI/L^2$ either from the Euler buckling formula or the reduction of Eq. (210) for $K_{lat} = 0$.

If $K_{lat}/(K_{lat})_{P=0}$ is plotted as a function of P'/P'_{crit} the function is nearly a straight line. Assuming that it is linear, and assuming a linear relation between change in temperature and change in the modulus of elasticity,

$$K = K_0 (1 - \alpha \Delta T) \left[1 - \frac{P}{P_{o\ crit} (1 - \alpha \Delta T)} \right] \quad (212)$$

where $P_{o\ crit}$ is the total buckling load for all the wires,

K_0 and $P_{o\ crit}$ are for $T = 0$,

$$\Delta T = \text{temperature change} \quad (213)$$

$$\alpha = \frac{\Delta E}{E \Delta T},$$

and

$$P = - \Delta P_o A \left(\frac{T_o + \Delta T}{T_o} \right) + C_o \Delta l (1 - \alpha \Delta T) \quad (214)$$

where P_o is the pressure difference between chambers A and B in Fig. 81 and C_o is the bellows spring constant, both for $\Delta T = 0$, and Δl is the initial deflection of the bellows. A' is the area of the ends of the chambers. Then,

$$K = K_0 \left[1 + \frac{\Delta P_o A'}{P_{o\ crit}} - \frac{C_o \Delta l}{P_{o\ crit}} + \left(-\alpha + \frac{\Delta P_o A'}{T_c P_{o\ crit}} + \frac{C_o \Delta l \alpha}{P_{o\ crit}} \right) \Delta T \right] \quad (215)$$

For temperature insensitivity, the coefficient of ΔT must be zero;

$$\left(\frac{C_o \Delta l}{P_o \text{ crit}} - 1 \right) \alpha = \frac{\Delta P_o A'}{T_o P_o \text{ crit}} \quad (216)$$

So then

$$K = K_o \left[1 + \frac{\Delta P_o A}{P_o \text{ crit}} - \frac{C_o \Delta l}{P_o \text{ crit}} \right] \quad (217)$$

where K is the lateral stiffness of the springs supporting the disk. In the physical system ΔP_o and Δl are both easily adjusted. Hence both K (and the frequency) and the temperature compensation can be adjusted.

The two assumptions of linearity made here, namely $\alpha = \text{a constant}$ and $K_{lat} = (K_{lat})_{P=0} \left[1 - P/P_{crit} \right]$ cannot be justified for really precise compensation without a much more extensive investigation of the relation α , between modulus of elasticity and temperature. Assume α actually is constant. For a 1000°F temperature range, the maximum P in Eq. (212) is 20 per cent of P_{crit} . The deviation of Eq. (212) from a straight line over this range is about ± 0.006 per cent. Remember, however, that a beam in bending is a linear spring only for small deflections. The size of the assumed linear range is related to the precision required.

6.7. Configurations to Provide Driving Force and Output

The first circular-motion oscillator designed and built consisted of a flat disk suspended by four wires as in Fig. 86. The circular path of the disk was in a plane adjacent to a plate containing air ports which were covered and uncovered by the motion. Pressure was supplied to the housing for the system. Output lines were connected to the ports in the base plate. The two crescent-shaped ports, shown in Fig. 86b and c, provided two outputs 180 degrees out of phase with other. (A photograph is shown on Fig. 87a).

The driving force for the disk was provided by vanes set at a spiral angle around its periphery. The flow through the vanes was greatest at the largest opening uncovered by the disk, and the flow force caused by the vanes was always tangential to the direction of the displacement of the disk. See Fig. 86c.

When tested, this oscillator showed some sensitivity to pressure because of two undesirable forces affecting the spring constant. One of

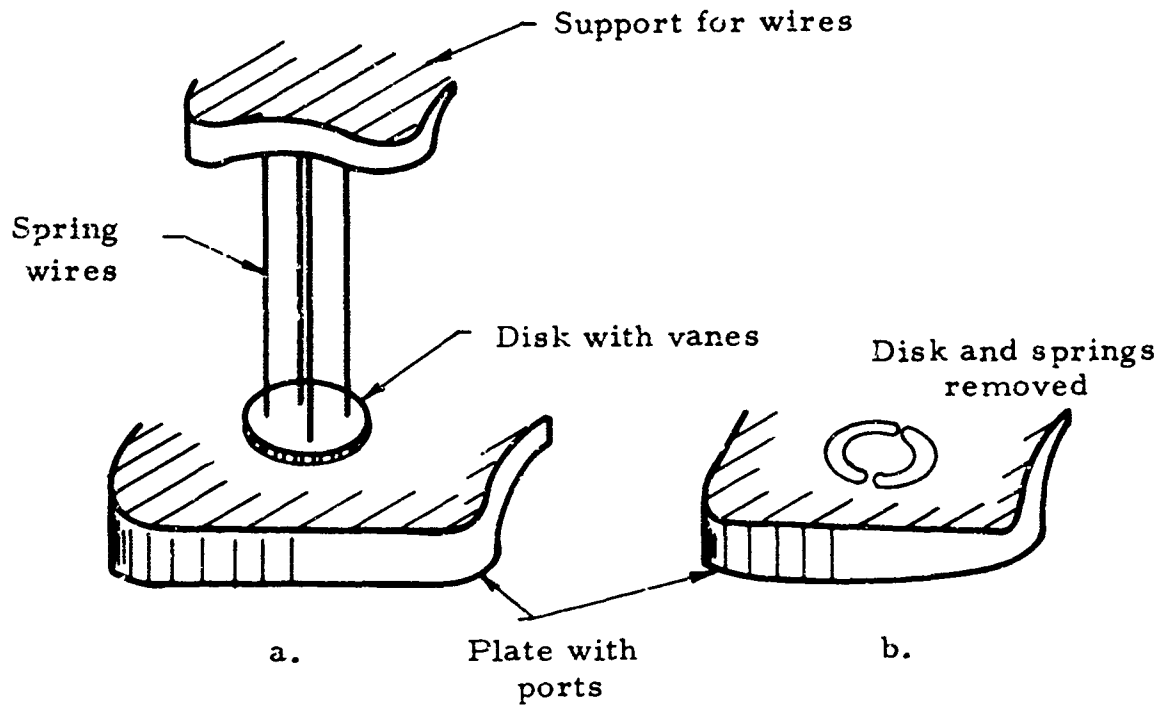


Fig. 86. First Test Oscillator.

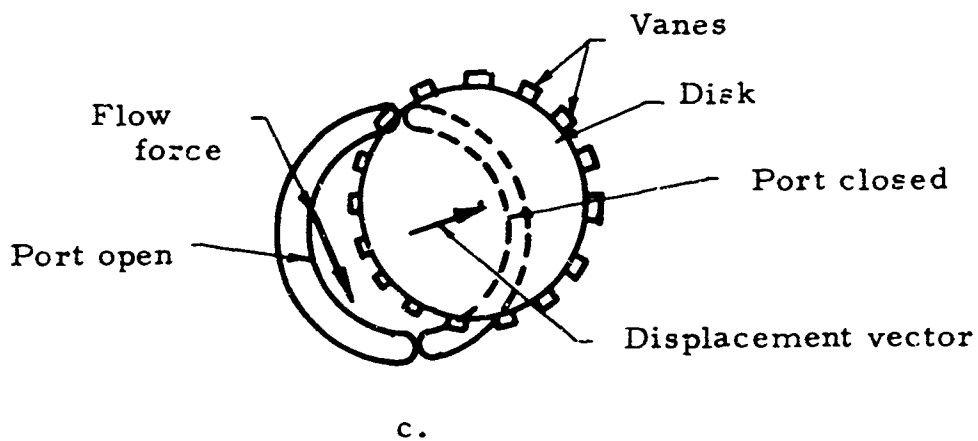


Fig. 86. First Test Oscillator.

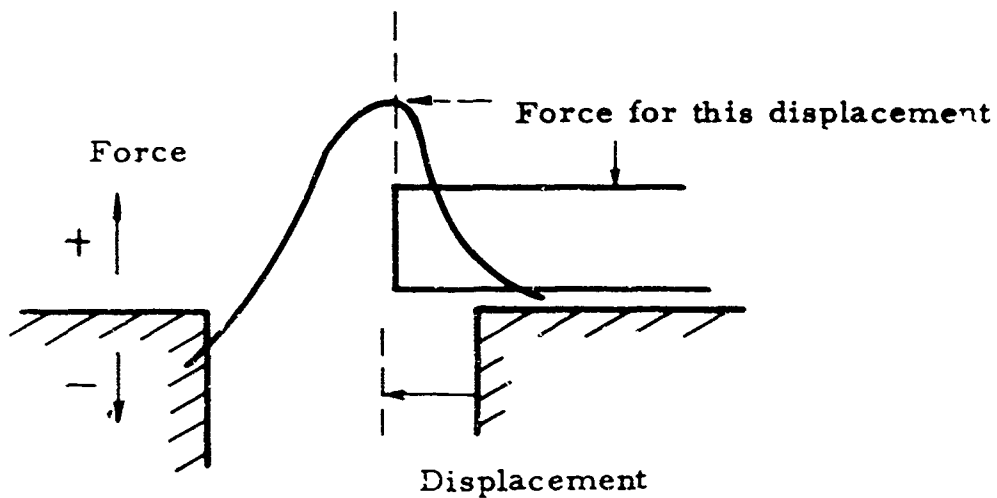


Fig. 87. Radial Flow Force on the Edge of a Disk.

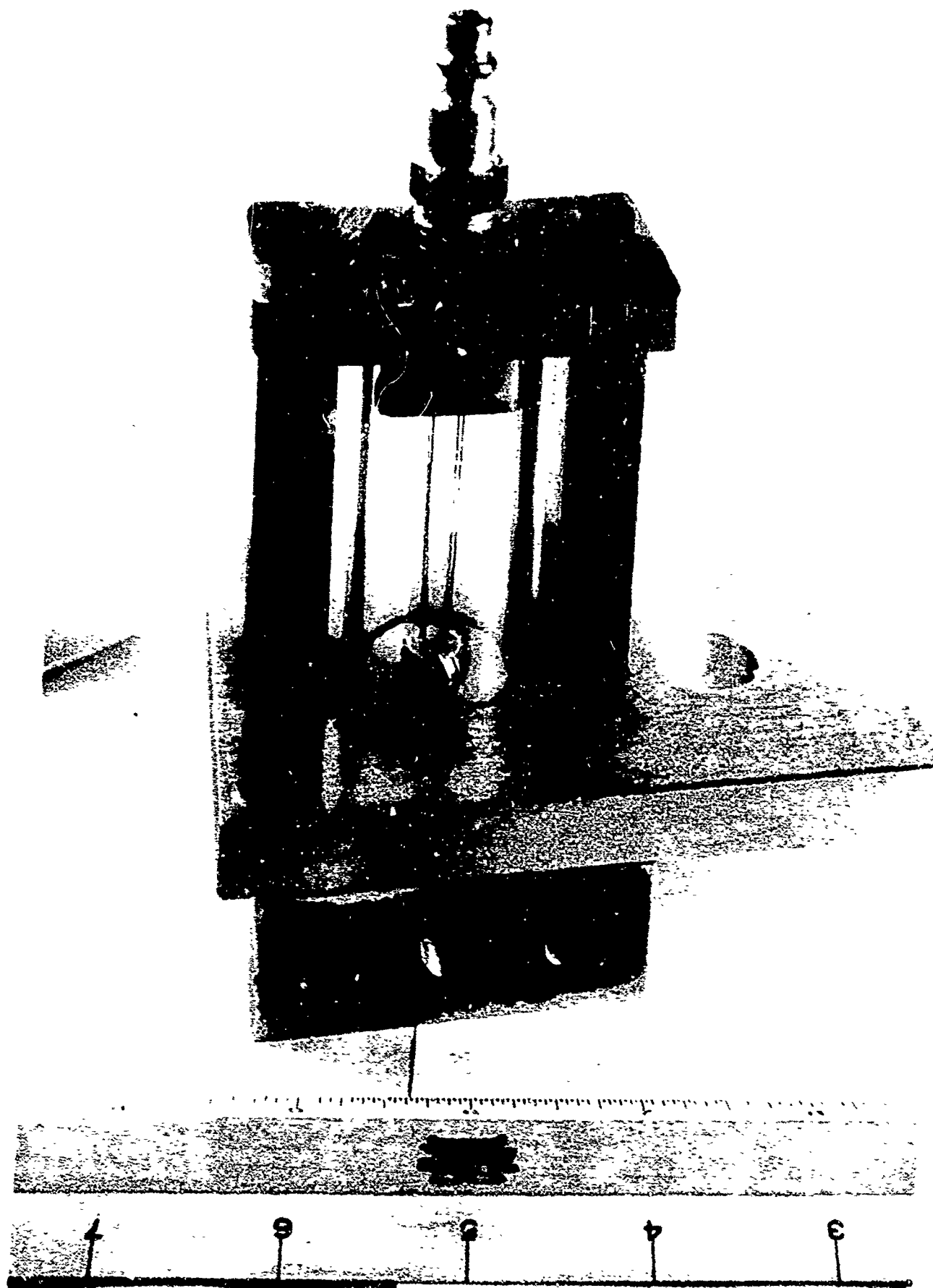


Fig. 87a. Photograph of First Test Oscillator.

these was the column loading on the face of the disk. The other radial pressure force was a result of flow into the partially closed ports.

The flow force on the edge of a plate closing a hole was measured roughly and found to be generally as shown in Fig. 87. Because of the skew of the curve, this radial force could not be balanced adequately by the corresponding force on the opposite edge of the disk.

Another design was built and tested. The vibrating disk had eight holes evenly spaced in a circle. Each hole was perpendicular to the radius at that point but slanted with respect to the axis of the disk. Thus, flow through a hole was given a velocity and momentum in the tangential direction. The base plate contained another ring of eight holes at a slightly greater radius. See Figs. 88 and 89b. A displacement of the disk from the center position resulted in a greater opening for flow on one side than the other, and therefore, a tangential flow force. As the amplitude became greater, however, the disk and plate holes overlapped, less so that the flow force was reduced. The amplitude was not limited, though. After the circular motion attained a certain amplitude, further increases in pressure caused the motion to continue to grow with an elliptical shape. The stability analysis was then made to understand this phenomenon.

It seems reasonable to expect that the flow forces arising from flow through a hole be less than the flow forces on an open edge, since the reduction of pressure by Bernoulli flow is felt at least partially all around the interior of the hole. The first of the two oscillators just described has a pressure sensitivity of about 1 per cent per psi supply pressure. The second had a sensitivity of about 0.02 per cent per psi. The comparison is crude because the oscillators were only roughly of the same size.

Both oscillators had the vibrating disk upstream so that the output could be taken directly from the base plate. A simple experiment, the results of which are summarized in Fig. 89, emphasized that it would have been better to place the disks downstream.

An oscillator with a pneumatic lag in the amplitude-sensing mechanism was considered but not built, even though the stability analysis had indicated

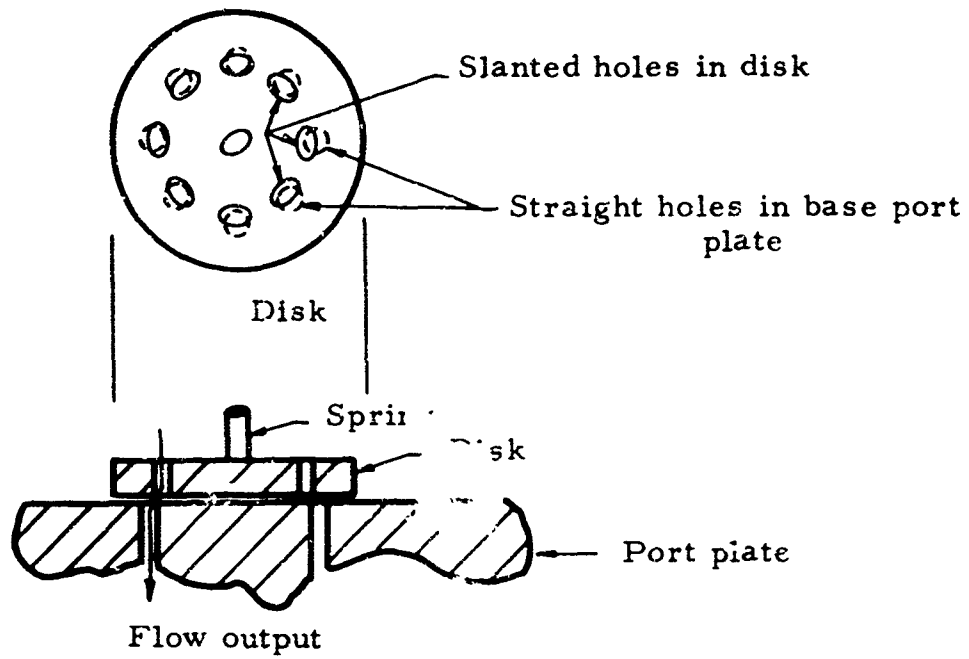


Fig. 88. Second Test Oscillator.

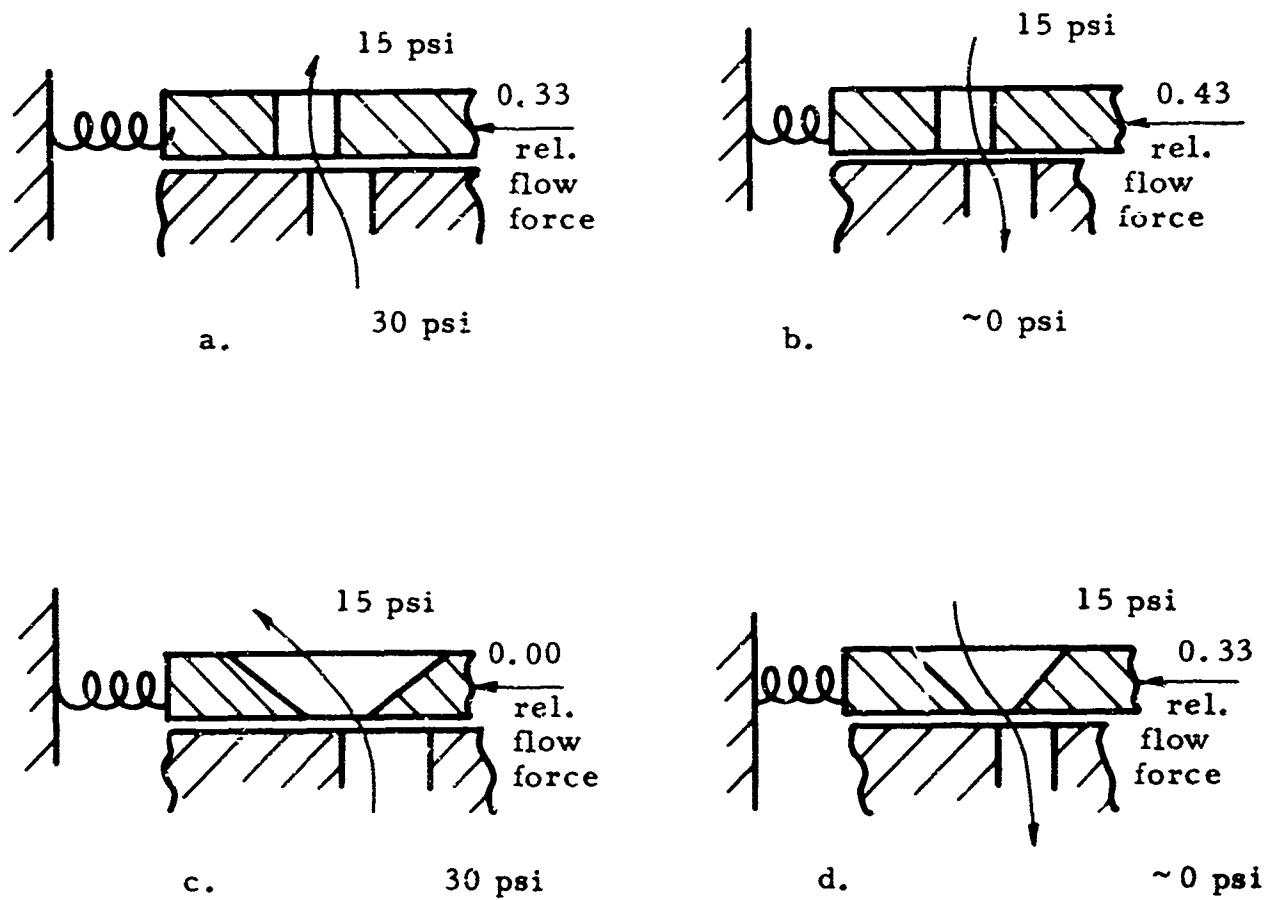


Fig. 89. Disk-Hole and Flow Configurations.

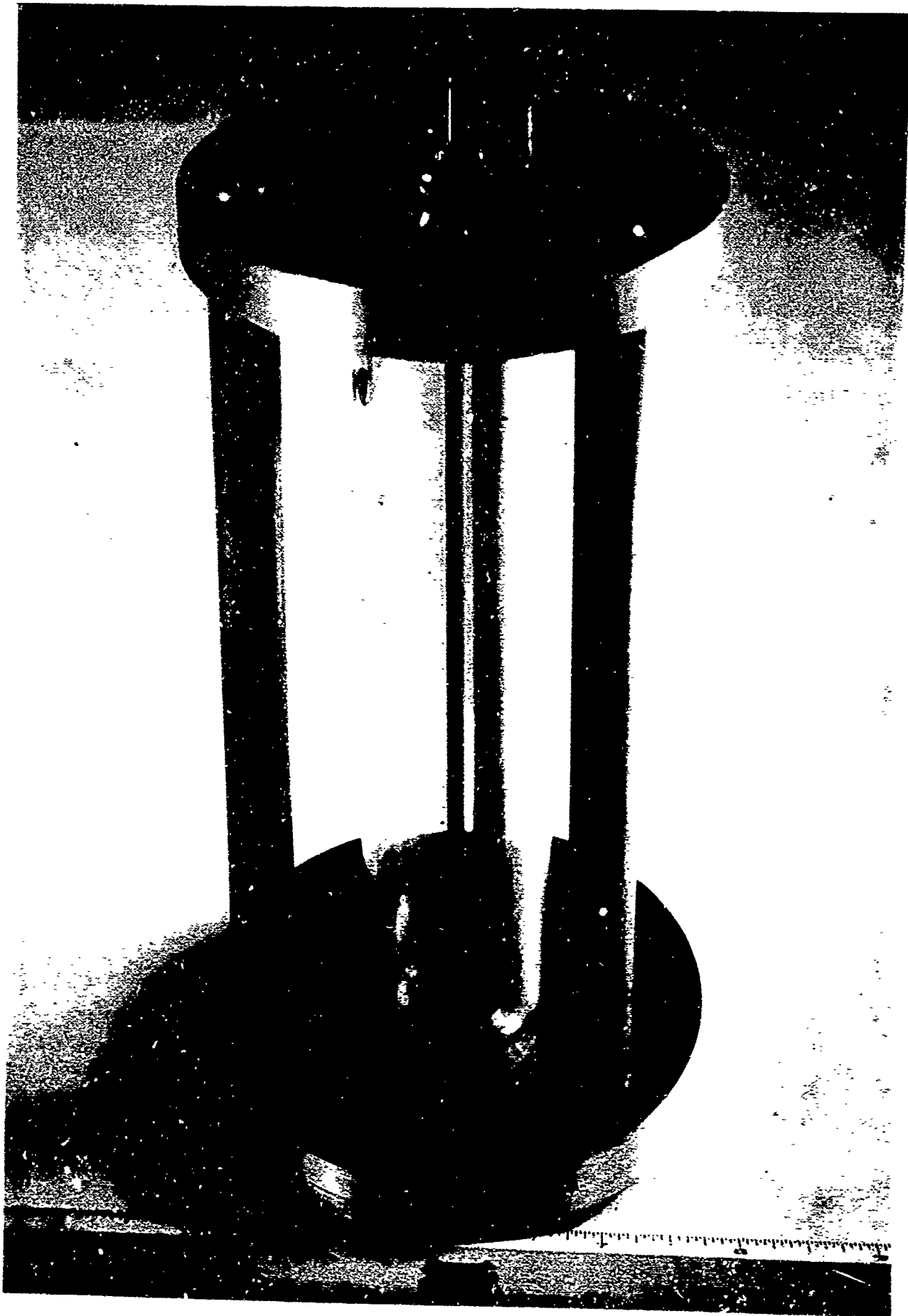


Fig. 89b. Photograph of Second Test Oscillator

that a lag was quite desirable. A possible configuration is given in Fig. 90. The holes in the upper disk which meter the supply air are aligned with the corresponding holes in the supply plate when the disk is centered, but become more and more misaligned (orbiting around the supply hole) as the amplitude of oscillation increases. The chamber causes a lag between changes in flow through the upper disk and the driving force provided by the vanes on the lower disk. The flow is in the proper direction for keeping the radial flow forces low, and consequently, the oscillator as shown has no useful output; auxiliary ports are necessary.

The third oscillator built was quite the same in principle as the second, but the flow was reversed. The disk was made very thin so that the sides of the holes would not interfere with the flow (see Fig. 91a) and vanes were placed immediately behind the holes to provide the driving force, as shown in Fig. 91b. Instead of being in a slightly larger ring, the holes in the supply plate were drilled in line with the holes in the disk and then half-plugged, as shown.

It is interesting to examine in greater detail the operation of this oscillator and to examine especially the action of the amplitude cutoff. Consider air flow in the configuration of Fig. 91b. The momentum of the fluid flowing through the holes is WV , where W is the mass flow rate and V is the velocity. If the vane is set at a 45 degree angle, then the lateral force on the vane is approximately $WV/\sqrt{2}$. This assumes that the flow is straight through the holes, which is not strictly true. In fact, with this assumption we overlook a small source of radial force which will be discussed later. It is assumed also that the velocity of the disk is small compared to the velocity of the air. It is, in fact, 30 inches/second for $\omega_0 = 500$ cps at an amplitude of 0.01 inch.

The product $WV/\sqrt{2}$ is now derived for both incompressible and compressible flow. For incompressible flow,

$$V = \sqrt{\frac{\Delta P}{\rho}} \quad (218)$$

where ΔP is the pressure drop across the holes and ρ is the fluid density.

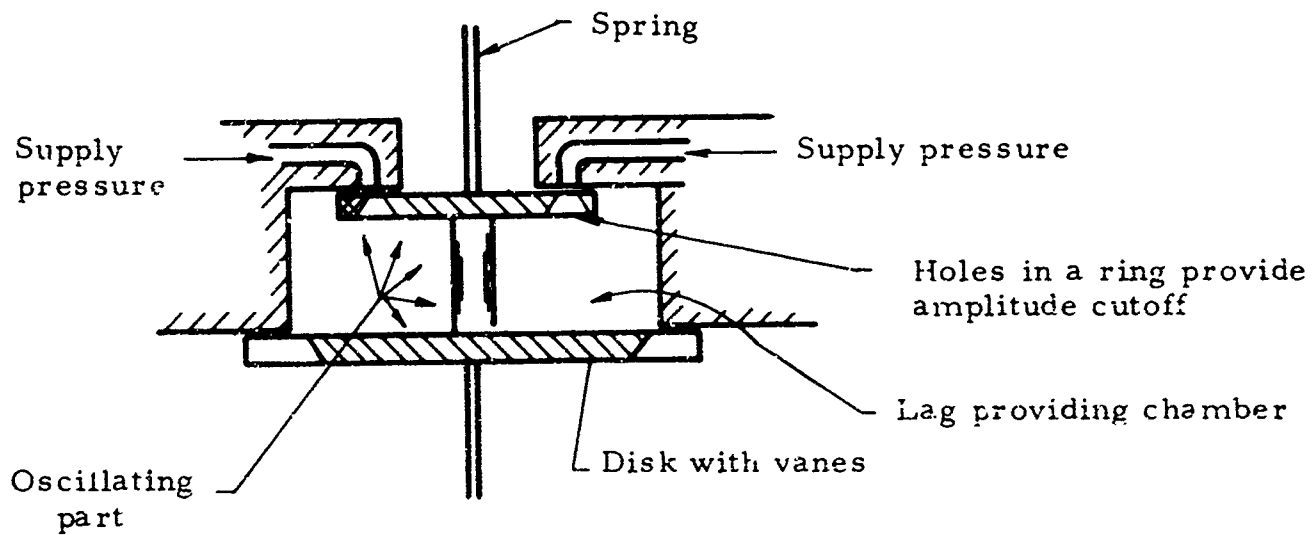


Fig. 90. Oscillator with a Pneumatic Lag in the Amplitude-Sensing Mechanism.

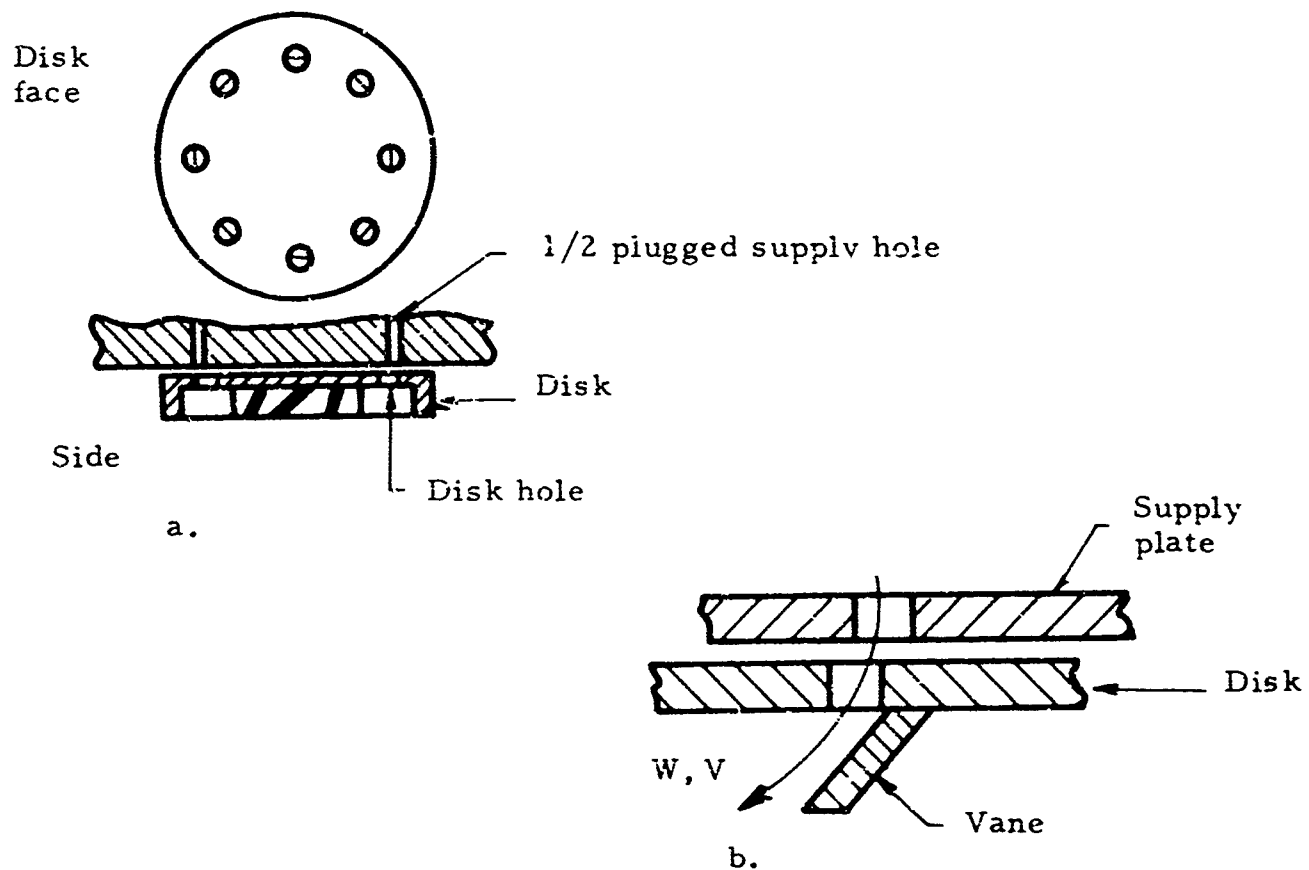


Fig. 91. Third Test Oscillator Driving Mechanism.

$$W = \rho VA \quad (219)$$

and

$$F = \frac{WV}{\sqrt{2}} = \frac{\rho V^2 A}{\sqrt{2}} = \frac{A \Delta P}{\sqrt{2}} \quad (220)$$

For isentropic compressible flow,

$$V = M \sqrt{\gamma RT} \quad (221)$$

where M is the Mach number, and γ is the ratio of specific heats.

$$WV = \rho V^2 A = \rho A M^2 \gamma RT \quad (222)$$

Using the equation of state

$$\rho = \frac{P}{RT} \quad (223)$$

we get

$$F = \frac{WV}{\sqrt{2}} = \frac{P A M^2 \gamma}{\sqrt{2}} = \frac{P_o A \left(\frac{P}{P_o} \right) M^2 \gamma}{\sqrt{2}} \quad (224)$$

where P_o is the stagnation (supply) pressure, and P is the pressure where V is taken. From isentropic flow tables (Ref. 46) $P/P_o M^2 \gamma$ can be calculated, and it is plotted as a function of P/P_o in Fig. 92. For sonic flow ($P/P_o < 0.528$), $P/P_o M^2 \gamma$ remains constant at 0.739.

In each of these cases the driving force, F , is proportional to an effective area, A . Figure 93 represents the disk given an X-direction displacement from its neutral position with respect to the supply plate. On each vane the momentum force, which is proportional to the common area of the supply plate hole and the disk hole at that location, is indicated by an adjacent vector in the figure. Ideally the net X-direction force on the disk is zero. This is not strictly true because the flow is given a slight deflection in going through the holes and impinges upon each vane with a slightly different initial angle. Setting each vane at a slight angle with the radius might correct this.

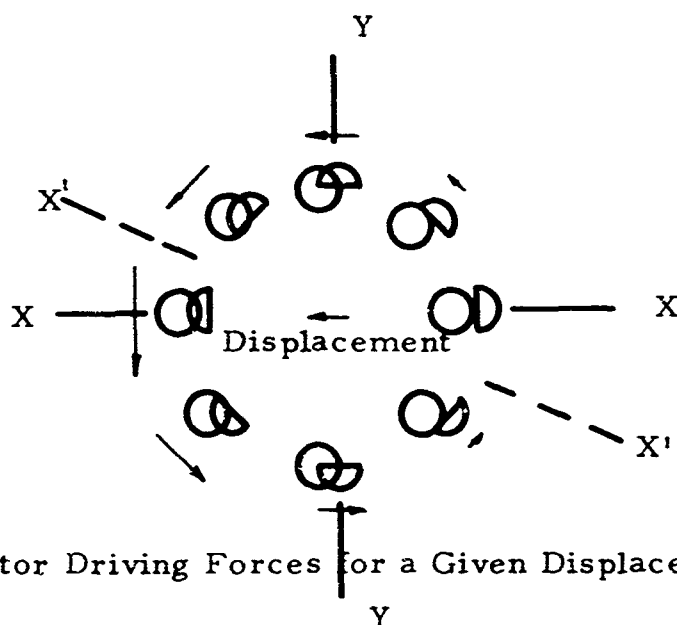
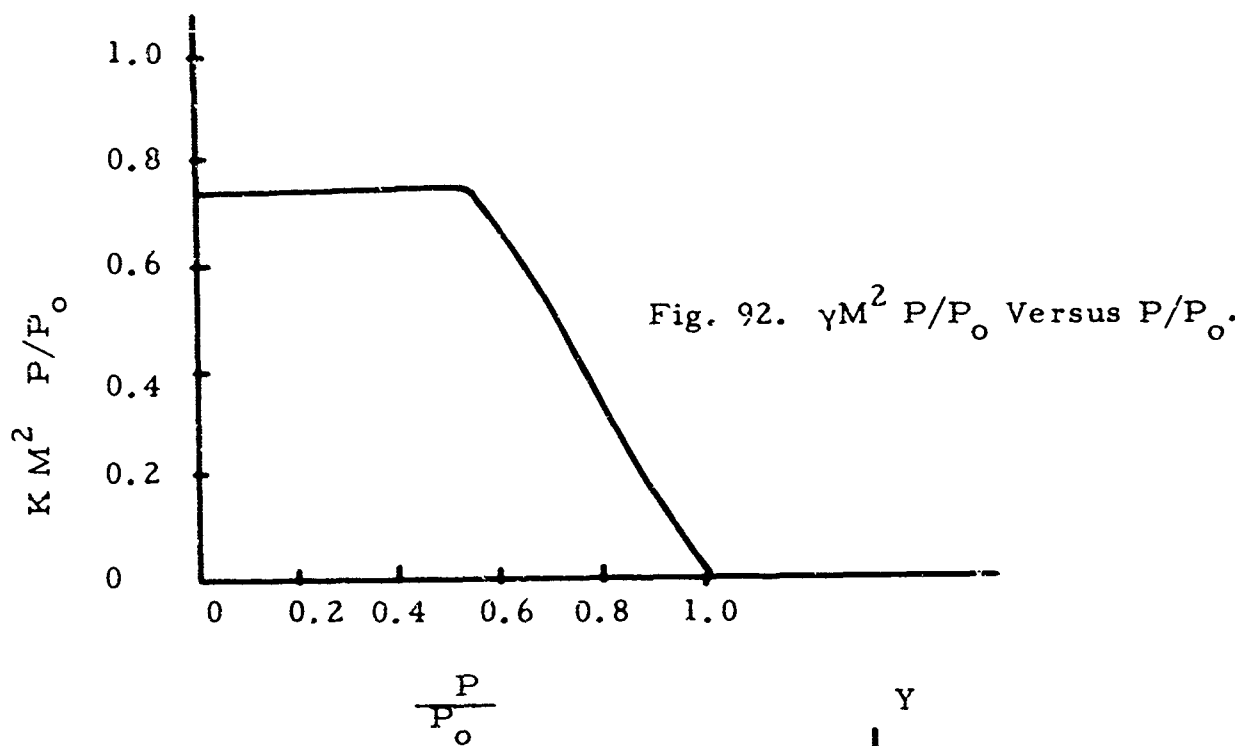


Fig. 93. Third Oscillator Driving Forces for a Given Displacement.

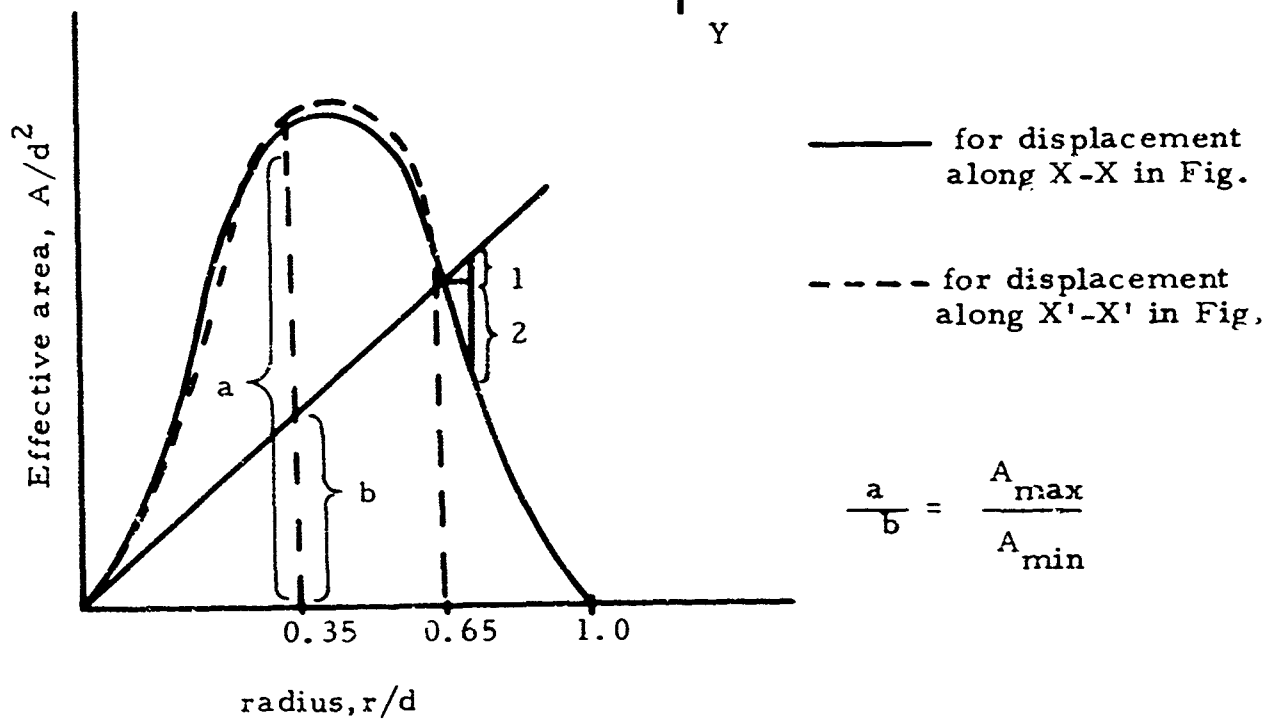


Fig. 94. Effective Area Versus Radius.

The net Y-direction force is the desired tangential driving force. This net force is proportional to the effective area, A, which is the sum of all the open areas multiplied by the proper angle cosines. This effective area was obtained graphically as a function of the displacement and is presented as Fig. 94.

In the stability analysis it was found that for $\omega_r = \omega_0/1.4$ the steepest permissible cutoff slope is about twice the damping-force slope. In Fig. 93 a straight line has been placed so that, at its intersection with the area curve, this relation between slopes is met. The area curve is proportional to the driving force, so the straight line is proportional to the damping force. This intersection gives the maximum amplitude of oscillation with circular motion as 0.66 times the diameter of the holes in the disk. To find the pressure range for the oscillator, a minimum useful amplitude must be chosen. The ratio of the maximum to the minimum driving force is determined by the multiplier needed to make the damping and area curves intersect at the minimum amplitude. If the minimum amplitude is 0.35 times the diameter of the disk holes, then the ratio of maximum to minimum driving force is found to be 2.35. If the driving force is proportional to the pressure (it is for critical flow and for incompressible flow), then the ratio of maximum to minimum pressure is also 2.35.

Different types of damping curve are shown in Fig. 95. The square-law damping is somewhat more realistic than the linear damping. The addition of Coulomb damping introduces a stable 200-amplitude equilibrium point, which can keep the oscillator from starting itself.

Equating the driving force to the damping force, we get

$$\frac{P'A}{\sqrt{2}} = 2\zeta_0 \omega_0^2 m r \quad (225)$$

where P' is a pressure function and m is the mass of the oscillating disk.

Since A is a function of the radius, the preceding equation can be rewritten

$$\frac{P'd}{2\zeta_0 \omega_0^2 m} = \frac{\frac{r}{d}}{\frac{A}{d^2}} \quad (226)$$

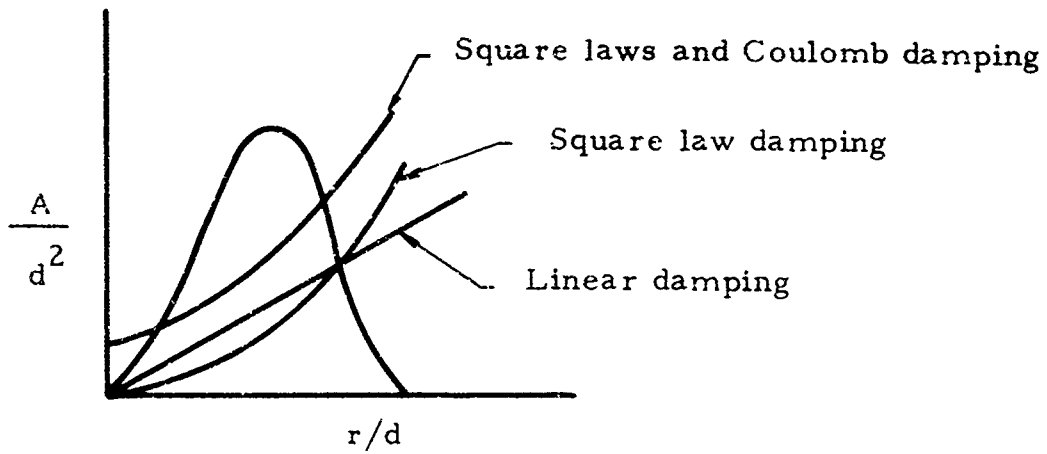


Fig. 95. Other Damping Curves.

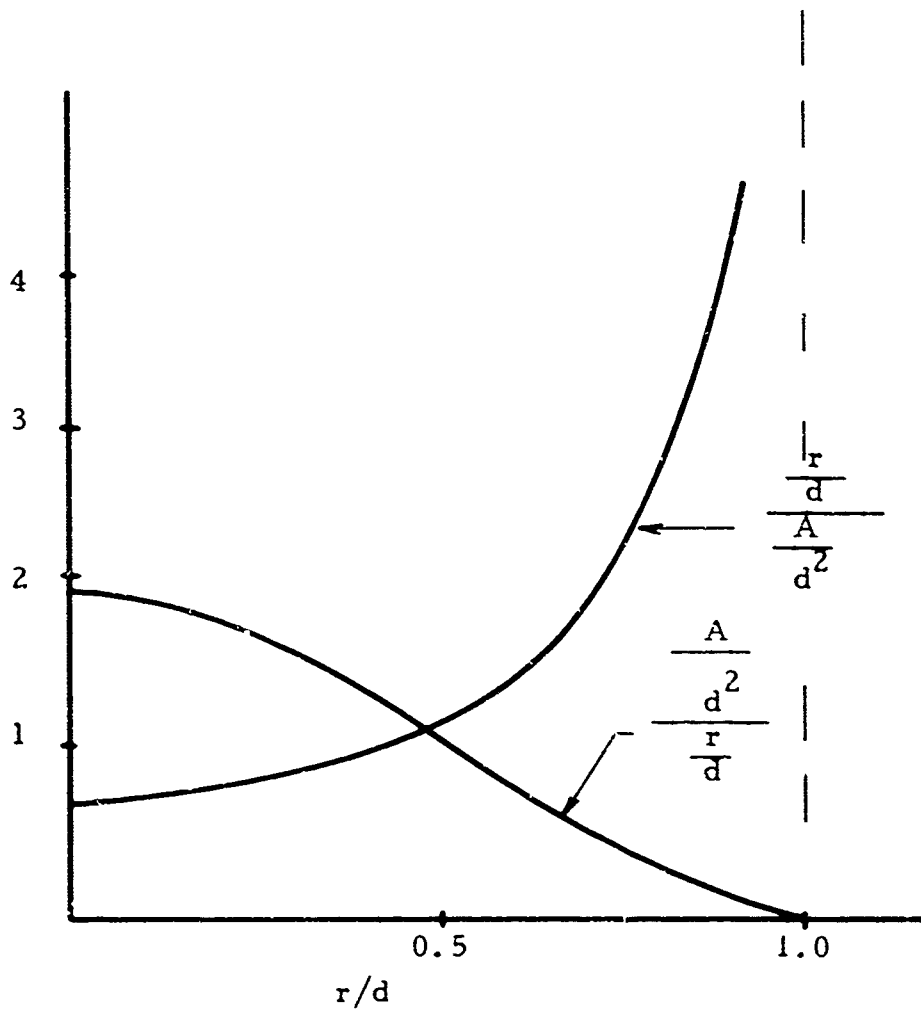


Fig. 96. $(r/d)/(A/d^2)$ and $(A/d^2)/(r/d)$ Versus r/d .

where $(r/d)/A/d^2$, a function of r/d alone, has been plotted in Fig. 96. The term on the left in Eq. (226) is independent of the size of the oscillator for geometrically similar oscillators. To show this, we write

$$\omega_{\theta} = \sqrt{\frac{K_{\theta}}{m}} \propto \sqrt{\frac{EI}{L^3}} \propto \sqrt{\frac{d^4}{d^3}} \propto \frac{1}{d}$$

This incidentally, is itself of interest, although not surprising.

Then

$$\frac{d}{2\zeta_{\theta} \omega_{\theta}^2 m} \propto \frac{d}{\zeta_{\theta} \frac{d^3}{d^2}} \propto \frac{1}{\zeta_{\theta}}$$

The damping force is

$$2\zeta_{\theta} \omega_{\theta}^2 \delta m \propto d^2 \zeta_{\theta}$$

The air damping force is proportional to the projected area of the moving parts and to their velocity, or for geometrically similar oscillators, d^2 .

Therefore,

$$\zeta_{\theta} \propto 1$$

The internal damping moment is given by the formula

$$\frac{M_d c}{I} = \sigma_d \quad (227)$$

where

$$\sigma_d \propto \dot{\epsilon} \propto \dot{\omega}_{\theta} \propto 1$$

Hence the internal damping force, proportional to M_d/L , is proportional to

$$\frac{I}{cL} \propto d^2$$

and again

$$\zeta_{\theta} \propto 1$$

Equation (226) would be used in determining the size of the oscillator for a specified frequency and supply pressure level. Some information about ζ_0 would be required.

6.8. Design of the Springs

The next task is the design of the spring support system for the disk. A minimal size is desired. For each wire, considered as a beam, the bending formula is

$$\delta = \frac{QL^3}{12EI} \quad (228)$$

and the spring constant is

$$\frac{Q}{\delta} = \frac{12EI}{L^3} \quad (229)$$

For the disk-spring system, the spring constant is affected by n , the number of wires:

$$K = \frac{n \cdot 12EI}{L^3} \quad (230)$$

where K is the spring constant, n is the number of half-wires, L is the wire length on each side of the disk. For a round wire, the moment of inertia, I , is $\frac{\pi c^4}{4}$, where c is the wire radius. The maximum moment on a wire is the product of the spring constant, the deflection, and the length:

$$M_{\max} = K\delta L \quad (231)$$

The maximum stress is given by the relation

$$\frac{M_{\max} c}{I} = \sigma_{b \max} \quad (232)$$

Equations (230), (231), and (232) combined yield the two equations,

$$c = \frac{L^2 \sigma_b}{12 E \delta} \quad (233)$$

and

$$K = \frac{3En\pi}{L^3} \left(\frac{L^2 \sigma_b}{12 E \delta} \right)^4 \quad (234)$$

Equation (234) rearranged gives

$$L^5 = \frac{K}{3En\pi} \left(\frac{12E\delta}{\sigma_b} \right)^4 \quad (235)$$

In operation,

$$\omega_0 = \sqrt{\frac{K}{m}} \quad (236)$$

so that

$$K = m \omega_0^2 \quad (237)$$

Equation (235) gives the minimum length for a specified disk configuration, natural frequency, and allowable stress.

6.9. Construction of the Third Oscillator

The output of the third oscillator was a flow of air modulated by the vibration of the disk. The output air and the driving force air were supplied separately. The modulation of the output flow was done by four ports in the disk arranged in a ring at a larger radius than the driving holes and vanes. There were corresponding ports in the adjacent stationary port plates, and the result was a set of four valves similar to conventional plates valves. In making four valves it was intended that different combinations of the outputs could give a single-phase output with frequency ω_0 , a push-pull output with a frequency ω_0 , a push-pull output with frequency $2\omega_0$,

and a single output with frequency $4\omega_0$. Details of the porting are shown in Fig. 97. The vibrating disk is detailed in Fig 98; Figs. 99 and 99a show the whole oscillator. Detail drawings of all the parts are in the Appendix.

The output valves were designed to balance the pressure forces on the faces of the disk. Baffles were put in to keep the jets at the valve openings from hitting the opposite sides of the holes and creating radial forces. Leakage flow channels, placed around each of the driving flow ports in the port plate adjacent to the disk led into an exhaust passage in the plate. By placing a slight restriction in the exhaust line downstream from the vanes and keeping the leakage flow exhaust line unrestricted, the axial pressure forces in the center of the disk could be balanced for a given pressure and approximately for neighboring pressures. This was not done in the tests of the oscillator, however, because the pressure sensitivity was already quite low.

The starting point in the design was the choice of a frequency, a convenient yet small amplitude, and a maximum allowable wire stress:

$$\begin{aligned}\omega_0 &= 500 \text{ cps} = \pi \times 10^3 \text{ rad/sec} \\ d &= 0.010'' \text{ (the hole size is roughly the amplitude)} \\ \sigma_b &= 60,000 \text{ psi with } E = 30 \times 10^6 \text{ psi}\end{aligned}$$

The layout of the disk came next, and as a result,

$$\begin{aligned}m &= 0.258 \times 10^{-5} \text{ lb. sec}^2/\text{in.} \\ n &= 8\end{aligned}$$

The value of K used was 120 per cent of the desired K to allow for an initial 20 per cent compression of the wires at ambient temperature. Equations (233) and (235) yielded a wire size of

$$\begin{aligned}L &= 0.706 \text{ in.} \\ c &= 0.00831 \text{ in.} \\ \text{diameter} &= 0.0166 \text{ in.} \\ \text{Area} &= 2.17 \times 10^{-4} \text{ in.}^2 \\ I &= 0.374 \times 10^{-8} \text{ in.}^4\end{aligned}$$

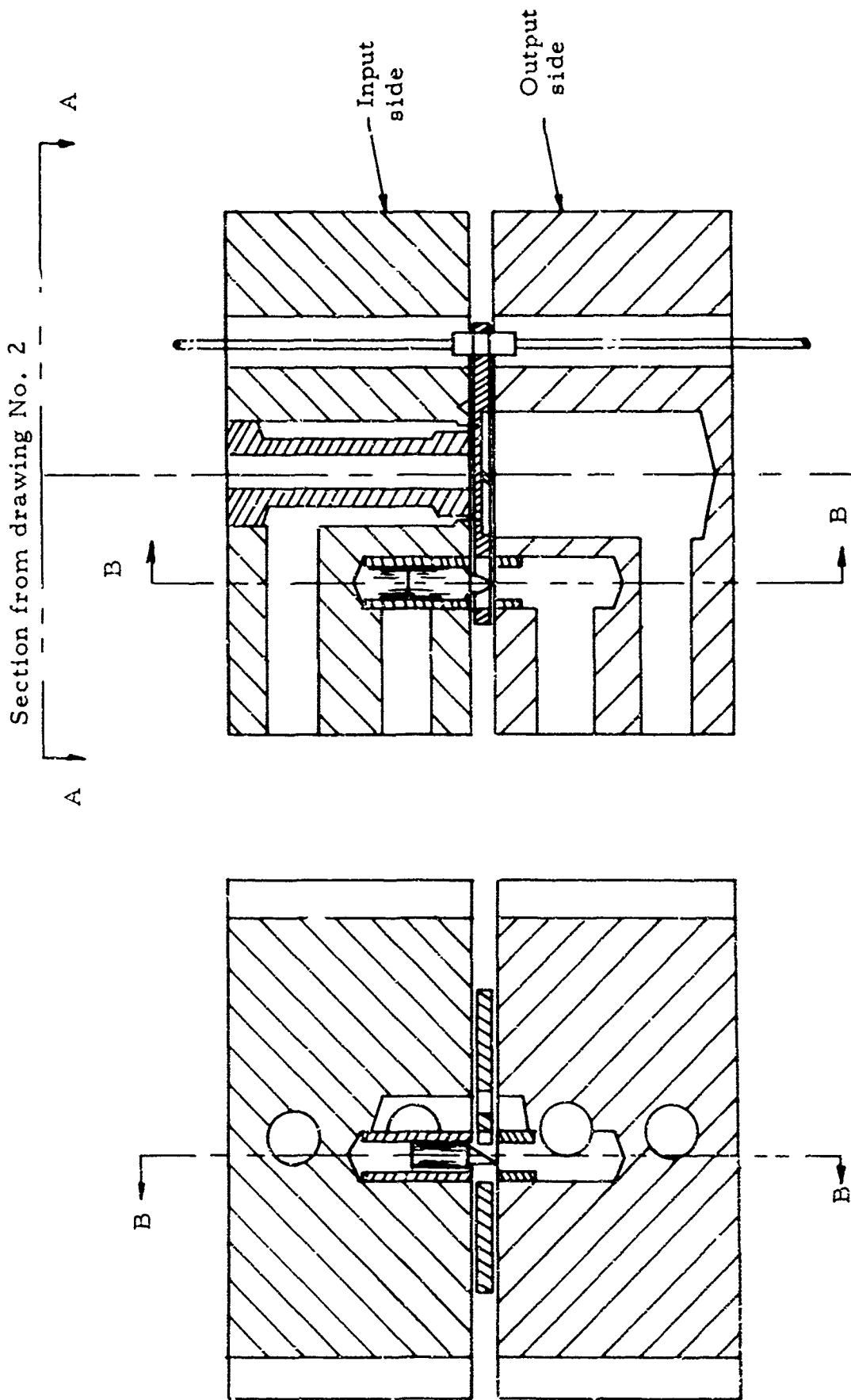


Fig. 97. Temperature-Insensitive Pneumatic Oscillator

Fig. 97. Temperature-Insensitive Pneumatic Oscillator

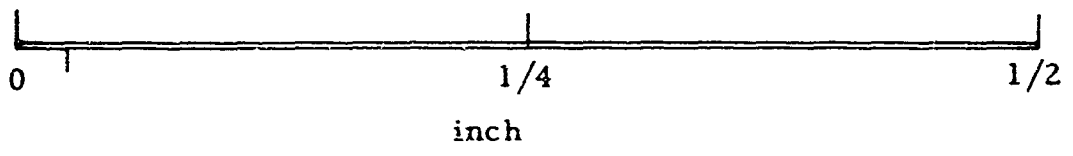
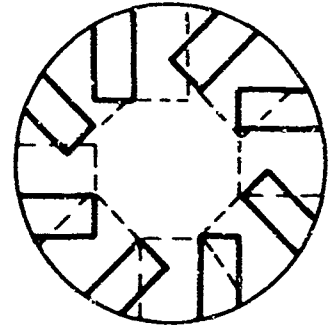
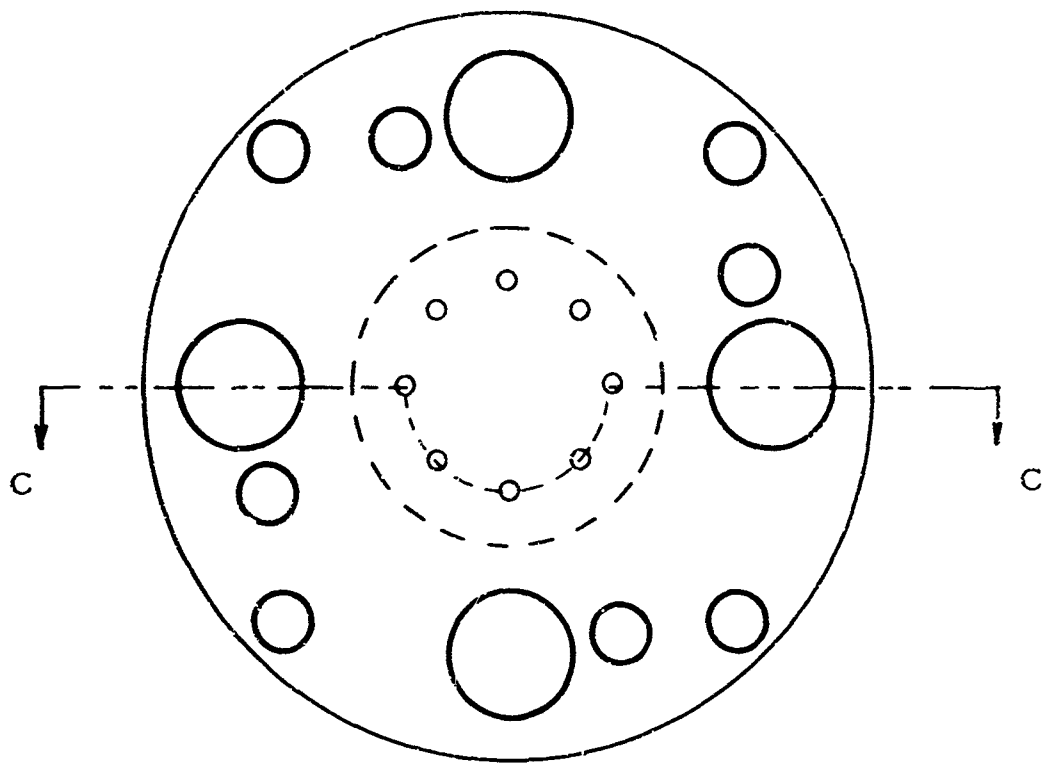


Fig. 98. Detail of Vibrating Disk

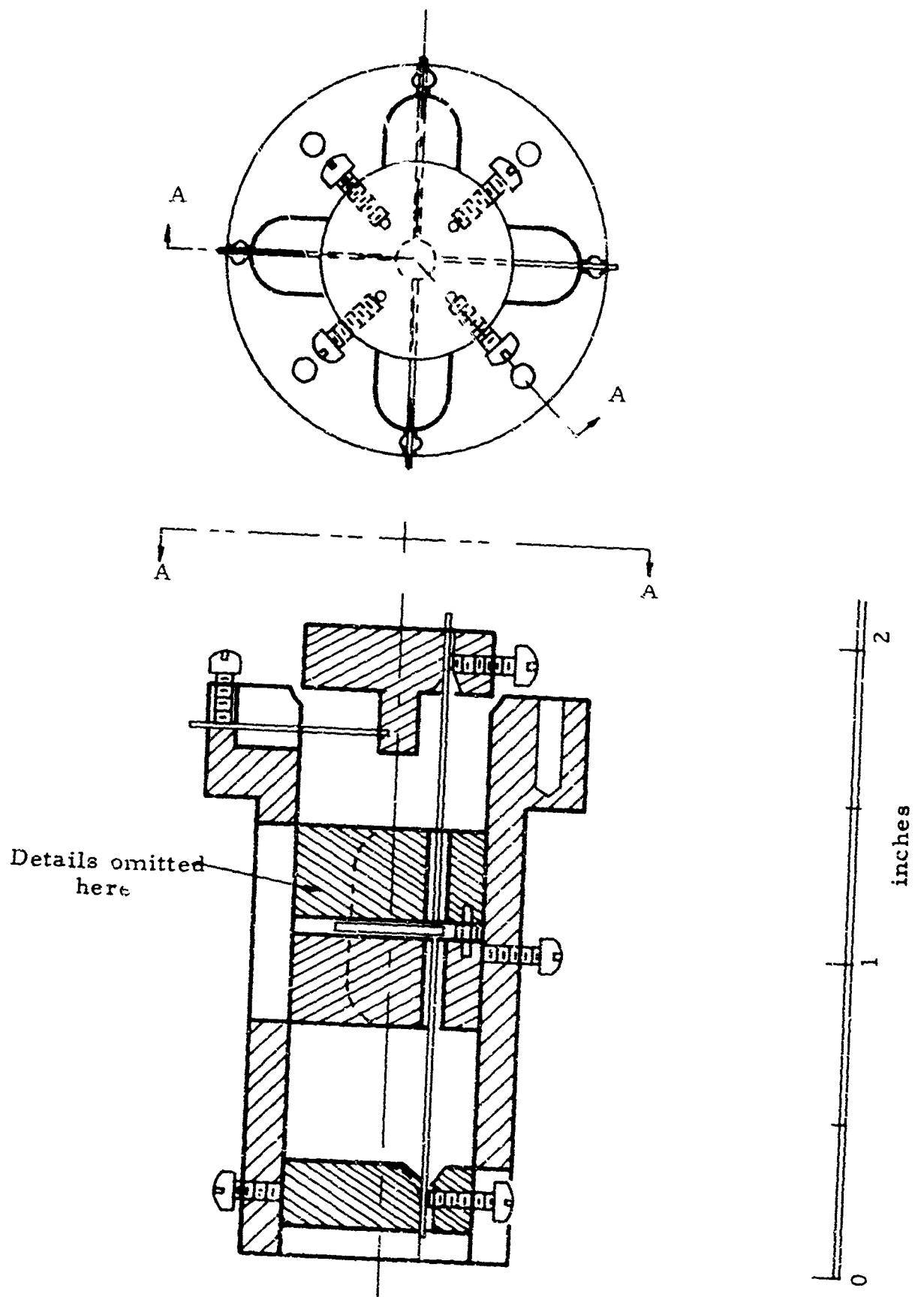


Fig. 99. Third Test Model Assembly.

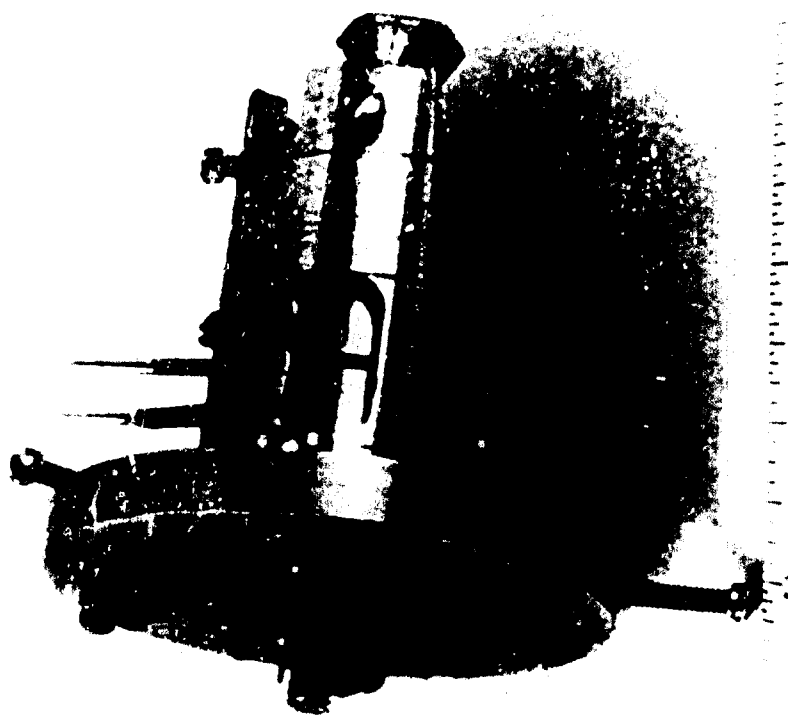


Fig. 99a. Photograph of Third Test Model Assembly.

Best Available Copy

Investigation showed that for a wire compression of 20 per cent of the buckling load, the maximum bending moment is 98 per cent of that of the uncompressed wire. The lesson is that for all practical purposes, the maximum stress in the wire can be calculated as the sum of the compressive stress and the maximum no-compression bending stress:

$$\sigma_{\max} = \sigma_b + \sigma_c$$

where σ_b is the fluctuating bending stress and σ_c is the constant compressive stress.

In the actual oscillator, the wire sizes were

$$L = 0.72 \text{ in.}$$

$$c = 0.0080 \text{ in.}$$

$$\text{diameter} = 0.0160 \text{ in.}$$

$$\text{Area} = 2.01 \times 10^{-4} \text{ in.}^2$$

$$I = 0.322 \times 10^{-8} \text{ in.}^4$$

We recall that the critical loading of a single wire is

$$P'_{\text{crit}} = \frac{\pi^2 EI}{L^2} \quad (238)$$

For all the wires together, the critical load is

$$P_{\text{crit}} = 4 P'_{\text{crit}} \quad (239)$$

Consequently, it was found that

$$P'_{\text{crit}} = 1.84 \text{ lb.}$$

$$0.2 P'_{\text{crit}} = 0.367 \text{ lb.}$$

$$\sigma_c = \frac{0.2 P'_{\text{crit}}}{\text{area}} = 1830 \text{ lb/in.}^2$$

$$\sigma_{\max} = (1.8 + 62) \times 10^3 \text{ lb/in.}^2$$

and

$$P_{\text{crit}} = 7.34 \text{ lb.}$$

$$0.2 P_{\text{crit}} = 1.47 \text{ lb.}$$

An estimation of the linearity of the spring can be obtained using the relation

$$K = K_o \left(1 - \frac{P}{P_{\text{crit}}} \right) \quad (212)$$

The axial stiffness of the wires is very great in comparison with the axial stiffness required in the end support. Hence, for a displacement, δ , of the disk, the axial displacement of one end support, the other being fixed, is $2 \delta^2/L$. The column loading caused by this displacement, is the product of the axial stiffness of the support and displacement, $2 K_a \delta^2/L$. The relative change in the lateral stiffness at the disk is therefore

$$\frac{2K_a \delta^2}{L P_{\text{crit}}} \quad (240)$$

and is a measure of the deviation from linearity.

In this test model, the movable end support was suspended on four wires each 0.47 inch long and of the same diameter as the disk spring wires. For this case, Eq. (230) yielded

$$K_a = \frac{12 n EI}{L^3} = 52 \text{ lb/in}$$

The mass of the end support was about 20 times the mass of the disk. It has been shown that for this situation the maximum radius for circular motion of 0.65 times the disk hole diameter, the minimum amplitude for operation is about 0.35 times the hole diameter. Then for the third oscillator, the deviation from linearity over the range of operation was

$$\frac{2K_a (\delta_{\text{max}}^2 - \delta_{\text{min}}^2)}{L P_{\text{crit}}} = 0.05 \text{ per cent}$$

The materials used were chosen for availability and machinability and would not be suitable for high-temperature applications. The disk, port plates, and end supports were brass, the springs were steel music wire, and the housing was structural steel. The effective diameter of the spring wire was made larger where it passed through the disk by forcing a short piece of hypodermic tubing over a slightly flattened portion of the wire; the tubing was then pressed into the disk. Getting the wire mountings tight and the internal damping to a minimum required installing the wires several times. Even then the wires had slightly different damping in different direction.

6.10. Testing of the Third Oscillator

Figure 100 is a representation of the test setup. A more elaborate setup would have been desirable but would have taken much more time than was available. For convenience, frequency change was measured as a function not of compression but of tension in the spring wires. All the air connections were made with 1/16 in. I.D. plastic tubing. Properly, the flows as well as the pressures should have been measured and the pressure-flow characteristics of the tubing obtained so that the actual pressures at the oscillator could be determined. Time did not permit this.

Each output line was equipped with a valve in series and a bleed valve. The valves in series allowed the output lines to be opened to the pressure transducer alternatively or in combinations. The bleed valves adjusted the pressure and flow levels of the output. The valves were small and simple, made with 6-32 screws in a plastic block.

There were three provisions for adjusting the position of the disk relative to that of the facing port plates. The spacing between them was adjusted by a screw through the base spring support and bearing upon the bottom port plate, controlling its vertical position. The clearance between the port plates was fixed by spacers. The port plates could be rotated in the housing to adjust angular position. The lateral position of the disk could be adjusted by adjusting the position of the top support for the springs. This adjustment was extremely difficult; it would have been better to make port plates adjustable laterally so that their position in all directions could be easily adjusted by screws while the oscillator was running.

The largest pressure signal at the output was obtained with the output line bleed valves completely closed. The leakage flow in the oscillator was more than the flow required for maximum output pressure. The only output measurements taken were pressure measurements with the bleed valves closed.

The output measurements were very disappointing. Figure 101 a and b, show five results for two different input conditions, stated there. These were taken with the oscillator in the same condition of adjustment which was the best adjustment obtained. Lack of good adjustment allied with inaccuracies in the oscillator parts were probably responsible for the unequalness of the different outputs. Notice that the driving force supply pressure for both the output measurements is quite a lot larger than the output supply pressure. With these two pressures equal, the oscillator would not run. Considerable damping was added by leakage flow in the clearance spaces. This damping needs to be taken into account in the design of an oscillator of this type.

The result of the frequency versus wire tension test is given in Fig. 102. These data were taken with the output supply shut off. The curving of the line could well be the result of error in measurement. Using equation (212) and the value of $P_{crit} = 7.34$ lb. obtained for this oscillator, we find that for a loading of 10 oz., K should increase by a factor of 1.085 and that ω_0 should increase by $\sqrt{1.085} = 1.042$. For no tension the frequency was 486 cps. This times 1.042 is 506 cps. The measured frequency for 10 oz. tension was, from the curve, 507 cps, and from the data point itself, 108.5 cps.

These frequency measurements were made by counting the number of cycles in oscilloscope photographs of leakage flow in the output lines. The sweep time was 2 milliseconds for 19 cm sweep. Better apparatus, such as a precise electronic oscillator, could beat against the pneumatic oscillator, indicating the short-time stability of the pneumatic oscillator frequency as well as the long-term changes.

With the output air supply turned off, the frequency as a function of driving force supply pressure was measured. As mentioned earlier

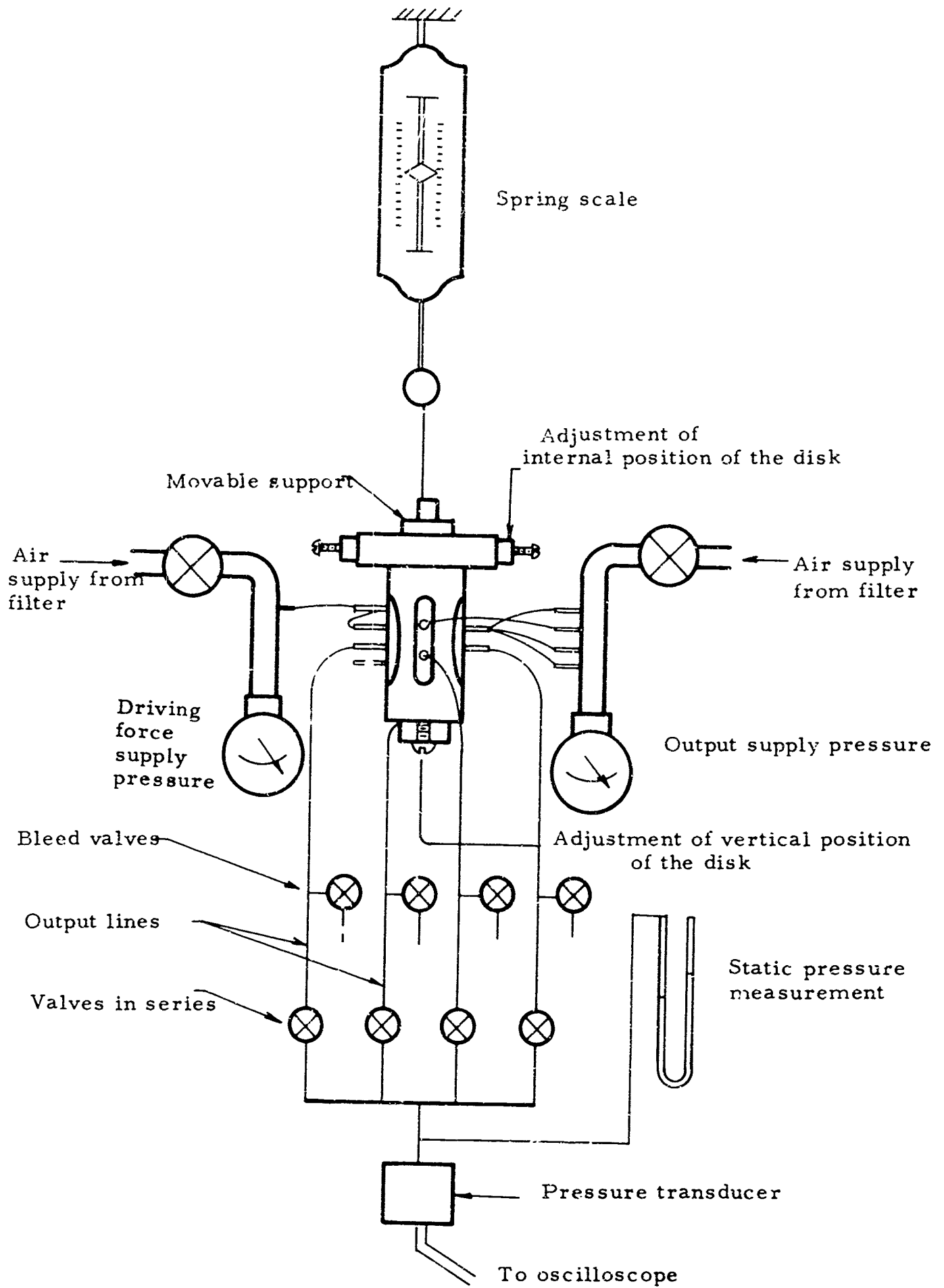
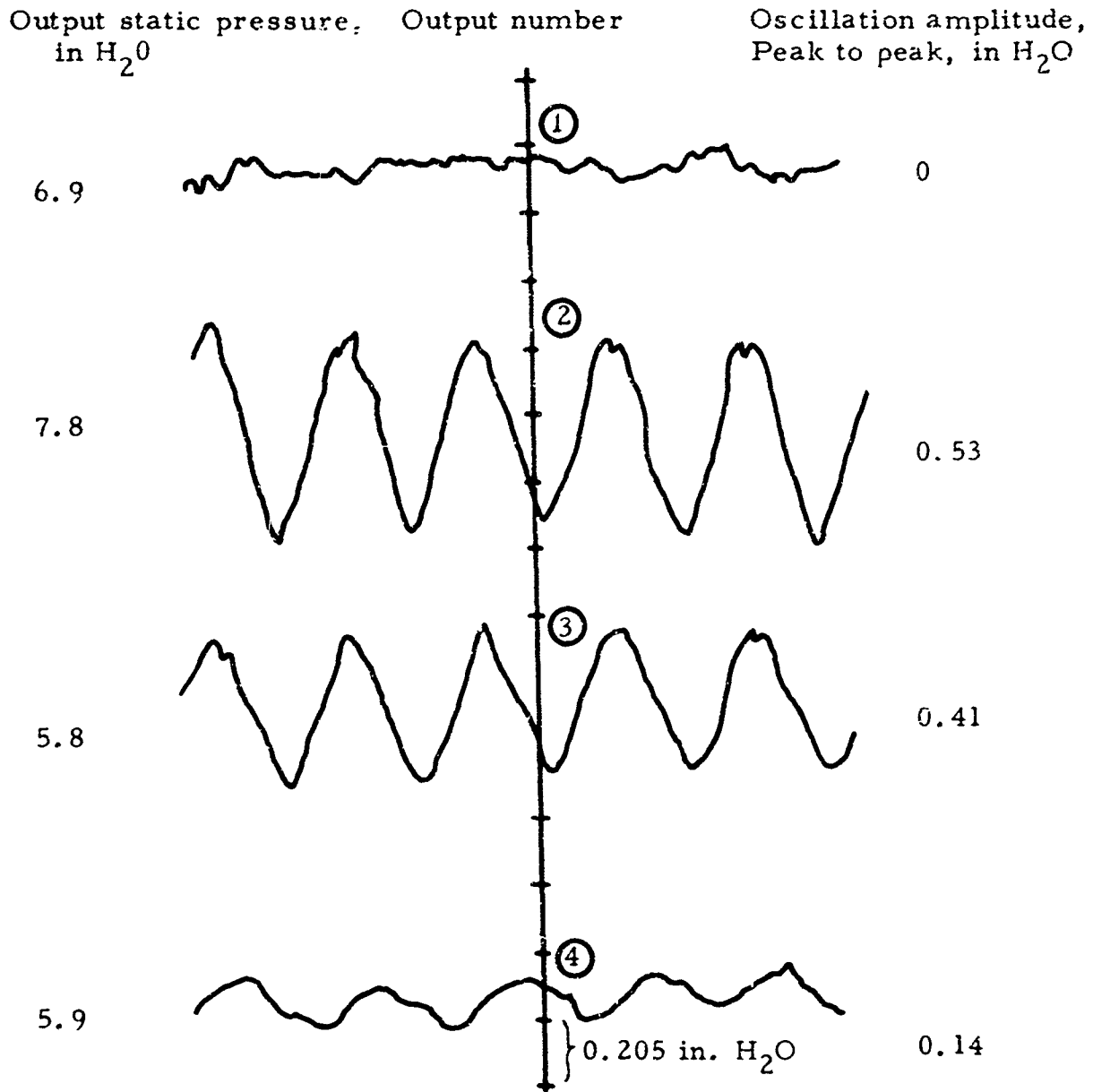
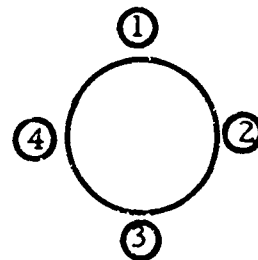


Fig. 100. Third Oscillator Test Setup.



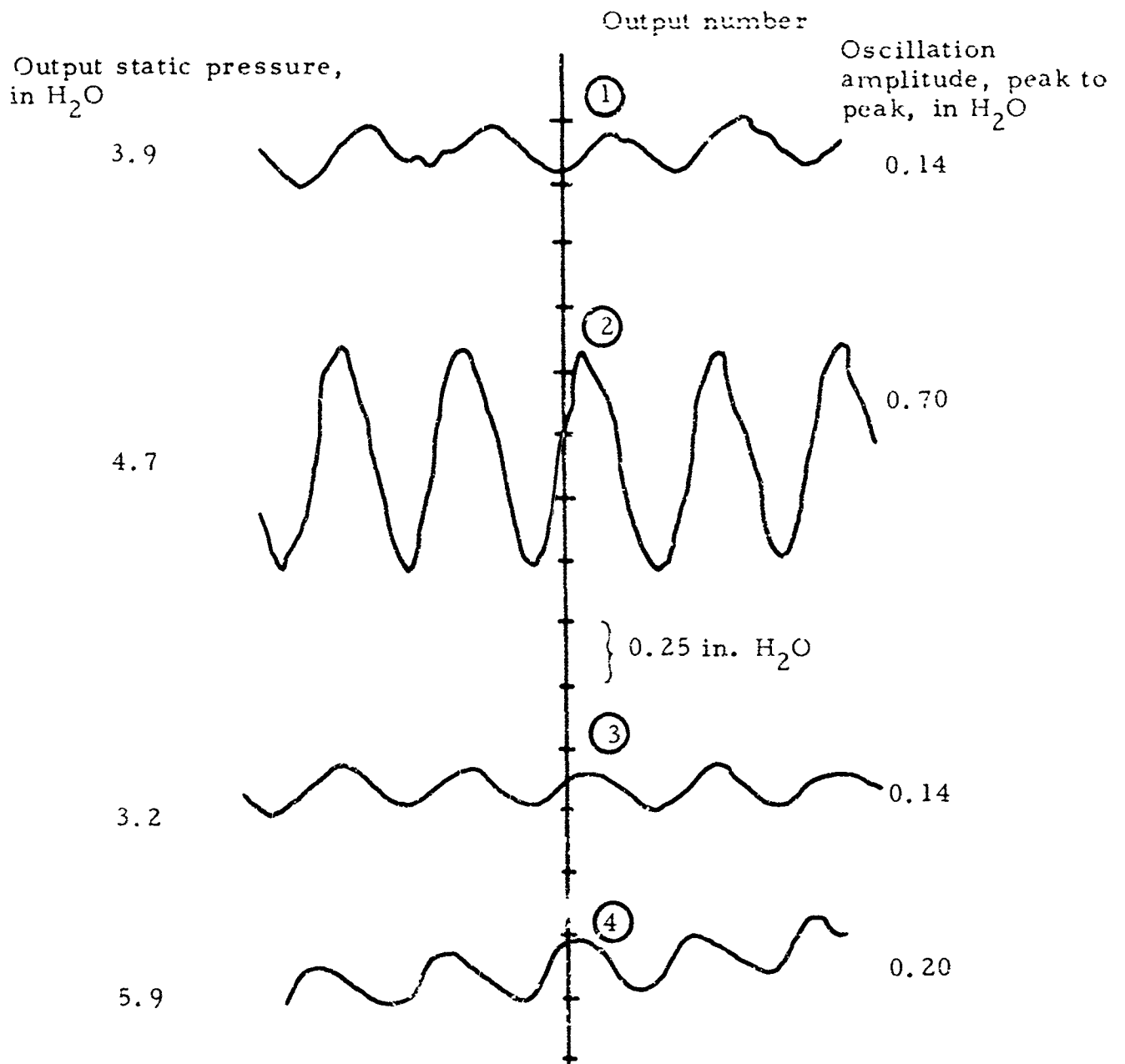
Driving force supply = 25 psig.

Output supply = 10 psig = 27.7 in. H_2O



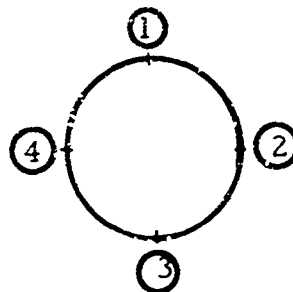
Geometric
relations
between
outputs

Fig. 101a. Third Oscillator Output (Tracings from Photographs).



Driving force supply = 25 psig

Output supply = 5 psig = 13.8 in H₂O



Geometric relations between the outputs

Fig. 101b. Third Oscillator Output (Tracings from Photographs).

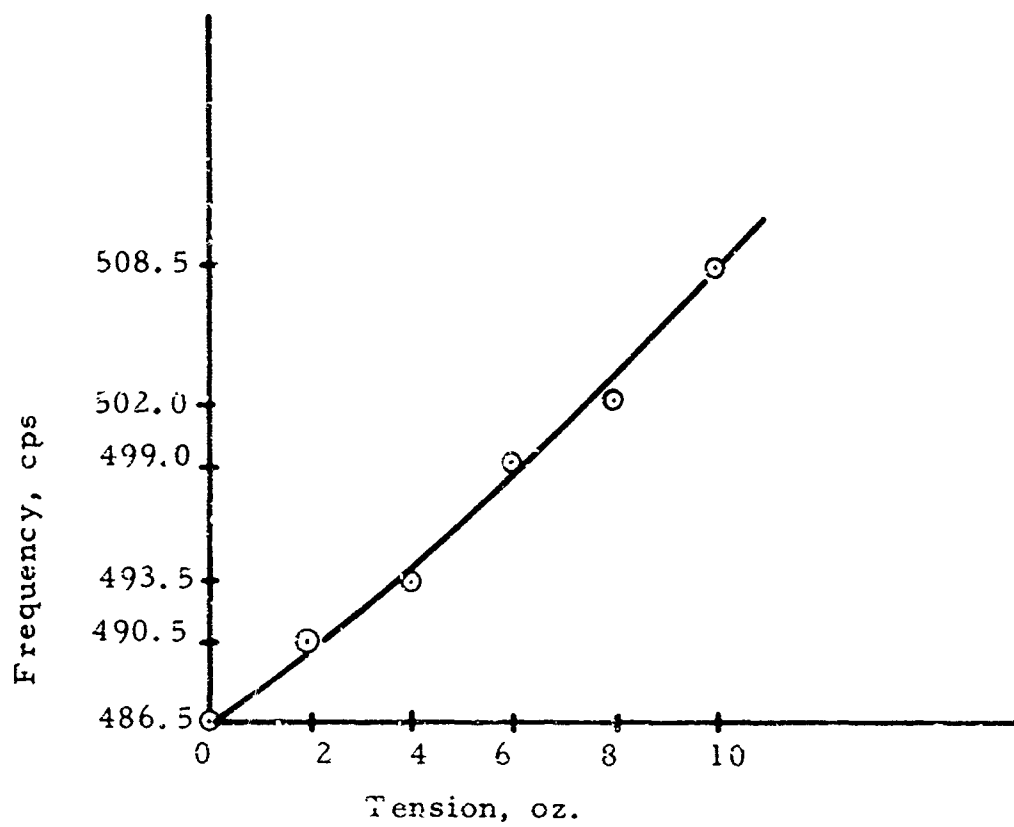


Fig. 102. Results of Frequency-Tension Test.

there was no force-balancing restriction in the exhaust line. The results are given in the following table.

Driving Force

<u>Supply Pressure, psig</u>	<u>Frequency, cps</u>
22	484.0
26	485.5
30	486.0
34	485.0
38	484.5

The frequency figures are precise to not more than ± 0.1 per cent, or 0.5 cps. The largest frequency difference is 2 cps for a pressure difference of 8 psi, or 0.05 per cent per psi.

6.11. Conclusions

Because of the output of the third oscillator was so small, one might conclude that it would be useful only for driving an amplifier, probably of the fluid-jet type. A different approach would, therefore, be to assume that anything vibrating would be useful if amplifiers were properly applied to it, and then to design something to vibrate with a constant frequency. An oscillator driven as the second and third oscillators were driven would merely use the exhaust behind the vanes to drive one, two, or more amplifiers.

A possible design of a very precise oscillator, and also one with relatively large clearances, is given in Fig. 103. The amplitude would not be large enough to pull the inner ends of the slots out of the air jets or the outer ends into the jet. Pressure forces on all surfaces perpendicular to radii would be nearly the same all around the disk. The driving-force versus radius curve would not turn downwards in the range of amplitudes of interest, so to make the oscillator operate at all properly, a jet amplifier control could be necessary.

Pitot tubes set beneath the slots at the proper radius and connected together would sense the amplitude and cause the jet supplying the oscillator to flip away from its receiver port when the oscillation amplitude became

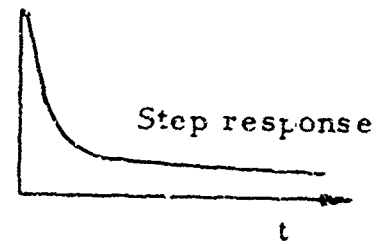
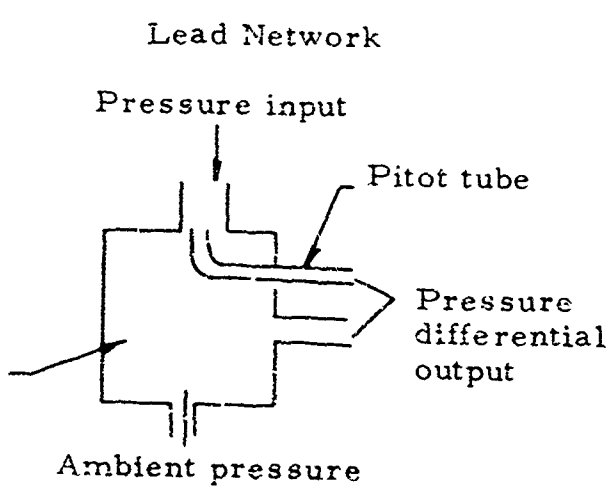
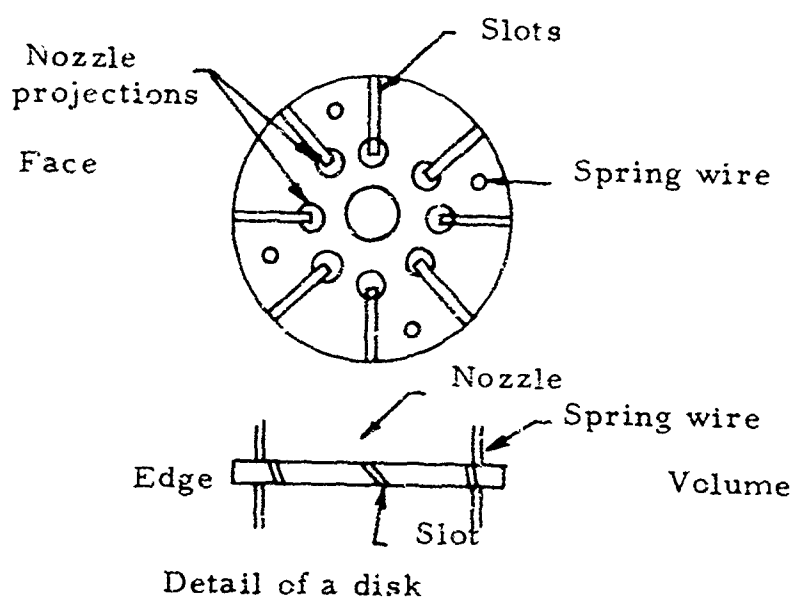
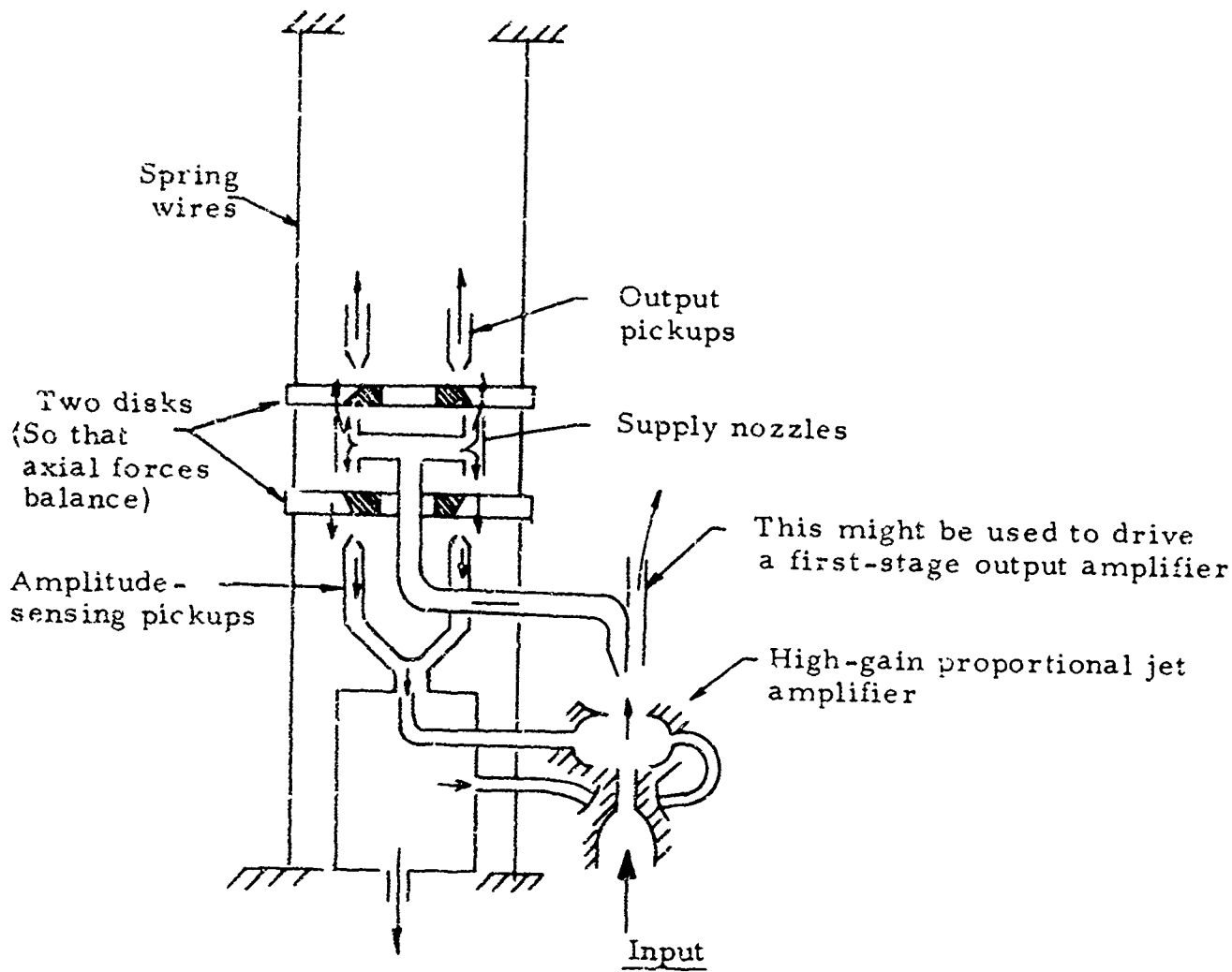


Fig. 103. Jet Amplifier-Controlled Oscillator.

too large. A pneumatic lead network could here be employed, furnishing almost ideal amplitude control if the lag inherent in the amplifier and lines was not too large. As shown, output pickups would mirror the amplitude-sensing pickups. Axial forces would be balanced by virtue of the twin-disk design.

Two subjects which might be investigated are the effect of external random vibration on the frequency of a circular-motion oscillator and the effects of slight variations of spring and damping constants with angle around the oscillator axis.

6.12. Other Oscillators

Quite different oscillator designs were briefly considered also. A pneumatic lag causes oscillation in the device shown in Fig. 104, but the driving force has a large component in phase with the flapper displacement. Since the lag parameters are pressure and temperature dependent, this oscillator has an additional temperature sensitivity and would need a good temperature-insensitive pressure regulator. With a bellows-column temperature compensator, it might be used if the requirement for precision was not too great. It has, over the circular-motion oscillator, the advantage of one-dimensional motion. Oscillation might be angular, rather than translational, so that a properly balanced oscillator would be insensitive to linear acceleration in any direction.

When the flow of a fluid is reduced, pressure forces are needed to change the momentum; these pressure forces are in phase with the velocity of the valve causing the change in flow. For the oscillator shown in Fig. 105, the motion of the oscillating member toward one side increases the restriction at a on one side and decreases it on the other side. The fluid momentum in region c increases on one side and decreases on the other. The pressure changes necessary to produce the momentum changes have opposite signs on the two sides of the oscillating member, and a net lateral force results. It is in phase with the rate of restriction change at a and the velocity of the oscillating member. By adjusting the restriction at b, the net steady-state pressure moments active on both sides of the oscillating member, including regions c and d, can be reduced to zero. Because of this sensitive adjustment, this oscillator would be quite sensitive to changes in the downstream impedance and would have to be used in connection with some form of amplifier. Furthermore, no convenient cut-off technique for high pressure is apparent.

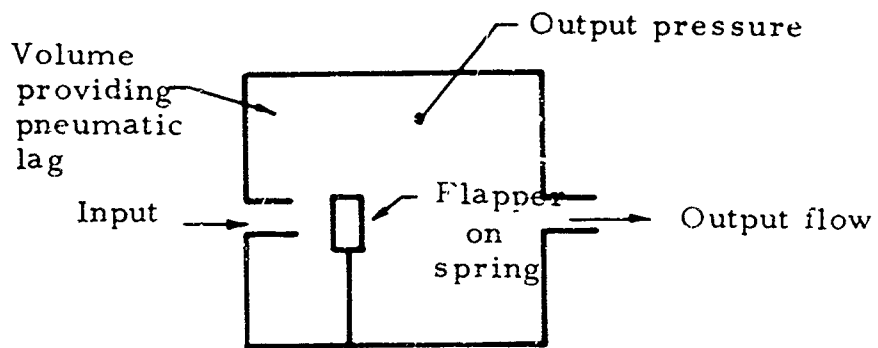


Fig. 104. Another Oscillator.

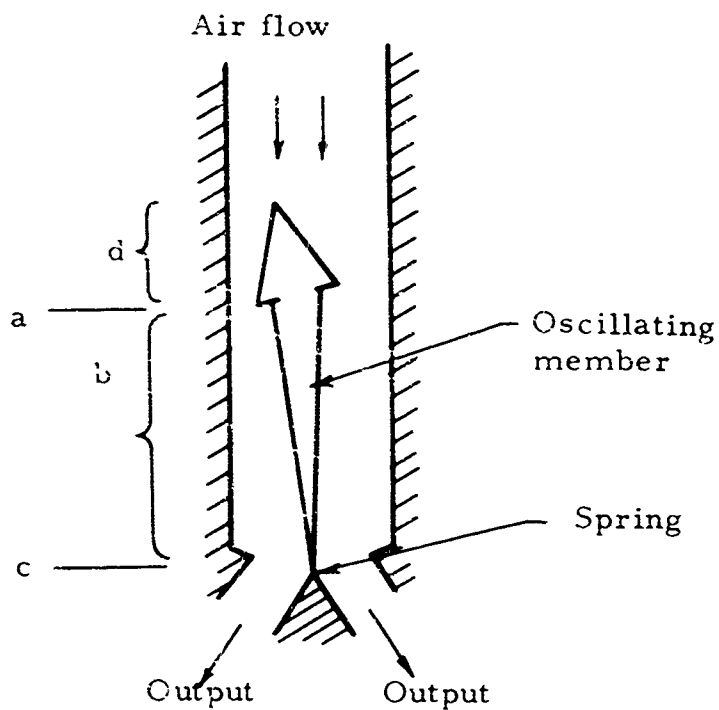
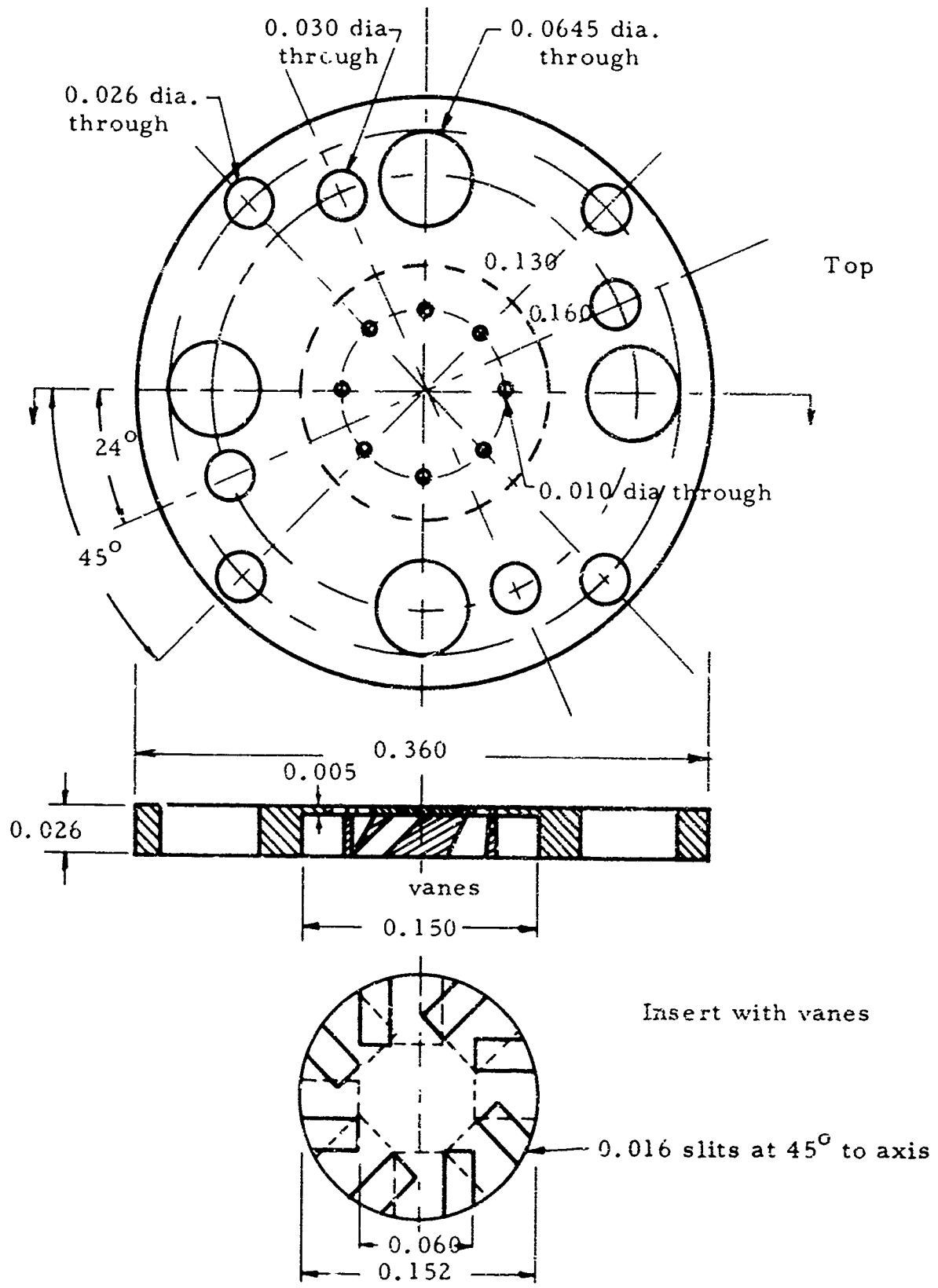
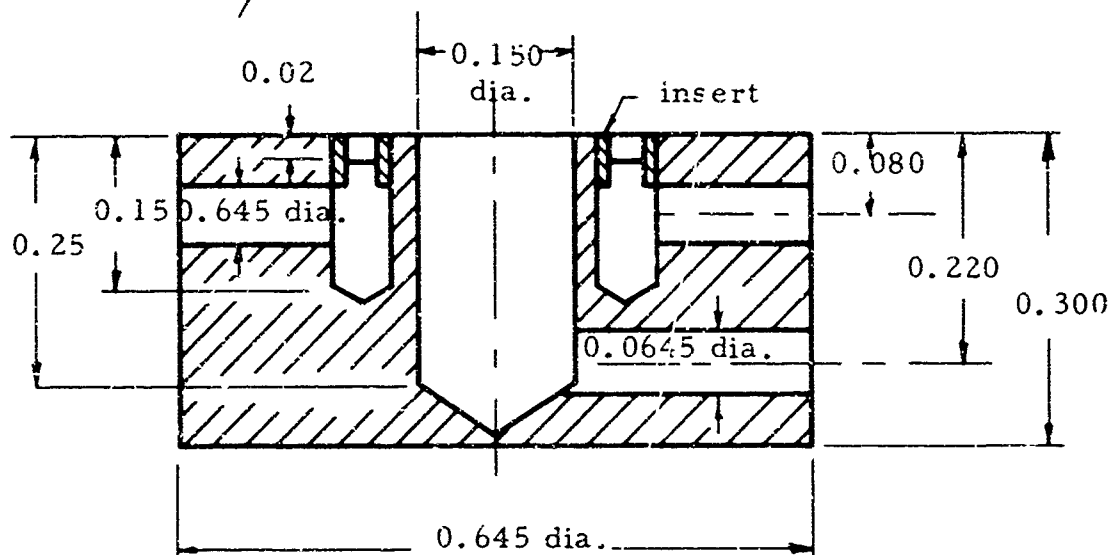
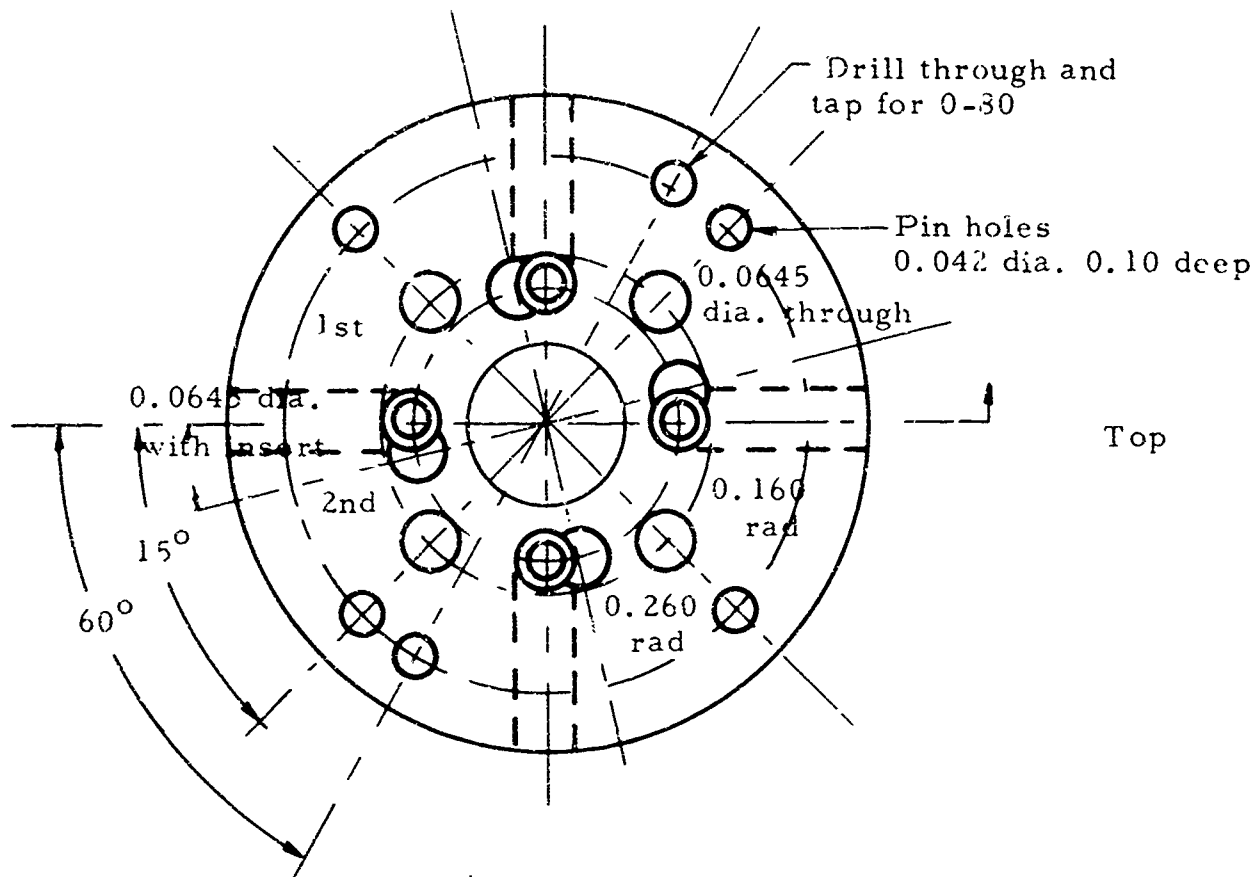


Fig. 105. Another Oscillator.



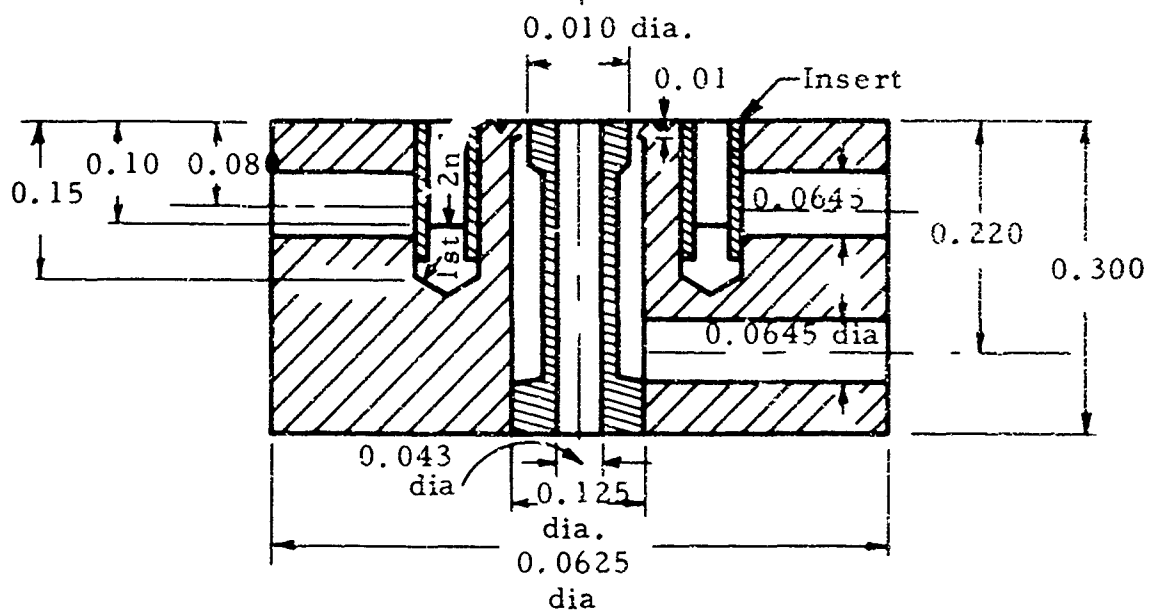
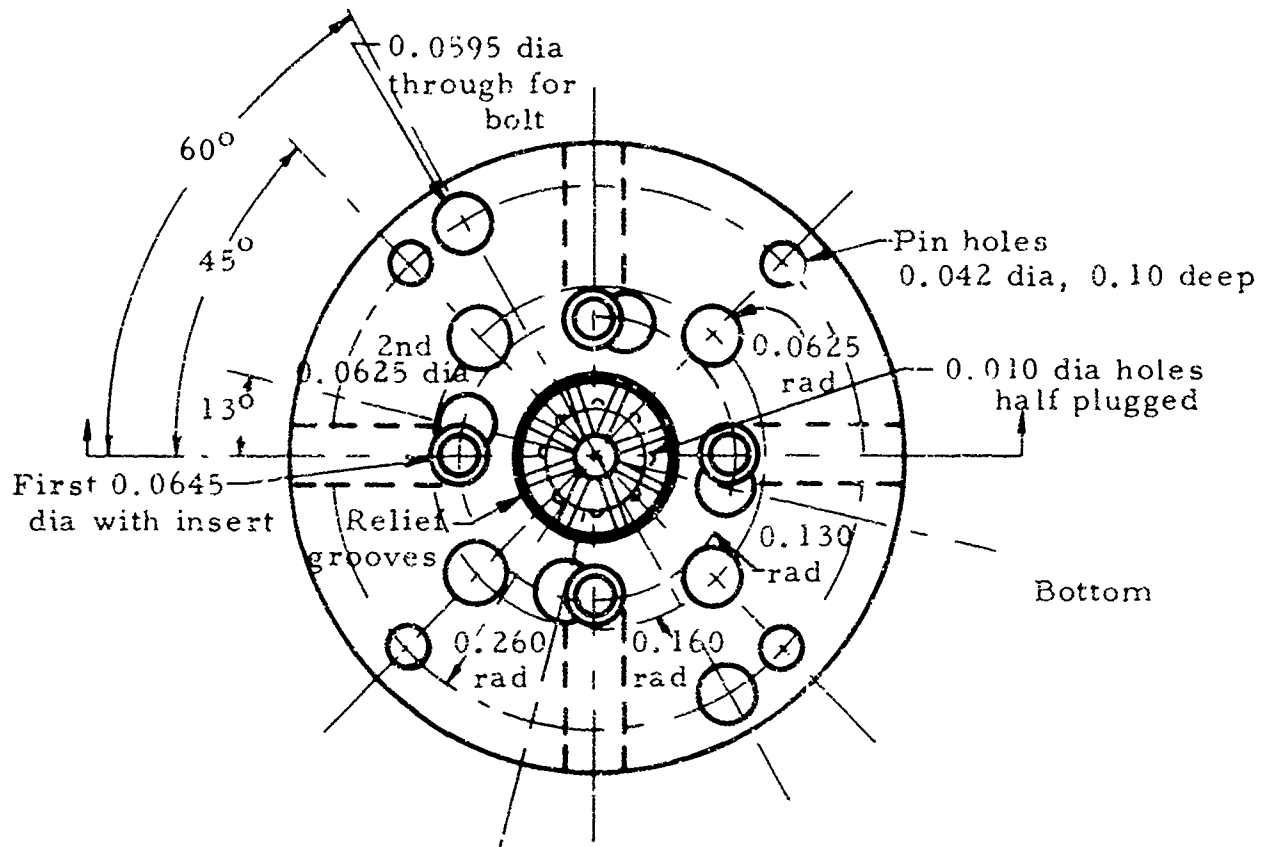
Scale: 10/1

Fig. 107. Detail of Vibrating Disk.



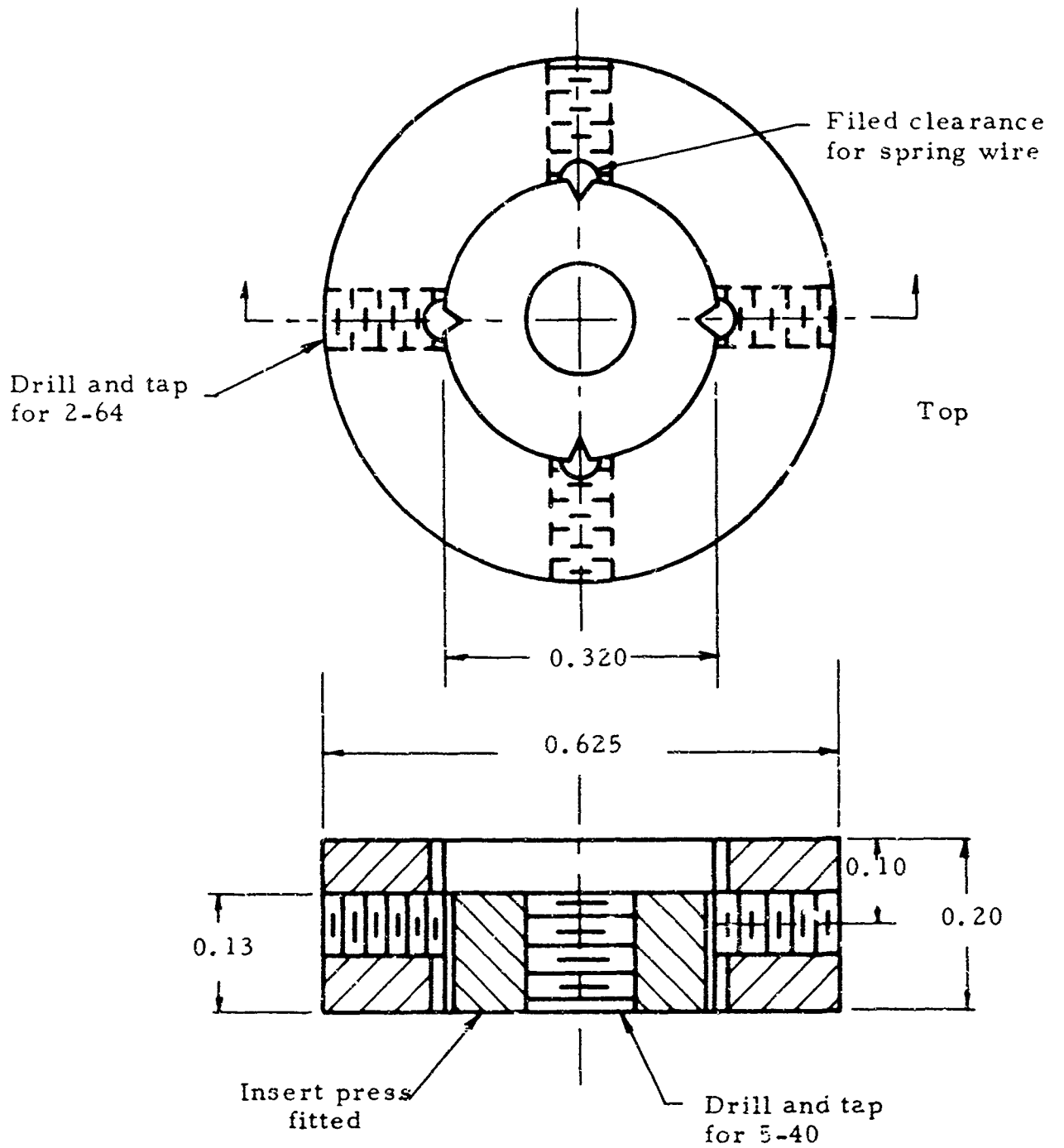
Scale 5/1

Fig. 108. Outlet Port Plate Detail.



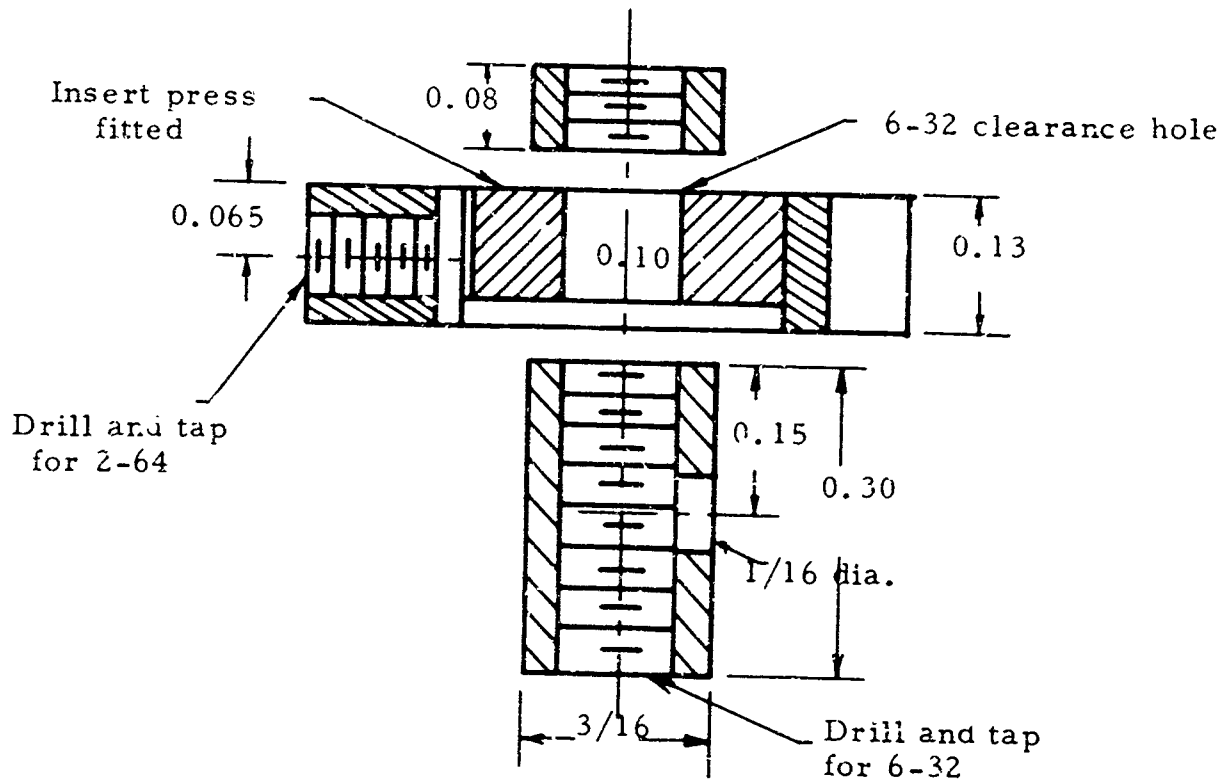
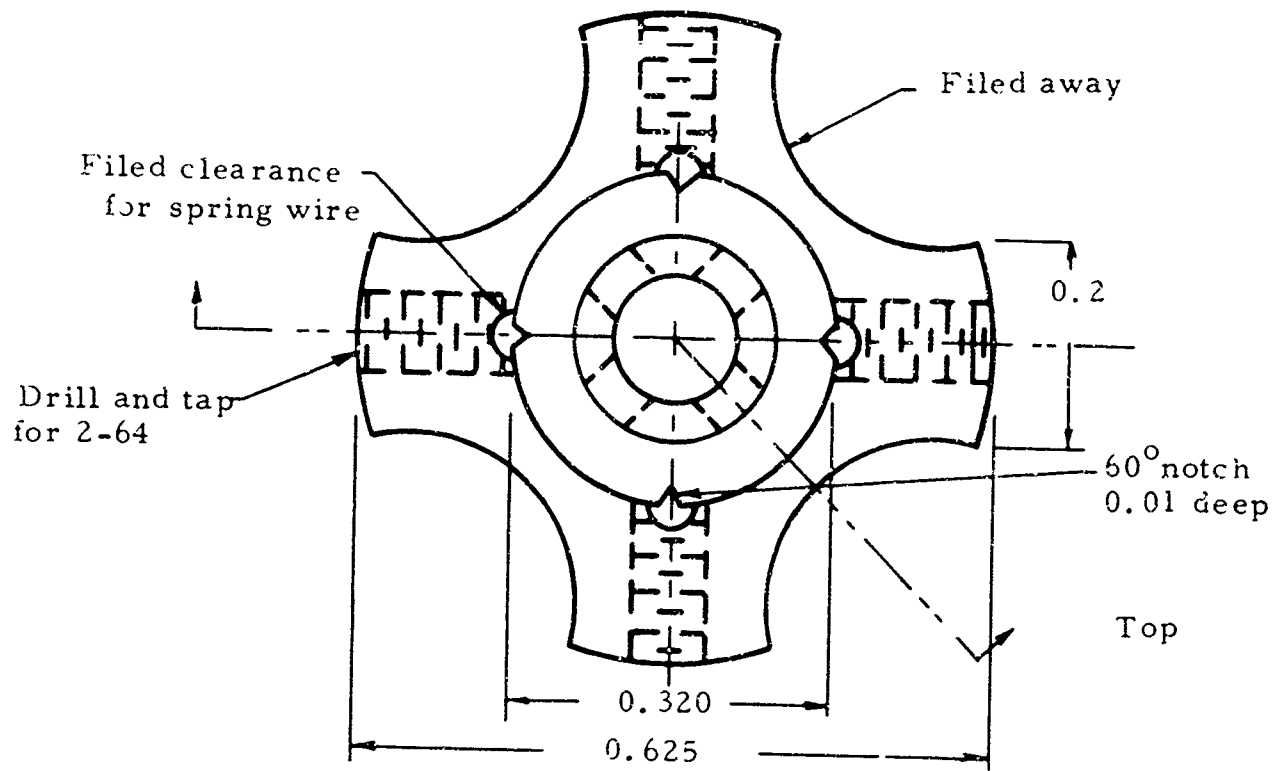
Scale: 5/1

Fig. 109. Inlet Port Plate Detail.



Scale: 5/1

Fig. 110. Bottom Support Detail.



Scale: 5/1

Fig. 111. Top Support Detail.

7. FLUID DIODE SENSOR

7.1. Introduction and Summary

The concept of fluid diodes used to sense the width of the wakes behind compressor blades, along with initial results of a study conducted by W. B. Bails, were given in the first annual report. This section is a continuation which assumes the reader is familiar with that report.

W. B. Bails presented his thesis, "Fluid Diode Sensor", in September 1963⁺, and performed a little analysis thereafter. Of the three "large-scale" diode types tested, only one, the "vortex diode", gave a resistance ratio approaching the desired value. The flow was turbulent. For corresponding small-scale models the flow was basically laminar; all the resistance ratios were reduced, with even that for the vortex diode being unsatisfactory. Nevertheless, dynamic tests were run, with the realization that better diodes would eventually be needed. The vortex diode appeared to have a low cut-off frequency, rendering it useless for the high frequency response required for blade-wake sensing.

Subsequently, A. A. Khaliq built a model of the Tesla diode which was briefly tested statically by F. Brown. The static operation was superior to that of the other diodes, although a turbulent flow is still essentially necessary. Further work should be done on these diodes, including dynamic testing; they seem to be a practical basis for a diode sensor.

7.2. Dynamic Analysis

The linearized dynamic analysis was presented in the first annual report. The nonlinear square-law analysis was carried so far as the step responses of the resistance-volume combination, but not to the steady-state solution to the complete square-wave input. This latter is outlined briefly below; complete details have been given by Bails in his thesis.

Three solution domains exist: unsaturated, partially saturated, and saturated. In the unsaturated case the individual step responses never reach

⁺ Available at cost from the Document Room, 3-156, Engineering Projects Laboratory, M. I. T., Cambridge, Mass. 02139.

the limiting values. In the partially saturated case the limiting value is reached for steps in one direction only; it is reached for steps in both directions in the fully saturated case.

The unsaturated case is shown in Fig. 112. Matching the response segments head-to-tail gives, in the steady state, the deviation between average and the middle value of pressure of

$$\bar{P} - P_m = \frac{P_f}{a + \gamma} \left\{ \left[\frac{a^3}{12} - \frac{a^2}{12} + a \right] f_2 + \left[\frac{\gamma^3}{12\beta^2} - \frac{\gamma^2}{2\beta} + \gamma \right] f_1 + \left[-\frac{a^3}{12} + \frac{a^2}{2} + \frac{\gamma^3}{12\beta^2} - \frac{\gamma^2}{2\beta} \right] \right\} \quad (241)$$

in which

$$f_1 = \frac{s_1 - P_m}{P_f} = \frac{\left[\left(\frac{a^2}{4} - a + 1 \right) \left(\frac{\gamma}{\beta} - \frac{\gamma^2}{4\beta^2} \right) + \left(\frac{a^2}{4} - a \right) \right]}{\left(1 + \frac{\gamma^2}{4\beta^2} - \frac{\gamma}{\beta} \right) \left(\frac{a^2}{4} - a + 1 \right) - 1} \quad (242)$$

$$f_2 = \frac{s_2 - P_m}{P_f} = \frac{\left[\left(\frac{\gamma}{\beta} - \frac{\gamma^2}{4\beta^2} \right) + \left(\frac{a^2}{4} - a \right) \left(1 - \frac{\gamma^2}{4\beta^2} - \frac{\gamma}{\beta} \right) \right]}{\left(1 + \frac{\gamma^2}{4\beta^2} - \frac{\gamma}{\beta} \right) \left(\frac{a^2}{4} - a + 1 \right) - 1} \quad (243)$$

For partial saturation in the forward direction, when

$$a \leq 2; \quad \gamma \geq 2\beta; \quad \frac{a}{\gamma} \leq \frac{1}{\beta} \quad (244)$$

the solution is

$$P - P_m = \frac{P_f}{a + \gamma} \left[-\frac{a^3}{6} + a^2 - a - \gamma + \frac{2}{3} \beta \left(-\frac{a^2}{2} + 2a \right) \right] \quad (245)$$

In the negative direction, when

$$a \geq 1; \quad \gamma \leq 2\beta; \quad \frac{a}{\gamma} \geq \frac{1}{\beta} \quad (246)$$

the solution becomes

$$\bar{P} - P_m = \frac{P_f}{a + \gamma} \left[-\frac{\gamma^3}{6\beta^2} - \frac{\gamma^2}{\beta} + a + \gamma + \frac{2}{3} \left(\frac{\gamma^2}{2\beta^2} - \frac{2\gamma}{\beta} \right) \right] \quad (247)$$

Finally, for the fully saturated case, when

$$a \geq 2; \quad \gamma \geq 2\beta \quad (248)$$

the solution is simply

$$\bar{P} - P_m = \frac{P_f}{a + \gamma} \left[\frac{4}{3} (\beta - 1) + a - \gamma \right] \quad (249)$$

The solutions over-all domains for a particular value $\left| \Delta\tau / \tau_{av} \right| = 0.7$ are plotted in Figs. 112 - 115. In Figs. 116 - 118 linear and nonlinear analyses are compared with some experimental data for a small value of $\left| \Delta\tau / \tau_{av} \right|$.

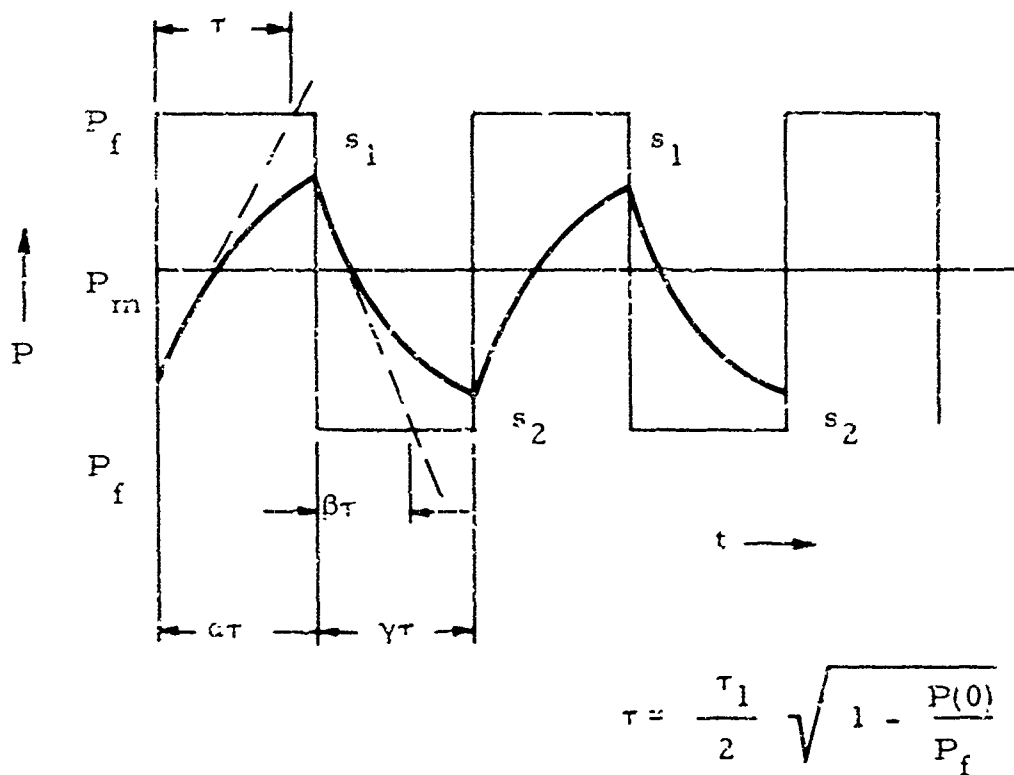


Fig. 112. Nonlinear Analysis of Response to Step-Function
"Unsaturated" Case.

es

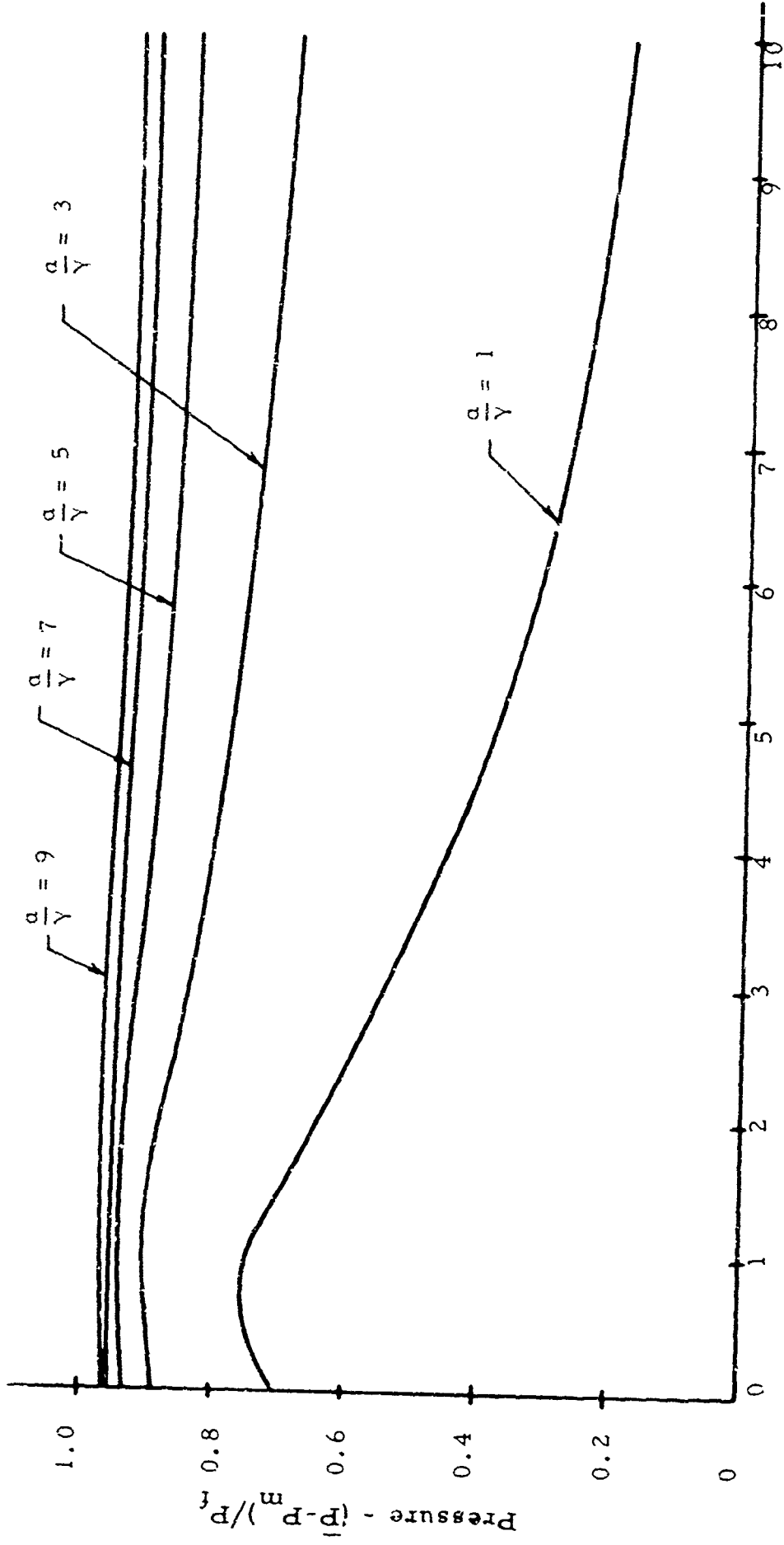


Fig. 113. Nonlinear Analysis of Single Diode Sensor, Forward, $\Delta\tau/\tau\omega = 0.7$.

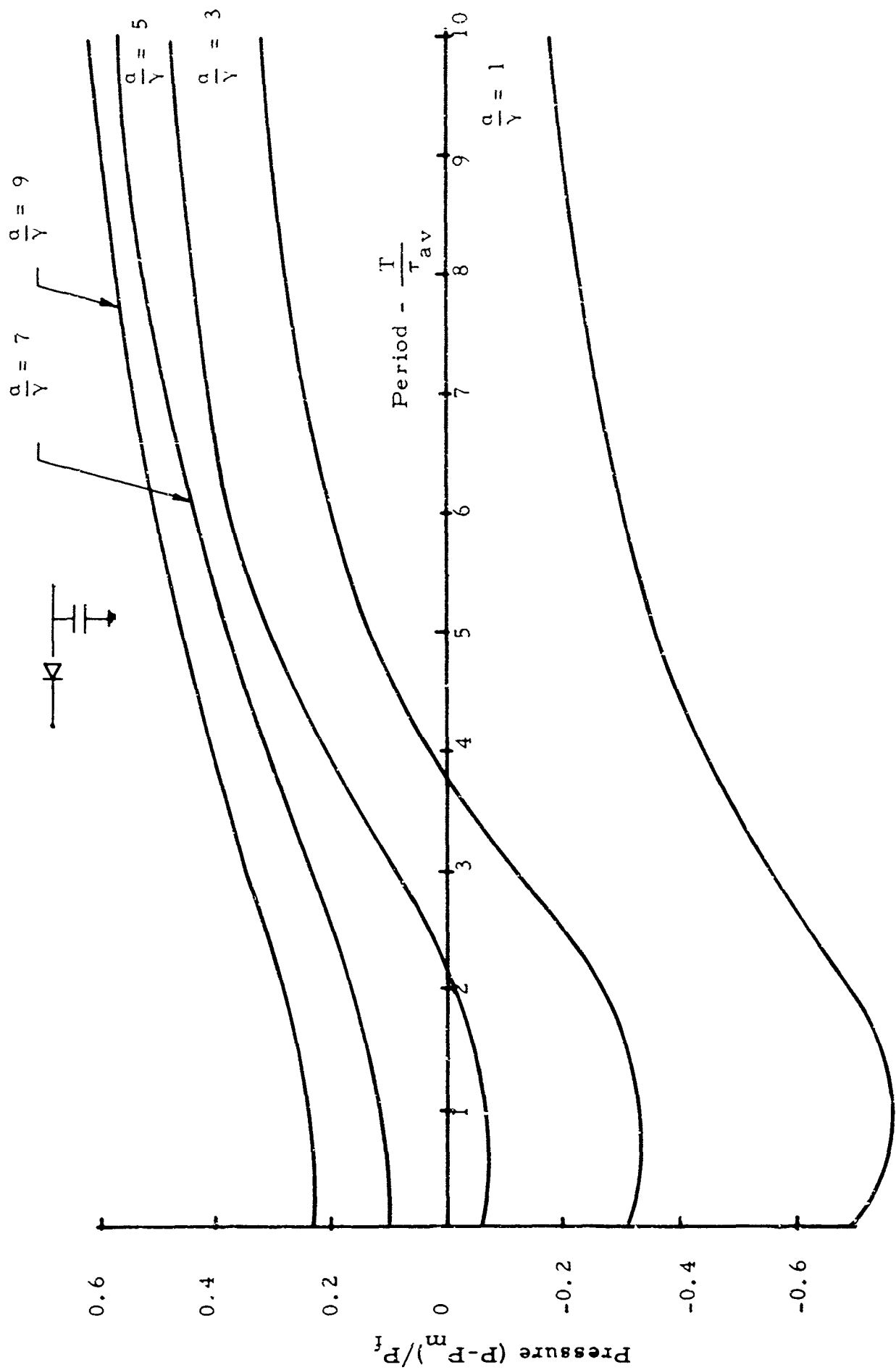


Fig. 114. Nonlinear Analysis of Single Diode Sensor, Reversed, $\Delta\tau/\tau_{av} = 0.7$.

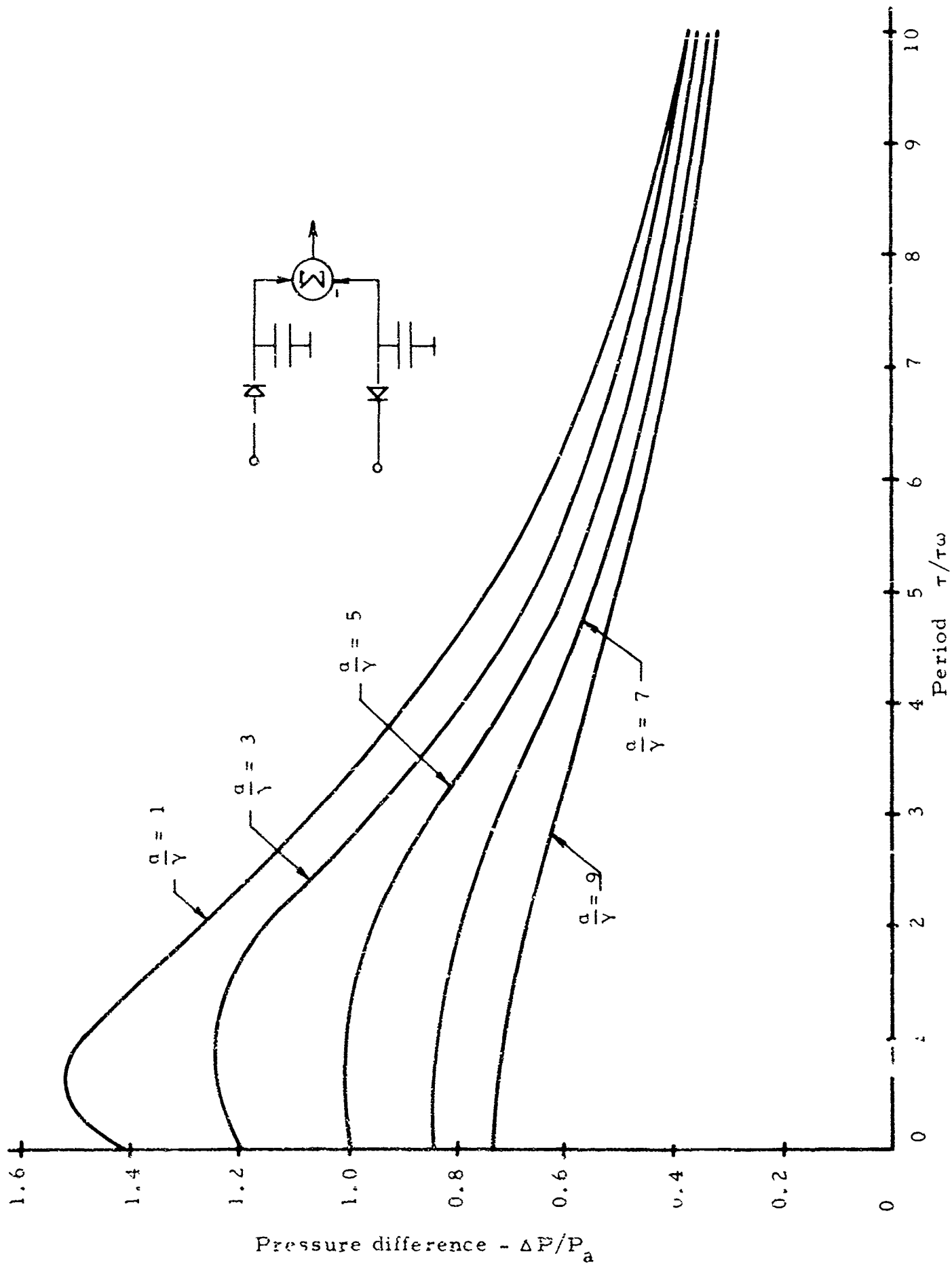


Fig. 115. Nonlinear Analysis of Pressure Difference in Diode Sensors With

7.3. Static Testing - Small-Scale Models

Three models of the nozzle diode were made, employing two basic designs. The two-dimensional diode, shown in Fig. 119b, was modeled directly from the large-scale water-table models using three cascaded nozzles. The other two diodes, shown in Fig. 119a, were three-dimensional, and contained six nozzles each. The vortex diode tested is shown in Fig. 120a and the diffuser diode in Fig. 120b.

The flow through these diodes was nominally laminar, as shown by Table 2 which reports the maximum Reynolds numbers. Since the flow in the large-scale models was turbulent, quite different performance would be expected, and in fact was observed. Experimental results are shown in Figs. 121 - 125. As mentioned earlier, only the vortex diode has even marginally satisfactory static characteristics. Approximate corresponding values of the linear and nonlinear parameters are given in Table 3.

7.4. Dynamic Testing - Small Scale Models

A schematic of the test setup is shown in Fig. 126. The slotted disk pictured in the first annual report was replaced with the disks pictured in Fig. 127, since the first disk was deflecting the jet significantly. Typical resulting dynamic pressures, measured with a 0.02-inch-diameter Kistler piezoelectric transducer, are shown in Fig. 128.

The final experimental results are given in Figs. 116 - 118 and 129 - 137. Since the static performances were already known, the principal interest here is any upper frequency limit to the characteristics. Such a limit is decidedly apparent for the vortex diode, which unfortunately was the only diode tested by Bails with even marginally satisfactory static performance. This limit apparently is inherent to the transient vortex-forming process. Detailed discussions of the experimental procedure and results are given in Bail's thesis.

The failure of the various diodes tested has led to the later work on the Tesla diode.

7.5. Static Testing - Tesla Diode

The Tesla diode tested is shown in Fig. 138 and 139. Tests were performed with hydraulic oil to achieve low, transitional, and high Reynold's numbers. (The characteristic distance used to compute the Reynold's number

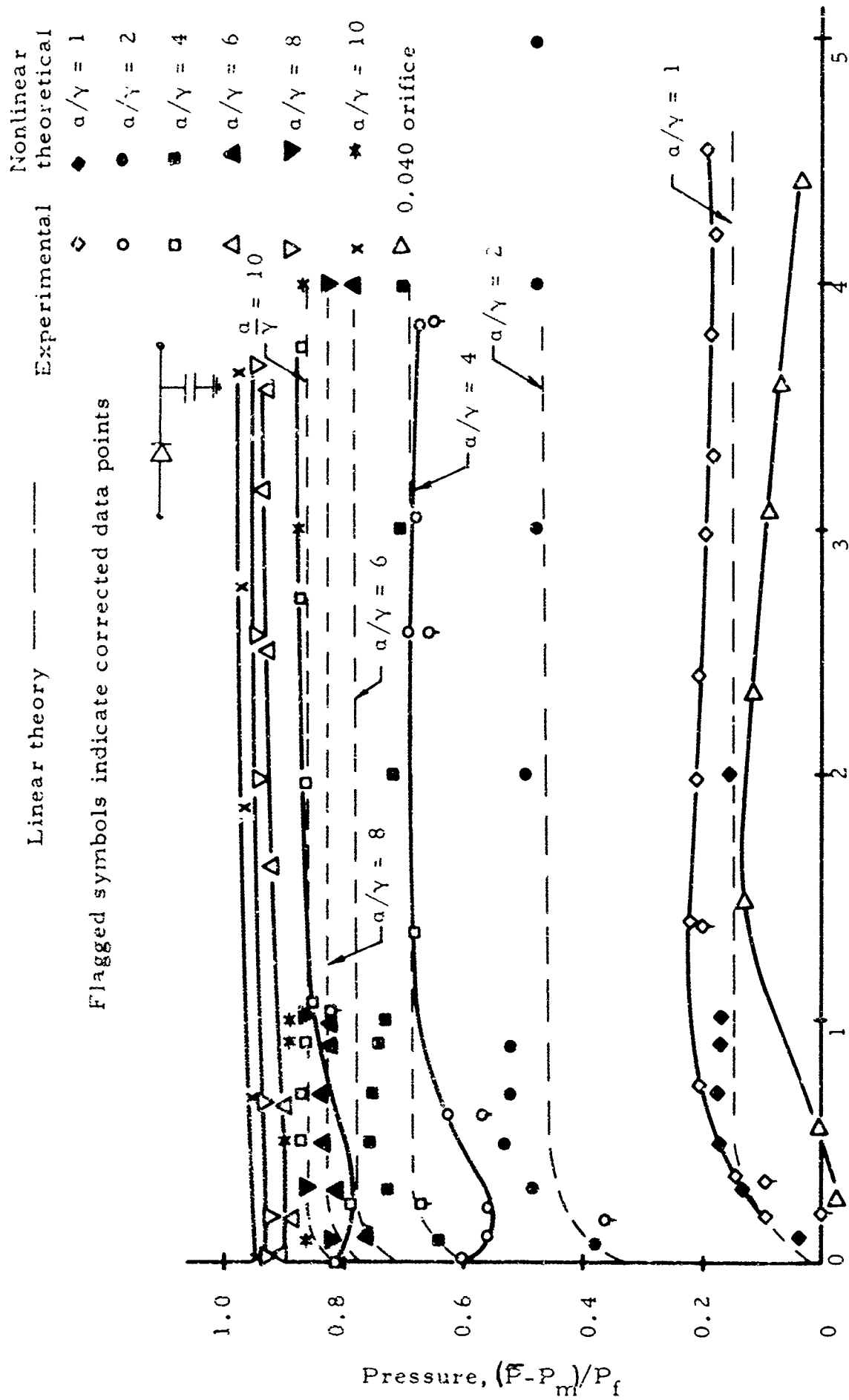


Fig. 116. Frequency Response, 3-D Nozzle Diode (0.040) Forward, With Linear and Nonlinear Theory.

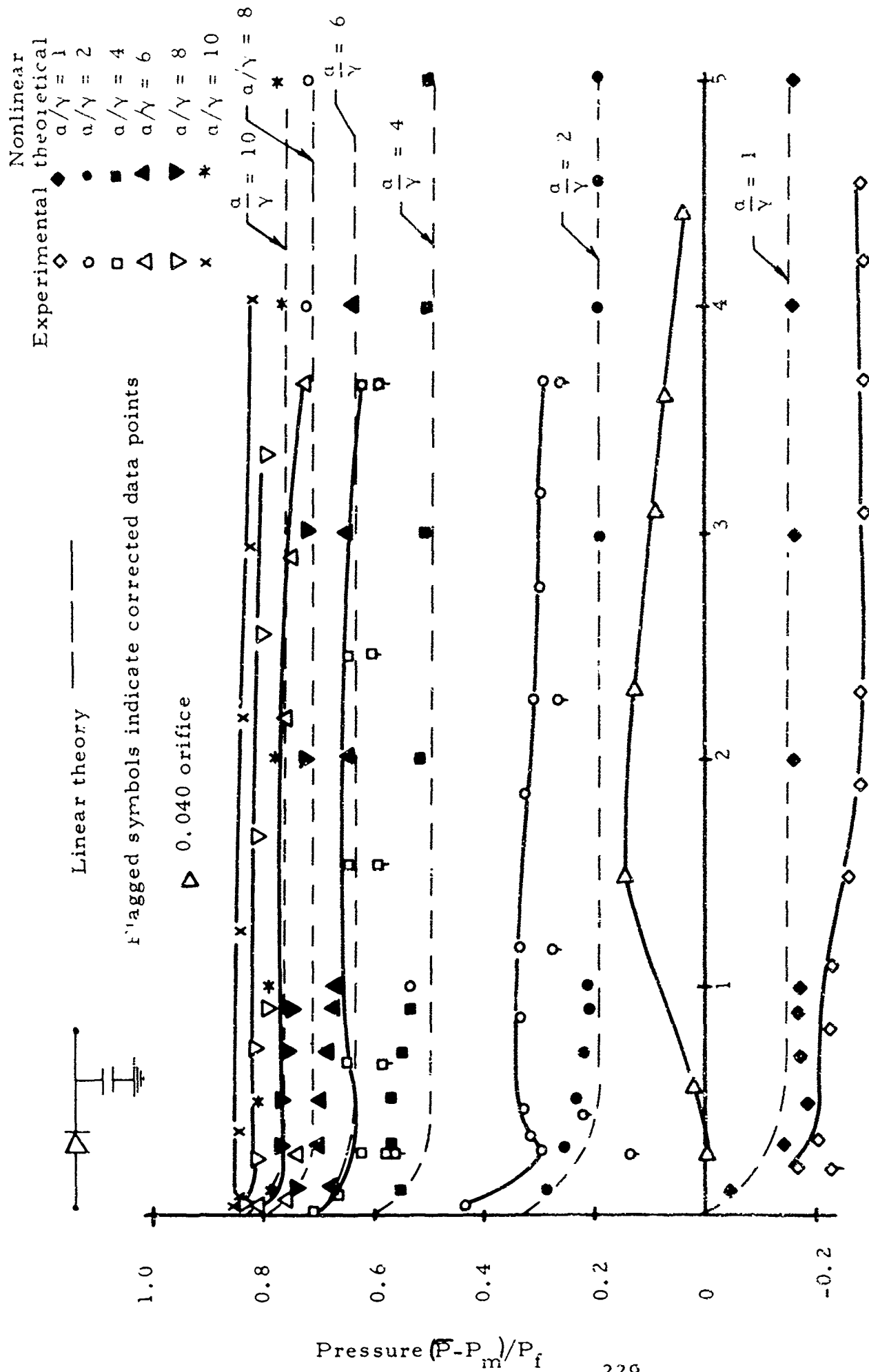


Fig. 117. Frequency Response - 3-D Nozzle Diode (040) Reverse, With Linear and Nonlinear Theory.

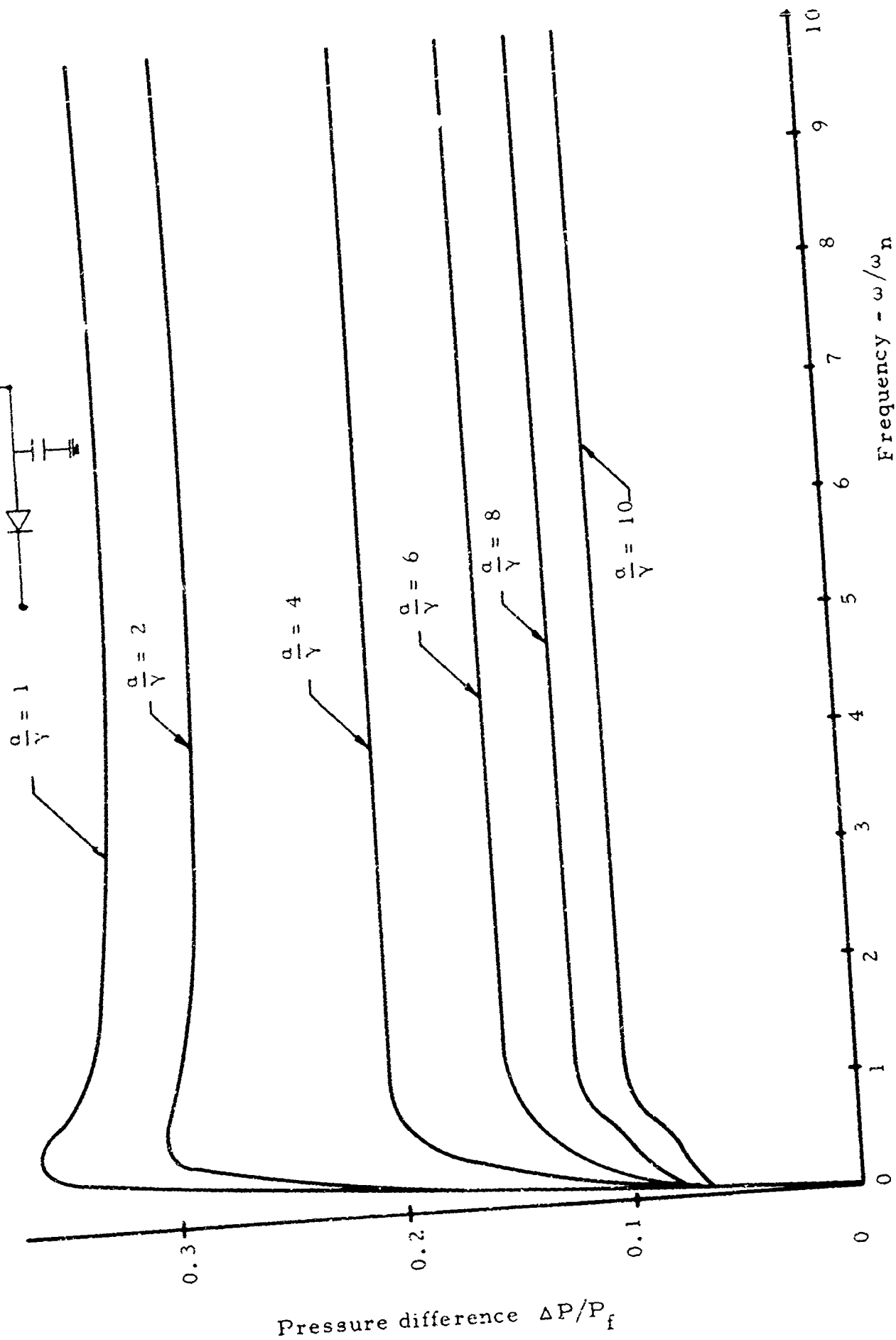
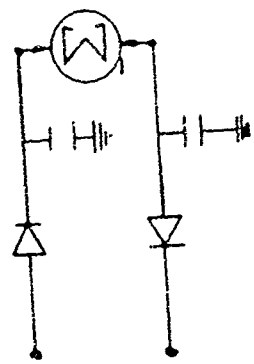


Fig. 118. Nonlinear Analysis of Pressure Difference in Diode Sensors With Opposite Polarity
 $\left| \frac{\Delta T}{T_0} \right| = 0.156$.

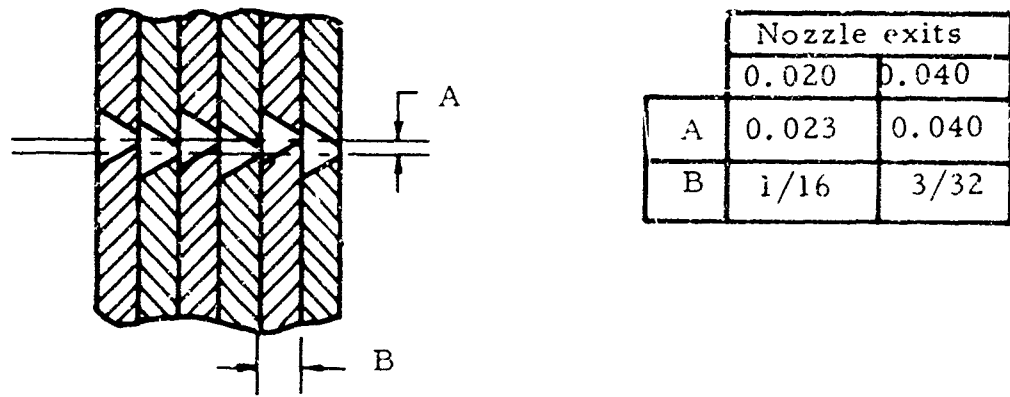
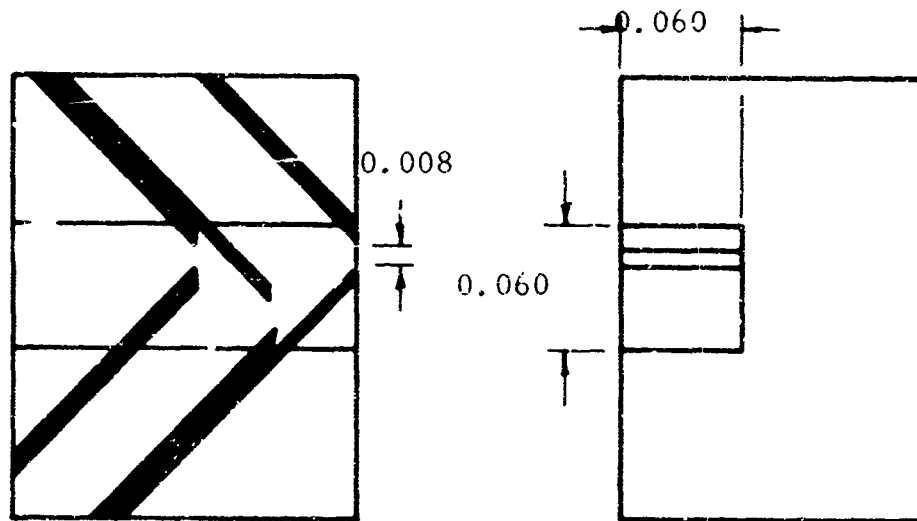
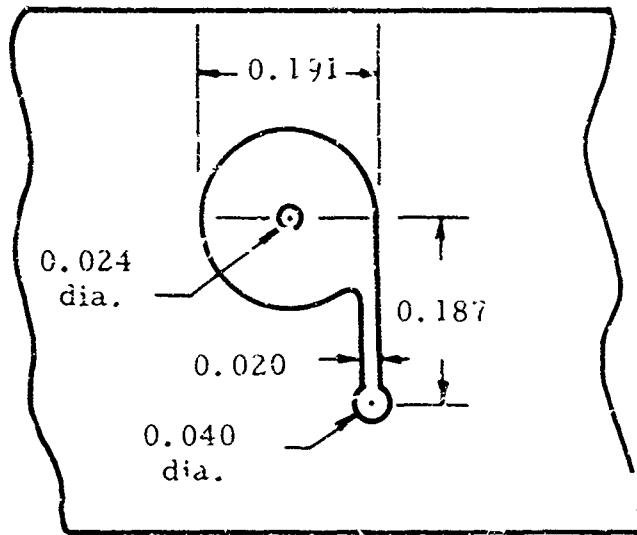


Fig. 119a. 3-D Nozzle Diode, Small Scale.



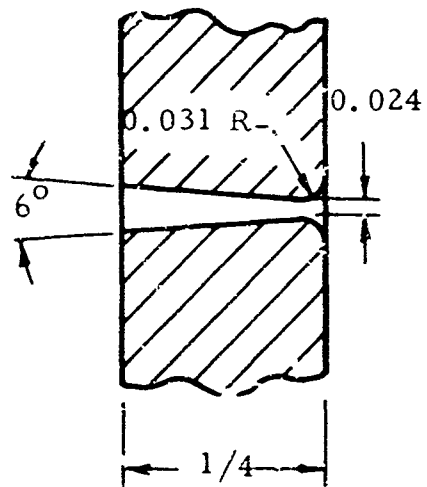
Nozzle wall widths
 Long wall 0.006 in.
 Short wall 0.010 in.

Fig. 119b. 2-D Nozzle Diode, Small Scale.



Diode is
1/16 in. deep

Fig. 120a. Vortex Diode, Small Scale.



Diode is
axisymmetric

Fig. 120t. Diffuser Diode, Small Scale.

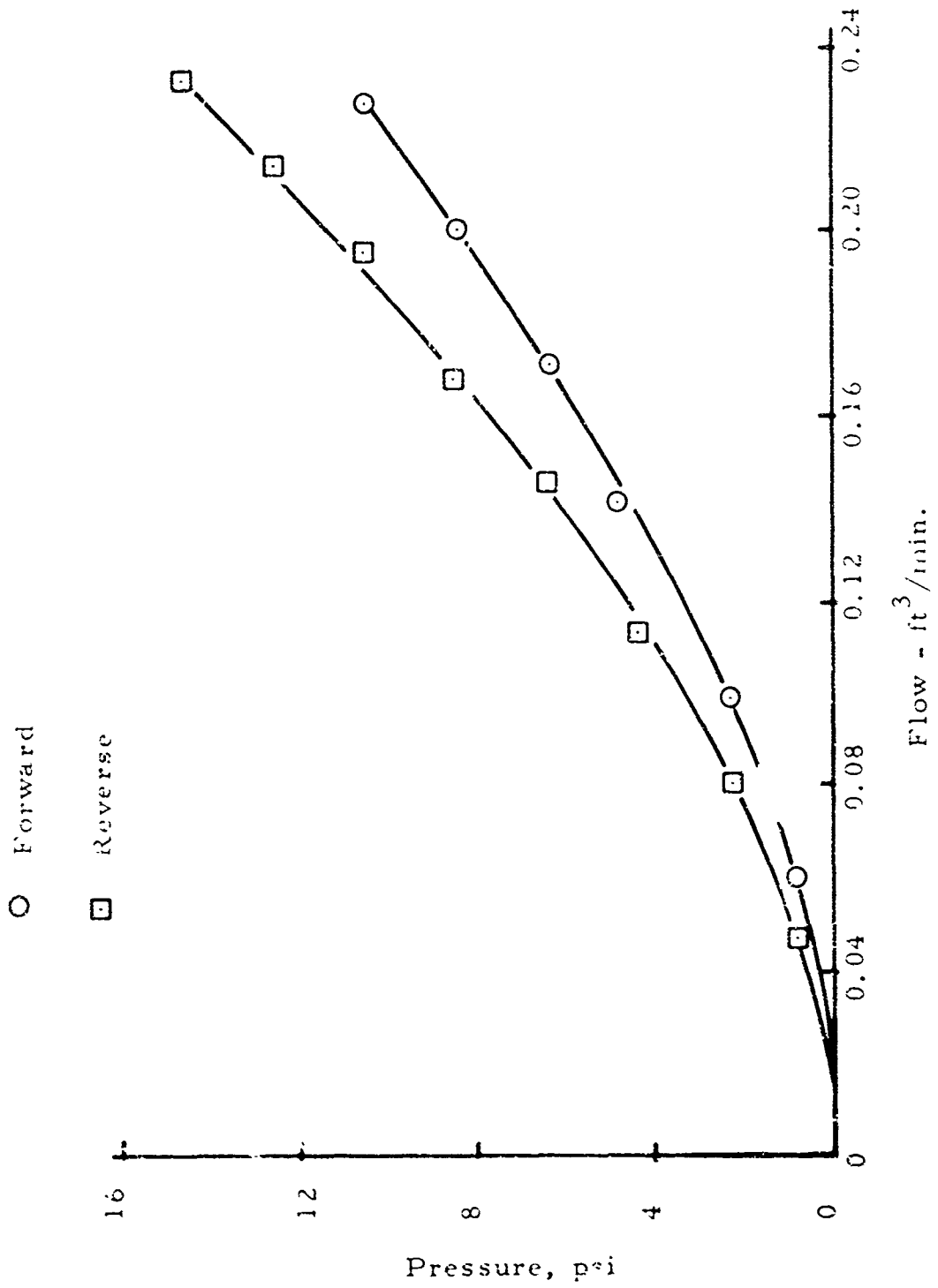


Fig. 121. Pressure-Flow Characteristics, 3-D Nozzle Diode (0.040), Small Scale.

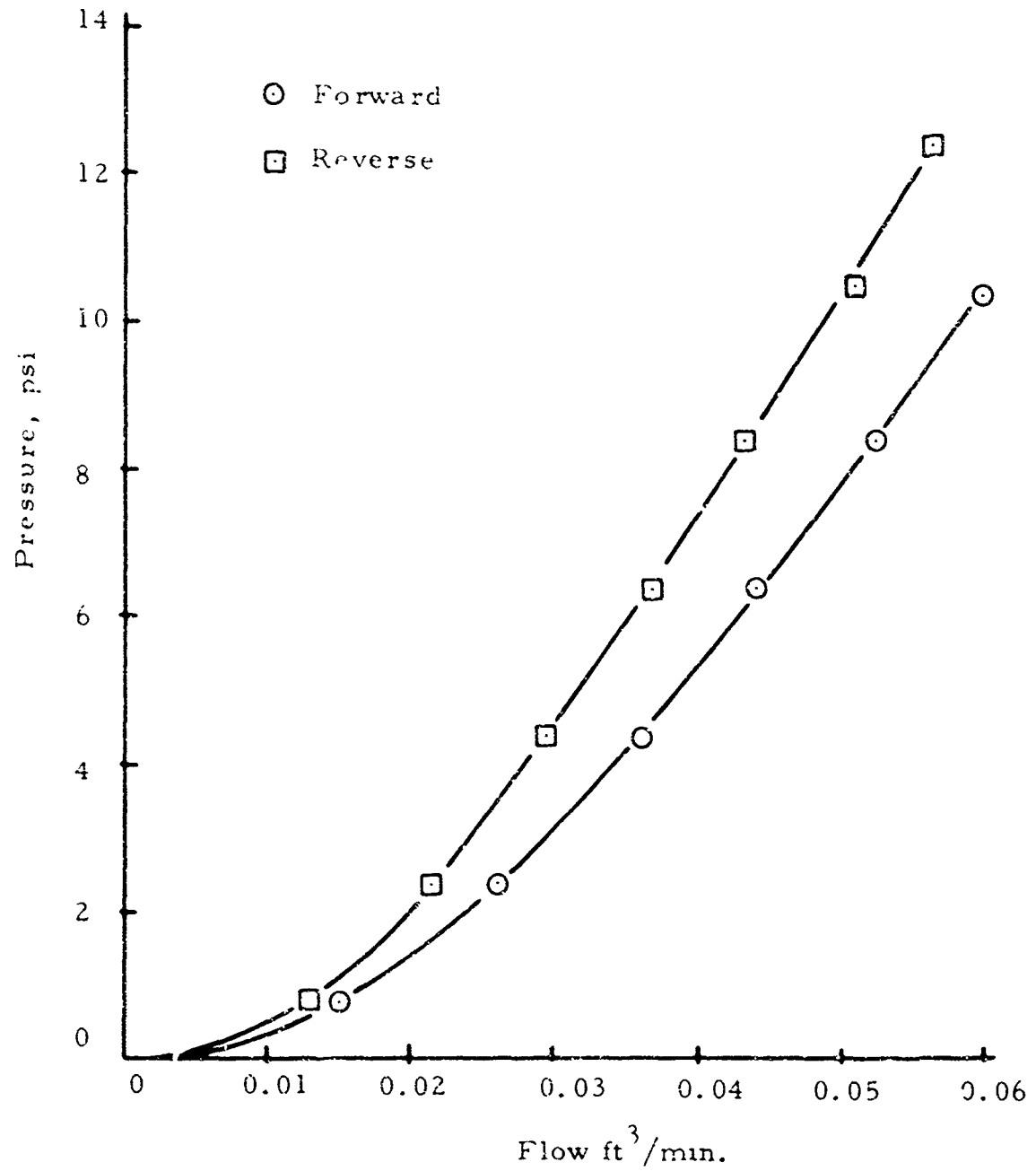


Fig. 122. Pressure-Flow Characteristics, 3-D Nozzle Diode, Small Scale. (0.020)

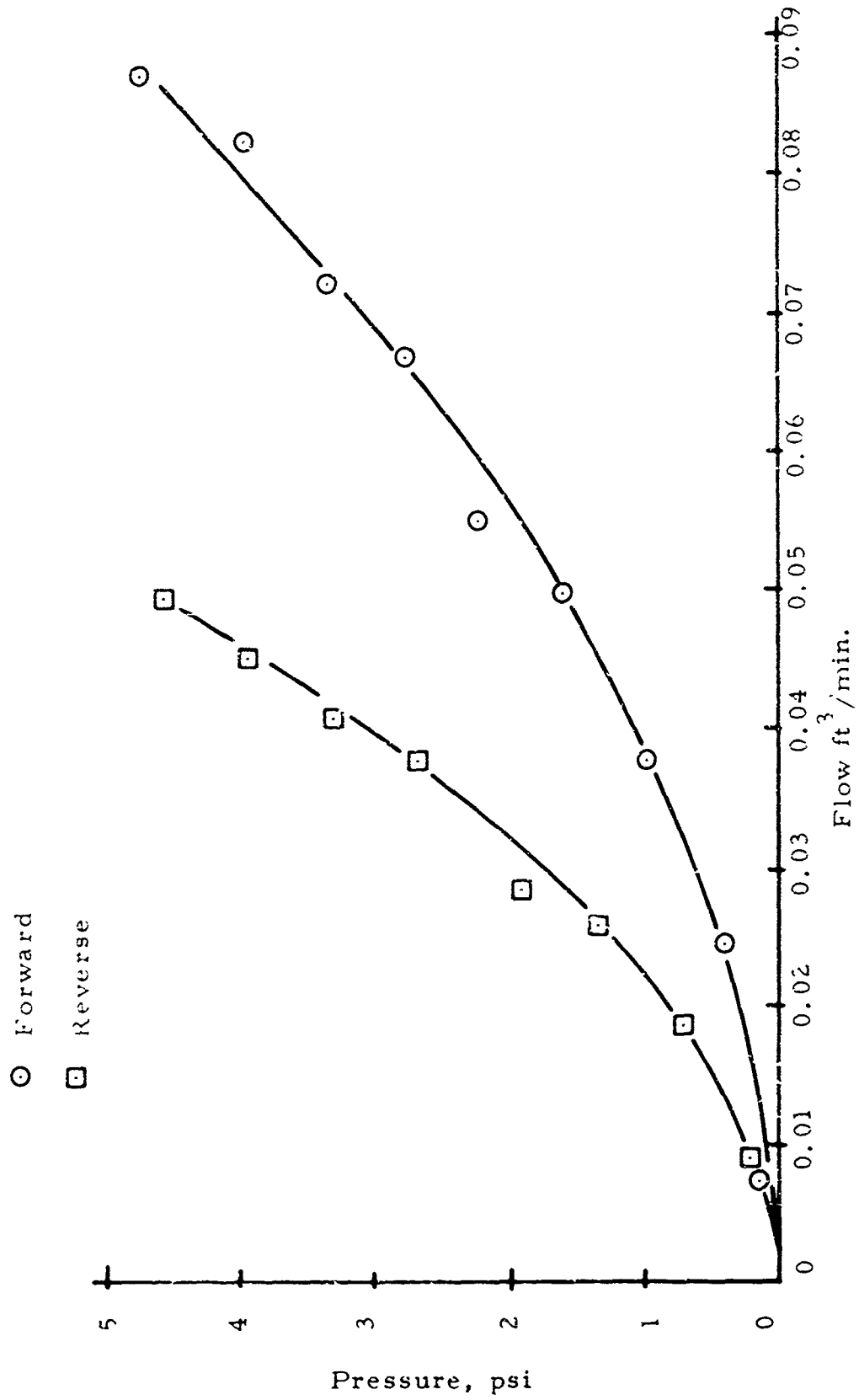


Fig. 123. Pressure-Flow Characteristics, 2-D Nozzle Diode, Small Scale.

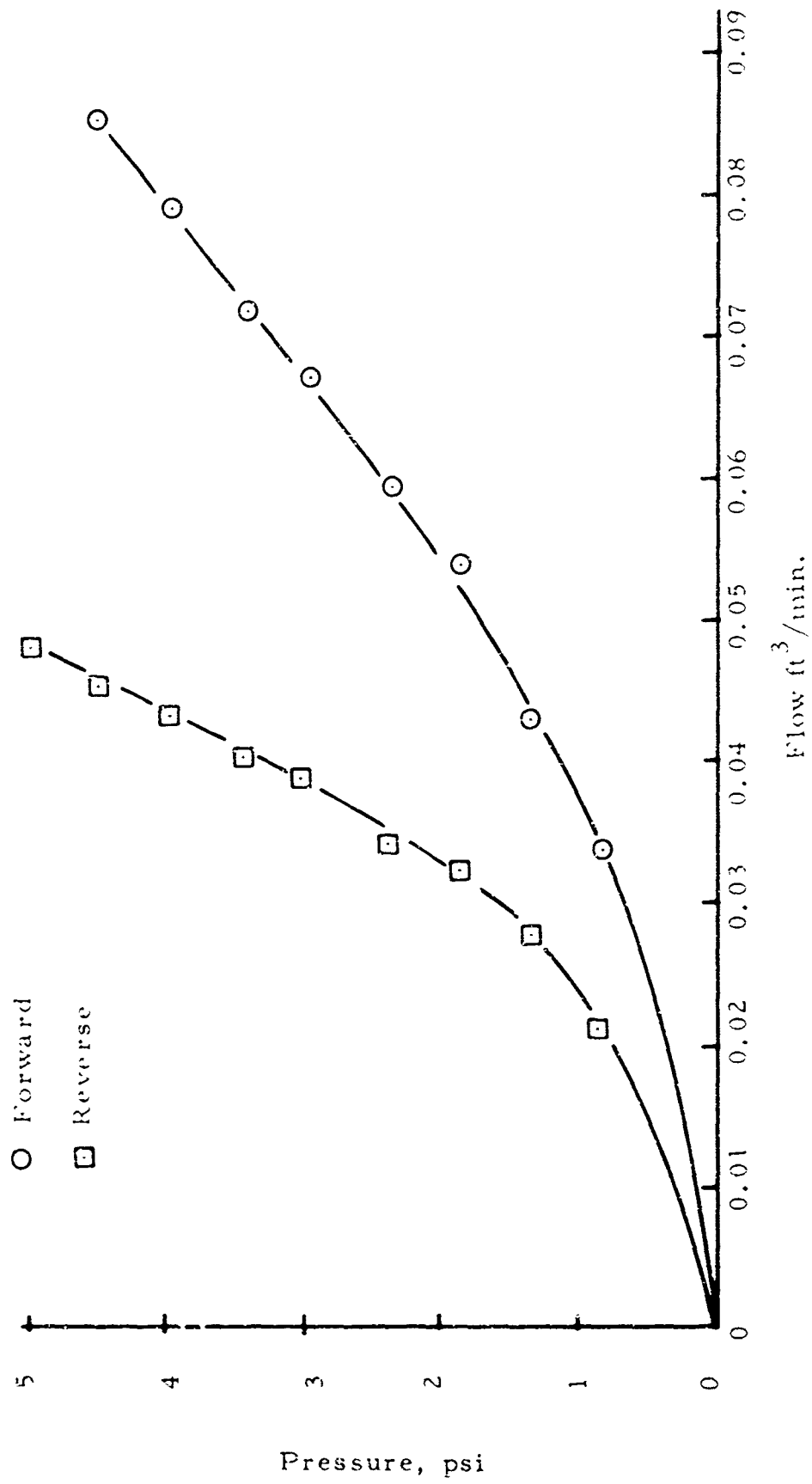


Fig. 124. Pressure-Flow Characteristics, Vortex Diode, Small Scale.

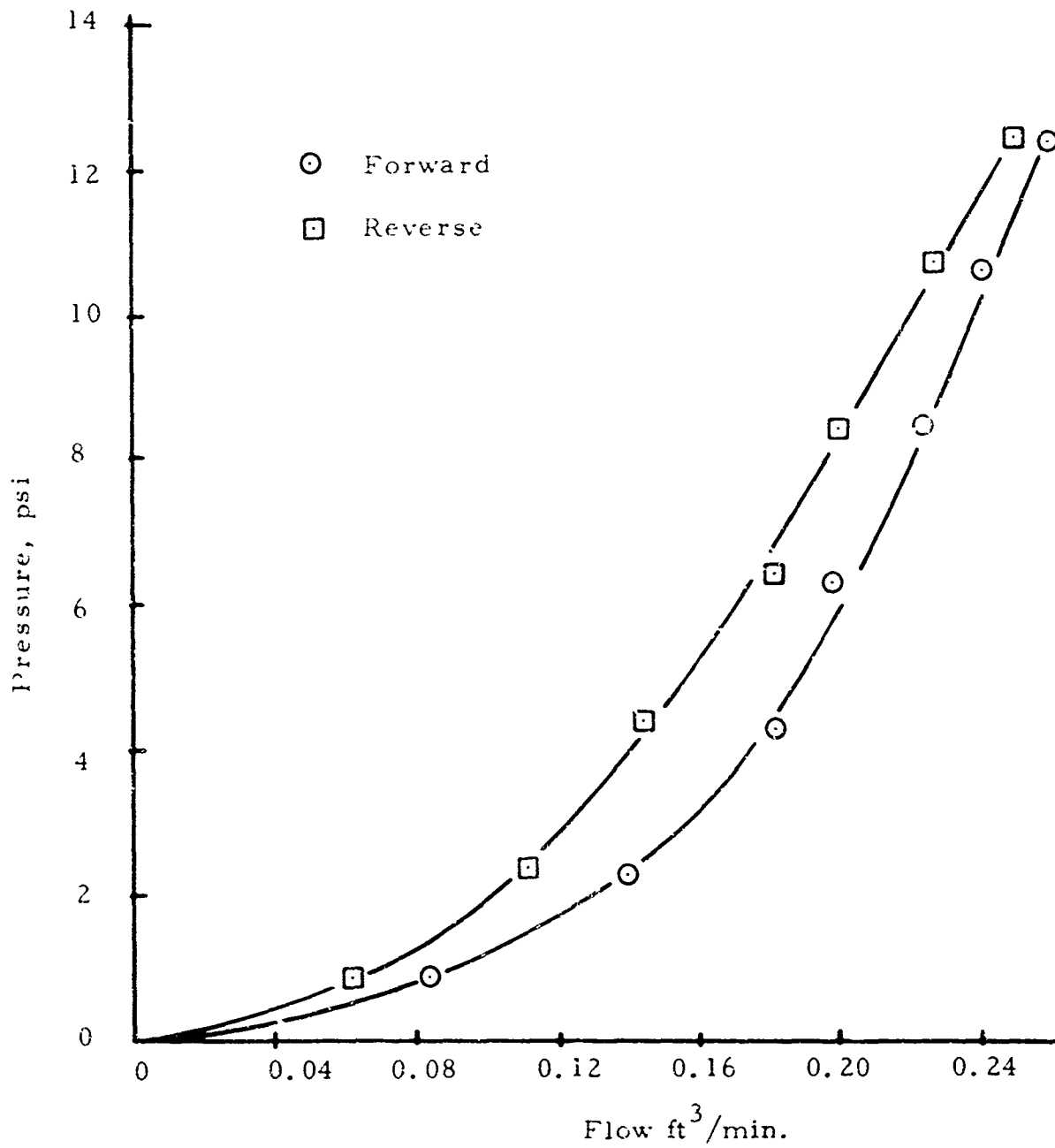


Fig. 125. Pressure-Flow Characteristics, Diffuser Diode, Small Scale.

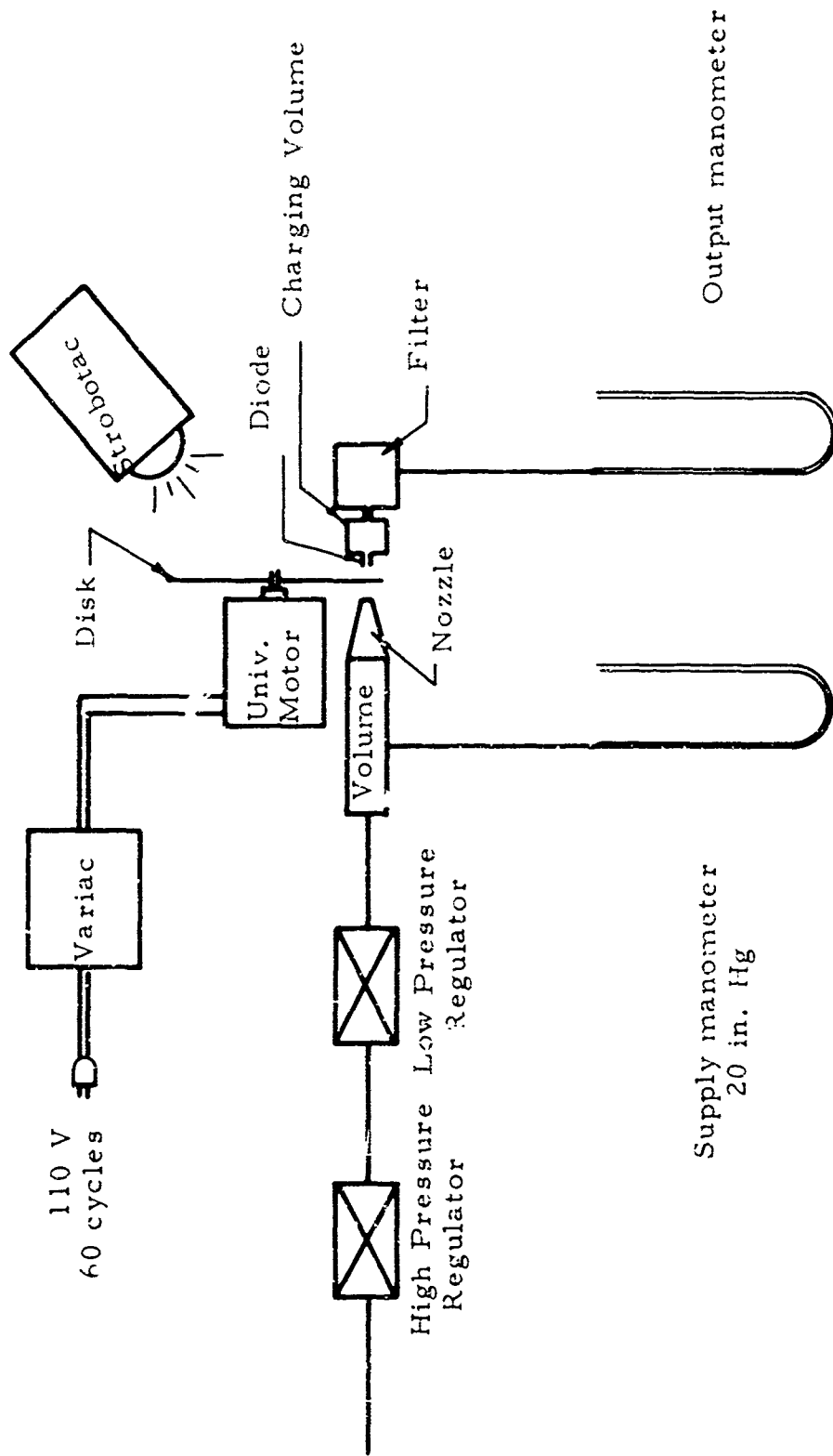
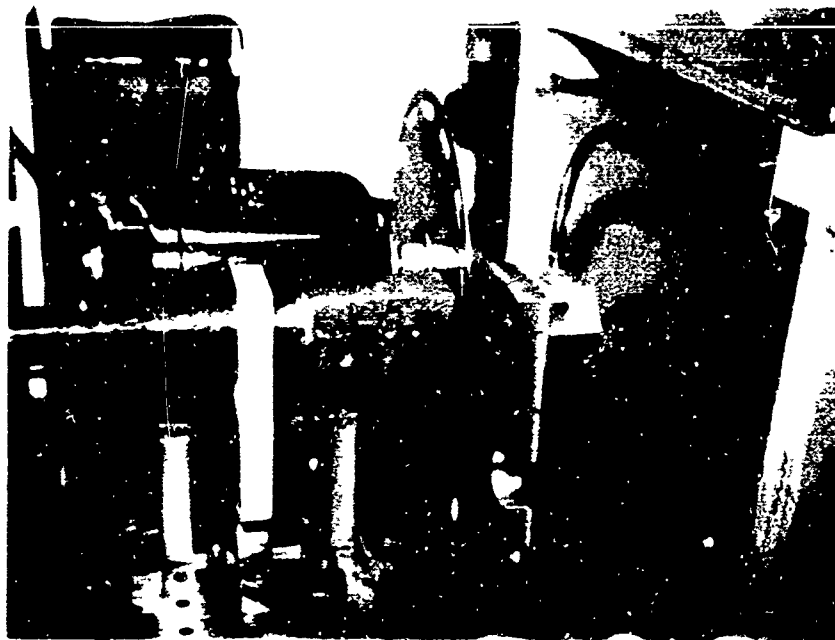


Fig. 126. Test Set Up Schematic.

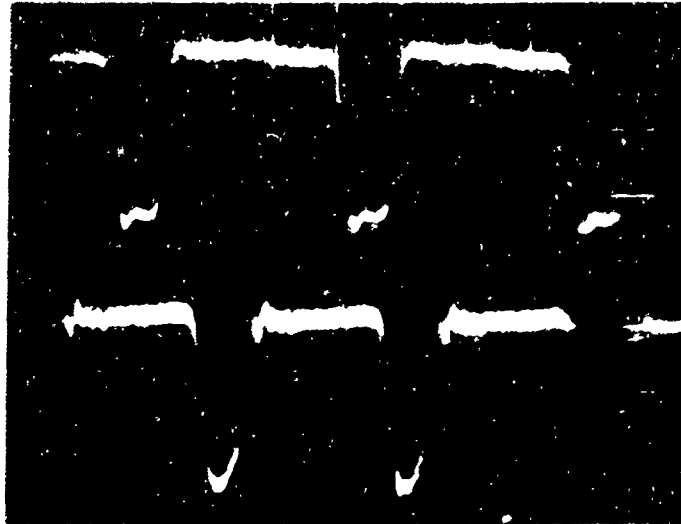


Pulse Generator with $\frac{a}{\gamma} = 1$ disc.



Section of $\frac{a}{\gamma} = 2-10$ disc.

Fig. 127. Pressure Pulse Generator.



55.6 cps

1724 cps

$$\frac{\alpha}{\delta} = 4$$



69 cps

1613 cps

$$\frac{\alpha}{\delta} = 6$$

Fig. 128. Signal From Pulse Generator

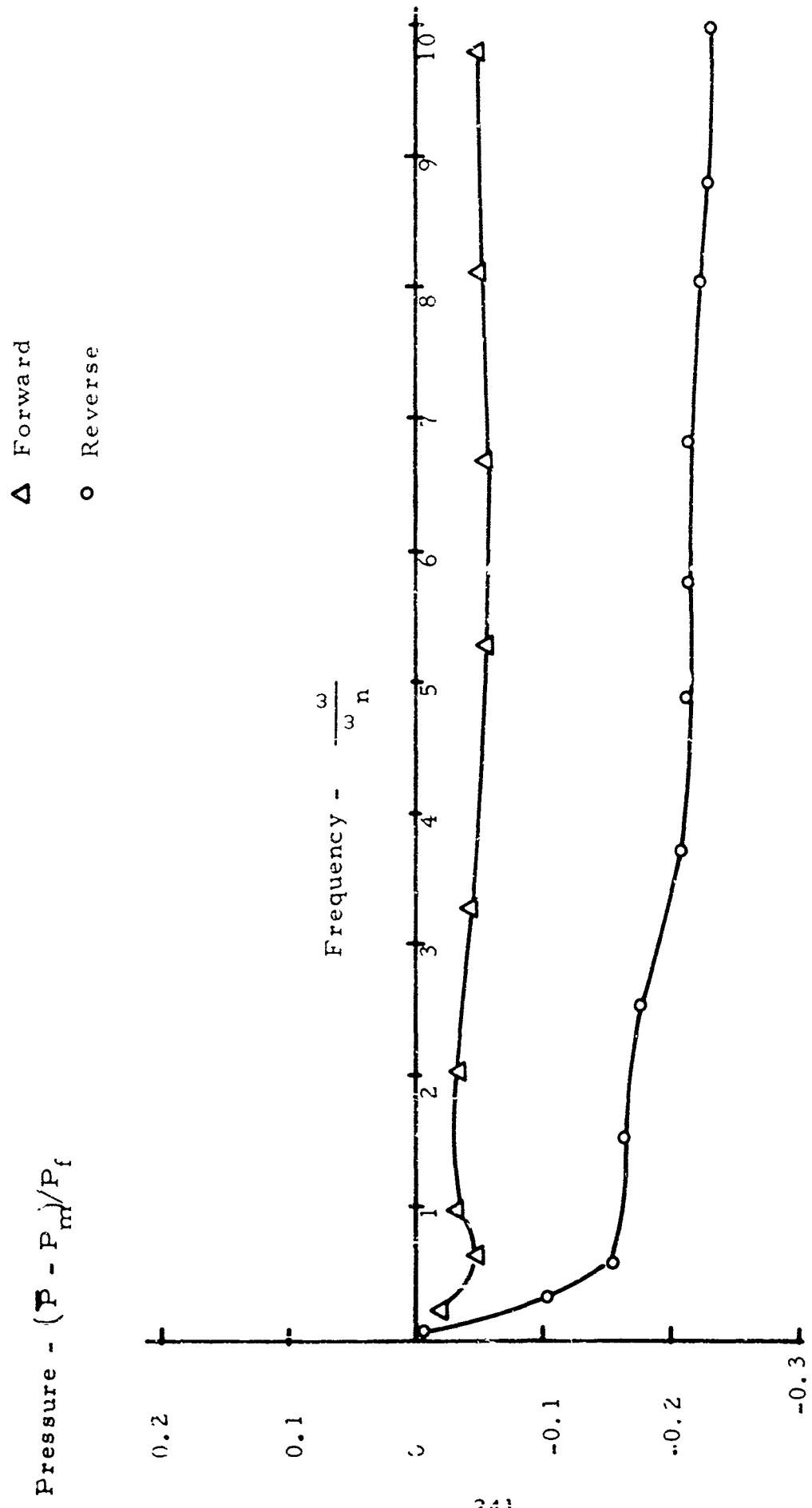


Fig. 129. Frequency Response, 2-D Nozzle Diode.

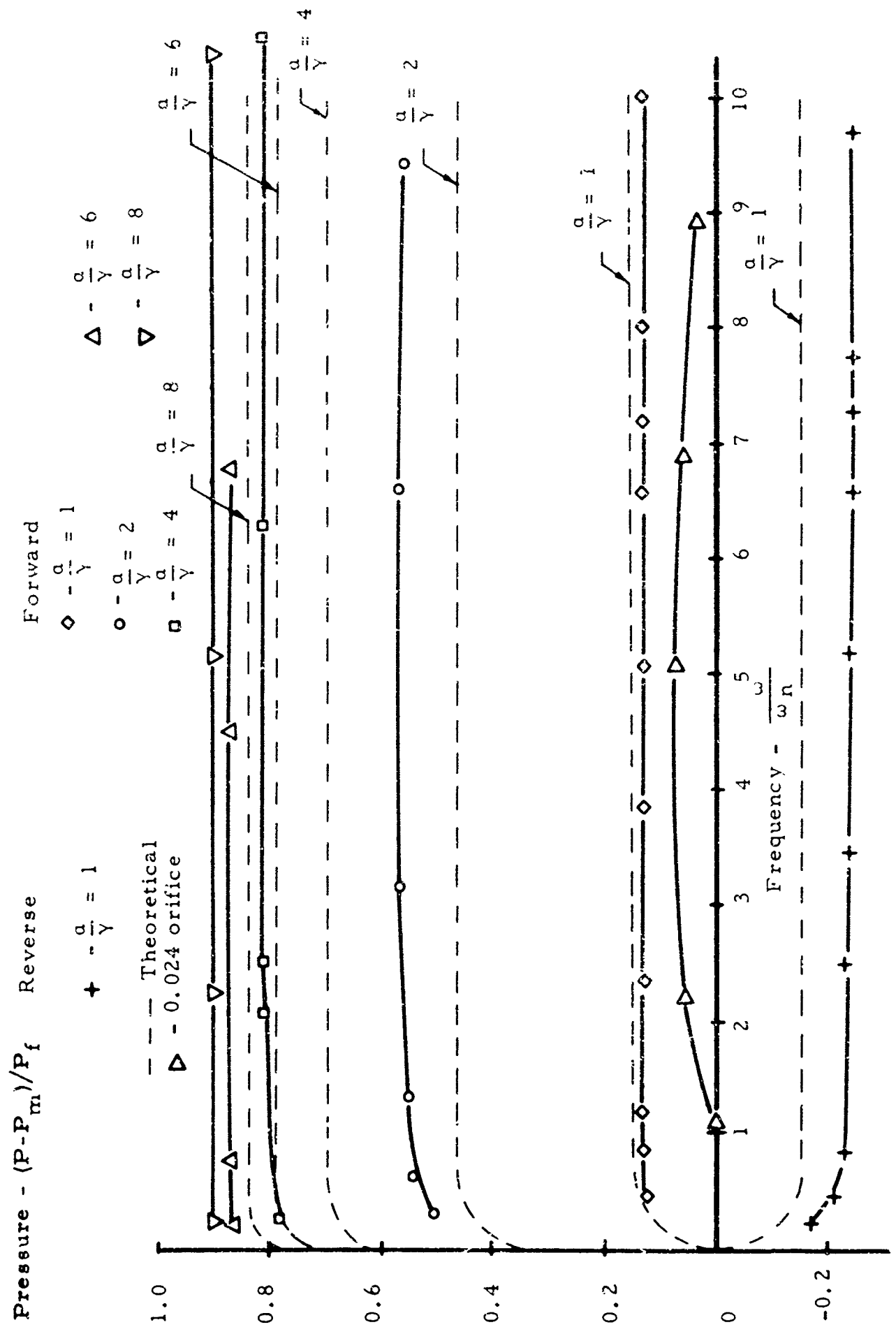


Fig. 130. Frequency Response, 3-D Nozzle Diode, (0.020).

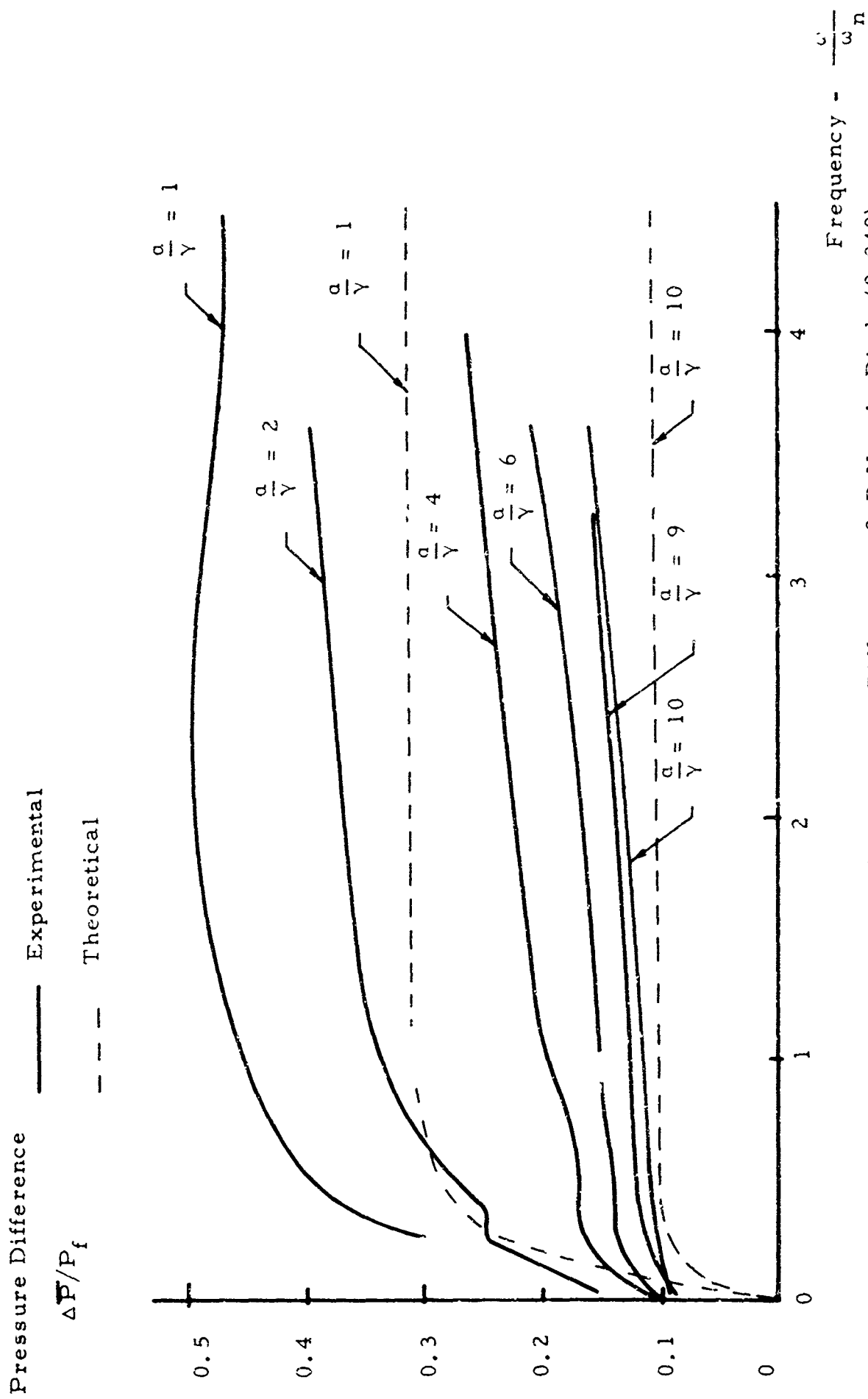


Fig. 131. Pressure Difference, 3-D Nozzle Diode (0.040).

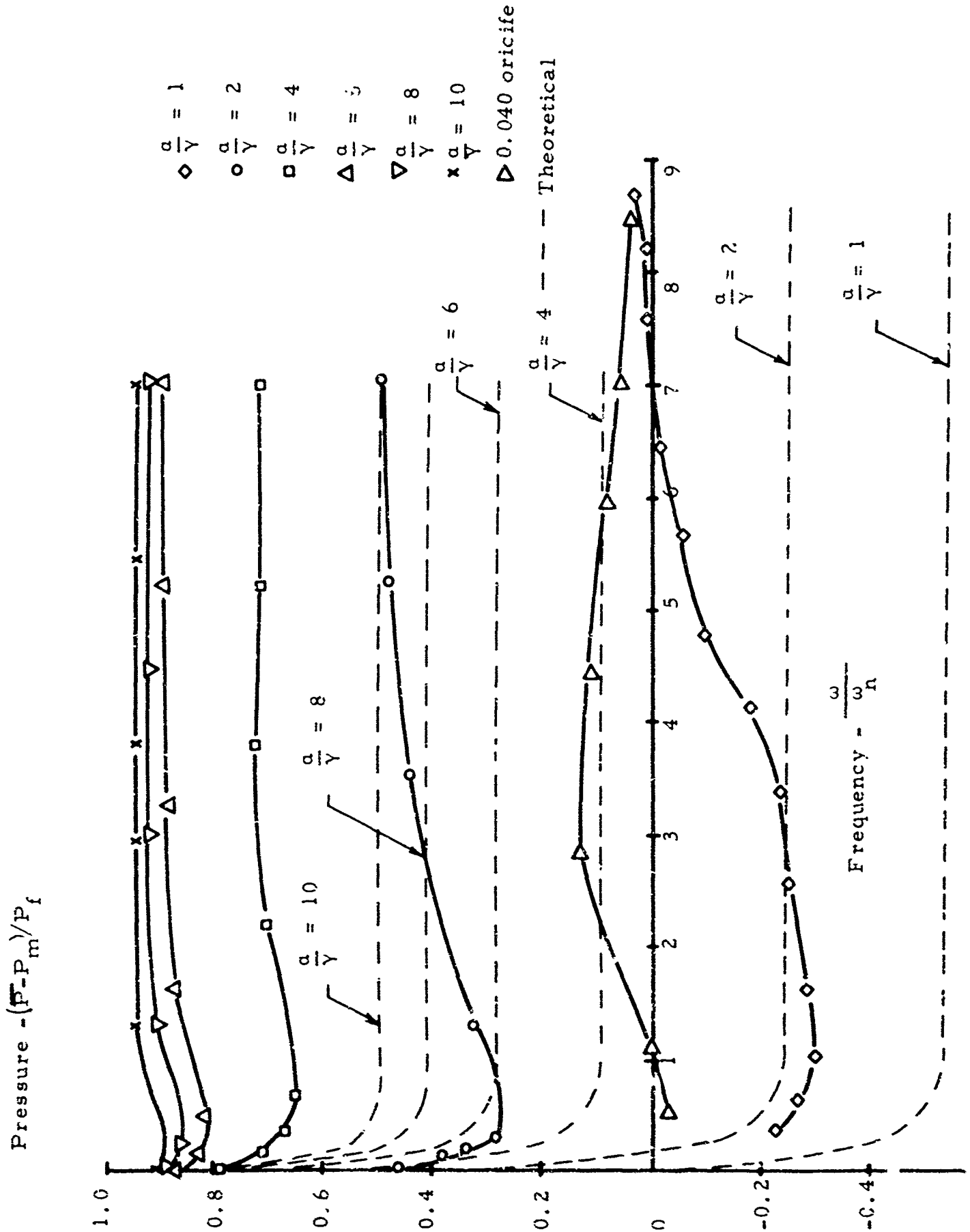


Fig. 132. Frequency Response, Vortex Diode, Reverse.

Pressure - $(\bar{P} - P_{in}) / P_f$

Experimental

- \diamond $\frac{a}{Y} = 1$
- \circ $\frac{a}{Y} = 2$
- \square $\frac{a}{Y} = 4$
- \triangle $\frac{a}{Y} = 6$
- ∇ $\frac{a}{Y} = 8$
- \times $\frac{a}{Y} = 10$
- \blacktriangleright - 0.024 orifice

--- Theoretical

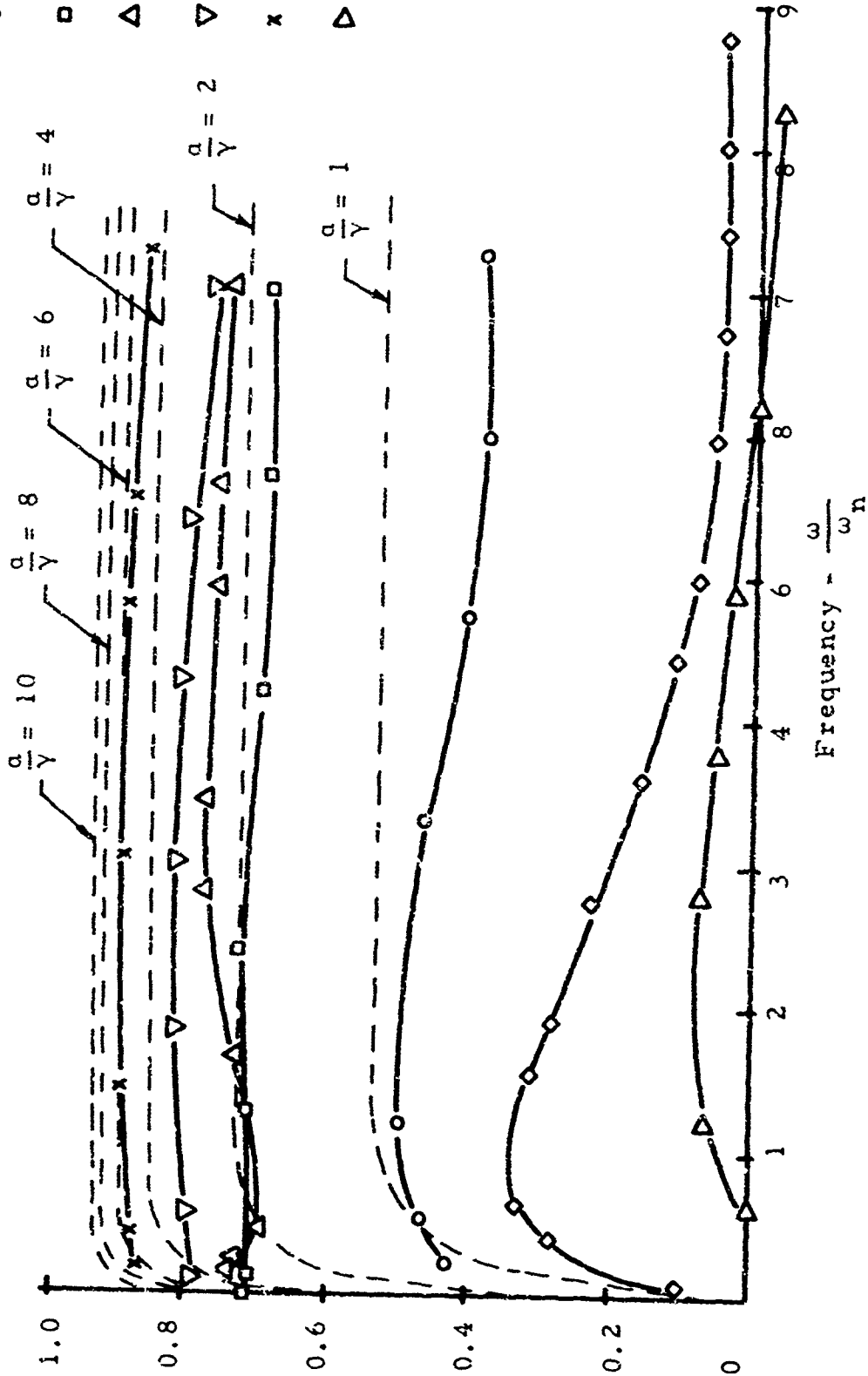


Fig. 133. Frequency Response, Vortex Diode, Forward.

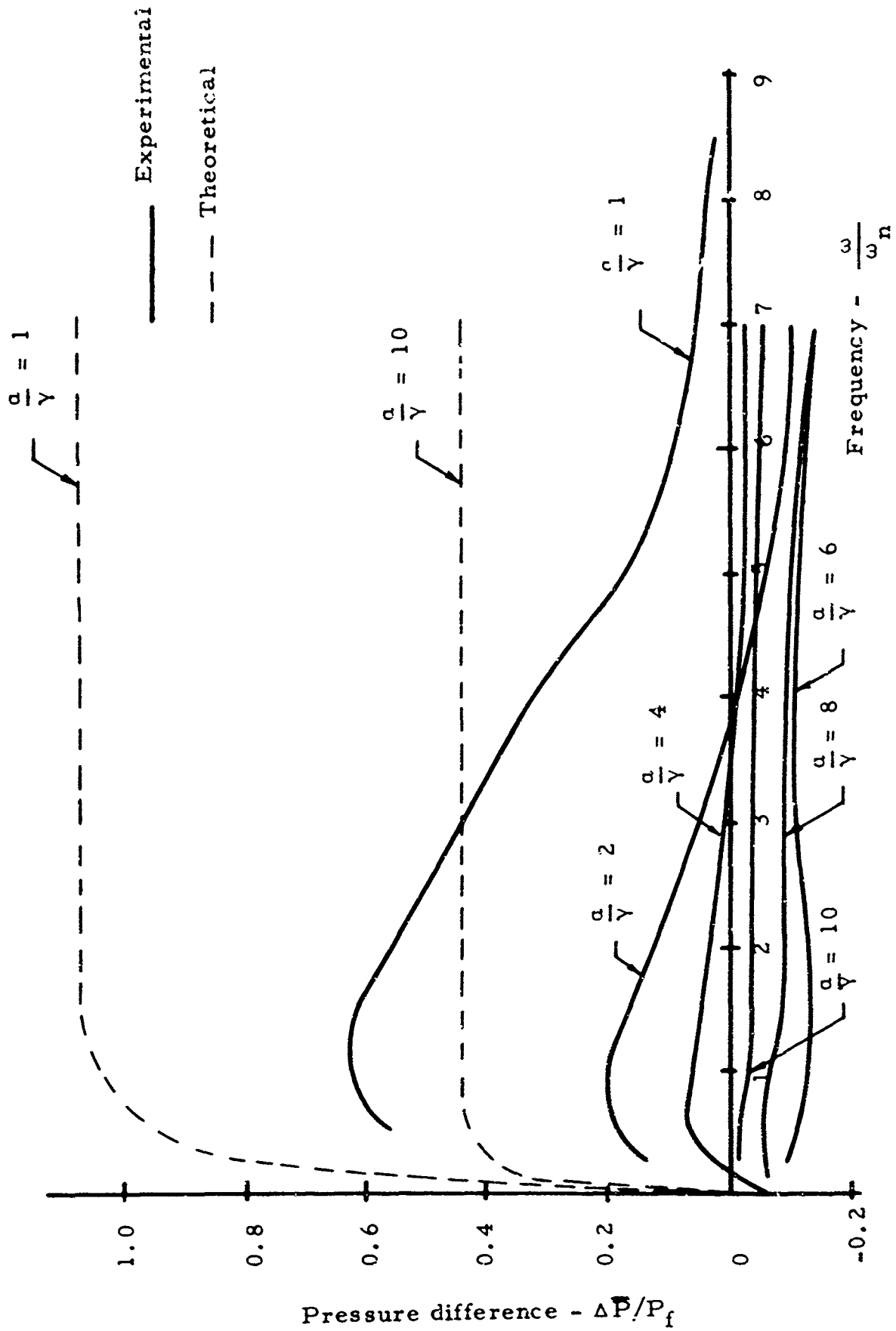


Fig. 134. Pressure Difference, Vortex Diode.

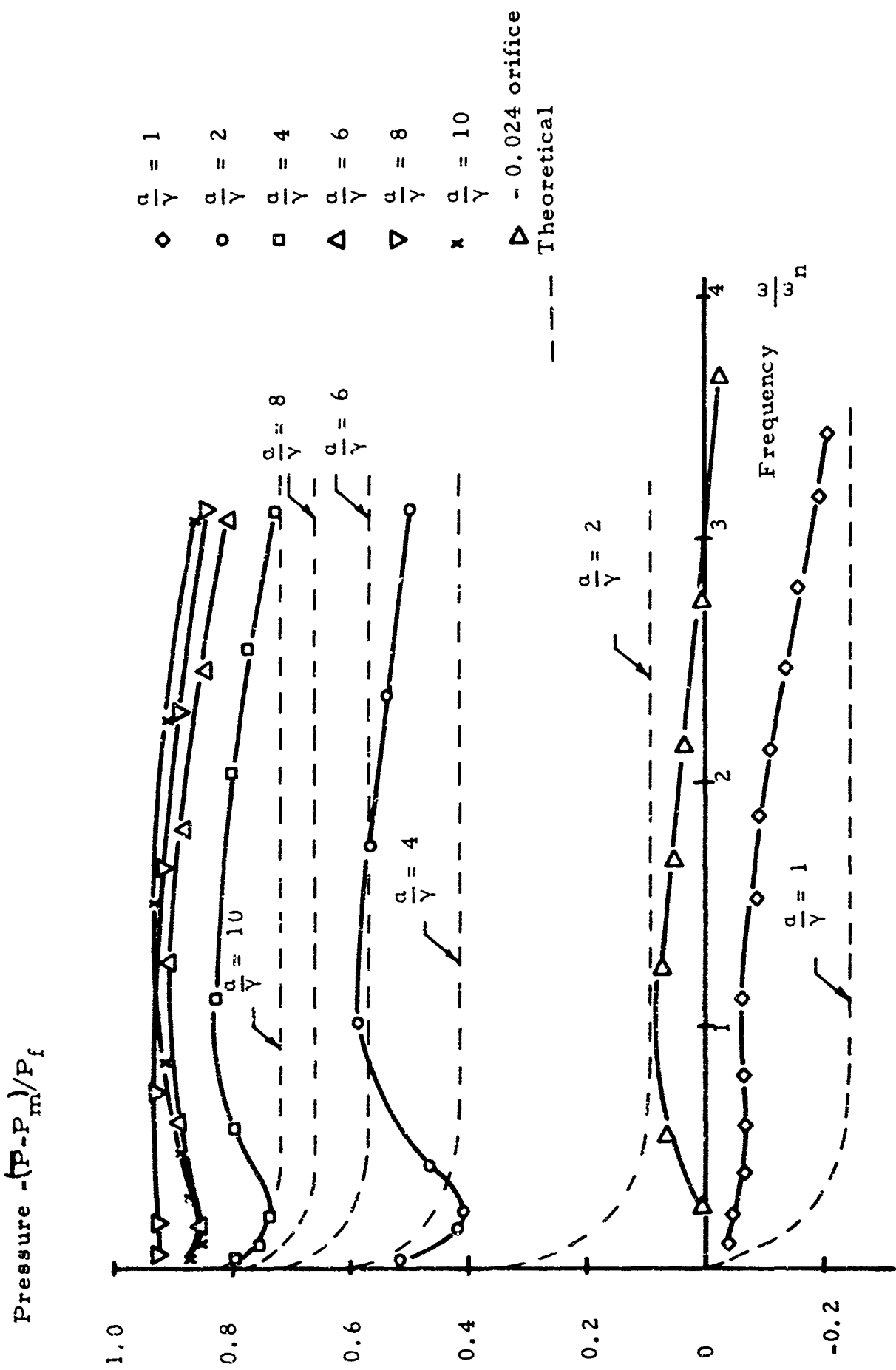


Fig. 135. Frequency Response, Diffuser Diode, Reverse.

Diode	Large Scale	Small Scale	Based On
Nozzle; 2-D	0.201×10^4	0.1065×10^4	Nozzle Exit Width
3-D (0.020)		0.409×10^4	Nozzle Exit Dia.
3-D (0.040)		0.819×10^4	Nozzle Exit Dia.
Vortex	1.32×10^4	0.0975×10^4	Tangential Slot Width
Diffuser	4.63×10^4	1.082×10^4	Small End Dia.

Table 2. Comparison of Maximum Reynolds Number
for Large and Small Scale Models

		LINEAR				NONLINEAR					
		τ_{av} (sec)	ω_n (cps)	β	$\frac{\Delta T}{\tau_{av}}$	τ_{av} (sec)	ω_n (cps)	β	$\frac{\Delta T}{\tau_{av}}$		
Diode	Direction										
Nozzle	Forward	0.0045	222	2.9	-0.488	0.00445	225	1.666	-0.1995		
2-D	Reverse	0.0045	222	0.345	0.488	0.00485	223	0.566	0.277		
Nozzle	Forward	0.00738	135.5	1.36	-0.1527	0.007855	127.2	1.165	-0.07625		
3-D(0.020)	Reverse	0.00738	135.5	0.735	0.1527	0.00788	126.8	0.81	0.105		
Nozzle	Forward	0.0021	476	1.37	-0.156	0.002024	494	1.136	-0.0637		
3-D(0.040)	Reverse	0.0021	476	0.73	0.156	0.002028	493	0.832	0.091		
Vortex	Forward	0.00404	247	3.33	-0.538	0.004635	216	1.75	-0.273		
	Reverse	0.00404	247	0.3	0.538	0.00468	214	0.5375	0.301		
Diffuser	Forward	0.001775	563	1.667	-0.25	0.002165	462				
	Reverse	0.001775	563	0.60	0.25	0.00223	449				

Table 3. Comparison of Linear and Nonlinear Adiabatic, Diode Characteristics

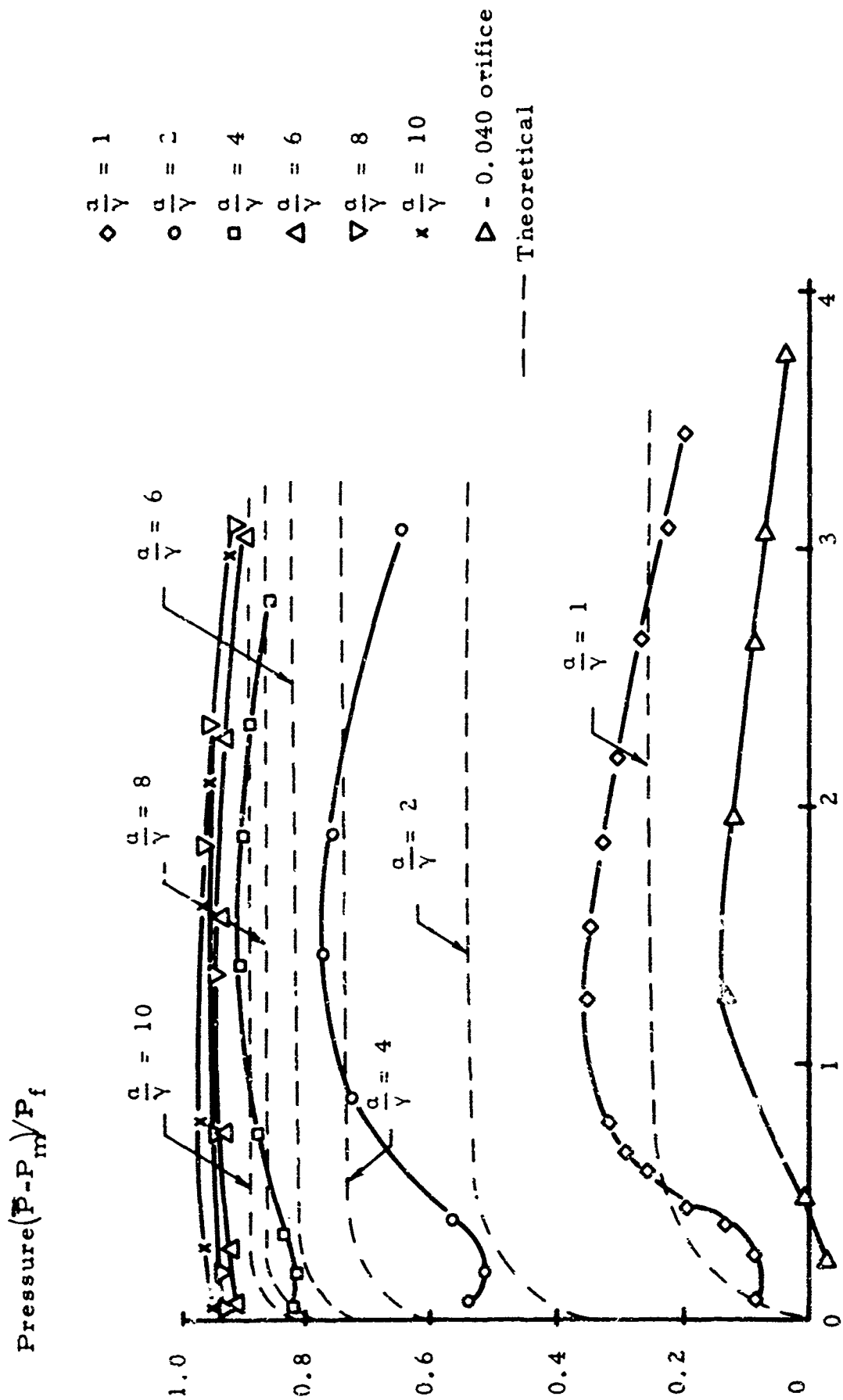


Fig. 136. Frequency Response, Diffuser, Diode, Forward.

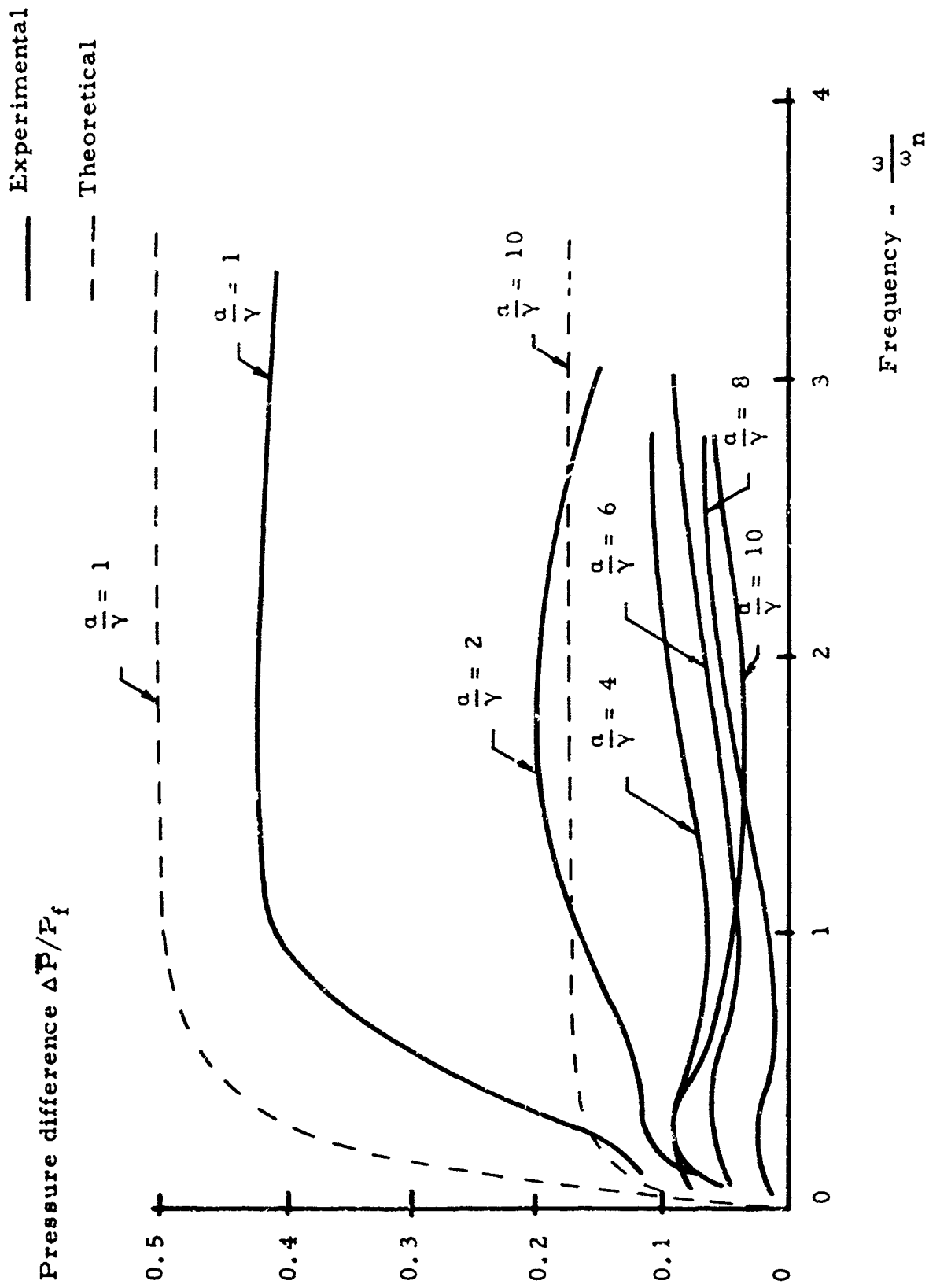


Fig. 137. Pressure Difference, Diffuser Diode.

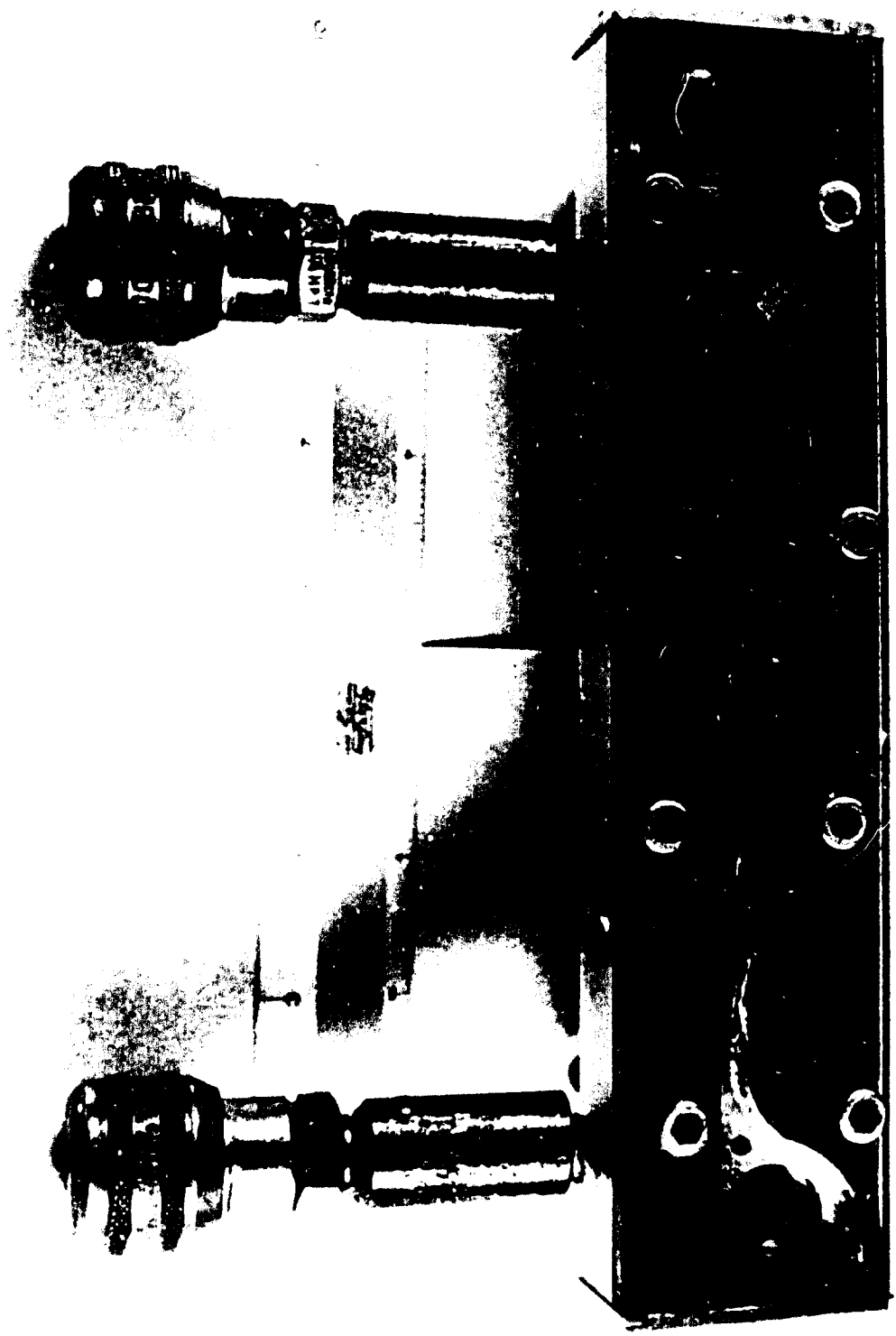


Fig. 135. Photograph of Tesla Diode.

Best Available Copy

is the narrowest width of the main channel, which is equal to the depth of the model, namely one-quarter inch).

The results are given in Fig. 139. In the laminar flow range ($Re < 100$) the diode is almost totally ineffective. Its effectiveness increases with Reynold's number as expected; the limiting value of the ratio of pressure drops at high flows was not actually found, but must be near 5.0. This is adequate for useful fluid diode sensors, although a somewhat higher value would be preferable. More stages of cusps should help.

A fundamental cause of the fall-off in performance of fluid diode sensors at high frequency can be traced to this Reynold's number effect. As frequency ascends, the flow rate of fluid sloshing back and forth is reduced, and the effectiveness of the diode consequently is diminished. A satisfactory design rule would be to expect significant attenuation in the performance of diode sensors when the peak Reynold's number falls below about 2000. This may occur at an insufficiently high frequency. Increasing the size of the device decreases this problem, but introduces wave-speed limitations. A compromise optimum size must exist.

Fig. 138. Photograph of Tesla Diode.

Pressure, drop, psi

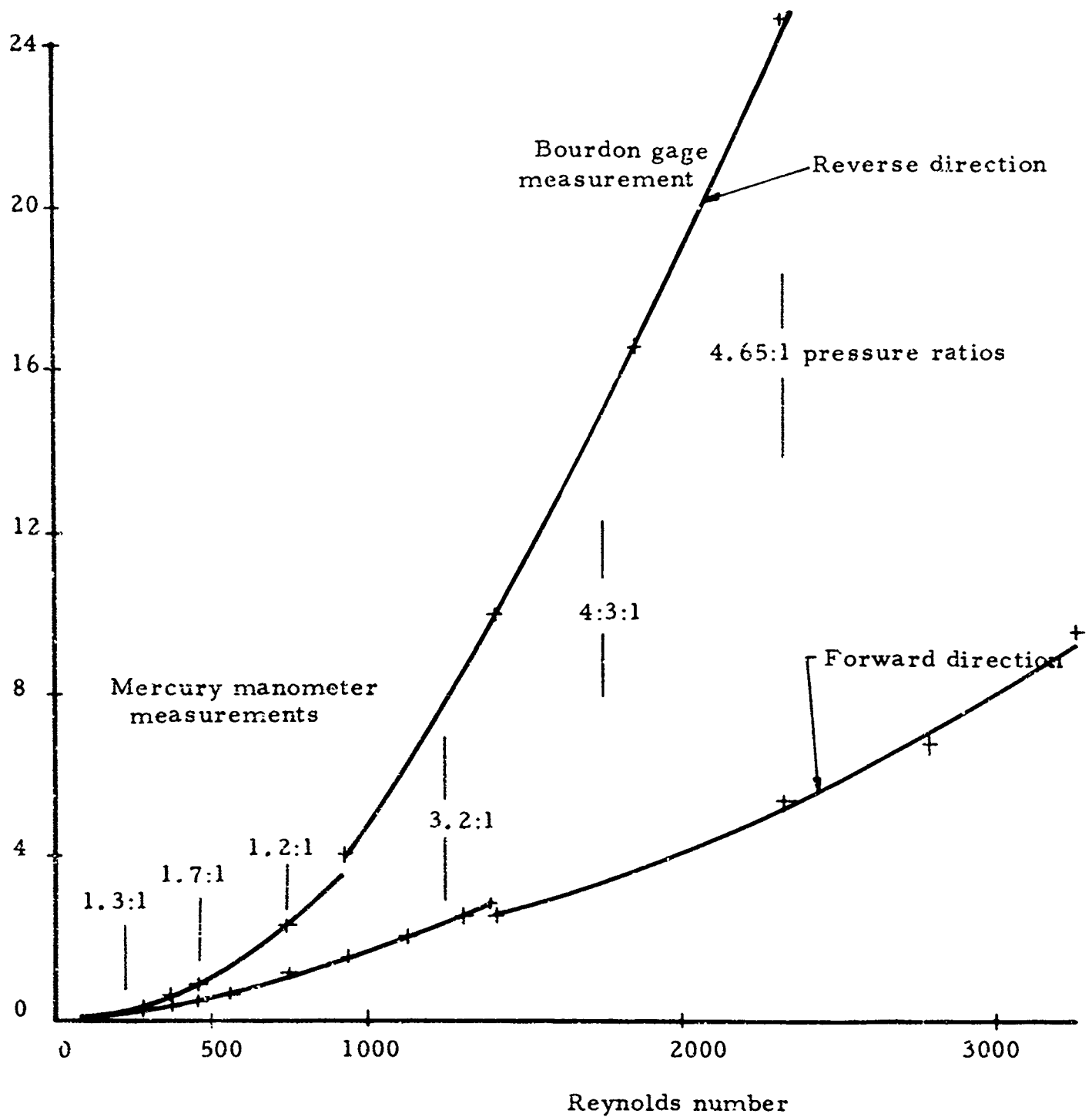


Fig. 139. Results of Static Measurements of Tesla Diode.

8. REFERENCES

1. Research and Development of Pneumatic Jet Relay System for Propulsion System Control, Engineering Projects Laboratory Report No. DSR 9159-1, Dept. of Mech. Engr., Mass. Inst. of Tech., Cambridge, Mass., 1 April 1962 - 31 March 1963. Prepared under Contract AF 33(657)-8384 for Power and Propulsion Laboratory, ASD, AFSC, Wright-Patterson Air Force Base, Ohio.
2. Basic Research and Development in Fluid Power Control for the United States Air Force for the period 1 October 1962 - 31 January 1963. Engineering Projects Laboratory, Mass. Inst. of Tech., Cambridge, Mass. ASD-TDR-63-609.
3. Reid, K. N. Jr., "Analytical and Experimental Study of the Static and Dynamic Performance of a Jet-Receiver-Diffuser," Proposal for Sc.D. Thesis, Dept. of Mech. Engr., Mass. Inst. of Tech., Cambridge, Mass., April 1963.
4. Grimmett, H. L., Entrainment in Air Jets. Thesis (Ph. D.), University of Illinois, Urbana, Illinois, 1950.
5. Reid, E. G., "Annular Jet Ejectors," NACA TN 1949, (1949).
6. Alexander, L. G., Baron, T., and Comings, E. W., Transport of Momentum, Mass, and Heat in Turbulent Jets. Engineering Experiment Station, University of Illinois, Technical Report No. 8, Contract N6-ori-71, Task Order No. XI, Office of Naval Research, September 1, 1950.
7. Alexander, L. G., Comings, E. W., Grimmett, H. L., and White, E. A., Transfer of Momentum in Jet of Air Issuing into a Tube, Technical Report No. 11, Contract N6-ori-71, Task Order No. XI, Office of Naval Research, Dept. of Navy, Flight Research Laboratory, Dept. of the Air Force, May 1, 1952.

8. Moissis, R. and Griffith, P., "Entrance Effects in a Two-Phase Slug Flow," ASME Paper No. 61-SA-30, presented at the ASME Summer Annual Meeting, Los Angeles, Calif., June 11-15, 1961.
9. Schlichting, H., Boundary Layer Theory, McGraw-Hill Book Co., Inc., 1960. (Translated by J. Kestin).
10. Reichardt, H., "On a New Theory of Free Turbulence," Journal of the Royal Aeronautical Society, Vol. XLVII, No. 390, June 1943.
11. Reddick, H. W., and Miller, F. H., Advanced Mathematics for Engineers, John Wiley and Sons, New York, 1955.
12. Patterson, G. N., "Modern Diffuser Design," Aircraft Engineering, Vol. 10, 1938, pp. 267-273.
13. Robertson, J. M., and Ross, D., "Water Tunnel Diffuser Flow Studies, Part I - Review of the Literature," Ordnance Research Laboratory, Penn State University, Report 7958-139, May 1949.
14. Kline, S. J., Abbott, D. E., and Fox, R. W., "Optimum Design of Straight-Walled Diffusers," Trans. ASME, Journal of Basic Engineering, March 1960, pp. 201-209.
15. Gibson, A. H., "On the Flow of Water Through Pipes and Passages Having Converging or Diverging Boundaries," Proc. Roy. Soc., Series A, Vol. 83, 1910. "On the Resistance to Flow of Water Through Pipes or Passages Having Divergent Boundaries," Trans. Roy. Soc., Edinburgh, Vol. XLVIII, 1911 - 1913.
16. Peters, H., "Conversion of Energy in Cross-Sectional Divergences under Different Conditions of Inflow," NACA TM 737, March 1934. Translated from Ingenieur - Archiv., Vol. II, 1931, pp. 92-107.
17. Basic Research and Development in Fluid Power Control for the United States Air Force for the period 1 June 1962 - 30 September 1962. Engineering Projects Laboratory, Mass. Inst. of Tech., ASD-TDR-63-100.

18. Leibowitz, H. , The Effect of Geometric Parameters on the Static Performance of an Axi-Symmetric Jet Modulator.
Thesis (S. B.), Dept. of Mech. Engr. , Mass. Inst. of Tech. ,
May 1963.
19. Brown, F. T. , "Fluid Jet Modulators and Systems," Chapter
16 of Special Notes on Instrumentation and Control for a Two-
Week Program held at the Mass. Inst. of Tech. , August 17 -
30, 1963.
20. Shapiro, A. H. , The Dynamics and Thermodynamics of
Compressible Fluid Flow, Vol. I. , The Ronald Press Co. ,
New York, 1953.
21. Paynter, H. M. , "Methods and Results from M. I. T. Studies
in Unsteady Flow," Journal Boston Society of Civil Engrs. ,
Vol. XXXIX, No. 2, April 1952.
22. Rule, J. T. , and Coons, S. A. , Graphics, McGraw-Hill Book
Co. , 1961.
23. Brown, F. T. , "Hydraulic and Pneumatic Transmission Lines,"
Special Notes for a Two-Week Program on Fluid Power Control
held at the Mass. Inst. of Tech. , June 1960.
24. Brown, F. T. , "The Transient Response of Fluid Lines," Trans.
ASME, Vol. 84, Series D. , No. 4, December 1962.
25. Robertson, J. M. , and Ross, D. , "Effect of Entrance Conditions
on Diffuser Flow," Trans. ASCE, Vol. 118, 1953, pp. 1063-1097.
26. Rohmann, C. P. , and Grogran, E. C. , "On the Dynamics of
Pneumatic Transmission Lines," Trans. ASME, May 1957.
27. Shapiro, A. H. , Siegel, R. , and Kiene, S. J. , "Friction Factor
in the Laminar Entry Region of a Smooth Tube," Proceedings
of the Second U. S. National Congress of Applied Mechanics,
June 1954, pp. 733-741.
28. Kinsier, L. E. , and Frey, A. R. , Fundamentals of Acoustics,
John Wiley and Sons, 1962.
29. Crandall, S. H. , Engineering Analysis, McGraw-Hill Book Co. ,
Inc. , 1956.

30. Kopal, Z., Numerical Analysis, John Wiley and Sons, Inc., New York, 1961, Chapter III.
31. Hildebrand, F. B., Introduction to Numerical Analysis, McGraw-Hill Book Co., New York, 1956, Chapter 3, p. 82.
32. Hildebrand, F. B., Methods of Applied Mathematics, Prentice-Hall, Inc., New Jersey, 1962, pp. 322-328.
33. Paynter, H. M., Analysis and Design of Engineering Systems, M. I. T. Press, Cambridge, Mass., 1960, p. 263.
34. Paynter, H. M., "On an Analogy Between Stochastic Processes and Monotone Dynamic Systems," Regelungstechnik, R. Oldenbourg (pub), Munich, 1957, pp. 243-250.
35. Brown, F. T., Pneumatic Pulse Transmission with Bistable Jet Relay Reception and Amplification. Thesis (Sc. D.), Dept. of Mech. Engr., Mass. Inst. of Tech., May 1962.
36. Nelson, S. E., The Step Responses of Liquid-Filled Lines. Thesis (S.M.), Dept. of Mech. Engr., Mass. Inst. of Tech., January 1964.
37. Brown, F. T., "On the Stability of Fluid Systems," Harry Diamond Laboratories' Symposium on Fluid-Jet Amplifiers and Systems, available Washington 25, D. C.
38. Brown, F. T., Gurski, R. J., Reid, K. N., and Bails, W. B., "Research and Development of Pneumatic Jet Relay System for Propulsion System Control," Progress Report to the Air Force under contract DSR 9159, March 1963.
39. Simson, A. K., A Theoretical Study of the Design Parameters of Subsonic Pressure Controlled, Fluid Jet Amplifiers. Thesis (Ph. D.), Dept. of Mech. Engr., Mass. Inst. of Tech., July 1963.
40. Brown, F. T., Pneumatic Pulse Transmission with Bistable-Jet Relay Reception and Amplification. Thesis (Sc. D.), Dept. of Mech. Engr., Mass. Inst. of Tech., May 1962.

41. VanKoevering, A. R., Experimental Load Characteristics of Fluid Jet Amplifiers. Thesis (S. M.), Dept. of Mech. Engr., Mass. Inst. of Tech., August, 1962.
42. Blackburn, J. F., Reethof, G., and Shearer, J. L., Fluid Power Control, Technology Press of M. I. T., and Wiley, New York, 1960.
43. Miner and Seastone, Handbook of Engineering Materials, John Wiley and Sons, 1955.
44. Roark, R. J., Formulas for Stress and Strain, McGraw-Hill Book Co., New York, 1959, Table VI.
45. DenHartog, J. P., Class Notes for Advanced Mechanics Course, Dept. of Mech. Engr., Mass. Inst. of Tech., 1964.
46. Shapiro, A. H., The Dynamics and Thermodynamics of Compressible Fluid Flow, Ronald Press, New York 1953, Vol. 1, Appendix B2.